

VORTICITY DYNAMICS AND CONTROL  
OF DYNAMIC STALL

NEAR TR 482

by

Patrick H. Reisenhel

Final Report

August 1994



Prepared under Contract DAAL03-92-C-0013

For

U.S. Army Research Office  
P.O. Box 12211  
Research Triangle Park, NC 27709-2211

19941128 133

APPROVED FOR PUBLIC RELEASE  
DISTRIBUTION UNLIMITED

NIELSEN ENGINEERING & RESEARCH, INC.  
526 Clyde Avenue, Mountain View, CA 94043-2212  
Telephone: (415) 968-9457 • Facsimile: (415) 968-1410

DTIC QUALITY INSPECTED 5

THE VIEWS, OPINIONS, AND/OR FINDINGS CONTAINED IN THIS REPORT ARE THOSE OF THE AUTHOR(S) AND SHOULD NOT BE CONSTRUED AS AN OFFICIAL DEPARTMENT OF THE ARMY POSITION, POLICY, OR DECISION, UNLESS SO DESIGNATED BY OTHER DOCUMENTATION

REPORT DOCUMENTATION PAGE				Form Approved OMB No. 0704-0188	
<small>Public reporting burden for this collection of information is estimated to average 1 hour per response, including the time for reviewing instructions, searching existing data sources, gathering and maintaining the data needed, and completing and reviewing the collection of information. Send comments regarding this burden estimate or any other aspect of this collection of information, including suggestions for reducing this burden, to Washington Headquarters Services, Directorate for Information Operations and Reports, 1215 Jefferson Davis Highway, Suite 1204, Arlington, VA 22202-4302, and to the Office of Management and Budget, Paperwork Reduction Project (0704-0188), Washington, DC 20503.</small>					
1. AGENCY USE ONLY (Leave blank)		2. REPORT DATE 94Aug18		3. REPORT TYPE AND Final Report 15 Apr 92 - 14 Jun 94	
4. TITLE AND SUBTITLE Vorticity Dynamics and Control of Dynamic Stall				5. FUNDING NUMBERS	
6. AUTHOR(S) Dr. Patrick H. Reisenhel				DAAL03-92-C-0013	
7. PERFORMING ORGANIZATION NAME(S) AND ADDRESS(ES) Nielsen Engineering & Research, Inc. 526 Clyde Avenue Mountain View, CA 94043-2212				8. PERFORMING ORGANIZATION REPORT NUMBER TR482 NEAR Contract No. 2398/C	
9. SPONSORING/MONITORING AGENCY NAME(S) AND ADDRESS(ES) U.S. Army Research Office P.O. Box 12211 Research Triangle Park, NC 27709-2211				10. SPONSORING/MONITORING AGENCY REPORT NUMBER ARO 29049.4-EG-5	
11. SUPPLEMENTARY NOTES The view, opinions and/or findings contained in this report are those of the author(s) and should not be construed as an official Department of the Army position, policy, or decision, unless so designated by other documentation.					
12a. DISTRIBUTION/AVAILABILITY STATEMENT Approved for public release; distribution unlimited.				12b. DISTRIBUTION CODE	
13. ABSTRACT (Maximum 200 words)  The goal of the research was to understand key issues of vorticity dynamics prior to, during, and after the initiation of dynamic stall. The first portion of this work examined the applicability of indicial theory to the prediction of dynamic stall. The research focused on extending the semi-analytical formalism of indicial theory to predict the vorticity fluxes and the vorticity accumulation at the leading edge during unsteady maneuver. In the second portion of this work, highly accurate two-dimensional solutions of the Navier-Stokes equations were used on a model problem to investigate the Reynolds number scaling of incipient flow separation between $Re = 50,000$ and $Re = 800,000$ . This portion of the work was motivated by the suggestion that the appearance of eruptive plumes of vorticity at high Reynolds number might be critical to the formation of the dynamic stall vortex. The results of the research appear to contradict the hypothesis that a form of Reynolds number bifurcation must take place at some intermediate laminar Reynolds number. Instead, self-similar behavior was observed, at least up to the time of formation of the primary stall vortex.					
14. SUBJECT TERMS unsteady flow separation, dynamic stall, mathematical modeling, computational fluid dynamics				15. NUMBER OF PAGES 128	
				16. PRICE CODE	
17. SECURITY CLASSIFICATION OF REPORT UNCLASSIFIED	18. SECURITY CLASSIFICATION OF THIS PAGE UNCLASSIFIED	19. SECURITY CLASSIFICATION OF ABSTRACT UNCLASSIFIED	20. LIMITATION OF ABSTRACT UL		

## TABLE OF CONTENTS

	page
Title Page .....	1
Report Documentation Page .....	3
Table of Contents .....	4
List of Appendices and Illustrations .....	5
STATEMENT OF THE PROBLEM STUDIED .....	9
SUMMARY OF MOST IMPORTANT RESULTS .....	9
Indicial Theory and the Prediction of Dynamic Stall .....	10
Reynolds Number Effects on a Model Problem of Leading Edge Stall .....	11
PUBLICATIONS .....	15
PARTICIPATING SCIENTIFIC PERSONNEL .....	16
Report of Inventions .....	17
Bibliography .....	18
Appendices .....	21

Accession For	
NTIS CRA&I	<input checked="" type="checkbox"/>
DTIC TAB	<input type="checkbox"/>
Unannounced	<input type="checkbox"/>
Justification .....	
By .....	
Distribution /	
Availability Codes	
Dist	Avail and/or Special
A-1	

## **LIST OF APPENDICES AND ILLUSTRATIONS**

### **List of Appendices**

Appendix A: Towards a Semi-Analytic Tool For the Prediction of Dynamic Stall (AIAA Paper No. 94-0537)

Appendix B: A Study of Reynolds Number Effects on Incipient Leading Edge Stall (AIAA Paper No. 94-2339)

Appendix C: Complement to AIAA Paper No. 94-2339

Appendix D: Further Results on the Reynolds Number Scaling of Incipient Leading Edge Stall

### **List of Figures**

Fig. C.1 Comparison of Instantaneous Vorticity Contours Computed Using ARC2D (Top) and ARC2D/8E (Bottom),  $tU/c = 0.030$ ,  $Re = 400,000$ . (Spacing between contours is  $\Delta\Omega = 80$ ; dashed lines indicate negative levels).

Fig. C.2(a) Comparison of Instantaneous Vorticity Contours Computed Using ARC2D (Top) and ARC2D/8E (Bottom),  $tU/c = 0.051$ ,  $Re = 400,000$ . (Spacing between contours is  $\Delta\Omega = 80$ ; dashed lines indicate negative levels). Continued on next page.

Fig. C.2(b) Detailed Comparison of Instantaneous Vorticity Contours Computed Using ARC2D (Top) and ARC2D/8E (Bottom),  $tU/c = 0.051$ ,  $Re = 400,000$ . Continued from previous page.

Fig. C.3 Comparison of Instantaneous Vorticity Contours Computed Using ARC2D (Top) and ARC2D/8E (Bottom),  $tU/c = 0.060$ ,  $Re = 400,000$ . (Spacing between contours is  $\Delta\Omega = 80$ ; dashed lines indicate negative levels).

Fig. C.4 Time-Step Sensitivity of Surface Flow Topology Evolution Calculated with ARC2D, and Comparison with ARC2D/8E Results. (Lines are zero skin friction contours;  $\Delta t_a$  is time-step based on freestream speed of sound).

Fig. C.5 Reynolds Number Scaling of the Time of Appearance of Incipient Primary (PS1) and Secondary (SS1, SS2, SS3, SS4) Separation Bubbles.

Fig. C.6 Comparison of Vorticity Fields Near the Time Beyond the End of Stage II for  $Re = 50,000$ ,  $Re = 100,000$ ,  $Re = 200,000$ , and  $Re = 400,000$ . The (Vortex-Induced) Formation of Eruptive Plumes of Vorticity is Visible at the three highest Reynolds Numbers.

Fig. C.7 Instantaneous Vorticity Field Beyond Stage II at  $tU/c = 0.078$ ,  $Re = 400,000$ .

Fig. C.8 Instantaneous Vorticity Field Beyond Stage II at  $tU/c = 0.081$ ,  $Re = 400,000$ .

- Fig. C.9 Instantaneous Vorticity Field Beyond Stage II at  $tU/c = 0.084$ ,  $Re = 400,000$ .
- Fig. C.10 Instantaneous Vorticity Field Beyond Stage II at  $tU/c = 0.087$ ,  $Re = 400,000$ .
- Fig. C.11 Instantaneous Vorticity Field Beyond Stage II at  $tU/c = 0.090$ ,  $Re = 400,000$ .
- Fig. C.12 Instantaneous Vorticity Field Beyond Stage II at  $tU/c = 0.093$ ,  $Re = 400,000$ .
- Fig. C.13 Instantaneous Vorticity Field Beyond Stage II at  $tU/c = 0.096$ ,  $Re = 400,000$ .
- Fig. C.14 Instantaneous Vorticity Field Beyond Stage II at  $tU/c = 0.099$ ,  $Re = 400,000$ .
- Fig. C.15 Instantaneous Vorticity Field Beyond Stage II at  $tU/c = 0.102$ ,  $Re = 400,000$ .
- Fig. D.1 Example of Two-Zone  $666 \times 91$  Computational O-Mesh used at  $Re = 800,000$ . Top: Complete Mesh Illustrating Grid Clustering in the Leading Edge Region of the Airfoil. Bottom: Detail of the Inner Grid (Zone 1) in the Leading Edge Region.
- Fig. D.2 Circumferential Grid Spacing Sensitivity of the Instantaneous Skin Friction Distribution at Four Instants in Time ( $Re = 800,000$ ).
- Fig. D.3 Temporal Evolution of Skin Friction Error With Respect to Finest Grid Solution ( $Re = 800,000$ ).
- Fig. D.4 Scaling of Skin Friction Error as a Function of Circumferential Grid Spacing at Four Instants in Time ( $Re = 800,000$ ). (Dashed lines indicate slopes associated with formal first, second, third, and fourth order accuracy).
- Fig. D.5 Contour Plot Indicating the Relative Magnitude of Artificial Dissipation Terms and Viscous Flux Terms in the Discretized Equations of Motion at  $tU/c = 0.06$ ,  $Re = 800,000$ .
- Fig. D.6 Temporal Evolution of the Vorticity Field at  $Re = 800,000$ . (Arrows indicate locations of skin friction sign reversal). (Continued on next page).
- Fig. D.6 Temporal Evolution of the Vorticity Field at  $Re = 800,000$ . (Arrows indicate locations of skin friction sign reversal). (Continued from previous page).
- Fig. D.7 Detailed Vorticity Contours Illustrating the Temporal Evolution of the Flowfield Around the Time of Vortex-Induced Eruption ( $Re = 800,000$ ).
- Fig. D.8 Contour Plot Illustrating the Space-Time Evolution of Skin at  $Re = 50,000$ . (Black lines indicate zero skin friction).
- Fig. D.9 Contour Plot Illustrating the Space-Time Evolution of Skin at  $Re = 100,000$ . (Black lines indicate zero skin friction).
- Fig. D.10 Contour Plot Illustrating the Space-Time Evolution of Skin at  $Re = 200,000$ . (Black lines indicate zero skin friction).

- Fig. D.11 Contour Plot Illustrating the Space-Time Evolution of Skin at  $Re = 400,000$ . (Black lines indicate zero skin friction).
- Fig. D.12 Contour Plot Illustrating the Space-Time Evolution of Skin at  $Re = 800,000$ . (Black lines indicate zero skin friction).
- Fig. D.13 Zero Skin Friction Contours Illustrating the Similarity of Surface Flow Topologies Across the Reynolds Number Range.
- Fig. D.14 Contour Plot Illustrating the Space-Time Evolution of the Pressure Coefficient at the Surface,  $Re = 50,000$ .
- Fig. D.15 Contour Plot Illustrating the Space-Time Evolution of the Pressure Coefficient at the Surface,  $Re = 100,000$ .
- Fig. D.16 Contour Plot Illustrating the Space-Time Evolution of the Pressure Coefficient at the Surface,  $Re = 200,000$ .
- Fig. D.17 Contour Plot Illustrating the Space-Time Evolution of the Pressure Coefficient at the Surface,  $Re = 400,000$ .
- Fig. D.18 Contour Plot Illustrating the Space-Time Evolution of the Pressure Coefficient at the Surface,  $Re = 800,000$ .
- Fig. D.19 Pressure Coefficient Distribution as a Function of Time,  $Re = 50,000$ .
- Fig. D.20 Pressure Coefficient Distribution as a Function of Time,  $Re = 100,000$ .
- Fig. D.21 Pressure Coefficient Distribution as a Function of Time,  $Re = 200,000$ .
- Fig. D.22 Pressure Coefficient Distribution as a Function of Time,  $Re = 400,000$ .
- Fig. D.23 Pressure Coefficient Distribution as a Function of Time,  $Re = 800,000$ .
- Fig. D.24 Contour Plot Illustrating the Space-Time Evolution of the Streamwise Pressure Gradient at the Surface,  $Re = 50,000$ .
- Fig. D.25 Contour Plot Illustrating the Space-Time Evolution of the Streamwise Pressure Gradient at the Surface,  $Re = 100,000$ .
- Fig. D.26 Contour Plot Illustrating the Space-Time Evolution of the Streamwise Pressure Gradient at the Surface,  $Re = 200,000$ .
- Fig. D.27 Contour Plot Illustrating the Space-Time Evolution of the Streamwise Pressure Gradient at the Surface,  $Re = 400,000$ .
- Fig. D.28 Contour Plot Illustrating the Space-Time Evolution of the Streamwise Pressure Gradient at the Surface,  $Re = 800,000$ .

- Fig. D.29 Temporal Evolution of the Pressure Field Illustrating Vortex Formation at  $Re = 800,000$ . ( $\delta(p/p_\infty)$  indicates the value spacing between successive contour lines).
- Fig. D.30 Schematic Illustration of the Methodology Used to Determine the Location of the Topological Center at  $tU/c = 0.03$ ,  $Re = 400,000$ . (The inset depicts the extent of the un-rotated, un-scaled recirculation region using iso-contours the Mach number, for  $M \leq 0.01$ . Lines in the main graph are instantaneous streamtraces).
- Fig. D.31 Temporal Evolution of the Pressure Field and of Streamtraces Illustrating the Connection between the Topological Center and the Formation of the Primary Vortex,  $Re = 100,000$ .
- Fig. D.32 Temporal Evolution of Surface Flow Topology and Primary "Vortex/Center" Trajectory at  $Re = 800,000$ . (Lines are zero skin friction contours; "VF" denotes vortex formation; "R" denotes rupture).
- Fig. D.33 Temporal Evolution of Key Features Used to Describe the Primary Vortex History at  $Re = 800,000$ . (○ jacobian, ■ pressure at the core).
- Fig. D.34 Reynolds Number Scaling of Onset Times for Primary Separation, Vortex Formation, and Rupture.
- Fig. D.35 Scaling of the Upstream Boundary Layer Thickness with Reynolds Number.
- Fig. D.36 Alternate Reynolds Number Scaling of Onset Times for Primary Separation, Vortex Formation, and Rupture, Using Various Characteristic Length Scales (Top: Radius of Curvature, Center: Boundary Layer Thickness, Bottom: Viscous Length Scale).
- Fig. D.37 Alternate Reynolds Number Scaling of Onset Times for Incipient Primary (PS1) and Secondary (SS1, SS2, SS3, SS4) Separation Bubbles, Using Various Characteristic Length Scales ((a) Airfoil Chord, (b) Radius of Curvature, (c) Boundary Layer Thickness, (d) Viscous Length Scale).
- Fig. D.38 Lift Coefficient Time Histories.
- Fig. D.39 Drag Coefficient Time Histories.
- Fig. D.40 Pitching Moment Coefficient Time Histories.
- Fig. D.41 Time History of the Integrated Tangential Vorticity Flux at the Leading Edge,  $Re = 800,000$ .
- Fig. D.42 Time History of the Integrated Normal Vorticity Flux at the Leading Edge,  $Re = 800,000$ .
- Fig. D.43 Time History of the Vorticity Accumulation at the Leading Edge,  $Re = 800,000$ .



## **STATEMENT OF THE PROBLEM STUDIED**

The goal of the present research was to address key issues of vorticity dynamics prior to, during, and after the initiation of dynamic stall and to develop a fundamental understanding of the physical phenomena taking place. The two major thrusts of the research were (1) to investigate the applicability of indicial theory to the theoretical prediction of dynamic stall, and (2) to analyze the Reynolds number scaling of key events in the dynamic stall process, at laminar Reynolds numbers significantly higher than could previously be computed.

The basic idea behind the first portion of this work is founded on recent evidence that unsteady separated flow may be *linearizable* with respect to its boundary condition, in a manner similar to linearization techniques used in unsteady transonic flow. This similarity (i.e., a nonlinear mean with time-linearizable unsteady component) suggests the applicability of powerful analytical tools such as linear and nonlinear indicial theory. The applicability of indicial theory to key aspects of the vorticity dynamics of dynamic stall could provide the basis for a fast prediction method. By its construction, this predictive capability would be semi-analytic and fast-running, making it well-suited for design and for flight simulation methods.

The second portion of this work focused on the Reynolds number scaling of incipient leading edge stall. It has been suggested that eruptive plumes of vorticity might play a critical role in the physics of vortex initiation/formation during leading edge dynamic stall. Numerical simulations at low Reynolds number do not seem to adequately predict this phenomenon. To explore the possibility of a "bifurcation" in Reynolds number, the scaling of incipient laminar separation, of vortex formation, and of shedding with respect to Reynolds number was investigated in detail. Navier-Stokes simulations were used to study a model problem in which a two-dimensional airfoil remains stationary at angle-of-attack, but for which the leading edge flow separates as a result of an impulsively applied no-slip boundary condition.

## **SUMMARY OF MOST IMPORTANT RESULTS**

The research performed under the present contract followed two paths. The first phase of the work (April 92 to August 93) was concerned with the validation of indicial theoretical concepts as applied to the prediction of the vorticity dynamics of dynamic stall. The second phase of the work (January 94 to June 94) was an investigation into high Reynolds number (up to 800,000, based on chord) leading edge vortical laminar flow phenomena related to stall, based on a model problem. The technical results are summarized in the appendices. Appendices A and B are copies of technical papers from conference proceedings. Appendices C and D contain previously unreported results.

## *Indicial Theory and the Prediction of Dynamic Stall*

Following the proposal for this work (Ref. 1), the first portion of this study began with the analysis of a pitching airfoil at a chord Reynolds number of 1,000. This Reynolds number was found to be too low, for several reasons. The first one is that this case does not simulate the leading edge type of stall that is of practical interest. The second one is that it does not exhibit the presence of eruptive plumes of vorticity which could be critical to the initiation of dynamic stall. The third reason is that, at low Reynolds numbers, the airfoil flow is always separated to varying degrees for fixed angle of attack, thus undermining the whole idea of applying indicial theory up to and in the vicinity of an effective bifurcation of the leading edge vorticity dynamics. Here, "bifurcation" refers to a hypothetical separation between a boundary layer-type of vorticity transport and a new mode of vorticity transport (normal to the wall) associated with the appearance of an eruptive plume of vorticity.<sup>2,3</sup>

Successful validation of indicial theory was immediately achieved at  $Re = 1,000$  under conditions of high frequency ( $\omega c/2U_\infty \sim 10$ ) and low amplitudes (i.e., fractions of a degree). However, for larger amplitude motions ( $\Delta\alpha = O(5^\circ)$ ) and/or higher Reynolds number ( $Re = 12,000$ ), application of linear indicial theory in its original form failed. The reasons for the failure were as follows: (1) the flow response is statically nonlinear when the airfoil is beyond static stall; (2) the incremental asymptotic flow response to an elementary change in the boundary conditions is inherently unsteady (chaotic) at the higher Reynolds numbers. Indicial theory does not address either of these situations.

In view of these findings, the second portion of the research concentrated on the development and validation of a modified version of indicial theory which was designed to circumvent the above problems. The resulting characteristic/indicial approach uses the response to a reference large amplitude motion which is analyzed and processed in the Laplace domain to infer an equivalent, re-scaled "indicial" function designated as the "characteristic response" of the system. The characteristic response can then be convoluted with the time derivative of the motion history to predict the flow response to arbitrary schedules of the boundary condition ( $\alpha$ , in this case). In essence, successful prediction using the Laplace domain characteristic method signifies, in a system exhibiting quasi-static amplitude nonlinearity, that the *phase dynamics* can still be treated linearly. This is, of course, the essence of the generalized superposition integral which underlies the entire formulation. Alternatively, the new method can be interpreted as the straight-forward application of indicial concepts, using a re-scaled indicial function, determined from the knowledge of the finite (rather than infinitesimal) response of the flow. This "stretching" takes into account quasi-static nonlinearity and retains the linear formalism of indicial theory.

By extending an essentially linear tool well into the nonlinear regime, loss of generality has been incurred. In the present case, the prediction method was shown to be reasonably accurate for a class of airfoil motions with arbitrary schedule  $\alpha(t)$  all having the same initial and final angles of attack. Specifically, the time history of the vorticity accumulation (defined over a small control volume at the leading edge of the airfoil) was shown to be predicted accurately by the theory for different pitch rates (including oscillatory motion), provided that the indicial function is inferred from the difference between the flow responses associated with any two airfoil motions  $\alpha(t)$  mentioned above. This new

approach was validated at  $Re = 12,000$  for a variety of pitching motions between  $\alpha = 10^\circ$  and  $\alpha = 15^\circ$ .

Under these conditions, reasonable predictive accuracy can be obtained (on the order of 10 to 15% on the vorticity fluxes). Typical results are given in Appendix A. To obtain higher accuracy, two avenues of research were considered. The first one is to extend the Laplace-domain formalism to nonlinear indicial theory. Efforts in this direction were undertaken towards the end of the second funding increment of this contract. As a first step, these efforts were specifically directed towards a piecewise linear version of the method. However, this method was not sufficiently validated, due to lack of time and to changes in research priorities for the second phase of this work (Jan. 94 through June 94). The second avenue of research involved the separation of deterministic (motion-related) and chaotic portions of the predicted signals. One of the difficulties associated with the application of the prediction method to laminar single-realization cases was the presence of significant chaotic fluctuations associated with vorticity dynamics downstream of the leading edge region. The chaotic unsteady effects are, to a large degree, *uncorrelated* with the change in boundary condition,  $\Delta\alpha(t)$ . In particular, the method can only predict the deterministic component of the flow response. For instance, for sufficiently large times, the predicted increment response  $\Delta\mu$  (between two finite-amplitude motions having same final angle-of-attack) equals zero, since the input  $\Delta\alpha$  to the method is zero for a time exceeding the length of the convolution. Yet, for sufficiently large Reynolds number,  $\Delta\mu(t) \neq 0$ . This is expected of deterministic methods with finite "memory." A similar problem was found in the artificial neural network predictions of Faller et al. (Ref. 2), for large times. Since this aspect of the prediction cannot be circumvented, a search for candidate dynamic stall "indicators" was undertaken. The basic idea is that, if  $\Delta\mu(t)$  is small, the prediction error will also be small. Thus, a suitable indicator must have the property that, in response to the airfoil motion, its time-history should exhibit a strong degree of determinism with respect to  $\Delta\alpha(t)$ .

The applicability of indicial theory hinges on the existence of flow quantities whose temporal behavior remains smooth throughout dynamic stall. A result of this research is that vorticity accumulation appears to be a suitable candidate as a dynamic stall "indicator" in which the deterministic (motion-related) component is dominant. Vorticity accumulation also happens to be predicted well by indicial theory as modified in this work. The applicability of the modified theory indicates that the phase dynamics are linear, and that a generalized superposition integral can be used to construct phase lags from elementary responses.

### ***Reynolds Number Effects on a Model Problem of Leading Edge Stall***

The study of a model problem was considered in which an airfoil is initially maintained at a fixed angle-of-attack ( $\alpha = 15^\circ$ ). A converged Navier-Stokes solution which is free of separation is obtained by using the zero-vorticity slip boundary condition. At some time  $t = 0$ , the no-slip boundary condition is impulsively turned on. The resulting developing flowfield is characterized by the complete absence of trailing edge stall, the existence of a well-defined time origin, and the independence of the initial condition on Reynolds number. This problem was originally conceived of in the initial part of the work, in order to mimic certain physical aspects of high Reynolds number flow in low Reynolds number simulations. In particular, this approach circumvents the "contamination" of the leading edge flow due to reverse flow emanating from the trailing edge region.

Incidentally, the properties of the flowfield associated with this model problem are also advantageous for the detailed study of the very initial stages of dynamic stall, as well as for the investigation of scaling effects with Reynolds number.

High Reynolds number laminar flow remains a difficult area of research. From a computational point of view, the currently accepted highest chord Reynolds number at which grid-independent results can be obtained is  $Re = 100,000$ .<sup>3</sup> With the present model problem and using a high-order differencing code, grid-converged solutions of the two-dimensional Navier-Stokes equations were obtained up to  $Re = 800,000$ . The importance of the high Reynolds number laminar research for dynamic stall stems from high Reynolds number asymptotics<sup>4</sup> and interacting boundary layer research<sup>5,6</sup> which suggest that eruptive plumes of vorticity may form in the leading edge boundary layer and act as a triggering mechanism leading to the formation of the primary dynamic stall vortex. Such eruptions (which differ from the standard vortex-induced eruption) have not yet been found in numerical solutions of the Navier-Stokes equations. A prevalent point of view<sup>5</sup> (and a strong possibility) is that, in an Eulerian reference frame, the mesh spacing to resolve this phenomenon cannot be afforded. Another possibility is that some form of bifurcation takes place at some intermediate, laminar Reynolds number. Since most numerical calculations are at low Reynolds number, the effects of viscosity may dissipate any tendency to spontaneously form these eruptive plumes. The main idea behind an analysis of the Reynolds scaling of key events in the dynamic stall process is that the emergence of new physics -even if poorly resolved- would result in modified scaling properties with respect to Reynolds number.

A high-order accuracy finite difference code was used for this part of the investigation. The code uses eighth-order spatial accuracy on the convective fluxes, on the metrics, and on the artificial dissipation, while retaining fourth-order accuracy on the viscous terms. The numerical method allows for the accurate resolution of a wavenumber range in each spatial direction equivalent to 80% of the wavenumber range for pseudo-spectral methods. Thus the required number of grid points is substantially reduced, compared to a standard second-order code. A more detailed description of the code can be found in Appendices C and D. High order accuracy was a critical element which permitted the extension of the model problem studies to Reynolds numbers considerably larger than previously possible.

At least two distinct stages of the incipient separation process were found. Stage I corresponds to the formation of a separation zone ("lifting" of the thin primary vorticity layer) which is initially symmetric about the location of maximum boundary layer thickness. This stage was found to exhibit qualitatively self-similar behavior over the investigated Reynolds number range ( $50,000 \leq Re \leq 800,000$ ,  $M_\infty = 0.2$ ), and ends with the accumulation of vorticity in the reattachment region of the separated vorticity layer. In Stage II, the accumulated vorticity develops into a vortex which subsequently induces a sequence of rapid events, including the formation of secondary flow and, at high Reynolds number, successive shear layer vortices which themselves induce secondary and tertiary flow patterns. This stage is the most difficult to compute, and issues of adequacy of the numerical resolution, diffusion of the vortices, and steepness of the induced pressure gradients are critical. At high Reynolds numbers, a second order method would be extremely expensive if it were to capture the essential physics.

At the beginning of this portion of the research, a number of important research issues were raised, in particular with respect to the relevance and applicability of high Reynolds

number asymptotic theory and interacting boundary layer calculation results (see, e.g., Ref. 5). The theory suggests the development of a tightly focused narrowing band eruption in the boundary layer. This eruption is a generic boundary layer response to a moving adverse pressure gradient zone outside the boundary layer. The presence of a vortex-induced eruption in Stage II is well-established, and has been observed in the present calculations at  $Re = 100,000, 200,000, 400,000$ , and  $800,000$ . Knight and Choudhuri's results<sup>7</sup> exhibit similar behavior at a Reynolds number as low as  $Re = 10,000$ . There is also reason to believe that this type of eruption would presumably also have taken place here at  $Re = 50,000$ , had the calculations been carried out further in time. **However, no eruption was ever observed during Stage I of the flow development, nor could an eruption (bifurcation) be inferred from the basic Reynolds number scaling properties of the flow.**

The present results indicate a smooth scaling behavior over the Reynolds number range  $50,000 \leq Re \leq 800,000$  in Stage I, and the well-defined emergence, from the lifting vorticity layer, of a topological "center" which precedes vortex formation. Qualitatively similar behavior was observed at all investigated Reynolds numbers. Furthermore, when taking into account the viscous scaling of the Stokes layer and/or boundary layer upstream, the specific dynamical events associated with incipient stall (such as the times of onset of primary and secondary separation bubbles, and of vortex formation) were found to scale according to simple power laws of the Reynolds number,  $Re^{-\eta}$ , with  $0.11 \leq \eta \leq 0.45$ . Self-similarity was also observed for the time of occurrence of vortex-induced eruptions (marking the onset of shedding of the primary stall vortex), between the Reynolds numbers of  $50,000$  and  $400,000$ . At  $Re = 800,000$ , new physics associated with complex interactions between vortices take place in the vicinity of the wall before the time of eruption. However, no qualitative changes were observed in Stage I.

The present results contradict the hypothesis that a form of bifurcation must take place at some intermediate laminar Reynolds number during Stage I, i.e., before the formation of a vortex. To reconcile these results with the implications of interacting boundary layer theory,<sup>6</sup> one of several conjectures may be made. These conjectures are listed below.

The first one concerns the Reynolds number of the simulations. Although  $Re = 800,000$  goes beyond the traditionally accepted  $Re = 100,000$  limit for laminar calculations of dynamic stall, the fact remains that this is a low Reynolds number flow. The Reynolds number range based on leading edge radius,  $b$ , was  $3,250 \leq Re_b \leq 12,800$ . Based on boundary layer thickness ( $\delta_{0,LE}$ ) and freestream velocity, the Reynolds number range was:  $46 \leq Re_\delta \leq 186$ . These are, of course, extremely low Reynolds numbers, compared to those considered in the high Reynolds number asymptotics and interacting boundary layer studies.

The second conjecture, also related to the Reynolds number, is that if a Reynolds number bifurcation in Stage I should occur, it will take place at a Reynolds number higher than those investigated in this study. It is, therefore, likely that transition and turbulence will be present. The effects of transition and turbulence could overwhelm the bifurcation phenomenon, thus making it very difficult to discern. Calculations at chord Reynolds numbers larger than  $800,000$  were not attempted in this study, in part because transition to turbulence may take place within the thin free shear layers. Although the present resolution is sufficient to resolve the primary Kelvin-Helmholtz instability (at least, for the primary free shear layer), the present calculations are no longer accurate when three-dimensional instabilities are present.

The third conjecture is that a self-focusing plume of vorticity must exist at the leading edge within the investigated Reynolds number range. In this scenario, the reason why this was not observed is because the phenomenon is *subscale* and cannot be resolved by Eulerian means. Although this is a theoretical possibility, experience teaches us that some sign of "activity," be it instability or other phenomenon, would have been visible in the calculations, especially since an eighth-order code was used. No such sign was discovered in any of the present calculations. Grid convergence was attained at all Reynolds numbers, and further grid refinements were not attempted. The prospect of further increasing grid resolution to repeat the same results was considered unproductive and risky; therefore, this avenue of research was not pursued.

The fourth conjecture pertains to the absence of a *moving* region of adverse pressure gradient. The physics of formation of eruptive plumes of vorticity are described by the high Reynolds number asymptotics and interacting boundary layer studies.<sup>4,5</sup> These studies specifically address the response of the boundary layer to a moving zone of adverse pressure gradient. In the present semi-impulsive problem at fixed angle of attack, there is very little temporal change in the leading edge pressure gradient. Except for an initial relaxation of the pressure gradient after imposing the no-slip condition, the region of adverse pressure gradient does not undergo any significant motion. This is different from a pitching airfoil situation. Whether or not this is significant is something that could be systematically investigated by superimposing a pitching motion to the present problem. However, this route was not pursued within the time frame of this study, for two reasons. The first one is the fact that vortex-induced eruptions take place, even though the motion of the vortex is very slight: the temporal strengthening of the circulation associated with the vortex appears to be by far the largest contributor. The second reason is that, if one considers the time scales involved for the entire process to complete (say, up to the point of shedding of the primary stall vortex), these correspond to only a fraction of a degree for a realistic airfoil motion. For example, for a hypothetical oscillatory motion at  $Re = 800,000$  at a reduced frequency  $k = \omega c / 2U = 0.02$  with a motion amplitude of  $5^\circ$ , the change in angle of attack,  $\Delta\alpha$ , from initiation to shedding, equals  $0.014^\circ$ . This would not be expected to produce any significant motion of the zone of adverse pressure gradient.

Finally, the results presented here suggest that the behavior of the flow started to change at  $Re = 800,000$ . Although these differences occurred in Stage II, it is useful to consider the broader picture and attempt to speculate as to what happens at higher Reynolds numbers. At  $Re = 800,000$ , a vortex-induced eruption takes place virtually underneath a merged primary vortex, as opposed to taking place between consecutive primary and shear layer vortices. The result is a fundamental change from a bulk convection of the vortex system at low Reynolds numbers to a sudden break-away from the surface at a point in time when the entire vortex system is confined to the leading edge region. As the Reynolds number becomes larger, the artificial distinction between Stages I and II will be blurred and not realistic. Transition effects will likely replace the elongated laminar bubble of Stage I by transitional and turbulent flow structures in the close proximity of the wall. If this is the case, the broader issue is to determine the conditions under which eruption of vorticity occurs if, as suggested by the present results, such an eruption acts as the trigger for vortex shedding.



## References

1. Reisenthel, P.H.: "Vorticity Dynamics and Control of Dynamic Stall," Nielsen Engineering & Research Proposal No. 2398, March 1991.
2. Faller, W., Schreck, S., and Luttges, M.: "Real-Time Prediction and Control of Three-Dimensional Unsteady Separated Flow Fields Using Neural Networks," AIAA Paper No. 94-0532.
3. Ghia, K.N., remarks after presentation of Abstract M4-1, 46th Annual Meeting of the American Physical Society Fluid Dynamics Division, Albuquerque, NM, November 1993.
4. Peridier, V.J., Smith F.T., Walker, J.D.A.: "Vortex-Induced Boundary Layer Separation. Part I. The Unsteady Limit Problem  $Re \rightarrow \infty$ ," *J. Fluid Mech.*, Vol. 232, 1991, pp. 99-131.
5. Peridier, V.J., Smith F.T., Walker, J.D.A.: "Vortex-Induced Boundary Layer Separation. Part II. Unsteady Interacting Boundary Layer Theory," *J. Fluid Mech.*, Vol. 232, 1991, pp. 133-165.
6. Doligalski, T.L., Smith, C.R., and Walker, J.D.A.: "Vortex Interactions With Walls," *Ann. Rev. Fluid Mech.*, Vol. 26, 1994, pp. 573-616.
7. Knight, D.R. and Choudhuri, P.G.: "2-D Unsteady Leading Edge Separation On a Pitching Airfoil," AIAA Paper 93-2977, 1993.

## PUBLICATIONS

Reisenthel, P.H.: "Application of Indicial Theory to the Prediction of Vorticity Fluxes at the Leading Edge of a Two-Dimensional Pitching Airfoil, *Bull. Am. Phys. Soc.*, Vol. 38, No. 12, Nov. 1993, p. 2315.

Reisenthel, P.H.: "Towards a Semi-Analytical Tool for the Prediction of Dynamic Stall," AIAA Paper No. 94-0537, 1994.

Reisenthel, P.H. and Childs, R.E.: "A Study of Reynolds Number Effects on Incipient Leading Edge Stall," AIAA Paper No. 94-2339, 1994.

Reisenthel, P.H.: "On the Reynolds Number Scaling of Incipient Leading Edge Stall," abstract submitted for the 47th Annual Meeting of the American Physical Society, Division of Fluid Dynamics, 20-22 November 1994.

Reisenthel, P.H.: "Further Results on the Reynolds Number Scaling of Incipient Leading Edge Stall," AIAA Paper No. 95-0780 (in preparation), 1995.

## ***PARTICIPATING SCIENTIFIC PERSONNEL***

Dr. Patrick H. Reisenthel, Chief Scientist and Principal Investigator  
Mr. Stanley C. Perkins, Senior Research Engineer  
Dr. Robert Childs, Executive Vice-President

No degrees were awarded to the above personnel during this contract.



**THIS PAGE INTENTIONALLY LEFT BLANK**

# REPORT OF INVENTIONS AND SUBCONTRACTS

(Pursuant to "Patent Rights" Contract Clause) (See Instructions on Reverse Side.)

Form Approved  
OMB No. 0704-0297  
Expires Jun 30, 1992

Public reporting burden for this collection of information is estimated to average 3 minutes per response, including the time for reviewing instructions, searching existing data sources, gathering and maintaining the data needed, and completing and reviewing the collection of information. Send comments regarding this burden estimate or any other aspect of this collection of information, including suggestions for reducing this burden, to Washington Headquarters Services, Directorate for Information Operations and Reports, 1215 Jefferson Davis Highway, Suite 1204, Arlington, VA 22202-4302, and to the Office of Management and Budget, Paperwork Reduction Project (0704-0297), Washington, DC 20503.

1a. NAME OF CONTRACTOR/SUBCONTRACTOR Nielsen Engineering		2a. NAME OF GOVERNMENT PRIME CONTRACTOR same as 1a		3. TYPE OF REPORT (X one) a. INTERIM <input checked="" type="checkbox"/> b. FINAL	
b. ADDRESS (Include ZIP Code) 526 Clyde Avenue Mountain View, CA 94043		c. CONTRACT NUMBER DAAL03-92-C-0013		4. REPORTING PERIOD (YYMMDD) a. FROM 920501 b. TO 940814	
		d. AWARD DATE (YYMMDD) same as 1d			

## SECTION I - SUBJECT INVENTIONS

3. "SUBJECT INVENTIONS" REQUIRED TO BE REPORTED BY CONTRACTOR/SUBCONTRACTOR (If "None," so state)		4. ELECTION TO FILE PATENT APPLICATIONS		5. CONFIRMATORY INSTRUMENT OR ASSIGNMENT FORWARDED TO CONTRACTING OFFICER	
a. NAME(S) OF INVENTION(S) (Last, First, MI)	b. TITLE OF INVENTION(S)	c. DISCLOSURE NO., PATENT APPLICATION SERIAL NO., OR PATENT NO.		6. (1) Yes (2) No	
None					

1. EMPLOYER OF INVENTOR(S) NOT EMPLOYED BY CONTRACTOR/SUBCONTRACTOR		9. ELECTED FOREIGN COUNTRIES IN WHICH A PATENT APPLICATION WILL BE FILED	
(1) (a) Name of Inventor (Last, First, MI) N/A	(2) (a) Name of Inventor (Last, First, MI)	(2) Foreign Countries of Patent Application	
(b) Name of Employer	(b) Name of Employer		
(c) Address of Employer (Include ZIP Code)	(c) Address of Employer (Include ZIP Code)		

## SECTION II - SUBCONTRACTS (Containing a "Patent Rights" clause)

6. SUBCONTRACTS AWARDED BY CONTRACTOR/SUBCONTRACTOR (If "None," so state)		6. OFAR "PATENT RIGHTS"		7. SUBCONTRACT DATES (YYMMDD)	
a. NAME OF SUBCONTRACTOR(S)	b. ADDRESS (Include ZIP Code)	(1) Clause Number	(2) Date (YYMM)	(1) Award	(2) Estimated Completion
None					

## SECTION III - CERTIFICATION

2. CERTIFICATION OF REPORT BY CONTRACTOR/SUBCONTRACTOR		(Not required if XX Small Business or Non-Profit organization.) (X appropriate box)	
a. NAME OF AUTHORIZED CONTRACTOR/SUBCONTRACTOR OFFICIAL (Last, First, MI)	c. I certify that the reporting party has procedures for prompt identification and timely disclosure of "Subject Inventions," that such procedures have been followed and that all "Subject Inventions" have been reported.		
b. TITLE	d. SIGNATURE	e. DATE SIGNED	

## BIBLIOGRAPHY

Acharya, M. and Metwally, M.H.: "Evolution of the Unsteady Pressure Field and Vorticity Production at the Surface of a Pitching Airfoil," AIAA Paper 90-1472, 1990.

Acharya, M. and Metwally, M.H.: "Unsteady Pressure Field and Vorticity Production Over a Pitching Airfoil," *AIAA J.*, Vol. 30, No. 2, 1992, pp. 403-411.

Carr, L.W.: "Progress in Analysis and Prediction of Dynamic Stall," *J. Aircraft*, Vol. 25, 1988, pp. 6-17.

Carr, L.W., Chandrasekhara, M.S., and Ahmed, S.: "A Study of Dynamic Stall Using Real Time Interferometry," AIAA Paper 91-0007, 1991.

Childs, R.E., Rodman, L.C., and Nixon, D.: "Methods for Computational Aeroacoustics," Nielsen Engineering & Research, NEAR TR 452, Aug. 1992.

Childs, R.E.: "Advanced Discretization Algorithm for CFD Methods," Nielsen Engineering & Research, NEAR TR 469, July 1993.

Doligalski, T.L., Smith, C.R., and Walker, J.D.A.: "Vortex Interactions With Walls," *Ann. Rev. Fluid Mech.*, Vol. 26, 1994, pp. 573-616.

Elliott, J.W., Cowley, S.J., and Smith, F.T.: "Breakdown of Boundary Layers: (i) On Moving Surfaces; (ii) In Self-Similar Unsteady Flows; (iii) In Fully Unsteady Flow," *Geophys. Astrophys. Fluid Dyn.*, Vol. 25, 1983, pp. 77-138.

Ericsson, L.E.: "The Problem of Dynamic Stall Simulation Revisited," AIAA Paper 93-0091, 1993.

Faller, W., Schreck, S., and Luttgies, M.: "Real-Time Prediction and Control of Three-Dimensional Unsteady Separated Flow Fields Using Neural Networks," AIAA Paper No. 94-0532.

Gendrich, C.P., Koochesfahani, M.M., and Visbal, M.R.: "Initial Acceleration Effects on the Flowfield Development Around Rapidly Pitching Airfoils," AIAA Paper 93-0438.

Ghia, K.N., Ghia, U., and Osswald, G.A.: "Characterization of Dynamic Stall Phenomenon Using Two-Dimensional Unsteady Navier-Stokes Equations," Presented at the NASA/AFOSR/ARO Workshop on the Physics of Forced Unsteady Separation, Moffett Field, CA, April 17-19, 1990.

Ghia, K.N., Yang, J., Osswald, G.A., and Ghia, U.: "Study of the Role of Unsteady Separation in the Formation of Dynamic Stall Vortex," AIAA Paper 92-0196, 1992.

Helin H.E.: "The Relevance of Unsteady Aerodynamics for Highly Maneuverable and Agile Aircraft," presented at the Symposium on Numerical and Physical Aspects of Aerodynamic Flows, Long Beach, CA, January 16-19, 1989.

Henk, R.W., Reynolds, W.C., and Reed, H.L.: "Experiments on an Unsteady, Three-Dimensional Separation," Presented at the NASA/AFOSR/ARO Workshop on the Physics of Forced Unsteady Separation, Moffett Field, CA, April 17-19, 1990.

Jenkins, J. E.: "Relationships Among Nonlinear Aerodynamic Indicial Response Models, Oscillatory Motion Data, And Stability Derivatives," AIAA Paper 89-3351, 1989.

Knight, D.R. and Choudhuri, P.G.: "2-D Unsteady Leading Edge Separation On a Pitching Airfoil," AIAA Paper 93-2977, 1993.

Lesieutre, D.J., Reisenhel, P.H., and Dillenius, M.F.E.: "An Unsteady Aerodynamics Model Based on Indicial Theory for Multidisciplinary Flight Simulations," NEAR TR 468, August 1993.

Lesieutre, D. J. and Reisenhel, P. H.: "A Practical Approach for Calculating Aerodynamic Indicial Functions with a Navier-Stokes Solver," AIAA Paper No. 94-0059, 1994.

Lorber, P.F. and Carta, F.O.: "Unsteady Separation Experiments on 2 D Airfoils, 3 D Wings, and Model Helicopter Rotors," Presented at the NASA/AFOSR/ARO Workshop on the Physics of Forced Unsteady Separation, Moffett Field, CA, April 17-19, 1990.

Nixon, D.: "Alternative Methods for Modeling Unsteady Transonic Flows," Unsteady Transonic Aerodynamics, Vol. 120 of Progress in Astronautics and Aeronautics, Ed. D. Nixon, AIAA, 1989.

Peridier, V.J., Smith, F.T., and Walker, J.D.A.: "Vortex-Induced Boundary-Layer Separation. Part 1. The Unsteady Limit Problem  $Re \rightarrow \infty$ ," *J. Fluid Mech.*, Vol. 232, pp. 99-131, 1991.

Peridier, V.J., Smith, F.T., and Walker, J.D.A.: "Vortex-Induced Boundary-Layer Separation. Part 2. Unsteady Interacting Boundary-Layer Theory," *J. Fluid Mech.*, Vol. 232, pp. 133-165, 1991.

Perry, A.E. and Chong, M.S.: "A Description of Eddying Motions and Flow Patterns Using Critical-Point Concepts," *Ann. Rev. Fluid Mech.*, Vol. 19, 1987, pp. 125-155.

Pulliam, T.H.: "Euler and Thin Layer Navier Stokes Codes ARC2D-ARC3D," Notes for Computational Fluid Dynamics User's Workshop, Tullahoma, TN, March 12-16, 1984.

Reisenhel, P.H.: "Vorticity Dynamics and Control of Dynamic Stall," Nielsen Engineering & Research Proposal No. 2398, March 1991.

Reisenhel, P.H. and Nixon, D.: "Application of Indicial Theory to the Prediction of Unsteady Separation," AIAA Paper 91-1742, 1991.

Reisenhel, P.H.: "Towards a Semi-Analytic Tool for the Prediction of Dynamic Stall," AIAA Paper 94-0537, 1994.

Reisenhel, P.H. and Childs, R.E.: "A Study of Reynolds Number Effects on Incipient Leading Edge Stall," AIAA Paper No. 94-2339, 1994.

Reisenhel, P.H.: "Further Results on the Reynolds Number Scaling of Incipient Leading Edge Stall," AIAA Paper No. 95-0780, 1995. *In preparation.*

Reynolds, W.C. and Carr, L.W.: "Review of Unsteady, Driven, Separated Flows," AIAA Paper 85-0527, 1985.

Rothmayer, A. and Bhaskaran, R.: "Theoretical Aspects of Stability and Transition in High Reynolds Number Dynamic Stall," AIAA Paper No. 94-2336, 1994.

Schreck, S. and Helin, H.E.: "Unsteady Vortex Dynamics and Surface Pressure Topologies on a Pitching Wing," AIAA Paper 93-0435, 1993.

Shih, C., Lourenco, L., Van Dommelen, L., and Krothapalli, A.: "Unsteady Flow Past an Airfoil Pitching at Constant Rate," *AIAA J.*, Vol. 30, 1992, pp. 1153-1161.

Tobak, M.: "On the Use of the Indicial Function Concept in the Analysis of Unsteady Motion of Wings and Wing-Tail Combinations," NACA Report 1188, 1954.

Tobak, M. and Chapman, G.T.: "Nonlinear Problems in Flight Dynamics Involving Aerodynamic Bifurcations," NASA TM 86706, 1985.

Van Dommelen, L.L. and Shen, S.F.: "The Spontaneous Generation of The Singularity In a Separating Boundary Layer," *J. Comp. Phys.*, Vol. 38, 1980, pp. 125-140.

Van Dommelen, L.L. and Shen S.F.: "The Genesis of Separation," *Numerical and Physical Aspects of Aerodynamic Flows*, New-York, Springer-Verlag, 1982, pp. 293-311.

Walker, J.D.A., Smith, C.R., Doligalski, T.L., and Cerra, A.W.: "Impact of a Vortex Ring on a Wall," *J. Fluid Mech.*, Vol. 181, 1987, pp. 99-140.

Weeks, W.T.: "Numerical Inversion of Laplace Transforms Using Laguerre Functions," *J. Assoc. Comp. Machinery*, Vol. 13, No. 3, July 1966, pp. 419-426.

## ***APPENDICES***

# TOWARDS A SEMI-ANALYTIC TOOL FOR THE PREDICTION OF DYNAMIC STALL

AIAA 94-0537

*Patrick H. Reisenethel\**  
Nielsen Engineering & Research, Inc.  
Mountain View, CA

## ABSTRACT

Direct numerical simulations are used to analyze in detail the vorticity dynamics of the leading edge region of a NACA0012 airfoil pitched about its 1/4 chord. The results presented in this paper illustrate how the formalism of indicial theory can be used to predict the integrated vorticity fluxes and the vorticity accumulation during unsteady maneuver. In particular, the flow response to large amplitude non-linear motions is shown to be predicted reasonably accurately, provided that the indicial functions of the flow are inferred in the Laplace domain and stretched to account for quasi-static non-linearity. The implication of this work is the possibility of developing a fast semi-analytical prediction method for incipient leading edge stall, which will be accurate within certain classes of maneuvers.

## NOMENCLATURE

### Symbols

A	Amplitude transfer function ( $A = A(\omega)$ )
$A_0$	Quasi-static amplitude ( $A_0 = A(0)$ )
c	Airfoil chord
const.	Constant
CFD	Computational Fluid Dynamics
DNS	Direct Numerical Simulation
f	Flow response
F	Frequency
k	Reduced frequency ( $k = (2\pi Fc)/(2U_\infty)$ )
L	Laplace transform
L.E.	Leading Edge
$M_\infty$	Freestream Mach number
Re	Chord Reynolds number ( $Re = U_\infty c / \nu_\infty$ )
s	Curvilinear (tangential) airfoil coordinate ( $0.0 \leq s \leq 1.0$ )
$\hat{s}$	Complex Laplace variable
t	Non-dimensional time ( $t = \hat{t} U_\infty / c$ )
T	Ramp time (non-dimensionalized with $U_\infty$ and c)
u	Streamwise velocity
$U_\infty$	Freestream velocity
v	Normal velocity
x	Streamwise coordinate
$\bar{x}$	Generic spatial coordinate
y	Normal coordinate
$y_N$	Coordinate locally perpendicular to the airfoil surface
$\alpha$	Angle of attack (in degrees unless otherwise specified)

$\varepsilon$	Forcing function
$\Delta$	Variation
$\Delta\phi$	Phase transfer function ( $\Delta\phi = \Delta\phi(\omega)$ )
$\Phi$	Total vorticity flux (convective and viscous)
$\Theta$	Vorticity flux angle
$\mu$	Flow response (generic notation)
$\mu_c$	Indicial function (generic)
$\nu$	Fluid kinematic viscosity
$\rho$	Fluid density
$\tau$	Time lag
$\omega$	Reduced angular frequency ( $\omega = 2\pi Fc/U_\infty$ )
$\Omega$	Vorticity
$\xi$	Time variable for a predefined motion $\alpha(\xi)$

### Subscripts

e	Evaluated at the outside edge of the boundary layer
o	Initial condition
n	Normal
t	Tangential
$\infty$	Freestream value

### Superscripts

-1	Inverse
-	Indicial function
*	Accumulation
+	Non-dimensional
^	Dimensional

## INTRODUCTION

The past two decades have seen a considerable amount of resources spent towards resolving the problem of dynamic stall. Despite some progress in both numerical prediction<sup>1</sup> and experimental<sup>2,3</sup> techniques, there are still too many unknowns to ensure successful transfer of this knowledge from basic research to applied research and exploratory development. A case in point is the design of helicopter rotor blades, which makes little use of dynamic stall results. Ideally, a successful blade design might be one which could benefit from the dynamic lift effect, without experiencing the enhanced torsional fatigue caused by shedding of a dynamic stall vortex.

The inability of the research community to provide designers involved in the aerodynamics of unsteady lifting surfaces with the appropriate tools is, without a doubt, related to the difficulty of the problem at hand and has been a source of constant frustration. The current understanding of the complex physics involved in dynamic stall is limited by such difficult and inter-

\*Chief Scientist, Member AIAA

related issues as three-dimensionality<sup>4</sup> and transition to turbulence (e.g., moving wall<sup>5</sup> effects), as well as fundamental scaling issues with Reynolds number<sup>6</sup> and additional physics introduced by compressibility effects.<sup>2</sup>

The basic idea behind the work presented in this paper is founded on recent evidence<sup>7</sup> that unsteady separated flow may be *linearizable* with respect to its boundary condition, in a manner similar to unsteady transonic flow.<sup>8</sup> This similarity (i.e., a non-linear mean flow with time-linearizable unsteady component) suggests the applicability of powerful analytical tools such as linear and non-linear indicial theory.<sup>9,10,11</sup> The applicability of indicial theory to dynamic stall, or its applicability to some key aspect of the vorticity dynamics associated with the dynamic stall process, could provide the basic element of a fast prediction method. By its construction, this predictive capability would be semi-analytic,<sup>7,8</sup> making it well-suited for *design* and for flight simulation techniques.

## OBJECTIVE AND APPROACH

The objective of this work is to attempt to either prove or disprove the applicability of the indicial theoretical concept, as applied to the dynamic stall process. The approach is to use direct numerical simulations (DNS) of dynamic stall for a well-documented two-dimensional configuration: that of a NACA0012 airfoil in pitch about the 1/4 chord position. Since indicial theory (summarized below) is applied here to the physics of incipient unsteady separation, it is essential that turbulence models (which would unavoidably "contaminate" the physics which are the very object of this analysis) be eliminated. Therefore, as a first step, the Reynolds numbers considered here are low ( $Re = 1,000$ ,  $Re = 12,000$ , and, in a model problem,  $Re = 100,000$ ), corresponding to laminar flow conditions.

The analysis is based on the hypothesis that the cause of dynamic stall is linked to the disparate characteristic times for the various physical processes that take place. The effect of the disparity in time scales is such that, for a given pitch rate, the following processes occur: *i*) at some critical time, the vorticity accumulated throughout the airfoil motion exceeds the maximum allowable for vorticity transport through an attached boundary layer model; at that time, normal vorticity transport component becomes important, and *ii*) the normal vorticity transport component is confined to a vortex feeding sheet or a sharply defined shear layer which may lead to the formation of the vortex. In steady flow the separation may start from a shear layer but rapidly becomes chaotic. In the dynamic case the time lags may allow the sustained development, or stability, of the vortex sheet, such that a vortex is formed. Once formed, the vortex may interact with the boundary layer below it, eventually giving rise to an eruptive plume of vorticity. The result of this eruption is to free the dynamic stall vortex from its feeding sheet, which is followed by the rapid convection of the vortex over the surface.

A key addition to this idea comes from recent work<sup>7</sup> in which it was found that if an impulsive change is given to the flow around a cylinder, the transient value of the shed vorticity flux at short times is considerably larger than the value for steady flow. It is noteworthy that the hypothesis that time lags are responsible for the delayed breakup of the vortex sheet is consistent with the findings of Henk et al.<sup>12</sup> who experimentally examined unsteady separated flows in a water tunnel.

Unlike pure Computational Fluid Dynamical (CFD) approaches, which, like experiments, produce numbers (but not necessarily insight), and are too expensive, the semi-analytical approach outlined below provides a guide to physical understanding since it allows the identification of cause and effect relationships.

**Indicial Method.** The present approach is based on the concept<sup>8</sup> that a characteristic flow variable  $f(x,t)$ , which describes the state of the flow, can be linearized with respect to its boundary condition,  $\epsilon(t)$ , if the variation of  $f(x,t)$  is a smooth function of  $\epsilon(t)$ . Since, in general, separation is a non-linear process, the function  $f(x,t)$  must be such that its variation with  $\epsilon(t)$  is smooth through separation; this allows the representation of  $f(x,t)$  in a Taylor series about some value of  $\epsilon$ ,  $\epsilon_0$ ; thus

$$f(\bar{x}, t) = f(\bar{x}, 0) + \Delta\epsilon \left. \frac{\partial f}{\partial \epsilon} \right|_{\epsilon=\epsilon_0} + \dots \quad (1)$$

If  $f(\bar{x}, 0)$  is zero (a zero initial condition), then an approximate solution is

$$f(\bar{x}, t) = \Delta\epsilon \left. \frac{\partial f}{\partial \epsilon} \right|_{\epsilon=\epsilon_0} \quad (2)$$

Equation (2) is an approximation which becomes more accurate as  $\Delta\epsilon \rightarrow 0$ . Also, Eq. (2) is exact if  $f(x,t)$  is a linear function of  $\epsilon(t)$ . If (2) is satisfied, then it can be shown<sup>8</sup> that a formal solution for  $f(x,t)$  is

$$f(\bar{x}, t) = \tilde{f}(\bar{x}, t) \epsilon(0) - \int_0^t \frac{d\epsilon(t-\tau)}{d\tau} \tilde{f}(\bar{x}, \tau) d\tau \quad (3)$$

where

$$\tilde{f}(\bar{x}, t) = \left. \frac{\partial f}{\partial \epsilon} \right|_{\epsilon=\epsilon_0} \quad (4)$$

Hence, if the forcing function (i.e., the boundary condition  $\epsilon$ ) is known and if  $\tilde{f}$  (the "indicial function") is known from some computation, then Eq. (3) gives the value of  $f(x,t)$  for *any schedule* of boundary conditions  $\epsilon(t)$  without the need to compute  $f$  from first principles. This has the effect of reducing computational requirements considerably. Furthermore, Eq. (3) is a semi-analytic relation between  $f(x,t)$  and its boundary condition  $\epsilon(t)$  which can give insight into the physical process involved.

If applicable, the formalism of the theory represented by Eq. (3) allows insight into the character of dynamic stall even though the actual details of the response are unknown. The analysis outlined above



illustrates the power of the method, a power that is greatly enhanced if details of the response are computed.

It may be difficult to comprehend how a linear equation can represent the non-linear behavior of separation, and therefore it is useful to illustrate how this concept represents an example of unsteady separated flow; in this case, the flow around an oscillating cylinder. This example is based on work published in Ref. 7 which shows that it is possible to predict the *time-dependent characteristics* of separation location and vorticity flux, based on the knowledge of the impulse response of the flowfield only. Previous experience with the application of indicial theory to the prediction of non-linear transonic flow<sup>8</sup> indicates that while the overall process may be non-linear, quantities which vary smoothly throughout the change in boundary condition can be accurately predicted using indicial theory. This applies in particular to integral quantities such as overall loads, provided that the topology of the flowfield does not change (e.g., appearance or disappearance of shock waves).<sup>13</sup>

Hence, the applicability of the indicial method to dynamic stall hinges on the existence of quantities which remain *smooth* throughout the phenomena associated with dynamic stall. As will be shown in the Results Section below, vorticity fluxes in the leading edge region appear to satisfy this requirement. Furthermore, even in the hypothetical case (not treated here) where a flow quantity of interest should undergo some form of bifurcation, the only requirement for predicting the *onset* of dynamic stall is that its unsteady component behave piecewise linearly on one side of (i.e., prior to) this bifurcation. For example, if the so-called vorticity eruption phenomenon<sup>14,15</sup> at the leading edge constitutes a bifurcation point, then the previous theoretical developments apply only to the physics of the flow up to the vorticity eruption process.

In order to effectively predict dynamic stall using indicial theory, two separate but related objectives must be achieved. First, the applicability of indicial theory must be demonstrated. Second, and in the event that the demonstration is successful, proof must be given that the flow quantity(ies) to which the theory applies are indeed precursors of the phenomenon itself. While some results towards this second objective (not shown here) are currently being obtained as part of the contract supporting this work, the limited objective of the present paper is to prove or disprove the applicability of indicial theory to the problem of incipient dynamic stall.

## RESULTS

All calculations presented in this paper have been performed with a modified version of NASA Ames' ARC2D<sup>16</sup> time-implicit finite difference computer code. Two computational grids were used: a  $169 \times 51$  grid for the  $Re = 1,000$  case and a  $169 \times 80$  for the  $Re = 12,000$  case. Details of the latter grid (O-mesh) are shown in Fig. 1 for the trailing and leading edge regions of the

airfoil. Fig. 1(b) illustrates the tangential clustering of the mesh in the region between 0 and 2 percent of chord from the leading edge. Also shown (grey shaded area) is a control volume over which integrated tangential and normal fluxes of the vorticity are computed and stored at each time step. A typical result (in which only a subset of flow vectors has been shown for clarity) appears in Fig. 2.

Although most of the quantitative results presented in this paper are for the  $Re = 1,000$  and  $Re = 12,000$  cases ( $M_\infty = 0.2$ ), sample results for a model problem related to dynamic stall ( $Re = 100,000$ ,  $M_\infty = 0.1$ ) will be presented first. The purpose of this model problem (described below) is to remove some of the complications and simplify the problem, in order to isolate relevant physics and better understand the vorticity dynamics associated with "incipient" dynamic stall.

### Model Problem

In the absence of compressibility effects, vorticity may only enter the flowfield by viscous diffusion from the boundary of the airfoil. The amount of vorticity is dictated by the tangential pressure gradient in the vicinity of the leading edge.<sup>17,18</sup> This pressure gradient would be *maximized* at any angle of attack if the flow remained completely attached such as in potential flow. In reality, the pressure gradient is "relieved" by flow separation, which acts to augment the effective leading edge radius "seen" by the outer potential flow. This idea is also based on corroborating evidence in stall experiments at high pitch rate, which show that the formation of a leading edge recirculation is delayed, thus creating a flowfield at the leading edge which initially "resembles" potential flow.

To approximate this condition, vorticity-free boundary conditions were implemented, resulting in steady initial conditions which were free of separation (see for example Fig. 3). At some initial time denoted  $t = 0$ , the no-slip boundary condition is impulsively applied. The vorticity field that rapidly develops after the imposition of the no-slip condition results in dynamic stall within a fraction of the convective time scale. The existence of a well-defined time origin for the various dynamical processes, the absence of a laminar bubble prior to stall, and the absence of any trailing edge separation are the key ingredients of the model problem. In addition, the initial conditions are independent of Reynolds number. The resulting unsteady flowfield (which will be the topic of a forthcoming AIAA Paper<sup>19</sup>) shares many of the characteristics of high Reynolds number, high pitch rate dynamic stall, with the exception of moving-wall and apparent mass effects.

The results shown in Figs. 4 and 5 illustrate the evolution of the vorticity field at successive instants of time shortly after turning on the no-slip boundary condition. Detailed analyses of the unsteady flowfield at  $\alpha = 45^\circ$  and  $\alpha = 30^\circ$  (not shown here) indicate that leading edge separation occurs extremely rapidly, and

that the process is essentially "smooth" in terms of vorticity dynamics. The surface flow topology corresponding to  $\alpha = 30^\circ$  is shown in Fig. 6(a) ( $Re = 100,000$ ), where the lines demarcate regions of forward and reverse flow along the airfoil surface. This is contrasted to the  $Re = 1,000$  case (Fig. 6(b), same scale) which exhibits neither shedding (indicated by oblique pairs of lines in Fig. 6(a)) nor secondary separation over the shown time interval ( $0.0 \leq t U_\infty / c \leq 0.1$ ). Secondary separation at  $Re = 1,000$  occurs some later time (see Fig. 7(b)) and, hence, the overall time scale for the onset of dynamic stall is larger both at the lower Reynolds numbers (see Fig. 6) and for lower angles of attack (note the doubling of the horizontal scale between the cases in Fig. 7). Such conditions are better suited for the purpose of detailed temporal analyses of vorticity fluxes and accumulation. Consequently the remainder of this paper is devoted to the low Reynolds number flowfields ( $Re = 1,000$  and  $Re = 12,000$ ) as a test bed for the applicability of indicial theory to the prediction of incipient dynamic stall.

A comparison of the time evolution of tangential and normal fluxes of the vorticity (for the control volume depicted in Fig. 1(b)) is shown in Fig. 8. Each line corresponds to the flux at a given (tangential or normal) position; the arrow indicates the direction of increasing coordinate. The fluxes are seen to peak and decay smoothly. An equivalent "flux angle,"  $\theta$ , at a fixed tangential location central to the control volume can be defined at each of the normal coordinates as  $\theta = \tan^{-1}(\phi_n / \phi_t)$ . Vorticity accumulation (not shown here) peaks at approximately  $t U_\infty / c = 0.003$ . This is followed by a gradual "turn" (see Fig. 8(c)) of the convective vorticity flux from a direction tangential to the surface ( $\theta = 0^\circ$ ) to an inclination  $\theta$  approaching  $45^\circ$ . While qualitatively similar peak-and-decay behavior of both normal and tangential vorticity fluxes was also observed for the case of real dynamic stall during steady pitch-up ( $d\alpha^+ / dt = 0.6$ ), the overall time scales (consistent with the results of Fig. 8) are typically larger than in the model problem at  $\alpha = 45^\circ$ .

### Validation of Indicial Theory

Having tentatively established the relative smoothness of the leading edge vorticity dynamics prior to, during, and immediately after the onset of dynamic stall, we now turn to some direct attempts at the validation of indicial theory. This section is divided into three parts. In the first part, validation of indicial theory is performed using small amplitude steps in the boundary conditions to determine the indicial responses of the flow directly. The second part details the implementation of indicial theory using a Laplace domain approach applicable to large amplitude (i.e., several degrees) motion, including cases where amplitude non-linearity is important. In the third part of the results, the accuracy of the proposed method is evaluated by inverting back to the time domain, and is applied to angular motions between  $\alpha = 10^\circ$  and  $\alpha = 15^\circ$  at a Reynolds number  $Re = 12,000$ .

### Part 1: Direct Validation, $Re = 1,000$ .

For the purpose of the present paper, only a limited set of conditions are considered, involving small oscillations about two angles of attack:  $\alpha = 16^\circ$  and  $\alpha = 30^\circ$ . The Mach and Reynolds numbers (respectively  $M_\infty = 0.2$  and  $Re = 1,000$ ) are fixed, and two types of indicial responses are computed. The conventional determination of an indicial function involves performing a step in the boundary condition (in this case,  $\alpha$ ) and recording the response, say  $\Delta\phi_t$  or  $\Delta\Omega^+$ . For  $t > 0$ ,  $\Delta\phi_t(t) / \Delta\alpha$  is the indicial response of  $\phi_t$  with respect to its boundary condition  $\alpha$  in the infinitesimal limit  $\Delta\alpha \rightarrow 0$ . For the case of a body in motion, it is more relevant to consider the dynamic indicial response, calculated as the Fréchet derivative<sup>9,10</sup> of  $\phi_t$  with respect to  $\alpha$ :

$$\begin{aligned} \tilde{\phi}_t(\alpha(\xi); t, \tau) &= \lim_{\Delta\alpha \rightarrow 0} \frac{\Delta\phi_t(\tau)}{\Delta\alpha} \\ &= \lim_{\Delta\alpha \rightarrow 0} \left[ \frac{\phi_t[\alpha(\xi) + H(\xi - \tau)\Delta\alpha] - \phi_t[\alpha(\xi)]}{\Delta\alpha} \right] \end{aligned} \quad (5)$$

where the step in boundary condition,  $\Delta\alpha$ , is applied at some time  $t = \tau$ , and  $H$  designates the Heaviside step function. The simple case of a ramp-and-hold motion is schematically illustrated in Fig. 9. For example, to obtain the dynamic indicial response on the lift, two lift responses, say to motions (a) and (b) in Fig. 9, are differenced and normalized by the magnitude of the step,  $\Delta\alpha$ . The difference between maneuvers (a) and (b) (at  $16^\circ$ ) or (c) and (d) (at  $30^\circ$ ) will be referred hereafter as the "indicial maneuver" or "indicial motion." In this Part 1 of the validation results, the step magnitude is small, consistent with the theory, and typically on the order of one tenth of one degree, or less.

Figure 10 compares indicial theoretical predictions (lines) and direct numerical simulation results (symbols) for both phase and amplitude of the fluctuating tangential vorticity flux. The direct numerical simulations involve ramping the airfoil from  $\alpha = 0^\circ$  to  $\alpha = 16^\circ$  at a constant pitch rate,  $d\alpha^+ / dt = 0.6$ . When the airfoil reaches the end of the ramp, it starts oscillating at a reduced angular frequency  $\omega$ . The phase ( $\Delta\phi$ ) and amplitude ( $A$ ) of the tangential flux response at 2% chord,  $\Delta\phi_t(t)$ , are measured after 5 or 6 cycles of the oscillation (to eliminate transient effects). Both  $\Delta\phi$  and  $A$  are defined relative to their quasi-static counterpart. The lines represent indicial theoretical predictions, assuming a single frequency oscillatory input,  $\varepsilon(\tau) = \Delta\alpha \times e^{i\omega\tau}$ . The dotted line corresponds to the prediction, Eq. (3), using the dynamic indicial response. The solid line corresponds to the same theoretical prediction using the static indicial response (dashed line in Fig. 9). The symbols are the result of direct numerical simulations for airfoil harmonic oscillations about  $\alpha = 16^\circ$ . The circles are associated with ramp-and-oscillate maneuvers, while the triangle corresponds to the case of an oscillation started from a steady angle of attack. For both types of maneuvers, the comparison is seen to be excellent.

A similar comparison ( $\alpha = 16^\circ$ ) is given in Fig. 11 for the phase and amplitude of the vorticity

accumulation,  $\Omega^*$ , between direct numerical simulations and the indicial theoretical prediction. The direct numerical simulations require each on the order of a half-hour to an hour on a CRAY Y-MP; whereas, the indicial theoretical prediction takes 30 seconds on a VAX-780 for 100 frequencies. As in Fig. 10, theory and numerical experiment agree well. But when the same experiment is repeated (Figure 12) for a hold-angle of  $30^\circ$  ((c) and (d) in Fig. 9), the agreement with indicial theory is poor. The non-linearity of the vorticity accumulation manifests itself in the form of a low frequency modulation superimposed on the basic forcing frequency (see inset of Fig. 12). A major difference between  $\alpha = 16^\circ$  (Figs. 10 and 11) and  $\alpha = 30^\circ$  (Fig. 12) is that the flow is asymptotically unsteady for the latter. At the low Reynolds number considered here, the solution at  $\alpha = 16^\circ$  is steady. It is important to realize, however, that for larger Reynolds numbers, for example  $Re = 12,000$  and beyond, the flow is both separated (to varying degrees) and unsteady at all angles of attack. Asymptotic (large time) unsteadiness *per se* does not preclude the use of indicial theory. However, it was found in the case of Fig. 12 that the indicial function itself (calculated from the relative response between maneuvers (c) and (d)) does not converge to steady state, a situation to which indicial theory does not apply.<sup>11</sup>

To circumvent this difficulty and extend the range of validity of indicial theory, a method was sought to increase the amplitude of the "indicial maneuver." The rationale behind this approach can be described as follows. Since the chaotic dynamics which "contaminate" the indicial responses are an inherent, insuppressible, feature of the flow at large Reynolds numbers and large angles of attack, a possible approach is to attempt instead to *minimize* the pseudo-random or chaotic component of the response. This can be achieved by maximizing the deterministic portion of the flow response through the use of large amplitude indicial motions. Of course there will be an upper limit to this approach, as one gets into the non-linear regime. In effect, the new approach (explained below, Part 2) relies on "finite amplitude" (say on the order of several degrees), rather than infinitesimal, indicial maneuvers. These are used to infer indicial responses in which the non-deterministic component is kept to a minimum.

#### Part 2: Laplace Domain Approach.

There are several difficulties associated with the calculation of finite step responses using CFD. Most often, CFD codes will not run for these conditions, except for the smallest of step sizes and, even so, using very small time steps. Even if a stable solution can be obtained, its accuracy is dubious because such changes in the boundary conditions are not consistent with the temporal and spatial orders of accuracy of the numerical methods being used.<sup>20</sup> Furthermore, the flow responses can be non-physical, introducing for example transient shocks and piston effects which are absent in the real flow. As mentioned previously, it stands to reason that indicial theory cannot be used when the physics contained in the indicial response(s) of the system differ

from the physics of the cases to be predicted. Thus, a straight-forward time domain application of the theory, as stated in Eqs. (3) to (5), cannot be realized unless the indicial motion approximates an infinitesimal step. To remedy this problem, we now consider the Laplace domain version of the indicial formalism.

The Laplace transform of Eq. (3) is given by

$$f(s) = s\tilde{f}(s)\varepsilon(s) \quad (6)$$

where  $\tilde{f}(s)$ ,  $\varepsilon(s)$ ,... designate the Laplace transforms of  $\tilde{f}$ ,  $\varepsilon$ , etc., respectively. Keeping in mind that  $f$  and  $\varepsilon$  represent changes with respect to a base line maneuver (denoted "1"), Eq. (6) can be inverted as follows

$$\tilde{f}(t) = \mu_\varepsilon(t) = L^{-1} \left[ \frac{1}{s} \frac{\mu_2(s) - \mu_1(s)}{\varepsilon_2(s) - \varepsilon_1(s)} \right] \quad (7)$$

where  $L$  designates the Laplace operator. In (7), maneuver "1" is characterized by the boundary condition schedule  $\varepsilon_1(t)$  and by the absolute flow response  $\mu_1(t)$ ; maneuver "2" is characterized by  $\{\varepsilon_2(t), \mu_2(t)\}$  which differs from  $\{\varepsilon_1(t), \mu_1(t)\}$  after time  $t = 0$  (see Figure 13). Naturally, one recovers the original formulation for

$$\varepsilon_2(t) = \varepsilon_1(t) + \Delta\varepsilon H(t) \quad (8)$$

with  $\Delta\varepsilon = \text{const}$ . In this case:  $\varepsilon_2(s) - \varepsilon_1(s) = \Delta\varepsilon/s$  and, obviously:  $\mu_\varepsilon(t) = \Delta\mu(t)/\Delta\varepsilon$ , which is the analog of Eq. (5) when (1) is exact. In the general case, however, note that, if Eq. (7) is used,  $\varepsilon_2$  and  $\varepsilon_1$  need not differ by a constant (see Fig. 13), nor does their difference need to be infinitesimal, which is the basis of the present method.<sup>21</sup>

The validation of the Laplace domain-based method, Eqs. (3) and (7), is first shown for low angles of attack with trailing edge flow separation ( $Re = 12,000$ ,  $M_\infty = 0.2$ ). To illustrate how the method works, consider Figs. 14 and 15. Both maneuvers smoothly ramp-up the angle of attack by a whole degree, from  $\alpha = 4^\circ$  to  $\alpha = 5^\circ$ . Figure 14 depicts the history of the tangential vorticity flux for the airfoil at rest (curve "1"), for the ramped motion (curve "2"), and for the differential response ("2"- "1"). The motion is the same fifth order polynomial ramp as in Refs. 20 and 21, chosen primarily for its smoothness (zero first and second derivatives at the end points). The motions considered in Figs. 14 and 15 differ only by the overall length of the ramp, or "ramp time," denoted  $T$ . Figure 14 depicts the case of a "fast" maneuver ( $T = 0.1$ ), and Fig. 15 that of a maneuver taking place over a period 40 times longer ( $T = 4$ ). Note that the difference curve ("2"- "1") in Fig. 14 is not the indicial response, but a so-called characteristic response from which the indicial response can be inferred, using (7). The goal is to evaluate whether the slow response ( $T = 4$ ) can be predicted from the application of indicial theory, when using the indicial function inferred from the fast maneuver (Fig. 14).

Figure 16 compares the result of the direct numerical simulations to the Laplace domain indicial prediction. Two pairs of curves are shown in the figure. In each pair, one curve represents the flux Laplace

transform from DNS and the other its prediction by the indicial method. For  $T = 4$ , the prediction is based, as previously mentioned, on an indicial function inferred from the  $T = 0.1$  maneuver. The two curves are virtually indistinguishable from one another over the entire Laplace spectrum, with the exception of the largest values of  $s$  (corresponding to the short time scales). The agreement is equally good for the second curve pair shown in Fig. 16, which illustrates the prediction accuracy for the fast maneuver, based on an indicial function inferred from the slow one (Fig. 15). This is, of course, to be expected for a system which would be perfectly linear.

In Figures 14 through 16, the motions that were considered were all of the same amplitude:  $\Delta\alpha = 1^\circ$ . In contrast, if one attempts to use the indicial function inferred from  $T = 0.1$  (Fig. 14) to predict a large amplitude maneuver from  $\alpha = 4^\circ$  to  $\alpha = 8^\circ$ , the quality of the prediction deteriorates significantly. This is indicated in Fig. 17 by the spread between DNS and prediction for  $s < 1$ . Note that all four curves in Fig. 17 are parallel to each other at small  $s$  and are, in fact, proportional to  $1/s$ . Therefore, the source of the discrepancy for large time is caused by amplitude non-linearity of the static response. In effect, the linear assumption that the increment in steady vorticity flux between  $\alpha = 4^\circ$  and  $\alpha = 8^\circ$  is four times that between  $\alpha = 4^\circ$  and  $\alpha = 5^\circ$  breaks down, even at these low angles of attack. This is to be expected for any angle change other than infinitesimal since, even for an attached flat plate boundary layer, the vorticity flux is proportional to  $U_\infty^2$ . In other words, the flow response must be non-linear. Given these facts, the question that the remainder of this paper attempts to answer is: to what extent can the formalism of indicial theory be used to predict the flow? And, if necessary, how must the theory be amended to handle the cases of interest?

In Fig. 18, the accurate prediction of the large amplitude case shown in Fig. 17 is achieved by using indicial theory based on an equivalent indicial response which is inferred from a large amplitude ramp maneuver, from  $\alpha = 4^\circ$  to  $\alpha = 8^\circ$  ( $T = 0.4$ ). This indicial maneuver differs in two ways from that considered previously: 1) the ramp time is  $T = 0.4$  (instead of  $T = 0.1$ ) because of limitations of the code (maximum  $d\alpha^+/dt$ ), and 2) the amplitude of the motion ( $\Delta\alpha = 4^\circ$ ) is now the same as the motion to be predicted. Making the amplitudes the same will, evidently, take care of the previous discrepancy due to quasi-static non-linearity. What the comparison of Fig. 18 shows, however, is that, once quasi-static amplitude non-linearity is taken into account, the unsteady phase lags are predicted accurately using the formalism of indicial theory. In other words, the unsteady component of the flow behaves almost linearly if the indicial function is appropriately stretched in amplitude. Since the comparisons of Figs. 16 and 18 are only along the real axis of the Laplace domain, they are to be regarded only as an indication that indicial theory, used in the above manner, can predict the vorticity dynamics of the flow. The real proof of concept must involve all of the Laplace

domain information (i.e., inversion back to the time-domain) and must apply to the case where leading edge separation is present. This validation exercise is the object of Part 3.

### Part 3: Validation of the Laplace Domain-Based Approach, $Re = 12,000$ .

In this section, the implementation of indicial theory as described in Part 2 is attempted for airfoil pitching motions ranging from  $\alpha = 10^\circ$  to  $\alpha = 15^\circ$ . For all of these cases, the Reynolds number is  $Re = 12,000$ , and the freestream Mach number is  $M_\infty = 0.2$ . Figure 19 illustrates the angular motions under consideration. These are characterized by the total ramp time,  $T$ , in the case of ramp-up or ramp-down motions, or by the frequency,  $F$ , in the case of oscillations (an equivalency between the two can also be defined by considering the first half of the oscillatory cycle to correspond to a smooth ramp, and vice-versa). The maneuver characteristics are summarized in Table 1, along with the airfoil motions considered in Part 2.

$\alpha (^\circ)$	$T$	$k = \pi F c / U_\infty$	$(d\alpha^+/dt)_{max}$
4 to 5	0.1	15.70	0.327
	4.0	0.39	0.008
4 to 8	0.4	3.93	0.327
	4.0	0.39	0.033
10 to 15	0.5	3.14	0.327
	0.7	2.24	0.234
	2.0	0.78	0.082
	2.5	0.63	0.065
	8.0	0.20	0.020

Table 1. Summary of Airfoil Motion Conditions

In the examples considered here, the various maneuvers are all referenced to the fastest ramp-up ( $T = 0.5$ ) motion in Fig. 19. This means that the raw vorticity flux or vorticity accumulation responses are all processed so that the relative flow response is defined with respect to the case  $T = 0.5$ . For example, the relative vorticity accumulation,  $\delta\Phi^*$ , for  $T = 2.5$  is defined as:

$$\delta\Phi^*(t) = \Phi_{T=2.5}^* - \Phi_{T=0.5}^* \quad (9)$$

and so on. It is this relative flow quantity that the indicial theory attempts to predict, in response to the relative change in angle of attack,  $\delta\alpha$ , defined as:

$$\delta\alpha(t) = \alpha_{T=2.5} - \alpha_{T=0.5} \quad (10)$$

The relative angle of attack variation is the input to the indicial prediction, and is shown in Fig. 20 (solid line). The other lines in Fig. 20 represent the relative motion,  $\delta\alpha$ , for the various ramp times and frequencies shown in Fig. 19.

Before discussing the results of the prediction method, an example of the computed flowfields being analyzed is shown in Fig. 21. Figure 21 depicts contours of the primary vorticity at two time instants during a



typical pitch-up maneuver ( $T = 0.5$ ). The flowfield solutions are rotated in the same reference frame for comparison purposes (the equations of motion are solved in an inertial frame of reference in which the airfoil is rotated). Figure 21 illustrates a typical result, obtained using the computational grid shown in Fig. 1. The vorticity contours at  $t = 0.4$  (80% into the maneuver) suggest the presence of an essentially attached shear layer (dashed lines) at the leading edge. The layer separates and rolls into a vortex some time later (solid lines), as is illustrated by the topological changes seen in Fig. 21.

The changes in the integrated vorticity fluxes and vorticity accumulation at the leading edge during vortical lift-off and roll-up have been examined in detail. Typical prediction accuracy is shown in Figs. 22 through 24.

Figures 22, 23, and 24 compare the DNS results for vorticity accumulation (solid line) to the indicial theoretical prediction (dashed line). The latter was transformed to the time domain by using a numerical inverse Laplace transform technique based on Laguerre functions.<sup>22</sup> The prediction is obtained using the method described in Part 2, where the indicial function is inferred in the Laplace domain from an indicial motion (indicial "pulse," in the present case) corresponding to the difference between the two fastest ramps,  $T = 0.5$  and  $T = 0.7$ . This indicial motion is shown as the short negative pulse in Fig. 20. Figure 22 compares the vorticity accumulation between DNS and prediction for a ramp-up motion with  $T = 2.5$ . The prediction is reasonably accurate at short times and even appears to capture some of the details of the flow response up to  $t = 2.5$ .

At large times, there are intrinsic, pseudo-random, fluctuations due to vortex shedding and other chaotic phenomena in the flow. Thus, the relative response is inherently unsteady, even long after the motion has ceased. This form of unsteadiness is uncorrelated with the motion itself. Recall that the predictions shown here are for single realizations. The use of phase-averaging on multiple realizations would presumably average out the non-deterministic portion of the signal and increase the accuracy of the prediction. Note that the prediction itself is based on a single realization of ramp maneuvers  $T = 0.5$  and  $T = 0.7$ . Again, realization averaging would be desirable to increase the accuracy of the prediction. The latter can only predict the *deterministic* unsteadiness caused by changes in the boundary conditions,  $\delta\alpha$ . In the present case, realization averaging was too expensive (using CFD-generated results), and was simulated instead by filtering out the fluctuating component of the indicial response for  $t > 3.2$  (recall that the indicial motion is completely over ( $\delta\alpha = 0$ ) by  $t = 0.7$ ).

In spite of the pseudo-random component of the fluctuation response, the accuracy of the prediction during the initial portion of the motion is clearly illustrated, both in the ramp cases, Figs. 22 and 23, and in the oscillatory case, Fig. 24. The slight undershoot and

overshoot of the prediction for  $t \leq 0.7$  are believed to be related to the accuracy of the inverse Laplace transform procedure, which is itself an approximation. The consistency with which even small scale fluctuations are initially captured by the indicial prediction in all three figures (22, 23, and 24) suggests that these fluctuations are deterministic in nature and, therefore, *can* be predicted using indicial theory, as described in Part 2. Even at large times, the indicial theoretical prediction appears to capture the essential features of the flow response. For example, Fig. 24, the phase, amplitude, and mean of the oscillatory vorticity accumulation appear to be predicted reasonably well.

## CONCLUDING REMARKS

Direct numerical simulations have been used to investigate whether indicial theory could be applied to the prediction of certain key aspects (vorticity dynamics characteristics) associated with dynamic stall.

Preliminary results at low Reynolds number ( $Re \leq 12,000$ ) and low Mach number suggest that integrated vorticity fluxes and vorticity accumulation at the leading edge are essentially smooth functions of their boundary condition. Based on this observation, the applicability of indicial theory was first evaluated directly in the time domain using step responses to calculate the indicial functions of the flow. For small motion amplitudes and high frequency, unsteady vorticity fluxes and accumulation were found to be predicted well by indicial theory.

For finite amplitude airfoil motions, large angles of attack, and/or larger Reynolds numbers, the straight forward application of indicial theory gave poor predictions. To circumvent some of the problems encountered under these conditions, a Laplace domain-based method using finite amplitude indicial motions was implemented and tested for linear and non-linear airfoil motions. For large amplitude ( $\Delta\alpha = 5^\circ$ ) non-linear maneuvers, it is shown that the linear formalism of indicial theory can be retained, provided that the indicial functions are *inferred* in the Laplace domain from a reference indicial motion having the same amplitude. In other words, the unsteady component of the flow behaves almost linearly if the indicial function is appropriately stretched in amplitude.

## ACKNOWLEDGMENT

The author gratefully acknowledges the support of this work by the Army Research Office under Contract No. DAAL03-92-0013, monitored by Dr. Thomas L. Doligalski. The author also wishes to thank Mr. Stanley C. Perkins at NEAR for his help on the processing of the data, as well as Dr. Lawrence W. Carr and the NASA Ames Research Center for supplying the supercomputer time needed for this project.

## REFERENCES

- Ghia, K.N., Ghia, U., and Osswald, G.A.: "Characterization of Dynamic Stall Phenomenon Using Two-Dimensional Unsteady Navier-Stokes Equations," Presented at the NASA/AFOSR/ARO Workshop on the Physics of Forced Unsteady Separation, Moffett Field, CA, April 17-19, 1990.
- Carr, L.W., Chandrasekhara, M.S., and Ahmed, S.: "A Study of Dynamic Stall Using Real Time Interferometry," AIAA Paper 91-0007, 1991.
- Acharya, M. and Metwally, M.H.: "Evolution of the Unsteady Pressure Field and Vorticity Production at the Surface of a Pitching Airfoil," AIAA Paper 90-1472, 1990.
- Schreck, S. and Helin, H.E.: "Unsteady Vortex Dynamics and Surface Pressure Topologies on a Pitching Wing," AIAA Paper 93-0435, 1993.
- Ericsson, L.E.: "The Problem of Dynamic Stall Simulation Revisited," AIAA Paper 93-0091, 1993.
- Lorber, P.F. and Carta, F.O.: "Unsteady Separation Experiments on 2 D Airfoils, 3 D Wings, and Model Helicopter Rotors," Presented at the NASA/AFOSR/ARO Workshop on the Physics of Forced Unsteady Separation, Moffett Field, CA, April 17-19, 1990.
- Reisenthel, P.H. and Nixon, D.: "Application of Indicial Theory to the Prediction of Unsteady Separation," AIAA Paper 91-1742, 1991.
- Nixon, D.: "Alternative Methods for Modeling Unsteady Transonic Flows," Unsteady Transonic Aerodynamics, Vol. 120 of Progress in Astronautics and Aeronautics, Ed. D. Nixon, AIAA, 1989.
- Tobak, M.: "On the Use of the Indicial Function Concept in the Analysis of Unsteady Motion of Wings and Wing-Tail Combinations," NACA Report 1188, 1954.
- Tobak, M. and Chapman, G.T.: "Nonlinear Problems in Flight Dynamics Involving Aerodynamic Bifurcations," NASA TM 86706, 1985.
- Jenkins, J. E.: "Relationships Among Nonlinear Aerodynamic Indicial Response Models, Oscillatory Motion Data, And Stability Derivatives," AIAA Paper 89-3351, 1989.
- Henk, R.W., Reynolds, W.C., and Reed, H.L.: "Experiments on an Unsteady, Three-Dimensional Separation," Presented at the NASA/AFOSR/ARO Workshop on the Physics of Forced Unsteady Separation, Moffett Field, CA, April 17-19, 1990.
- Nixon, D.: private communication, November 1991.
- Peridier, V.J., Smith, F.T., and Walker, J.D.A.: "Vortex-Induced Boundary-Layer Separation. Part 1. The Unsteady Limit Problem  $Re \rightarrow \infty$ ," *J. Fluid Mech.*, Vol. 232, pp. 99-131, 1991.
- Peridier, V.J., Smith, F.T., and Walker, J.D.A.: "Vortex-Induced Boundary-Layer Separation. Part 2. Unsteady Interacting Boundary-Layer Theory," *J. Fluid Mech.*, Vol. 232, pp. 133-165, 1991.
- Pulliam, T.H.: "Euler and Thin Layer Navier Stokes Codes ARC2D-ARC3D," Notes for Computational Fluid Dynamics User's Workshop, Tullahoma, TN, March 12-16, 1984.
- Reynolds, W.C. and Carr, L.W.: "Review of Unsteady, Driven, Separated Flows," AIAA Paper 85-0527, 1985.
- Helin H.E.: "The Relevance of Unsteady Aerodynamics for Highly Maneuverable and Agile Aircraft," presented at the Symposium on Numerical and Physical Aspects of Aerodynamic Flows, Long Beach, CA, January 16-19, 1989.
- Reisenthel, P.H., Childs, R.E., and Perkins, S.C.: "Application of Indicial Theory to the Analysis of Unsteady Leading Edge Stall," AIAA Paper 94-2339 to be presented at 25th AIAA Fluid Dynamics Conference, June 20-23, 1994, Colorado Springs, CO.
- Lesieutre, D.J., Reisenthel, P.H., and Dillenius, M.F.E.: "An Unsteady Aerodynamics Model Based on Indicial Theory for Multidisciplinary Flight Simulations," NEAR TR 468, August 1993.
- Lesieutre, D. J. and Reisenthel, P. H.: "A Practical Approach for Calculating Aerodynamic Indicial Functions with a Navier-Stokes Solver," AIAA Paper No. 94-0059, 1994.
- Weeks, W.T.: "Numerical Inversion of Laplace Transforms Using Laguerre Functions," *J. Assoc. Comp. Machinery*, Vol. 13, No. 3, July 1966, pp. 419-426.

## FIGURES

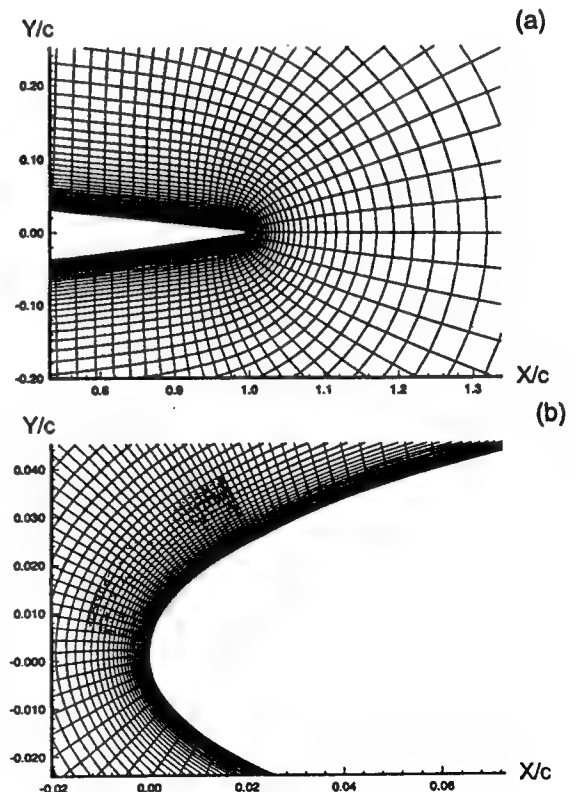


Fig. 1 Illustration of Computational Grid used at  $Re = 12,000$ ; (a) Trailing Edge Region; (b) Leading Edge (grey area indicates the control volume used for the calculation of integrated tangential and normal fluxes of vorticity).

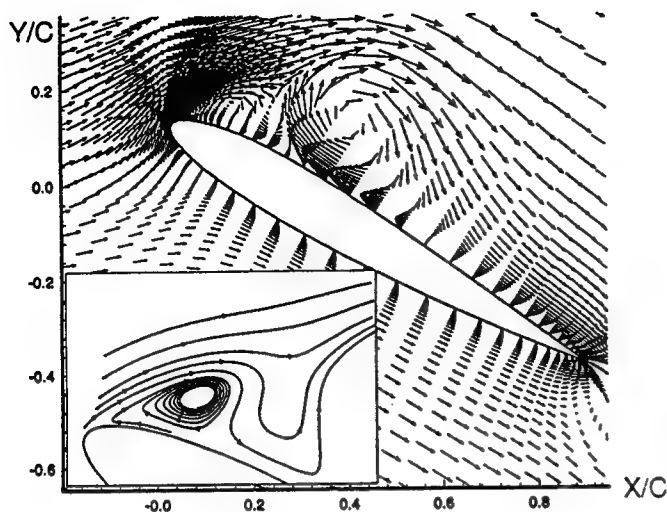


Fig. 2 Velocity Vector Plot Illustrating a Typical Numerical Solution for  $Re = 1,000$ ,  $d\alpha^+/dt = 0.6$ ,  $M_\infty = 0.2$ .

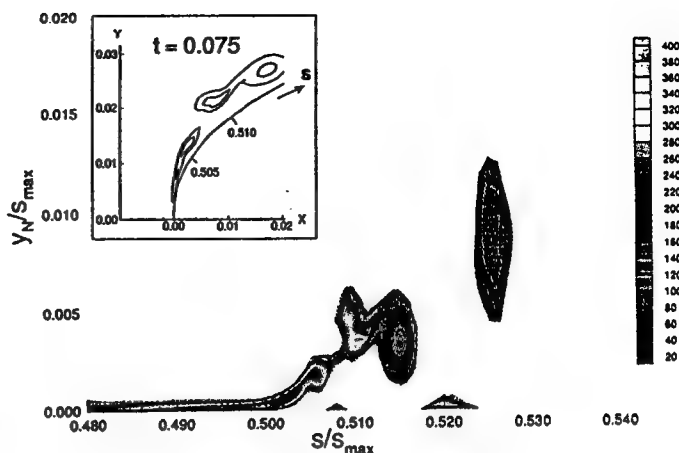


Fig. 5 Vorticity Contours in Tangential/Normal Space and Physical Space (Inset) at time  $tU_\infty/c = 0.075$  After the Application of the No-Slip Boundary Condition ( $M_\infty = 0.1$ ,  $\alpha = 45^\circ$ ,  $Re = 100,000$ ).

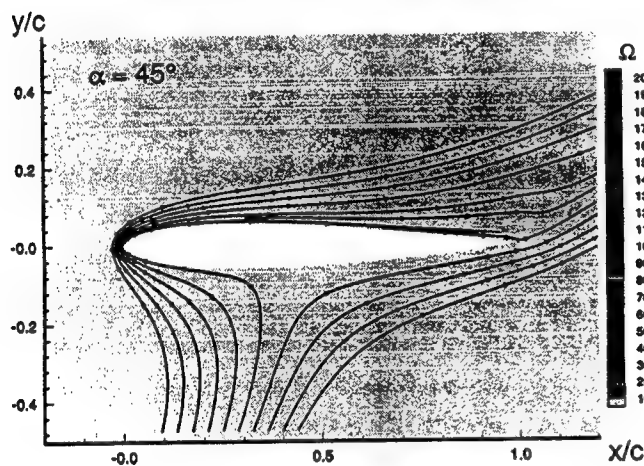


Fig. 3 Streamlines Illustrating the Absence of Flow Separation for the Initial Flowfield Used in the Model Problem ( $M_\infty = 0.1$ ,  $t = 0.0$ ).

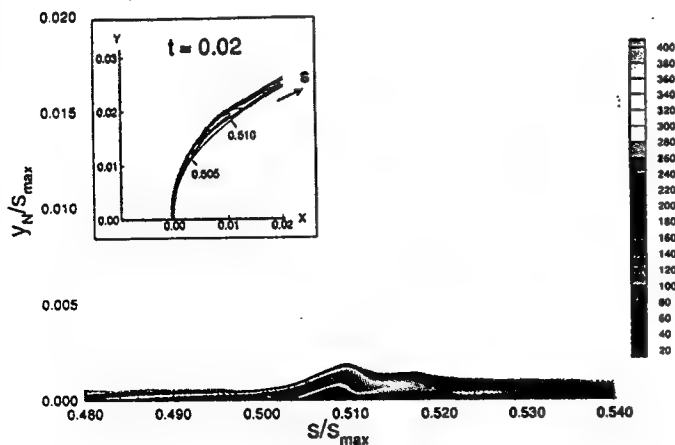


Fig. 4 Vorticity Contours in Tangential/Normal Space and Physical Space (Inset) at time  $tU_\infty/c = 0.020$  After the Application of the No-Slip Boundary Condition ( $M_\infty = 0.1$ ,  $\alpha = 45^\circ$ ,  $Re = 100,000$ ).

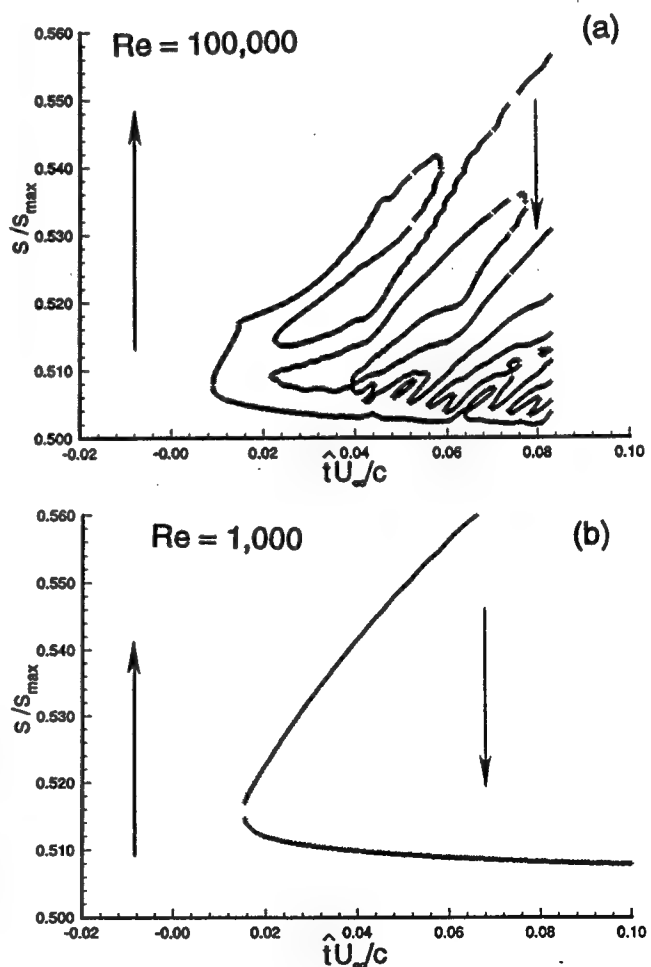


Fig. 6 Comparison of Surface Flow Topology at  $Re = 100,000$  (Top) and  $Re = 1,000$  (Bottom) for  $\alpha = 30^\circ$  and  $M_\infty = 0.1$  (lines demarcate changes in the flow direction along the surface; leading edge at  $s/s_{\max} = 0.5$ ; arrows indicate flow direction).

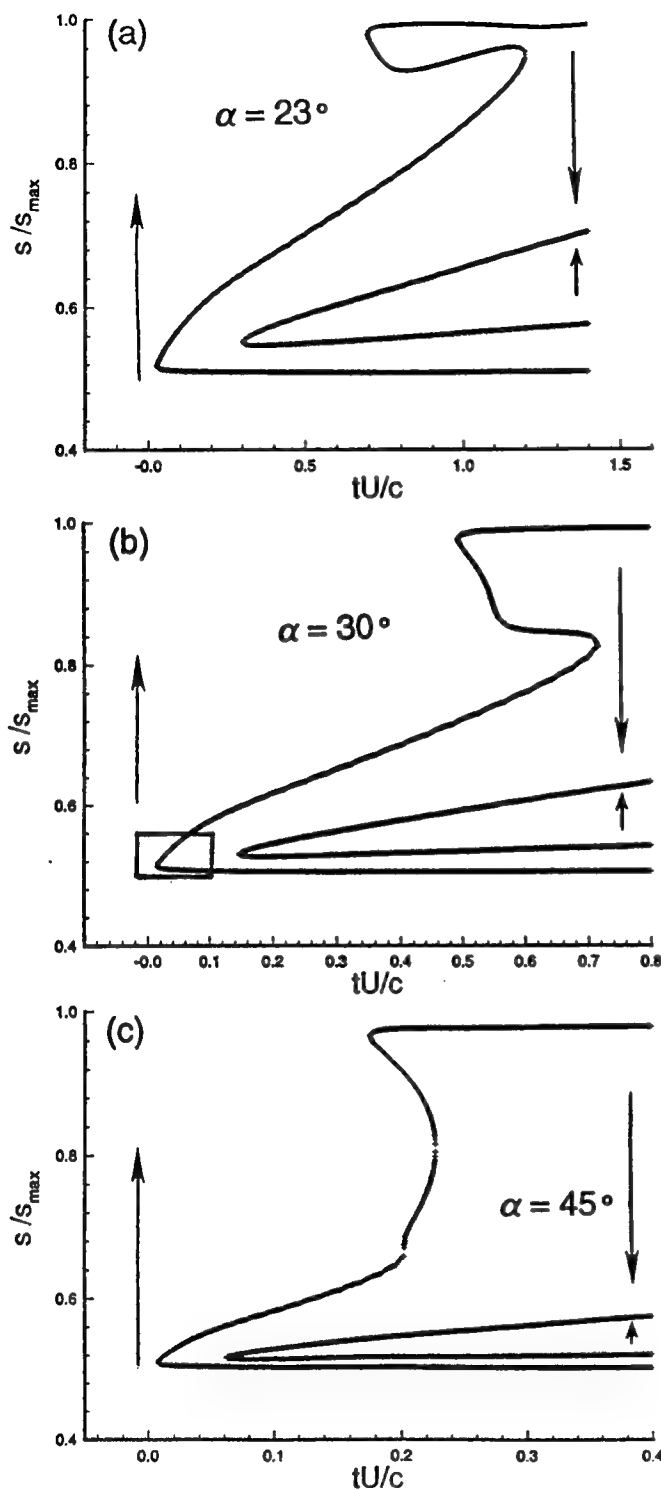


Fig. 7 Comparison of Surface Flow Topology Diagrams at  $Re = 1,000$  Between  $\alpha = 23^\circ$ ,  $\alpha = 30^\circ$  and  $\alpha = 45^\circ$  for  $M_\infty = 0.1$  (lines demarcate changes in the flow direction along the surface; leading edge at  $s/s_{\max} = 0.5$ ; arrows indicate flow direction).

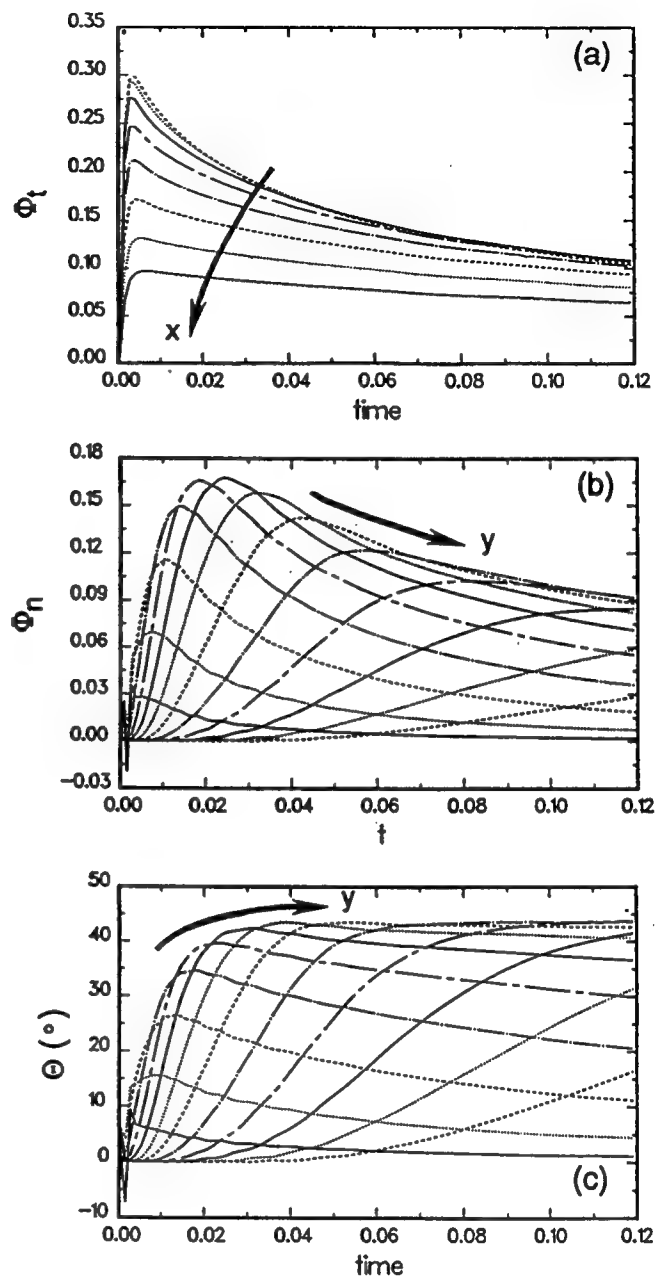


Fig. 8 Temporal Evolution of the Integrated Tangential Vorticity Flux (Top), Integrated Normal Vorticity Flux (Center), and Flux Angle (Bottom) of the Leading Edge Vorticity ( $M_\infty = 0.1$ ,  $Re = 1,000$ ,  $\alpha = 45^\circ$ ). (Arrows indicate direction of increasing coordinate (streamwise coordinate in top graph; normal coordinate in center and bottom graphs).



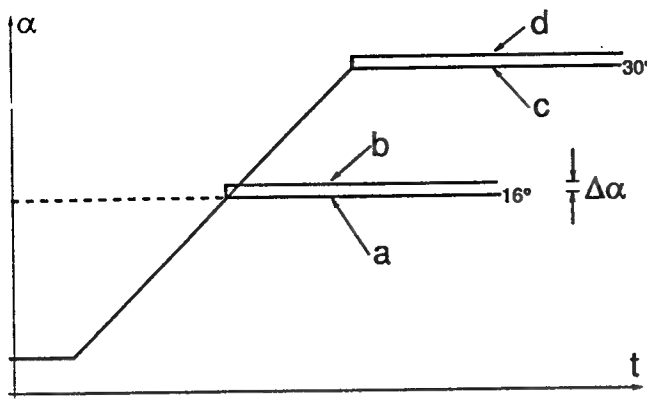


Fig. 9 Schematic Representation Illustrating the Basic Procedure Involved in Calculating the Dynamic Indicial Function.

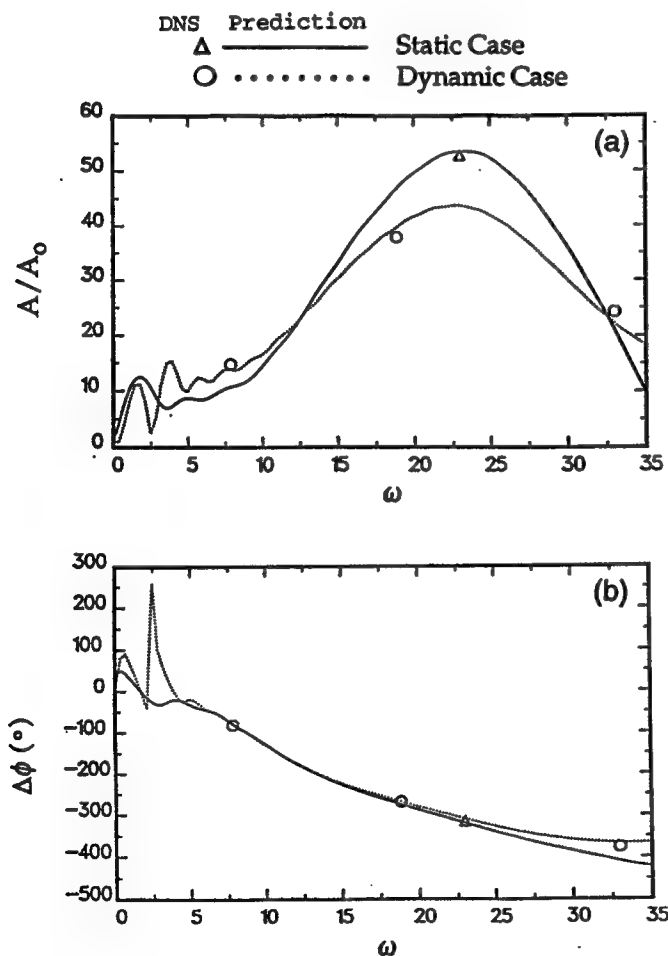


Fig. 10 Comparison Between Indicial Theoretical Prediction (Lines) and Direct Numerical Simulations (Symbols) for the Fluctuating Tangential Vorticity Flux at  $Re = 1,000$ ,  $M_\infty = 0.2$ ,  $\alpha = 16^\circ$ . (—— Static Indicial Response; . . . . Dynamic Indicial Response ( $d\alpha^+/dt = 0.6$ )).

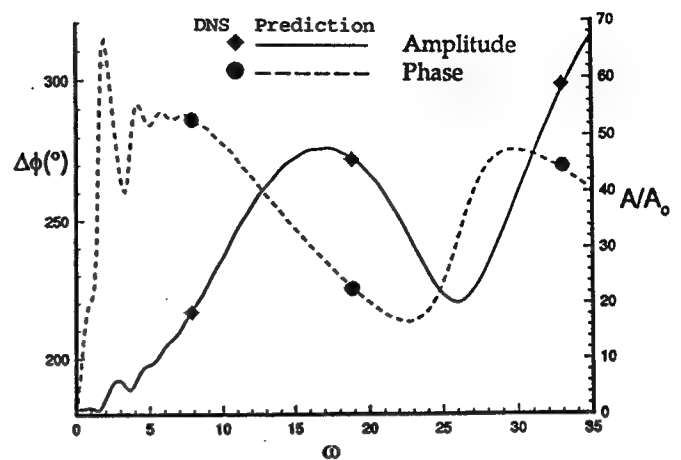


Fig. 11 Comparison Between Direct Numerical Simulation (Symbols) and Indicial Theoretical Prediction of Phase (Dashed Line) and Amplitude (Solid Line) for the Accumulated Vorticity,  $\Omega^*$ , at  $Re = 1,000$ ,  $M_\infty = 0.2$ ,  $\alpha = 16^\circ$ .

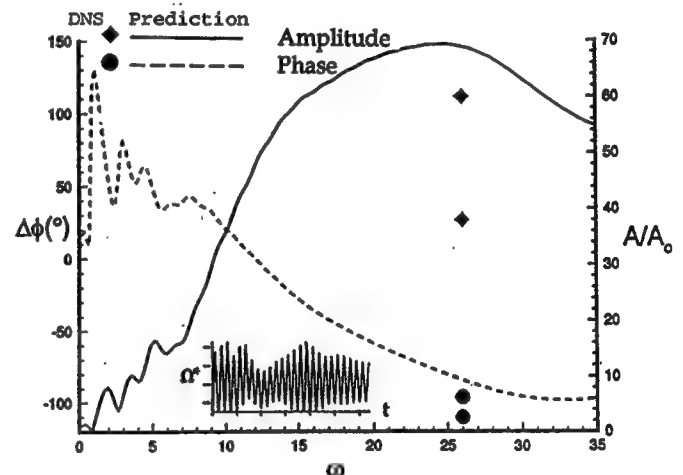


Fig. 12 Comparison Between Direct Numerical Simulation (Symbols) and Indicial Theoretical Prediction of Phase (Dashed Line) and Amplitude (Solid Line) for the Accumulated Vorticity,  $\Omega^*$ , at  $Re = 1,000$ ,  $M_\infty = 0.2$ ,  $\alpha = 30^\circ$ . The Inset in the Bottom Figure Illustrates the Presence of a Low Frequency Modulation of the Output at  $\alpha = 30^\circ$ .

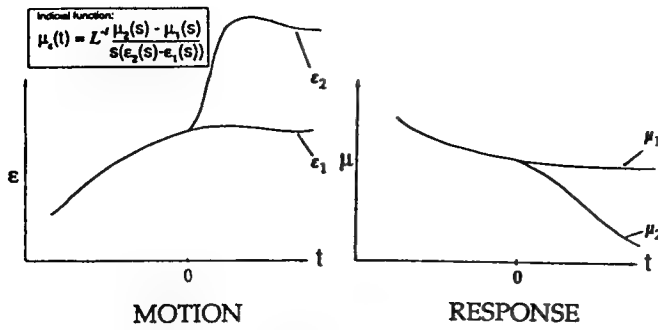


Fig. 13 Schematic Illustrating the Use of Finite Amplitude Indicial Motions to Infer the Indicial Function in the Laplace Domain.

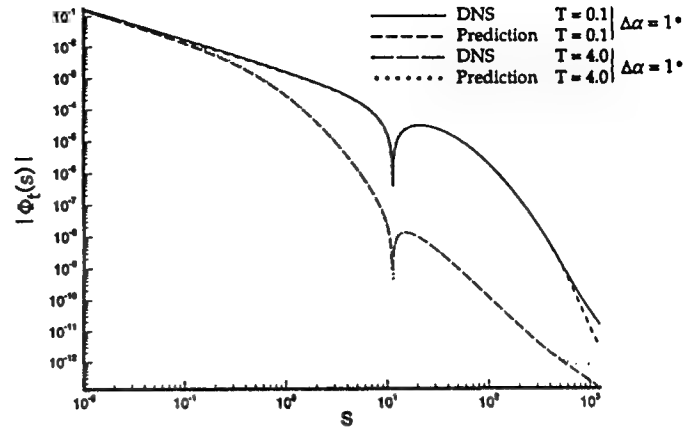


Fig. 16 Laplace Domain Comparison of Indicial Theoretical Prediction Versus Direct Numerical Prediction,  $Re = 12,000$ ,  $\alpha = 4^\circ \rightarrow 5^\circ$ .

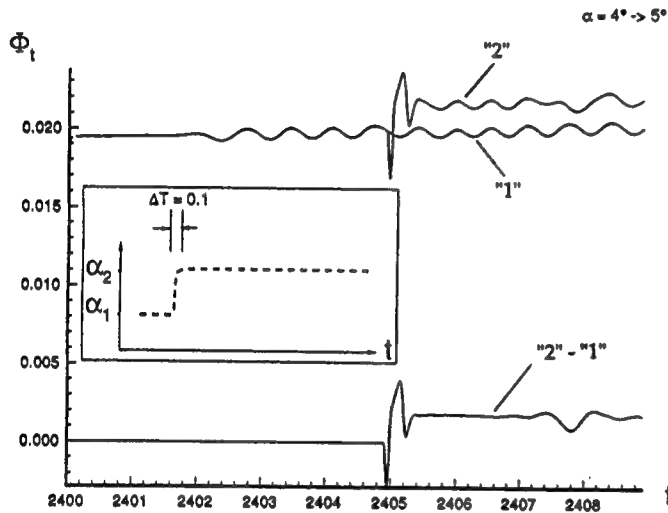


Fig. 14 Illustration of the Procedure Used to Infer the Indicial Function: Integrated Tangential Vorticity Flux at 2% chord,  $Re = 12,000$ ,  $T = 0.1$ .

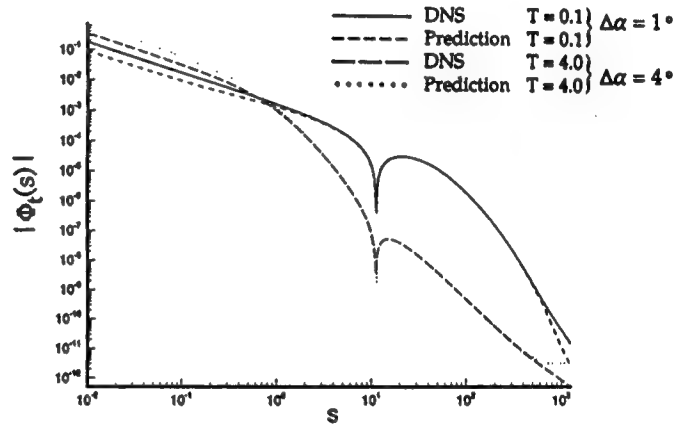


Fig. 17 Laplace Domain Comparison of Indicial Theoretical Prediction Versus Direct Numerical Prediction Illustrating the Deterioration of Accuracy for Large Time in the Presence of Quasi-Static Non-Linearity,  $Re = 12,000$ ,  $\alpha = 4^\circ \rightarrow 8^\circ$ .

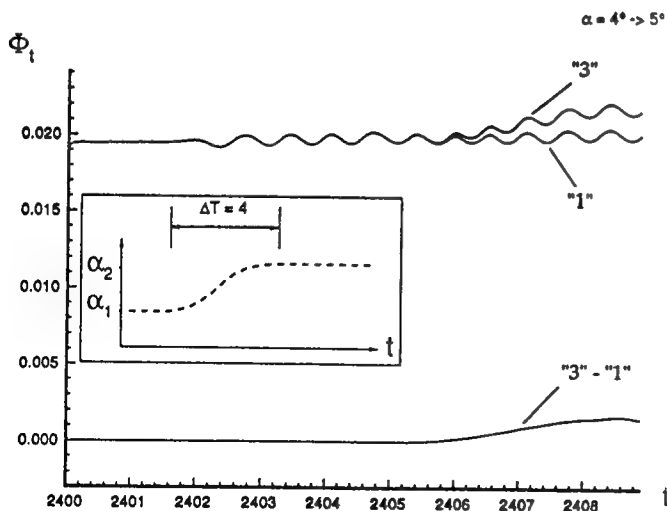


Fig. 15 Illustration of the Procedure Used to Infer the Indicial Function: Integrated Tangential Vorticity Flux at 2% chord,  $Re = 12,000$ ,  $T = 4$ .

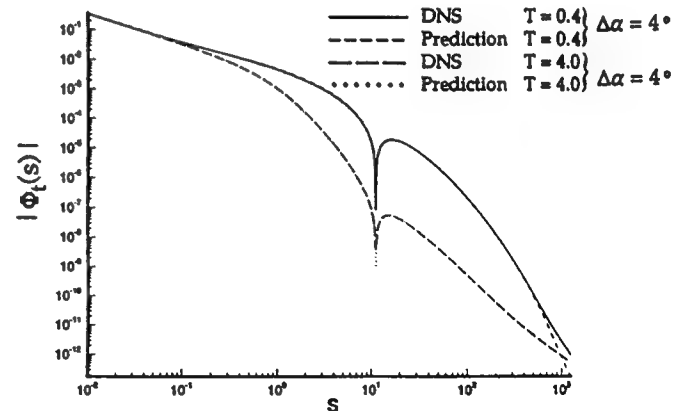


Fig. 18 Laplace Domain Comparison of Indicial Theoretical Prediction Versus Direct Numerical Prediction Illustrating the Recovered Accuracy of the Prediction When Inferring the Indicial Function from the Appropriate Response,  $Re = 12,000$ ,  $\alpha = 4^\circ \rightarrow 8^\circ$ .

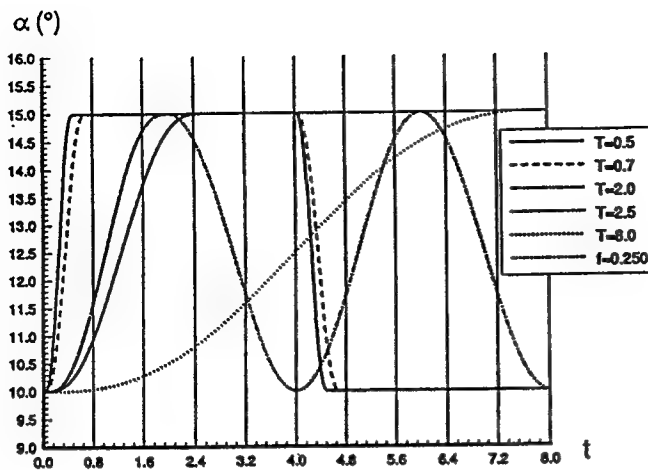


Fig. 19 Angle of Attack Histories Considered for the Validation of the Laplace Domain-Based Characteristic Function Approach (T: Ramp Time, F: Frequency).

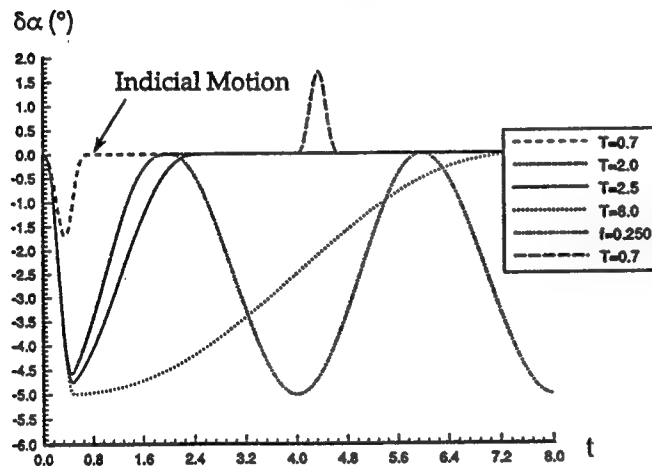


Fig. 20 Actual Inputs to the Prediction Method,  $\delta\alpha = \alpha(t) - \alpha_{ref}(t)$ .

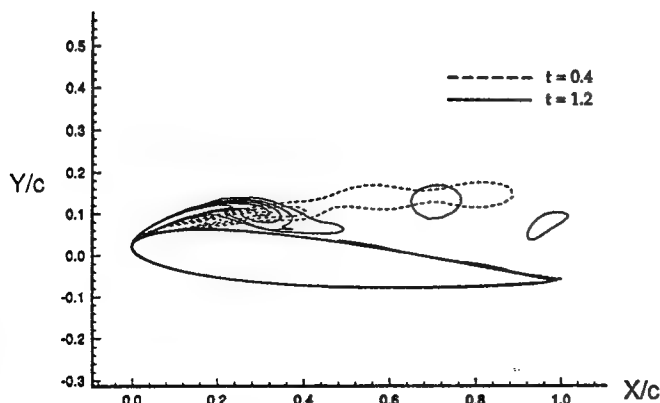


Fig. 21 Comparison of Primary Vorticity Contours Computed at Two Instants in Time During Ramp Motion,  $10^\circ \leq \alpha \leq 15^\circ$  ( $T = 0.5$ ),  $Re = 12,000$ ,  $M_\infty = 0.2$ .

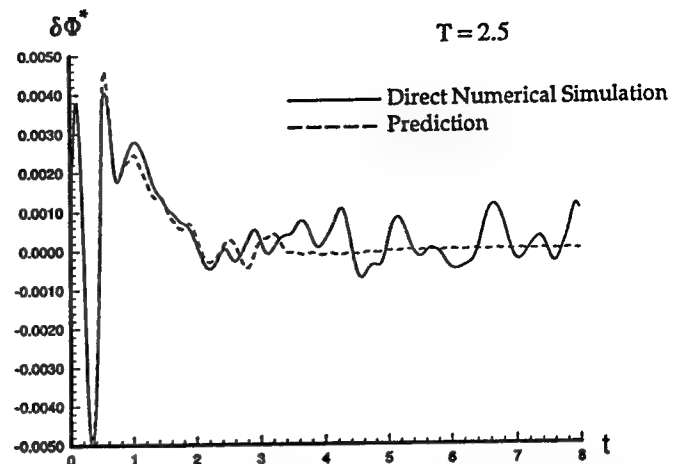


Fig. 22 Theoretical Prediction Versus Direct Numerical Simulation for Vorticity Accumulation During Ramp-Up Motion,  $10^\circ \leq \alpha \leq 15^\circ$  ( $T = 2.5$ ),  $Re = 12,000$ ,  $M_\infty = 0.2$  (——— ARC2D, - - - - Theoretical Prediction).

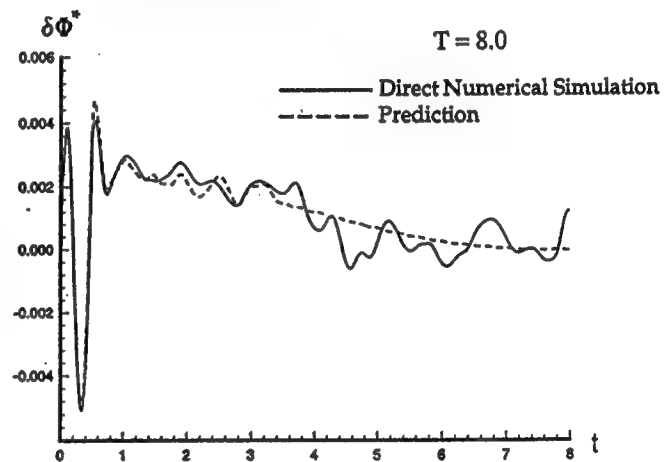


Fig. 23 Theoretical Prediction Versus Direct Numerical Simulation for Vorticity Accumulation During Ramp-Up Motion,  $10^\circ \leq \alpha \leq 15^\circ$  ( $T = 8.0$ ),  $Re = 12,000$ ,  $M_\infty = 0.2$  (——— ARC2D, - - - - Theoretical Prediction).

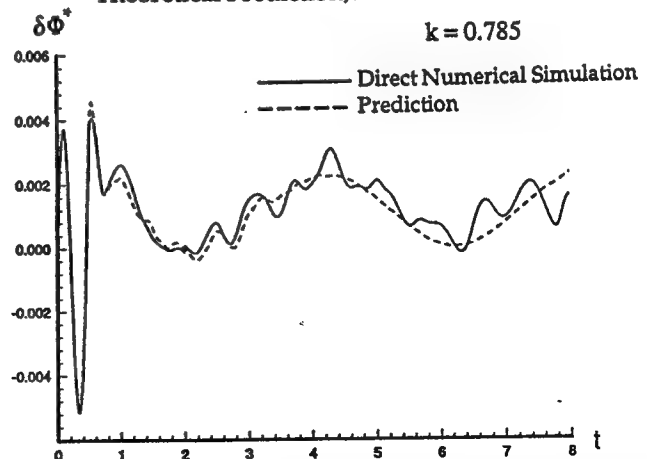


Fig. 24 Theoretical Prediction Versus Direct Numerical Simulation for Vorticity Accumulation During Oscillatory Motion,  $10^\circ \leq \alpha \leq 15^\circ$  ( $F = 0.25$ ),  $Re = 12,000$ ,  $M_\infty = 0.2$  (——— ARC2D, - - - - Theoretical Prediction).

**THIS PAGE INTENTIONALLY LEFT BLANK**

# A STUDY OF REYNOLDS NUMBER EFFECTS ON INCIPIENT LEADING EDGE STALL

Patrick H. Reisenhofer\* and Robert E. Childs\*\*  
Nielsen Engineering & Research, Inc.  
Mountain View, CA

## ABSTRACT

It has been suggested that eruptive plumes of vorticity might play a critical role in the physics of vortex formation during leading edge dynamic stall. Numerical simulations at low Reynolds number do not seem to adequately predict this phenomenon. To explore the possibility of a "bifurcation" in Reynolds number, we investigate in detail the scaling of incipient laminar separation, vortex formation, and shedding with respect to Reynolds number. Numerical simulations are used to study a model problem in which a two-dimensional airfoil remains stationary at angle-of-attack, but for which the leading edge flow separates as a result of an impulsively applied no-slip boundary condition. The calculations are laminar ( $50,000 \leq Re \leq 400,000$ ), and are performed for  $\alpha = 15^\circ$  and  $M_\infty = 0.2$ . The resulting surface flow topology is analyzed as a function of Reynolds number. The results obtained thus far appear to contradict the hypothesis that a form of bifurcation takes place at some intermediate laminar Reynolds number. Furthermore, times and locations for the onset of separation bubbles, vortex formation, and feeding sheet rupture are found to scale according to various power laws of the Reynolds number,  $Re^{-\eta}$ , with  $0.11 \leq \eta \leq 0.45$ .

## NOMENCLATURE

### Symbols and Abbreviations

c	Airfoil chord
const.	Constant
CFD	Computational Fluid Dynamics
$C_f$	Skin friction coefficient ( $C_f = 2\tau_w/(\rho_\infty U_\infty^2)$ )
D	Dilatation ( $D = \partial u/\partial x + \partial v/\partial y$ )
dy	Normal grid spacing
J	Jacobian ( $J = \partial u/\partial x \partial v/\partial y - \partial u/\partial y \partial v/\partial x$ )
L.E.	Leading Edge
$M_\infty$	Freestream Mach number
p	Pressure
PS	Primary separation (same as PS1)
PS1	First primary separation
PS2	Second primary separation
R	Rupture
Re	Chord Reynolds number ( $Re = U_\infty c/\nu_\infty$ )
s	Curvilinear surface coordinate
SS1	First secondary separation
SS2	Second secondary separation

SS3	Third secondary separation
SS4	Fourth secondary separation
t	Time, measured from the instant the no-slip boundary condition is applied
TS1	First tertiary separation
TS2	Second tertiary separation
u	X-component of velocity
$U_\infty$	Freestream velocity
v	Y-component of velocity
Vtx	Vortex
x	Coordinate aligned with the airfoil
y	Normal coordinate
$\alpha$	Angle of attack
$\delta$	Boundary layer thickness
$\Delta$	Variation
$\Delta x$	Circumferential grid spacing
$\nu$	Fluid kinematic viscosity
$\rho$	Fluid density
$\tau_w$	Wall shear stress
$\Omega$	Vorticity

### Subscripts

e	Evaluated at the outside edge of the boundary layer
F	Vortex formation
inf	Freestream value
LE	Leading edge
max	Maximum
min	Minimum
n	Normal
o	Initial condition
t	Tangential
w	Evaluated at the wall
$\Omega$	Based on vorticity
$\infty$	Freestream value

## INTRODUCTION

In recent years, research into model problems of unsteady flow separation<sup>1-5</sup> has shown the propensity of boundary layers to form eruptive plumes of vorticity. Their connection to the dynamic stall<sup>6-12</sup> process at high Reynolds numbers is discussed in Ref. 13. Specifically, two types of eruptions are distinguished. The first one is a vortex-induced eruption. This type is associated with the secondary separation provoked by the presence of a primary vortex and with the subsequent, nonlinear, induction which results from this interaction. This eruption process has been observed<sup>14,15</sup> and computed<sup>16</sup> in a number of flows. The second type of eruption is conjectured<sup>13</sup> to be a spike-like boundary layer response to the pressure gradient. This spike would presumably occur on the upstream side of the primary separation bubble, allowing boundary layer vorticity to spill away

\*Chief Scientist, Member AIAA

\*\*Executive Vice-President, Member AIAA

from the surface and eventually roll-up into the primary vortex. Unfortunately, numerical simulations at low Reynolds number do not seem to be able to predict this second type of eruption.<sup>17</sup> Numerical calculations are possibly too diffusive, or cannot resolve some of the critical sub-scale physics.<sup>18,1,13</sup> Another possibility is that the Reynolds number must be sufficiently large for a sharp eruption to take place.<sup>13</sup> The investigation of the existence of a "bifurcation" in Reynolds number, i.e., the possibility that a *qualitative* change in the behavior of the flow might occur as the Reynolds number is increased, is the subject of this study.

## OBJECTIVE AND APPROACH

The objective of this work is to investigate in detail the scaling of incipient laminar separation, vortex formation, and shedding with respect to Reynolds number. The study addresses the dynamics of vorticity at the leading edge of a two-dimensional airfoil and has application to dynamic stall. The specific goals are to analyze the above scaling properties in terms of topological changes of the flowfield, both volumetric and on the surface of the airfoil.

The method of approach is to use numerical simulations of a model problem, in which the airfoil remains stationary at angle-of-attack, but for which the leading edge flow separates as a result of impulsively applying the no-slip boundary condition. This model problem is well-suited for the desired investigation of Reynolds number effects because the initial conditions are independent of Reynolds number and because the temporal and spatial scales involved are small. These characteristics contribute to substantial savings in computer resources, as compared to full calculations of dynamic stall at "high" Reynolds number (say,  $Re \geq 100,000$ ). The accuracy and reliability of current turbulence models is insufficient for flow physics investigations; therefore, the present investigation is limited to "high" Reynolds number laminar simulations of the two-dimensional Navier-Stokes equations.

No experimental data is available for this model problem. Therefore, the accuracy of two-dimensional Navier-Stokes simulations can only be validated by means of careful grid convergence studies and by comparisons between different simulations of the same case. Two codes are used for this comparison: a version of NASA Ames's ARC2D Navier-Stokes solver<sup>19</sup> using a time-implicit integration mode and second-order spatial accuracy, and a specially developed time-explicit eighth-order accurate version referred to as ARC2D/8E.

## RESULTS

### Model Problem

The study of a model problem was considered, in which the airfoil is maintained at a fixed angle of attack and the no-slip boundary condition is impulsively

applied. The surface boundary conditions are a prescribed tangential slip velocity distribution  $u_t(s)$  for  $t < 0$ , and zero velocity for  $t \geq 0$ . The tangential slip velocity at  $t < 0$  is determined from the requirement that  $\Omega_w = 0$  everywhere at the surface. These boundary conditions result in attached flow at  $t = 0$  which has the property of being independent of Reynolds number. Subsequent to the application of the no-slip condition, an unsteady flowfield develops. This flowfield is characterized by the complete absence of trailing edge separation over the time scales of interest, and the existence of a well-defined time origin. These factors are beneficial in terms of studying the initial stages of leading edge dynamic stall, including scaling effects with Reynolds number.

Based on our previous (unpublished) work on this model problem, at least two distinct stages of the incipient separation process are found. Stage I corresponds to the formation of an initially symmetric (bubble-shaped) separation of the thin primary vorticity layer which lifts away from the surface. This stage appears to exhibit qualitatively similar behavior between Reynolds numbers over the investigated range (up to 500,000, based on chord), and ends with the beginning of asymmetry (lopsided bubble), first evidenced by the accumulation of vorticity in the reattachment region of the separated vorticity layer.

In Stage II, the accumulated vorticity develops into a vortex which subsequently induces a sequence of rapid events, the first of which is the formation of a secondary recirculation region at the surface. Stage II, in the present context, is defined as ending with the "rupture" of the feeding vortex sheet, and the subsequent convection of the primary dynamic stall vortex.

Of the two stages distinguished above, Stage II is the most difficult one to compute, and issues of adequacy of the numerical resolution, diffusion of the vortices and steepness of the induced pressure gradients are critical. At high Reynolds numbers, a second-order method is extremely expensive if it is to capture the essential physics. The special feature of ARC2D/8E is the inclusion of a high-order accuracy scheme which permits the extension of the model problem studies to Reynolds numbers considerably larger than previously possible ( $Re = 100,000$  and up).

### ARC2D/8E code

The results presented here are obtained using the high-order code ARC2D/8E. The computational method consists of central, eighth-order, finite-difference spatial discretization, and an explicit third-order Runge-Kutta time integration scheme. Eighth-order accuracy is also implemented for the calculation of the convective fluxes, metric terms, and artificial dissipation. Viscous fluxes are computed with fourth-order accuracy. The order of the central differencing scheme degenerates to second-order at the wall. The high-order artificial dissipation algorithm does not affect modes in the solution which are accurately resolved by the discretization scheme.

The accuracy of the algorithm has been validated in various studies.<sup>20,21</sup> The advantage of the high-accuracy scheme is that true accuracy can be attained for roughly half of the grid-resolved wave number range. In comparison, a second-order method is only accurate over approximately 5 to 10% of the spectral range, while spectral methods typically resolve approximately two thirds of the theoretical range. Thus, only a few points (on the order of five) are required to resolve a shear layer with an eighth-order method. Such considerations are critical when attempting to capture the physics of high Reynolds number flows.

#### *Flow Conditions and Grid Convergence Studies*

Four Reynolds numbers have been investigated in this study; these are (based on chord): 50,000, 100,000, 200,000, and 400,000. All simulations are for a fixed angle of attack  $\alpha = 15^\circ$ , and fixed freestream Mach number  $M_\infty = 0.2$ . The results shown here are all computed for a NACA0012 airfoil with a rounded trailing edge (radius of curvature  $r/c = 0.0092$ ). This ensures that the CFL requirements with the present O-grid are not dictated by the trailing edge region. The computational grids used in the present study are highly clustered in the leading edge region of the airfoil. An example of a computational grid used in this study is shown in Fig. 1. For this grid, 476 points were used in the circumferential direction, 340 of which were placed in the first 4% of chord on the upper surface of the airfoil. For the grid convergence studies, the grid sizes ranged from 224 to 476 in the circumferential direction, and between 60 and 83 for the normal direction, with the outer boundary located approximately seven chord lengths away from the airfoil.

The effect of circumferential grid spacing is illustrated in Figs. 2 and 3. Skin friction was used as a sensitive indicator of the accuracy of the solutions. Figure 2 ( $Re = 200,000$ ,  $tU/c = 0.084$ ) illustrates the collapse of the calculated skin friction profiles in the region of interest as the minimum circumferential spacing,  $\Delta x_{min}/c$ , is reduced from  $1.0 \times 10^{-3}$  to  $1.25 \times 10^{-4}$ . The minimum circumferential grid spacing is representative of the grid in the critical region  $0.01 \leq x/c \leq 0.04$ , where the grid was designed to be nearly uniform in the streamwise direction. The last two grid resolutions ( $\Delta x_{min}/c = 2.5 \times 10^{-4}$  and  $1.25 \times 10^{-4}$ ) yield virtually identical results. The value  $\Delta x_{min}/c = 1.25 \times 10^{-4}$  was retained for  $Re = 200,000$  and  $Re = 400,000$ , while  $\Delta x_{min}/c = 2.5 \times 10^{-4}$  and  $\Delta x_{min}/c = 5 \times 10^{-4}$  were used for  $Re = 100,000$  and  $Re = 50,000$ , respectively. The test of Fig. 2 is considered to be fairly stringent, as the resolution requirements for the collapse of the  $C_f$  profiles become more demanding at large times. This form of sensitivity to initial conditions is illustrated in Fig. 3 at four different chordwise positions. Again, it is seen that grid convergence is attained for  $\Delta x_{min}/c = 2.5 \times 10^{-4}$ .

The effect of normal grid spacing at  $Re = 200,000$  is shown in Fig. 4. In this figure, the "error" is computed as the L-1 norm of the difference between the skin friction distribution and the "converged" skin friction

distribution at some fixed time instant during Stage I. The "converged"  $C_f$  distribution corresponds to the best grid resolution, characterized by a normal grid spacing at the wall of  $dy_{le}/c = 1.25 \times 10^{-5}$ . Also indicated in Fig. 4 are the characteristic slopes associated with formal third- and fourth-order accuracy. The data presented here is seen to lie somewhere between the two, which is not surprising since in Stage I the process is expected to be viscous-dominated, and since fourth-order accuracy is the maximum achievable for the viscous fluxes with the present code. In general, lower than fourth-order accuracy is expected near the wall, since the formal accuracy of the differencing schemes degrades as one approaches the boundary. Based on the result of Fig. 4, a value of  $dy_{le}/c = 2.5 \times 10^{-5}$  was selected for  $Re = 200,000$  and 400,000. The same value was retained for  $Re = 100,000$ , while a value of  $dy_{le}/c = 5 \times 10^{-5}$  was used for  $Re = 50,000$ . With these choices of parameters, the normal grid spacing at the wall in the first 10% of chord is better, in terms of viscous units, than  $\Delta y_w^+ = 1$  on average, and between 0 and 4 instantaneously.

#### *Anatomy of the Flowfield*

A typical time sequence of the developing vorticity field is shown in Fig. 5. At the very initial stages, a Stokes layer forms after the imposition of the no-slip boundary condition. This is followed by the development of a thin recirculation bubble along the surface, the leading and trailing edges of which are marked "PS" (primary separation). The bubble is initially symmetric, but eventually becomes lopsided (see, for example,  $t = 0.054$  in Fig. 5). This marks the end of Stage I. Shortly after, a vortex forms some distance away from the wall in the downstream region of the primary recirculation zone. This vortex, in turn, induces a secondary separation bubble. This first instance of secondary separation is demarcated by the symbols SS1, visible for  $t \approx 0.069$  in Fig. 5. As the separating primary shear layer, or vorticity feeding sheet, experiences instability and roll-up, multiple vortices form. As in the case of the primary vortex, these induce new secondary separation zones. For instance, the leading and trailing edges of the second secondary separation are indicated in Fig. 5 by the symbols SS2. These multiple secondary recirculation zones eventually strengthen to the point where they too become vortices which, depending on the Reynolds number, may induce a tertiary separation, and so on. In Fig. 5, counter-clockwise vorticity is indicated by dashed lines. From the last two graphs of Fig. 5, we note that there is a point in time at which mutual induction between the primary dynamic stall vortex and the first secondary (counter-rotating) vortex leads to an eruption of vorticity away from the wall. This eruption appears to serve as a trigger for the rupturing of the vorticity feeding sheet, in agreement with Refs. 16 and 22. After the vortex sheet rupture, the primary dynamic stall vortex is free to convect away from the leading edge, as may be seen from the last graph of Fig. 5.

A comparison of the pressure fields at the various Reynolds numbers is given in Fig. 6 at  $tU/c = 0.102$ .



Although the different flowfields are not at the same stages of development (the larger the Reynolds number, the more advanced the solution), the presence of vortex cores can be clearly seen from the existence of closed low pressure contours. To accurately resolve the secondary flows induced by these complex pressure fields, it is important to capture as high a portion of the wavenumber spectrum as possible. Thus, use of the high-order accuracy code ARC2D/8E is essential at the higher Reynolds numbers. As previously mentioned, ARC2D/8E uses eighth-order linear and nonlinear artificial dissipation. At the relatively high Reynolds numbers considered in this study, a concern is the level of artificial dissipation, compared to the "natural" viscous dissipation of the flow. This comparison was performed in a systematic manner at all Reynolds numbers. For all cases investigated, the total flux contribution due to artificial dissipation was less than 0.1% of the viscous contribution, in all vortical regions of the flow. This ratio progressively increases away from the body, as viscous fluxes become negligible and the artificial dissipation increases due to the coarser grid resolution.

Figure 7 depicts the space-time evolution of the skin friction in the leading edge region of the flow, for  $Re = 50,000$  and  $Re = 200,000$ . Such surface representations are found to correlate well with the instantaneous topological structure of the flow. A noticeable feature is the presence, particularly at the higher Reynolds numbers, of a "latency" period (e.g., Fig. 7,  $0.078 \leq tU/c \leq 0.090$ ,  $Re = 200,000$ ), during which the vortex system grows in strength, with little change in either size or position. This is a result of a nearly stationary solution of the equations of motion. The end of this latency period is associated with the "rupture" of the vorticity feeding sheet and the release of the primary vortex, as indicated in Fig. 7 by the change in slope of the skin friction contours. Again, the phenomenon is more clearly marked at the higher Reynolds numbers, although the basic phenomenon is believed to be still present at  $Re = 50,000$ . At the lower Reynolds numbers, viscous diffusion tends to blur some of these effects. Most of the calculations performed in this study are stopped shortly after the end of Stage II, since our goal is to study the physics of incipient vortex formation and dynamic stall. At the final time instant of the calculations, the released vortex has traveled a short distance from the remainder of the attached vortex system.

The space-time skin friction diagram of Fig. 6 can be simplified somewhat by considering only the zero contours of skin friction. In this manner, the resulting lines delimit adjacent regions of forward and reverse flow. This permits the identification of primary, secondary and, if applicable, tertiary separation regions. The resulting surface flow topology at  $Re = 100,000$  is shown in Fig. 8, where the symbols PS, SS1, SS2, TS1, and TS2 designate respectively the onset of primary separation, "first" secondary separation, "second" secondary separation, "first" tertiary separation, and "second" tertiary separation, as identified in Fig. 5. In

addition, "R" indicates the time of vortex sheet rupture, corresponding to the end of the previously mentioned latency period and the beginning of free convection of the primary dynamic stall vortex. The solid symbols indicate the trajectory of the topological "center" associated with the instantaneous streamlines. Reference 17 illustrates how critical point theory<sup>23</sup> can be used as a sensitive means to analyze the topology of the velocity field. In particular, this work<sup>17</sup> was able to pinpoint the origin of the primary stall vortex. Using similar concepts, it is found in the present flowfields that the critical points are "centers," characterized by essentially zero dilatation,  $D$ , and positive Jacobian,  $J$ . Immediately after the onset of surface flow reversal in Fig. 8 (marked "PS"), the value of the Jacobian nears zero and, hence, the center is degenerate and its topology is associated with pure shear. Although the center does not become a vortex per se until approximately  $tU/c = 0.057$  (shortly before the onset of secondary flow separation "SS1"), it is noteworthy that its trajectory correlates well with the downstream edge of the primary and induced secondary bubbles.

The relation between the topological center and a vortex was elucidated by Perry and Chong.<sup>23</sup> In the present study, the point at which the center is associated with the core of a vortex was found to be most clearly defined by the pressure field. For a fairly long portion of time during Stage I, ( $tU/c \leq 0.05$  in Fig. 8), the vorticity field topology corresponds to a lifted vorticity layer beneath which a thin region of reverse flow exists. During this portion, the location of the topological center "rides" the vorticity line, gradually moving from front to back and settling at about two thirds of the bubble extent. In contrast to the rather benign behavior of the vorticity during that portion, the end of Stage I is marked by a sudden change from boundary layer-like behavior (negligible normal pressure gradient) to vortex-like behavior, characterized by the presence of closed pressure contours associated with a low pressure core. At later stages of the evolution of the flow, local pressure and vorticity fields act to reinforce each other. The vorticity accumulates further in the low pressure region, and increased vorticity results in a further lowering of the pressure. This interaction rapidly results in a formed vortex and marks the beginning of what was referred to earlier as Stage II. At that point, vorticity and pressure fields associated with vortices are well-correlated. An example at the end of Stage II is given in Fig. 9. The top graph in Fig. 9 illustrates the strong induced normal entrainment of vorticity immediately "behind" the (second) dynamic stall vortex at  $Re = 400,000$ . The bottom graph shows the corresponding instantaneous pressure field.

The connection between flowfield topology and vortex formation is further explored in Fig. 10. In this figure, the initial temporal increase of the Jacobian value at the critical point is characteristic of the emergence of a center, from pure shear to "pancake"-like to nearly circular. After the point of vortex formation (associated with the formation of a low pressure core), the Jacobian increases further, with marked stages coinciding with



the onsets of secondary and tertiary separation. Most importantly, the evolution of the formed vortex is characterized by a distinctive drop in core pressure. This feature was observed at all of the investigated Reynolds numbers.

### Reynolds Number Scaling

A comparison of zero skin friction diagrams for  $Re = 100,000$ ,  $Re = 200,000$ , and  $Re = 400,000$  is given in Fig. 11. As in Fig. 8, the symbols indicate the times and locations associated with the onset of flow separation regions, and are generically indicated for  $Re = 400,000$ . Although not repeated in the figure, the same symbols also apply to the topological features associated with the other Reynolds numbers. Also, note the presence of a second primary separation (PS2). The latter was also present at  $Re = 100,000$ , but is not visible on the scale of Figs. 8 and 11. This second primary separation is associated with a re-separation of the boundary layer downstream of reattachment. As the Reynolds number increases, the overall scale of the leading edge bubble/vortex system diminishes, and the reattached flow still experiences an adverse pressure gradient which causes it to undergo a mild separation. The evidence gathered thus far suggests that, over the investigated range, this second primary separation is completely independent and does not interfere with the leading edge vortex system. For the purpose of clarity,  $Re = 50,000$  is not shown in Fig. 11. The important point illustrated by this figure is the remarkable degree of similarity, including details, between results at the Reynolds numbers studied. This similarity is further exploited, below, to extract basic scaling relationships.

Instantaneous vorticity fields for  $Re = 50,000$ ,  $100,000$ ,  $200,000$ , and  $400,000$  are compared in Fig. 12. The value of the vorticity contours is kept identical between the four flowfields. The time instant chosen for this representation corresponds approximately to the end of Stage II, i.e., the "rupture" of the feeding vortex sheet and the subsequent release of the dynamic stall vortex. The vortex systems in Fig. 12 differ primarily in strength and scale but exhibit topological similarity. This figure shows the relative physical scale of the vortical flowfields as a function of Reynolds number. Their qualitative similarity is seen more clearly in the expanded views provided in Fig. 13.

From zero skin friction plots such as Fig. 11, one can determine with reasonable accuracy the time of onset of the various separation bubbles, as well as their corresponding location. The scaling of the separation time of onset with respect to Reynolds number is summarized in Fig. 14. The lines in the plot correspond to straightforward power fits, based on the four data points. The time of incipient separation for the primary bubble is found to scale as  $Re^{-0.11}$ , while the first, second, and third occurrences of secondary separation are found to scale as  $Re^{-0.30}$ ,  $Re^{-0.40}$ , and  $Re^{-0.44}$ , respectively. For reference, the Reynolds number scaling of the upstream boundary layer is indicated in Fig. 15. It is clear that the boundary layer thickness  $\delta_n$ , at the leading edge of the

airfoil, scales as  $Re^{-1/2}$  within measurement uncertainty. Therefore, the various separation events do not scale on the upstream boundary layer thickness alone, as expected from previous model flow separation studies.<sup>4,5</sup>

As a final note, in addition to the scaling of incipient bubble separation, the times and locations of vortex sheet "rupture," as well as those associated with vortex formation, have been recorded for the investigated Reynolds numbers. "Vortex formation" is defined, rather imprecisely at this time, as the transition between an elongated separation bubble (characterized primarily by counter-flowing streams separated by a shear layer) and a vortex structure (characterized by significant normal momentum transfer and the existence of a low pressure core). The time instants corresponding to the primary separation onset (PS1), vortex formation, and shear layer rupture are also shown (Fig. 16) to scale approximately as simple power laws of the Reynolds number. Specifically, the time instant corresponding to vortex formation scales as  $Re^{-0.27}$ , while that of rupture approximately scales as  $Re^{-0.45}$ . Similar power law scalings are found to govern the location of these events, as shown in Fig. 17.

If some form of boundary layer eruption *leading to the formation* of the primary dynamic stall vortex were to take place, modified scaling properties would be expected from the emergence of new physics. In particular, the vorticity spill-over associated with a tightly focused eruption would presumably result in early vortex formation and rupture. Instead, the present results indicate a smooth scaling behavior and the well-defined emergence, from the lifting vorticity layer, of a topological center which precedes vortex formation.

### CONCLUDING REMARKS

Preliminary results into the Reynolds number scaling of two-dimensional incipient flow separation, vortex formation, and rupture from its feeding sheet indicate the existence of qualitatively similar behavior between the chord Reynolds numbers of 50,000 and 400,000. The results obtained thus far appear to contradict the hypothesis that a form of bifurcation may take place at some intermediate laminar Reynolds number: while the flow solutions obtained at  $Re = 50,000$  are naturally more dissipative than for the highest Reynolds numbers computed in this study, it remains that the sequence of phenomena leading to the release of a simulated dynamic stall vortex bear strong qualitative similarities. In particular, times and locations of onsets of specific dynamical events are found to scale according to simple power laws of the Reynolds number,  $Re^{-\eta}$ , with  $0.11 \leq \eta \leq 0.45$ .

### ACKNOWLEDGMENT

The authors gratefully acknowledges the support of this work by the Army Research Office under Contract No. DAAL03-92-0013, monitored by Dr. Thomas L.

Doligalski. The authors also wish to thank Dr. Lawrence W. Carr and the NASA Ames Research Center for supplying the supercomputer time needed for this project.

## REFERENCES

1. Van Dommelen, L.L. and Shen S.F.: "The Genesis of Separation," *Proc. Symp. on Numerical and Physical Aspects of Aerodynamic Flow*, Long Beach, CA, ed. T. Cebeci, 1982, pp. 293-311.
2. Elliott, J.W., Cowley, S.J., and Smith, F.T.: "Breakdown of Boundary Layers: (i) On Moving Surfaces; (ii) In Self-Similar Unsteady Flows; (iii) In Fully Unsteady Flow," *Geophys. Astrophys. Fluid Dyn.*, Vol. 25, 1983, pp. 77-138.
3. Walker, J.D.A., Smith, C.R., Doligalski, T.L., and Cerra, A.W.: "Impact of a Vortex Ring on a Wall," *J. Fluid Mech.*, Vol. 181, 1987, pp. 99-140.
4. Peridier, V.J., Smith F.T., Walker, J.D.A.: "Vortex-Induced Boundary Layer Separation. Part I. The Limit Problem  $Re \rightarrow \infty$ ," *J. Fluid Mech.*, Vol. 232, 1991, pp. 99-131.
5. Peridier, V.J., Smith F.T., Walker, J.D.A.: "Vortex-Induced Boundary Layer Separation. Part II. Unsteady Interacting Boundary Layer Theory," *J. Fluid Mech.*, Vol. 232, 1991, pp. 133-165.
6. Carr, L.W.: "Progress in Analysis and Prediction of Dynamic Stall," *J. Aircraft*, Vol. 25, 1988, pp. 6-17.
7. Acharya, M. and Metwally, M.H.: "Evolution of the Unsteady Pressure Field and Vorticity Production at the Surface of a Pitching Airfoil," AIAA Paper 90-1472, 1990.
8. Ghia, K.N., Ghia, U., and Osswald, G.A.: "Characterization of Dynamic Stall Phenomenon Using Two-Dimensional Unsteady Navier-Stokes Equations," Presented at the NASA/AFOSR/ARO Workshop on the Physics of Forced Unsteady Separation, Moffett Field, CA, April 17-19, 1990.
9. Lorber, P.F. and Carta, F.O.: "Unsteady Separation Experiments on 2 D Airfoils, 3 D Wings, and Model Helicopter Rotors," Presented at the NASA/AFOSR/ARO Workshop on the Physics of Forced Unsteady Separation, Moffett Field, CA, April 17-19, 1990.
10. Carr, L.W., Chandrasekhara, M.S., and Ahmed, S.: "A Study of Dynamic Stall Using Real Time Interferometry," AIAA Paper 91-0007, 1991.
11. Ericsson, L.E.: "The Problem of Dynamic Stall Simulation Revisited," AIAA Paper 93-0091, 1993.
12. Schreck, S. and Helin, H.E.: "Unsteady Vortex Dynamics and Surface Pressure Topologies on a Pitching Wing," AIAA Paper 93-0435, 1993.
13. Doligalski, T.L., Smith, C.R., and Walker, J.D.A.: "Vortex Interactions With Walls," *Ann. Rev. Fluid Mech.*, Vol. 26, 1994, pp. 573-616.
14. Shih, C., Lourenco, L., Van Dommelen L., and Krothapalli, A.: "Unsteady Flow Past an Airfoil Pitching at Constant Rate," *AIAA J.*, Vol. 30, 1992, pp. 1153-1161.
15. Gendrich, C.P., Koochesfahani, M.M., and Visbal, M.R.: "Initial Acceleration Effects on the Flowfield Development Around Rapidly Pitching Airfoils," AIAA Paper 93-0438.
16. Ghia, K.N., Yang, J., Osswald, G.A., and Ghia, U.: "Study of the Role of Unsteady Separation in the Formation of Dynamic Stall Vortex," AIAA Paper 92-0196, 1992.
17. Knight, D.R. and Choudhuri, P.G.: "2-D Unsteady Leading Edge Separation On a Pitching Airfoil," AIAA Paper 93-2977, 1993.
18. Van Dommelen, L.L. and Shen, S.F.: "The Spontaneous Generation of The Singularity In a Separating Boundary Layer," *J. Comp. Phys.*, Vol. 38, 1980, pp. 125-140.
19. Pulliam, T.H.: "Euler and Thin Layer Navier Stokes Codes ARC2D-ARC3D," Notes for Computational Fluid Dynamics User's Workshop, Tullahoma, TN, March 12-16, 1984.
20. Childs, R. E.: "Advanced Discretization Algorithm for CFD Methods," Nielsen Engineering & Research, NEAR TR 469, July 1993.
21. Childs, R. E., Rodman, L. C., and Nixon, D.: "Methods for Computational Aeroacoustics," Nielsen Engineering & Research, NEAR TR 452, Aug. 1992.
22. Acharya, M. and Metwally, M.H., 1992: "Unsteady Pressure Field and Vorticity Production Over a Pitching Airfoil," *AIAA J.*, Vol. 30, No. 2, 1992, pp. 403-411.
23. Perry, A.E. and Chong, M.S.: "A Description of Eddy Motions and Flow Patterns Using Critical-Point Concepts," *Ann. Rev. Fluid Mech.*, Vol. 19, 1987, pp. 125-155.

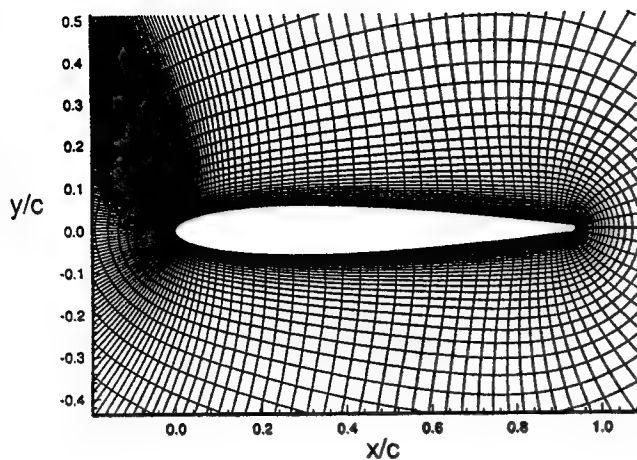


Fig. 1 Example of Computational Mesh Illustrating Grid Cluster in the Leading Edge Region.

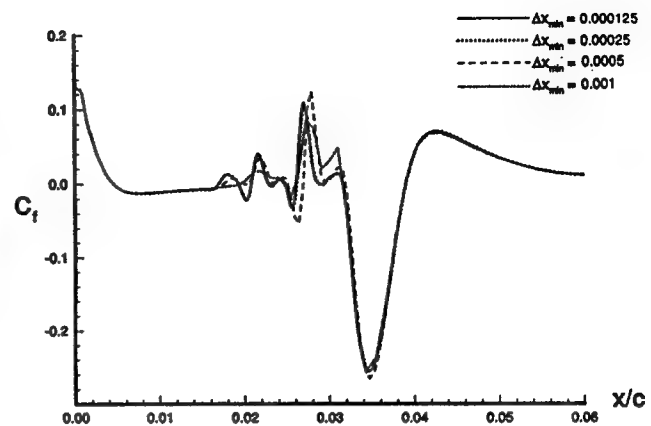


Fig. 2 Skin Friction Profiles Illustrating Grid Convergence as a Function of Circumferential Grid Spacing ( $Re = 200,000$ ).

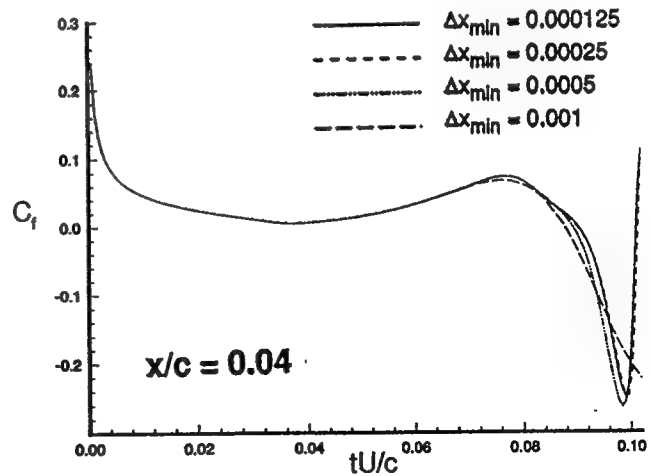
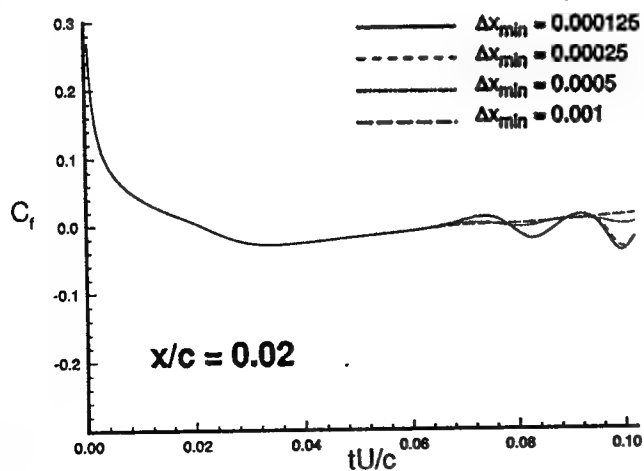
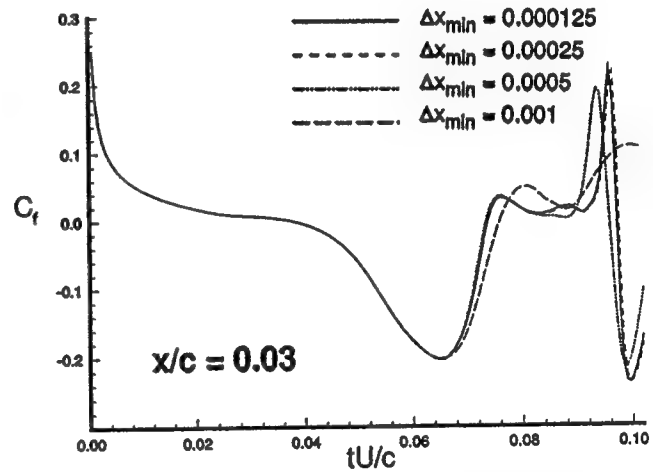
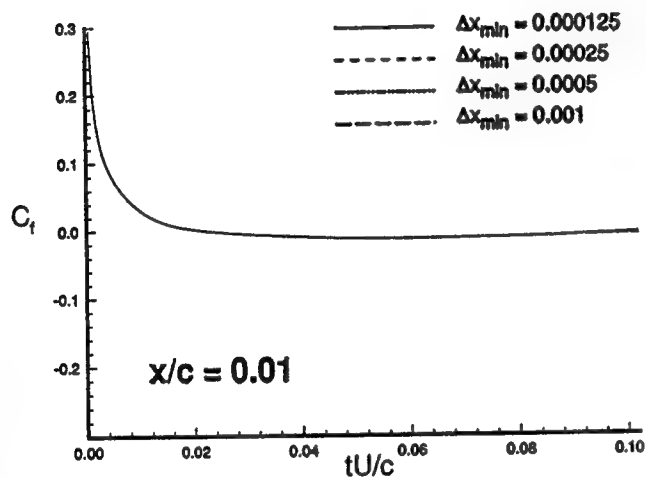


Fig. 3 Circumferential Grid Spacing Sensitivity of Skin Friction Time Histories at Various Chord Locations ( $Re = 200,000$ ).

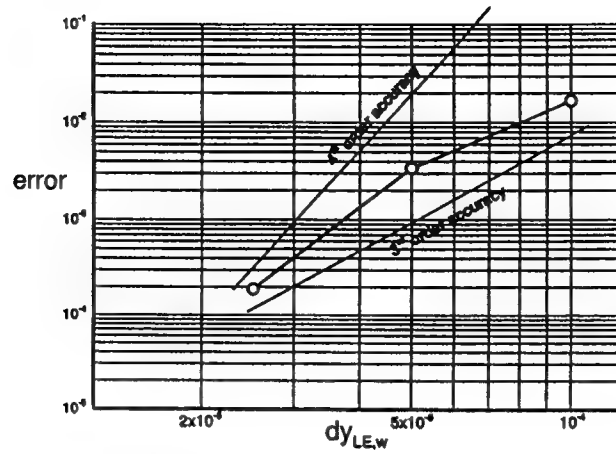


Fig. 4 Skin Friction Error as a Function of Normal Grid Spacing at the Wall ( $Re = 200,000$ ).

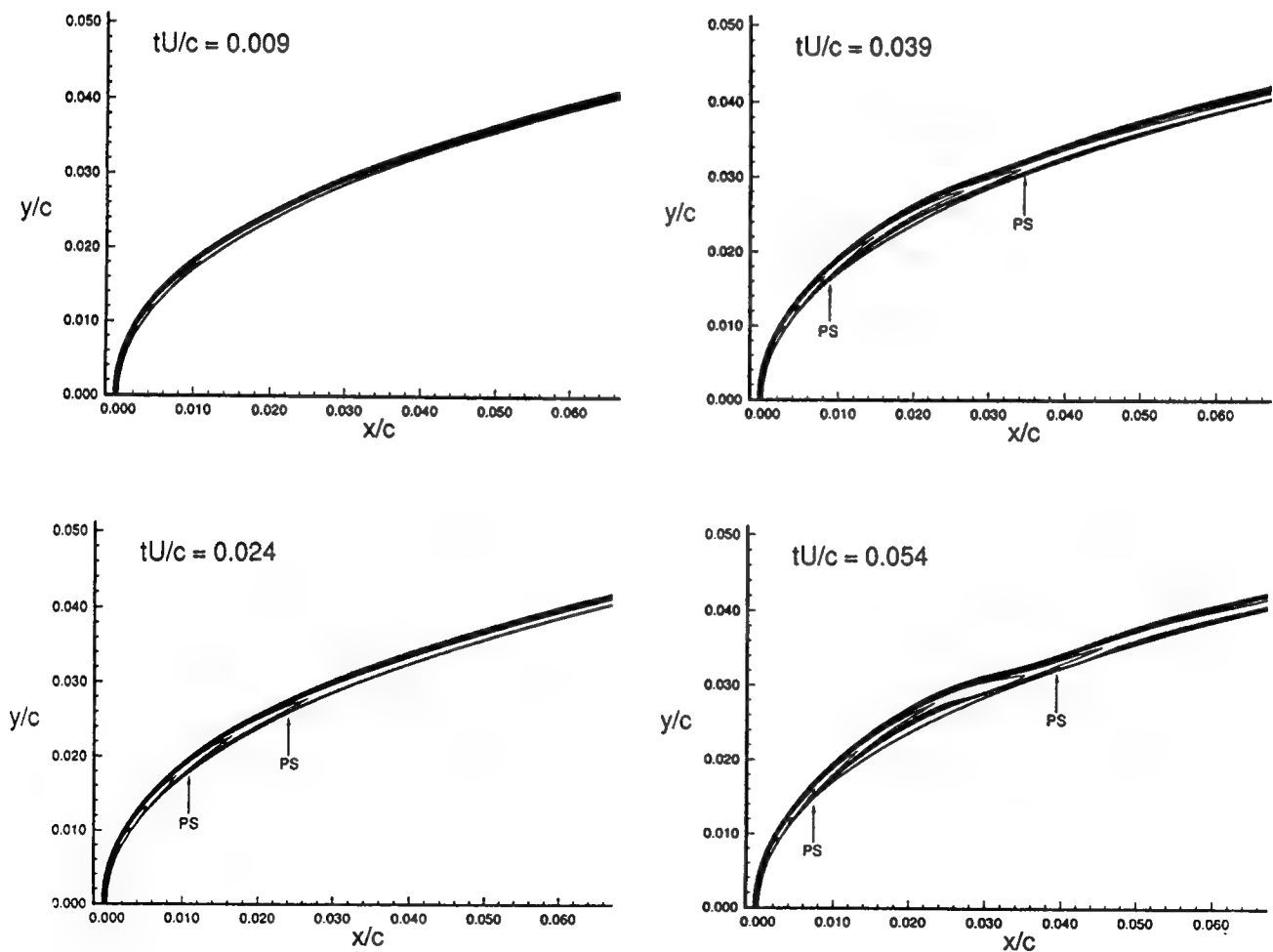


Fig. 5a Typical Temporal Evolution of the Vorticity Field ( $Re = 100,000$ ). Arrows Indicate Locations of Skin Friction Sign Reversal. (continued on next page)

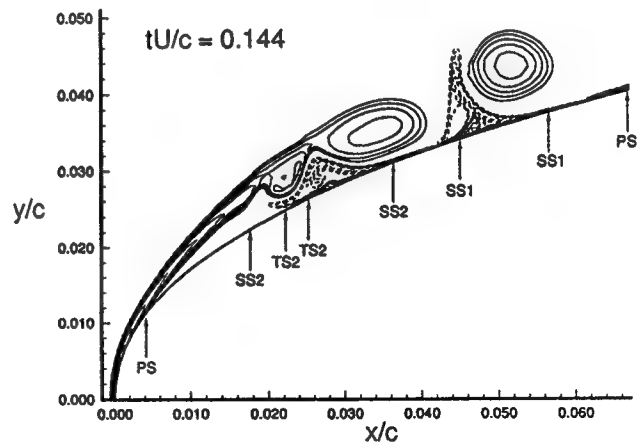
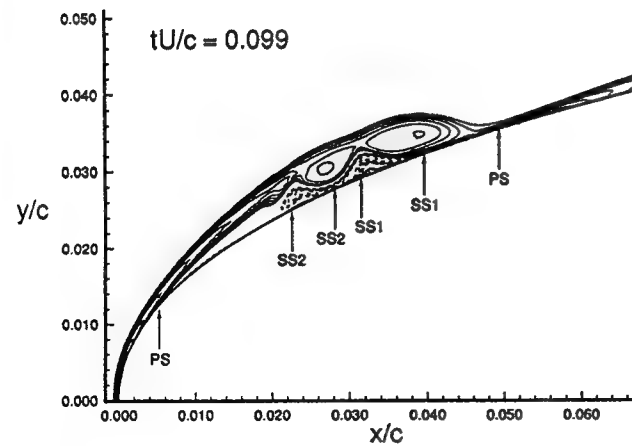
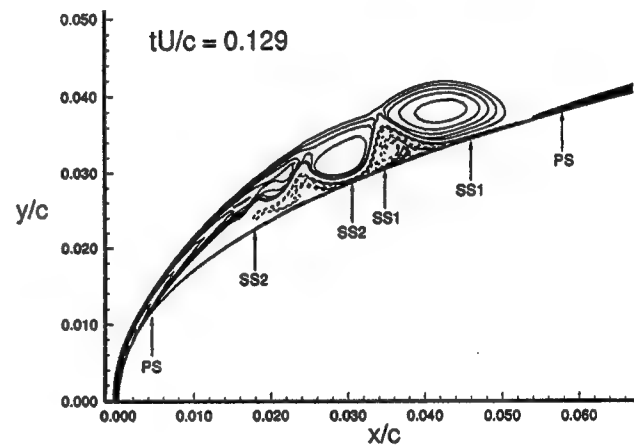
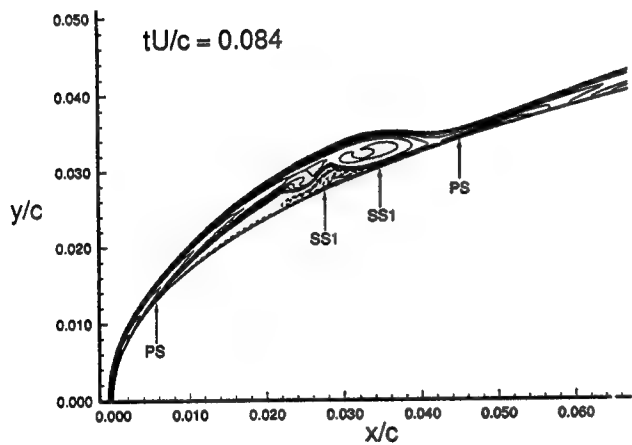
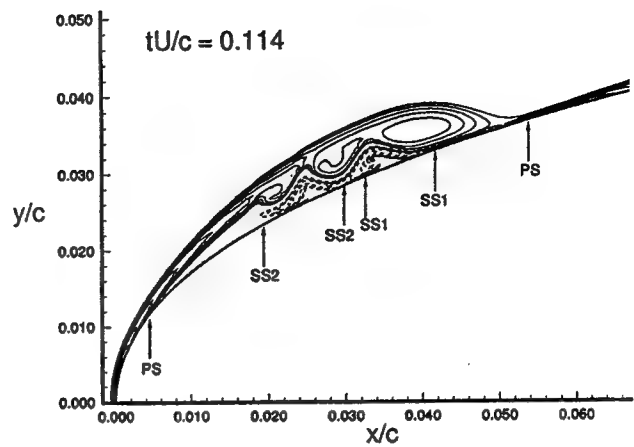
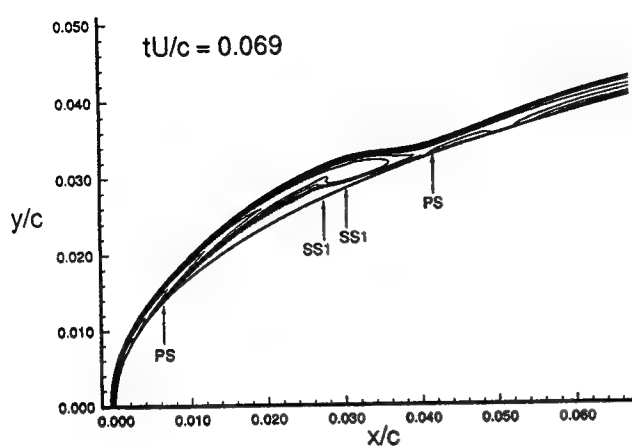


Fig. 5b

Typical Temporal Evolution of the Vorticity Field ( $Re = 100,000$ ).  
Arrows Indicate Locations of Skin Friction Sign Reversal.  
(continued from previous page)

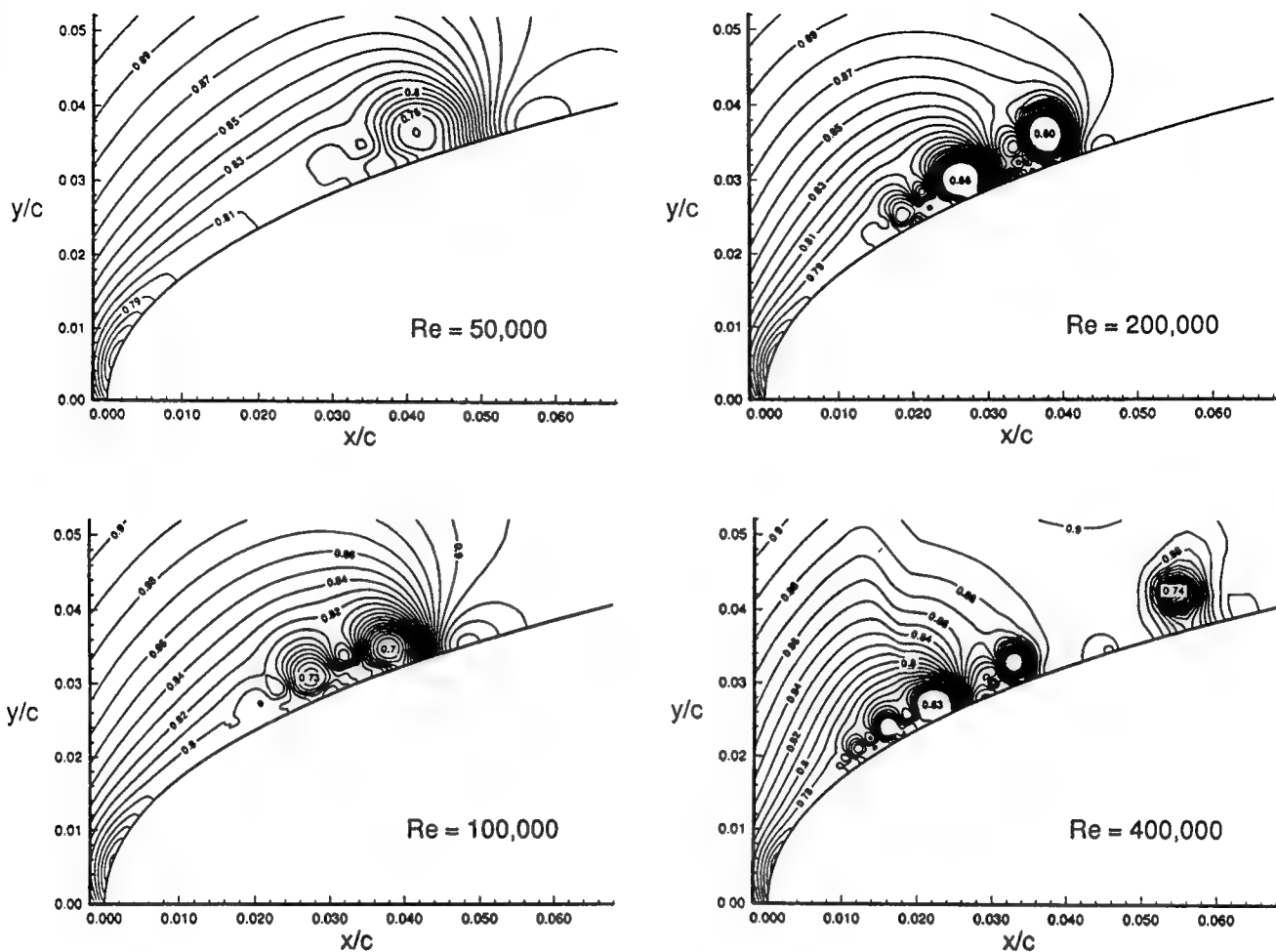


Fig. 6 Reynolds Number Comparison of Pressure Fields at  $tU/c = 0.102$ .

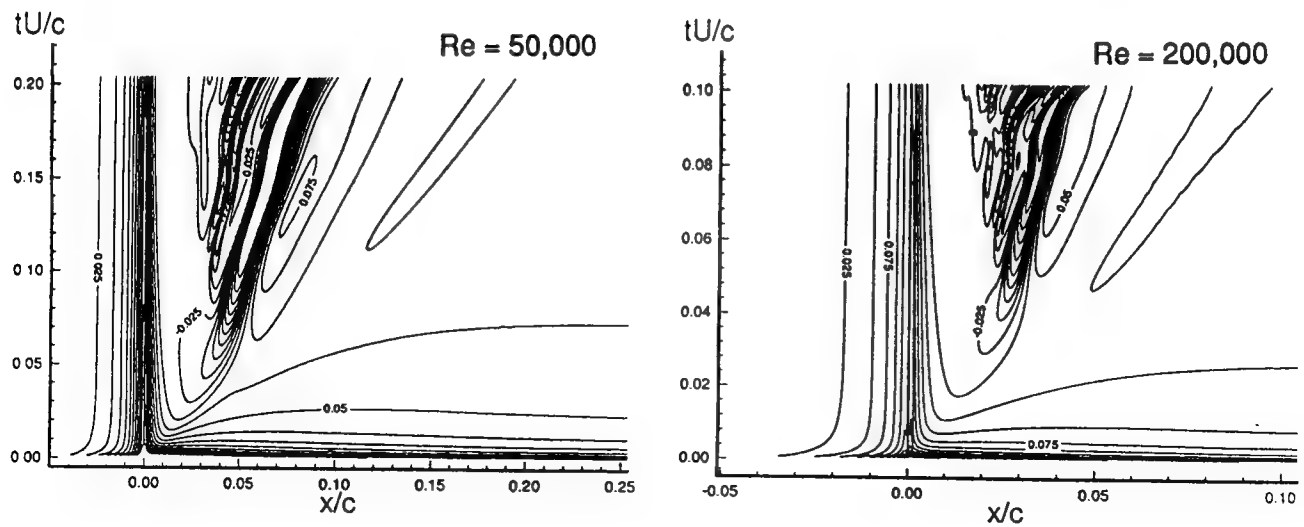


Fig. 7 Space-Time Evolution of Skin Friction at Two Reynolds Numbers.

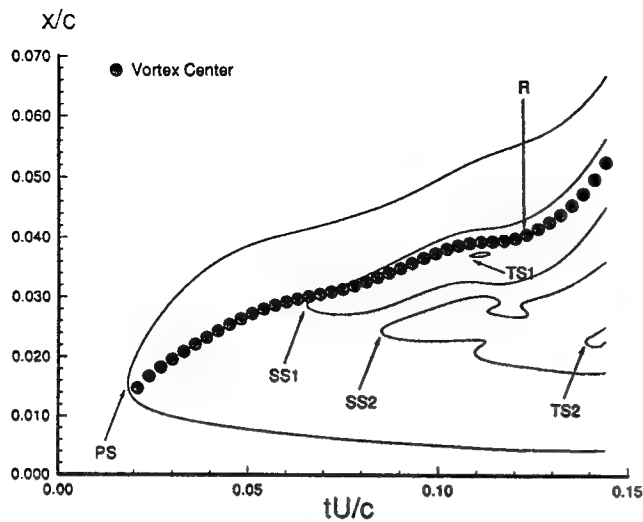


Fig. 8 Temporal Evolution of Surface Flow Topology and Primary "Vortex" Trajectory at  $Re = 100,000$ . Lines are Zero Skin Friction Contours. "R" Denotes the Time of Rupture of the Vorticity Feeding Sheet.

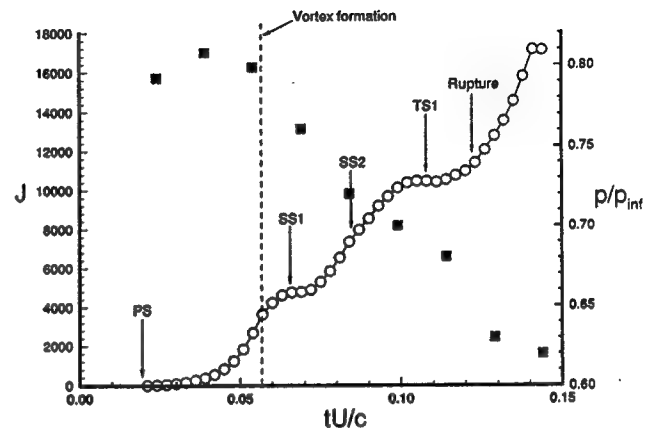


Fig. 10 Temporal Evolution of Key Features Used to Describe the Primary Vortex (O Jacobian, ■ Pressure at the Core).

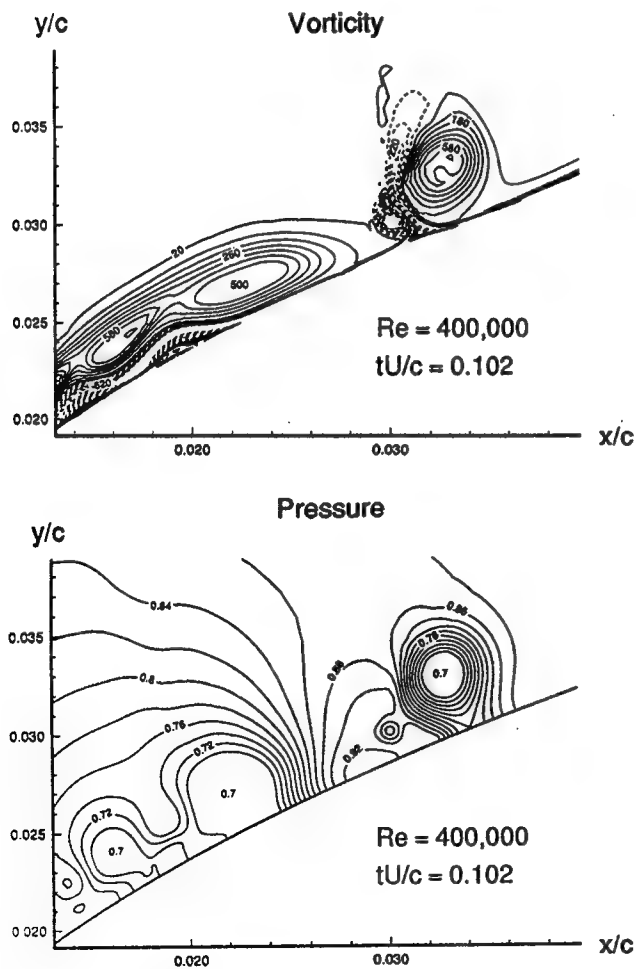


Fig. 9 Vorticity and Pressure Fields Illustrating (a) Vortex Release and Normal Entrainment After Rupture and (b) Low Pressure Cores.

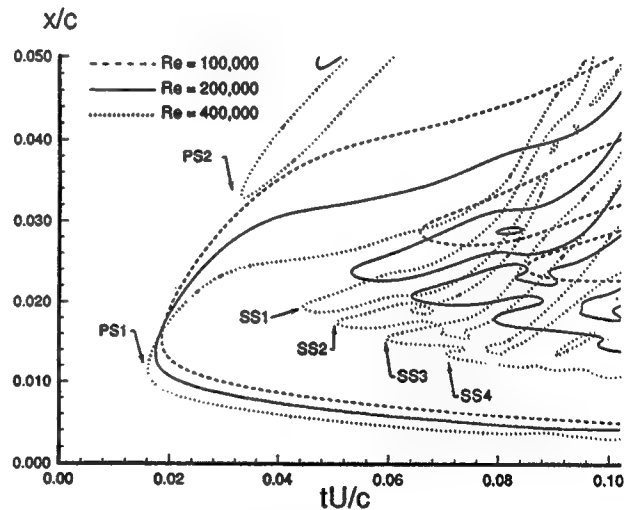


Fig. 11 Similarity of Surface Flow Topologies across Reynolds Numbers.



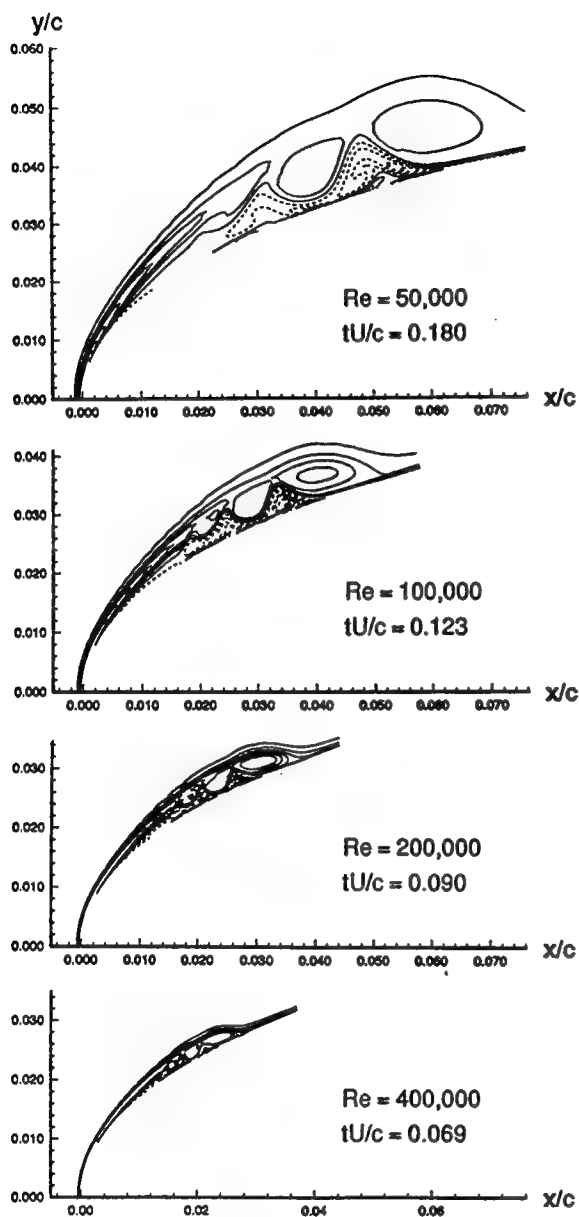


Fig. 12 Comparison of Vorticity Fields at the End of Stage II, for  $Re = 50,000$ ,  $Re = 100,000$ ,  $Re = 200,000$ , and  $Re = 400,000$ . (Scale is Maintained the Same Between Plots).

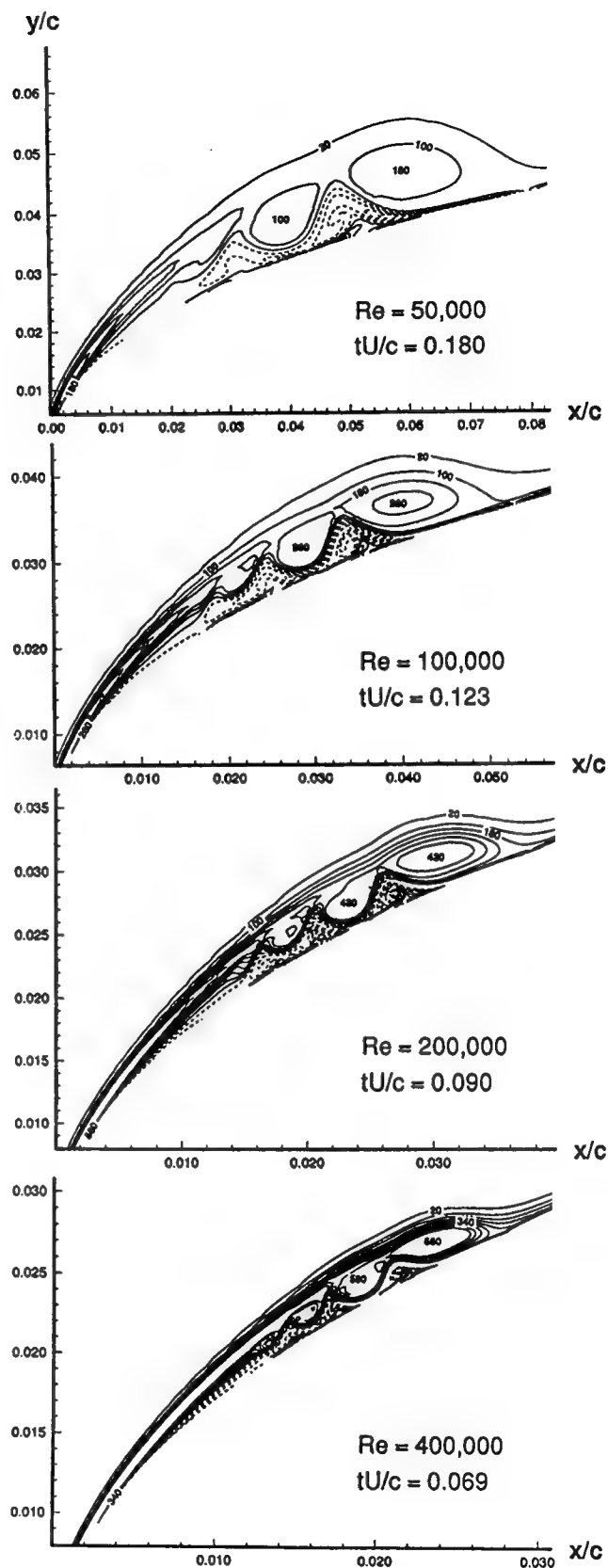


Fig. 13 Expanded View of the Vorticity Fields Shown in Fig. 12 Illustrating Their Qualitative Similarity at the End of Stage II.

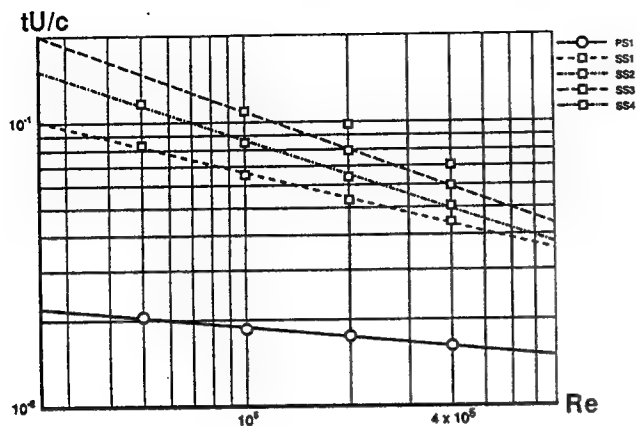


Fig. 14 Reynolds Number Scaling of Time of Appearance of Incipient Primary (PS1) and Secondary (SS1, SS2, SS3, SS4) Separation Bubbles (see Fig. 11).

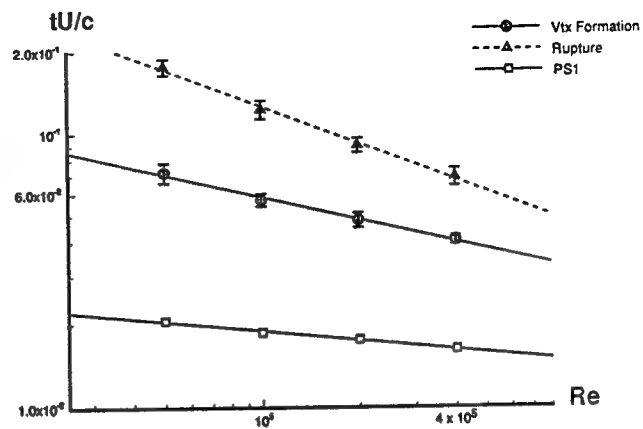


Fig. 16 Reynolds Number Scaling of Time of Vortex Formation and Time of Vortex Sheet Rupture. Corresponding Spatial Locations are Shown in Fig. 17.

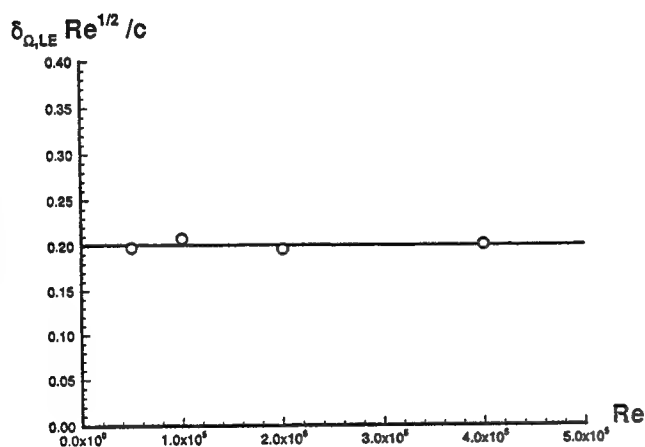


Fig. 15 Inverse Square Root Scaling of the Upstream Boundary Layer Thickness with Reynolds Number.

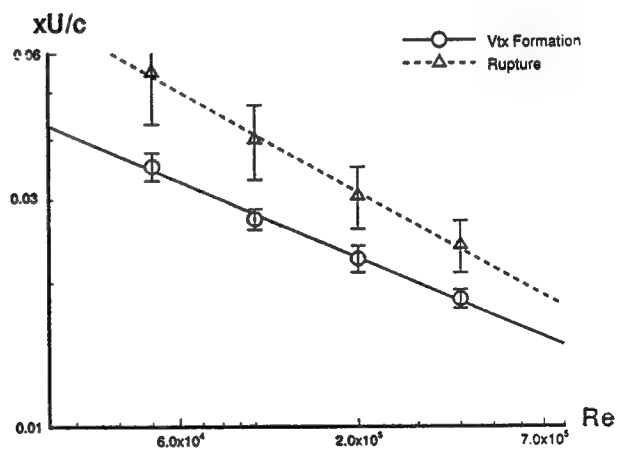


Fig. 17 Reynolds Number Scaling of Location of Vortex Formation and Location of Vortex Sheet Rupture. Corresponding Temporal Scaling is Given in Fig. 16.

**THIS PAGE INTENTIONALLY LEFT BLANK**

**APPENDIX C**  
**COMPLEMENT TO AIAA PAPER NO. 94-2339**

## APPENDIX C -- TABLE OF CONTENTS

	page
Title Page .....	C-1
Table of Contents .....	C-2
Comparison Between ARC2D/8E and ARC2D .....	C-3
Reynolds Number Scaling .....	C-4
References .....	C-4
Figures	

## COMPLEMENT TO AIAA PAPER NO. 94-2339

Several results not shown in AIAA Paper No. 94-2339 are summarized here to clarify the methods used and provide further documentation of the cases computed in that paper.

Comparison between ARC2D/8E and ARC2D. As mentioned in Ref. C1, p. 2, no experimental data is available to compare against the model semi-impulsive problem. Therefore the accuracy of the calculations was verified by two means. The first one is through careful grid convergence studies. The second was to compare the computed results from two different codes. The two codes that were used in this study are NASA Ames's ARC2D Navier-Stokes finite difference solver, and a specially developed explicit eighth-order accurate version named ARC2D/8E.

A summary of the grid convergence studies performed at  $Re = 200,000$  is given in Appendix B. These studies were carried out using the ARC2D/8E code. Appropriate computational meshes for  $Re = 100,000$  and  $Re = 400,00$  were conservatively designed from these results and from simple scaling laws relating grid spacing to Reynolds number. A separate grid resolution study for the  $Re = 800,000$  case is given in Appendix D. The present section concerns an exercise which was not reported in Ref. C1, namely the comparison between the results of the implicit second-order code ARC2D<sup>C2</sup> and the explicit eighth-order code ARC2D/8E.

Figures C.1 through C.3 compare the vortical flowfield computed with ARC2D and ARC2D/8E at successive times,  $tU/c = 0.030, 0.051, \text{ and } 0.060$ , for the chord Reynolds number  $Re = 400,000$ . The results are in good agreement, both qualitative and quantitative, at short times. However, the ARC2D solution breaks down (Fig. C.3) at later times. This behavior is consistent with the appearance of fine scales in the flowfield, the (numerical) growth of which cannot be contained by the artificial dissipation scheme used in ARC2D. In contrast, the solution remained stable throughout the calculation with ARC2D/8E. The computational method used in ARC2D/8E consists of central, eighth-order, finite-difference spatial discretization, and an explicit third-order Runge-Kutta time integration scheme. Eighth-order accuracy is implemented for the calculation of the convective fluxes, eighth-order for the metric terms, and eighth-order for the artificial dissipation. Viscous fluxes are computed with fourth-order accuracy. The order of the central difference scheme degenerates to second order at the wall. The high-order artificial dissipation algorithm does not affect modes in the solution which are accurately resolved by the discretization scheme. The accuracy of the algorithm has been validated in various studies.<sup>C3,C4</sup> The advantage of the high-accuracy scheme is that true accuracy can be attained for roughly half of the grid-resolved wave number range. In comparison, a second-order method is only accurate over approximately 5 to 10% of the spectral range, while spectral methods typically resolve approximately two thirds of the theoretical range. Such considerations are critical when attempting to capture the physics of high Reynolds number flows, and are believed to relate to the failure of ARC2D at large times.

From the results shown in Figs. C.1 and C.2, it is tempting to conclude that the use of ARC2D might be justified provided that one is only interested in topological changes of the flow at early times. Indeed, if it can be argued that ARC2D is as accurate as ARC2D/8E for a specific purpose, then the implicit algorithm (resulting in higher Courant numbers and, thus, less computational work) would seem more attractive. In reality however, ARC2D, when

run with a CFL number of 15 produced poor results in comparison to ARC2D/8E, even for the prediction of the time of first flow reversal at the surface. The results for ARC2D were found only to begin to achieve time-step independence for CFL numbers lower than three. This is illustrated in the surface flow topology diagram comparison of Fig. C.4. For reference, ARC2D/8E was run with a CFL number of 1.5. Taking into account the extra costs associated with matrix inversion, the computational savings associated with running ARC2D, rather than ARC2D/8E, were minimal for this problem. Therefore ARC2D/8E was the program of choice for this study. In Appendix D, results computed with ARC2D/8E for a chord Reynolds number  $Re = 800,000$  are presented.

From the ARC2D calculations with  $(\Delta t)a/c = 9.4 \times 10^{-5}$  (solid line in Fig. C.4) we show, for completeness, the computed characteristic times associated with critical changes of the surface flow topology during the early stages of flow development. These are indicated as shaded symbols in the Reynolds number scaling plot of Fig. C.5. The open symbols correspond to the ARC2D/8E runs at various Reynolds numbers, from  $Re = 50,000$  to  $Re = 400,000$ . As in Appendix B, the notation used here is as follows: the time of first occurrence of the primary flow separation is denoted "PS1." Successive times for the occurrence of secondary flow separation regions are denoted (in their order of appearance) "SS1," "SS2," "SS3," etc. Similarly, tertiary separation is denoted "TS1," "TS2," and so on. The results presented in Fig. C.5 indicate that the ARC2D determinations of PS1, SS1 and SS2 fall within the uncertainty range of the power-law fits discussed in Appendix B.

Reynolds Number Scaling. Similarly to Fig. C.5, simple scaling relationships were given in Appendix B for the times of primary vortex formation and primary vortex release (or "rupture" of the feeding vorticity sheet). Figures 12 and 13, p. 12, of Appendix B illustrated the qualitative similarity of the vortical flowfields at the end of Stage II. This qualitative similarity is carried one step further in Fig. C.6. In this figure, instantaneous vorticity fields for  $Re = 50,000$ ,  $Re = 100,000$ ,  $Re = 200,000$ , and  $Re = 400,000$  are compared; the value of the vorticity contours is kept identical between all four flowfields. The time instant is chosen to be on the order of 15% ( $\pm 2\%$ ) beyond the point of rupture of the feeding vorticity sheet. A vortex-induced eruptive plume of vorticity is visible at the three higher Reynolds numbers depicted in Fig. C.6. In all likelihood the flowfield at  $Re = 50,000$  would also exhibit the same type of eruption at a slightly later time. This is based on the overall similarity of the flowfields and observations at higher Reynolds numbers at earlier times.

Further details of the temporal evolution of the flowfield at  $Re = 400,000$  (Figs C.7 through C.15) reveal the existence of multiple vortex-induced eruptions (see, e.g., Fig. C.9). After the end of Stage II (i.e., the rupture of the primary vortex feeding sheet), Reynolds number similarity, in the sense described in Appendix B, is not observed. In addition to multiple ejections, vortex pairing events take place. Some of these complex vortical interactions take place earlier still at higher Reynolds numbers. This is described further in Appendix D, for the  $Re = 800,000$  case.

## References

- C1. Reisenthel, P.H. and Childs, R.E.: "A Study of Reynolds Number Effects on Incipient Leading Edge Stall," AIAA Paper No. 94-2339, 1994.
- C2. Pulliam, T.H.: "Euler and Thin Layer Navier Stokes Codes ARC2D-ARC3D," Notes for Computational Fluid Dynamics User's Workshop, Tullahoma, TN, March 12-16, 1984.



- C3. Childs, R.E., Rodman, L.C., and Nixon, D.: "Methods for Computational Aeroacoustics," Nielsen Engineering & Research, NEAR TR 452, Aug. 1992.
- C4. Childs, R.E.: "Advanced Discretization Algorithm for CFD Methods," Nielsen Engineering & Research, NEAR TR 469, July 1993.

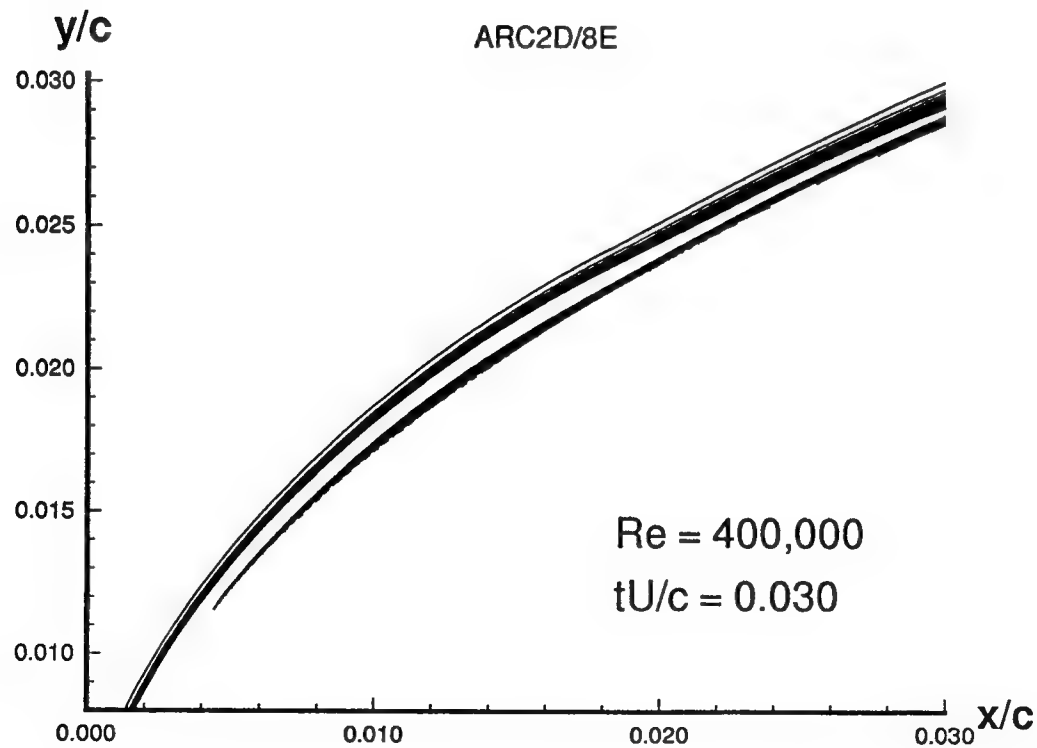
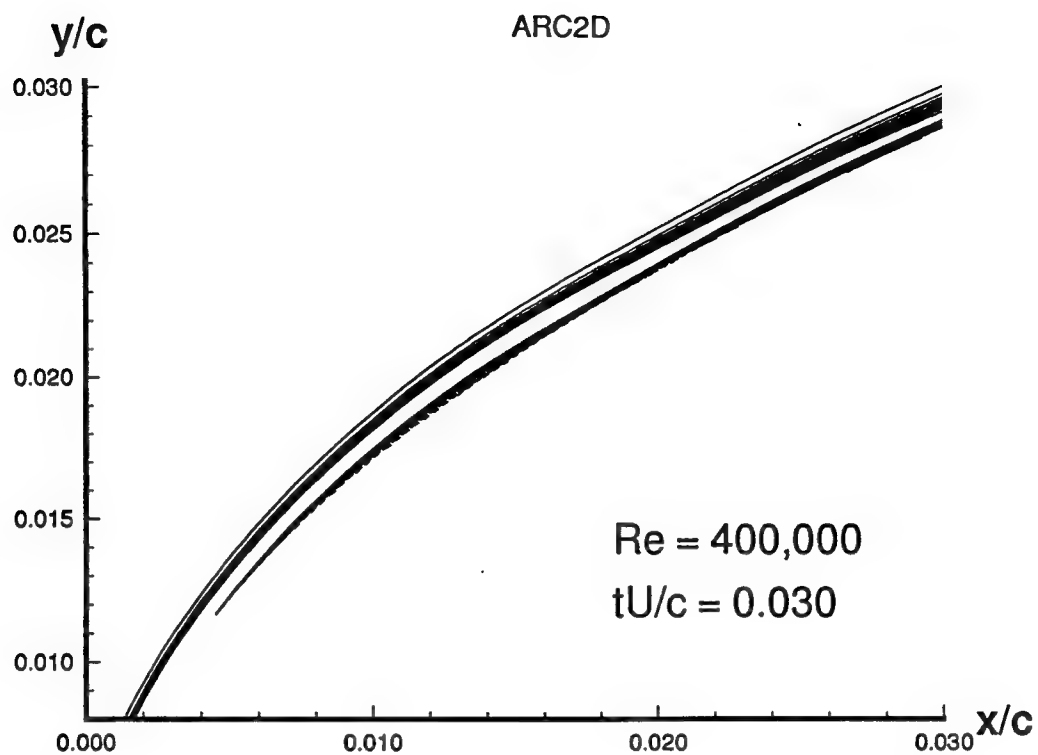


**Fig. C.1** Comparison of Instantaneous Vorticity Contours Computed Using ARC2D (Top) and ARC2D/8E (Bottom),  $tU/c = 0.030$ ,  $Re = 400,000$ . (Spacing between contours is  $\Delta\Omega = 80$ ; dashed lines indicate negative levels).

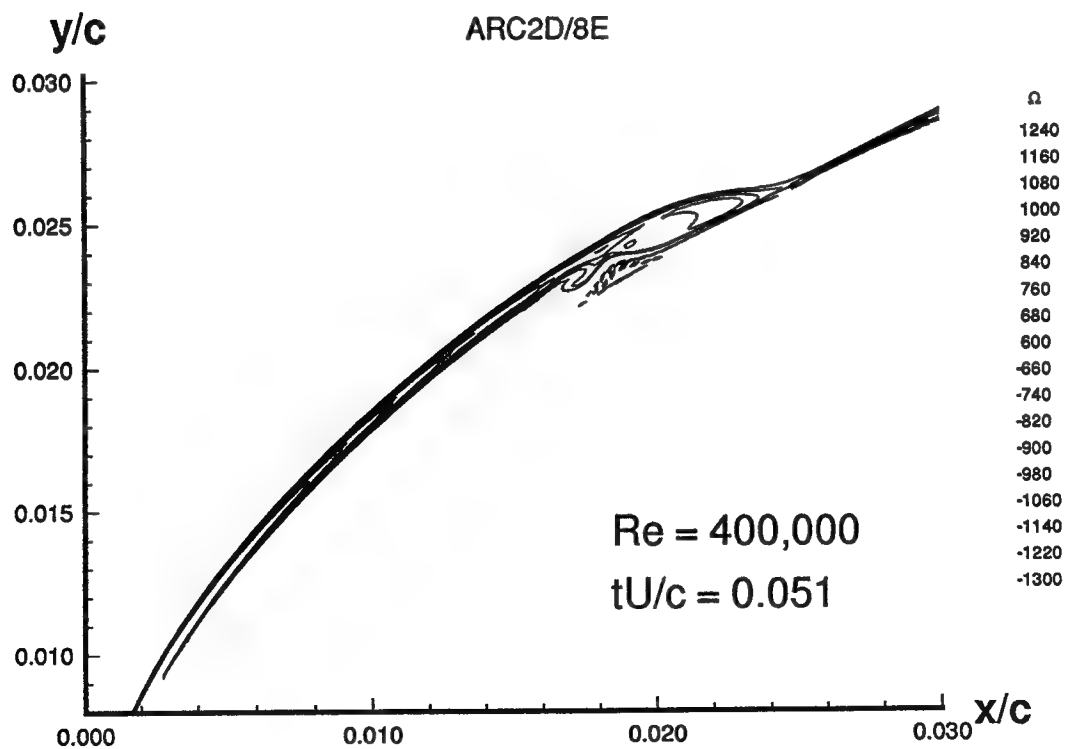
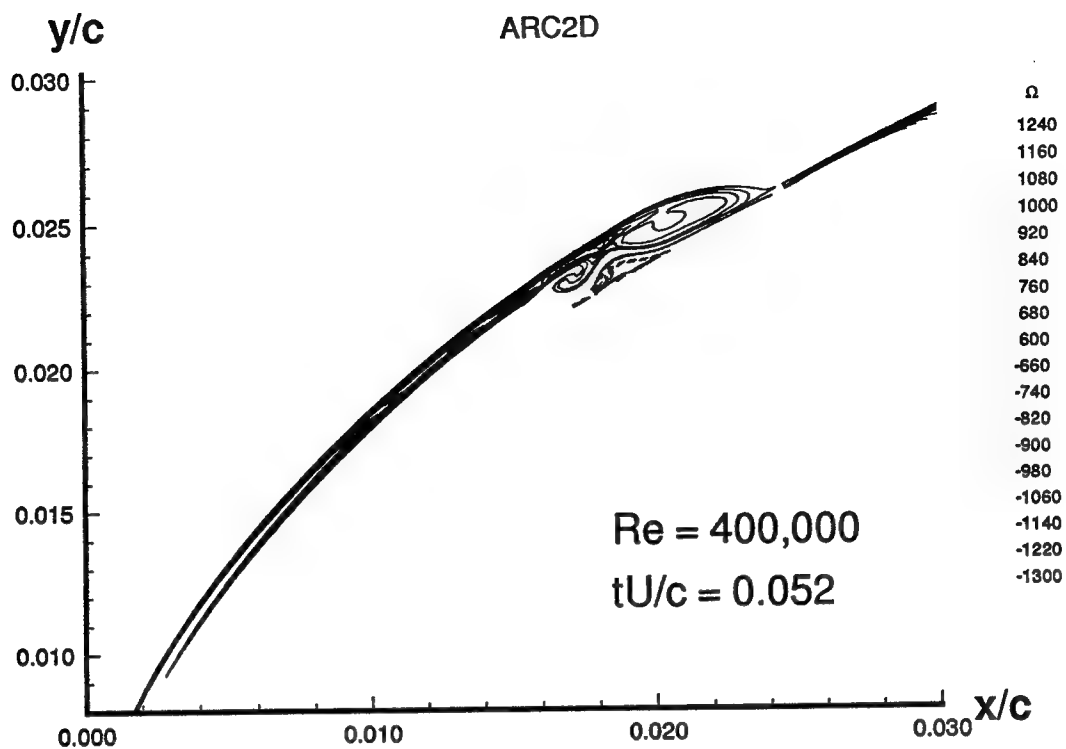


**Fig. C.2(a) Comparison of Instantaneous Vorticity Contours Computed Using ARC2D (Top) and ARC2D/8E (Bottom),  $tU/c \approx 0.051$ ,  $Re = 400,000$ . (Spacing between contours is  $\Delta\Omega = 80$ ; dashed lines indicate negative levels). Continued on next page.**

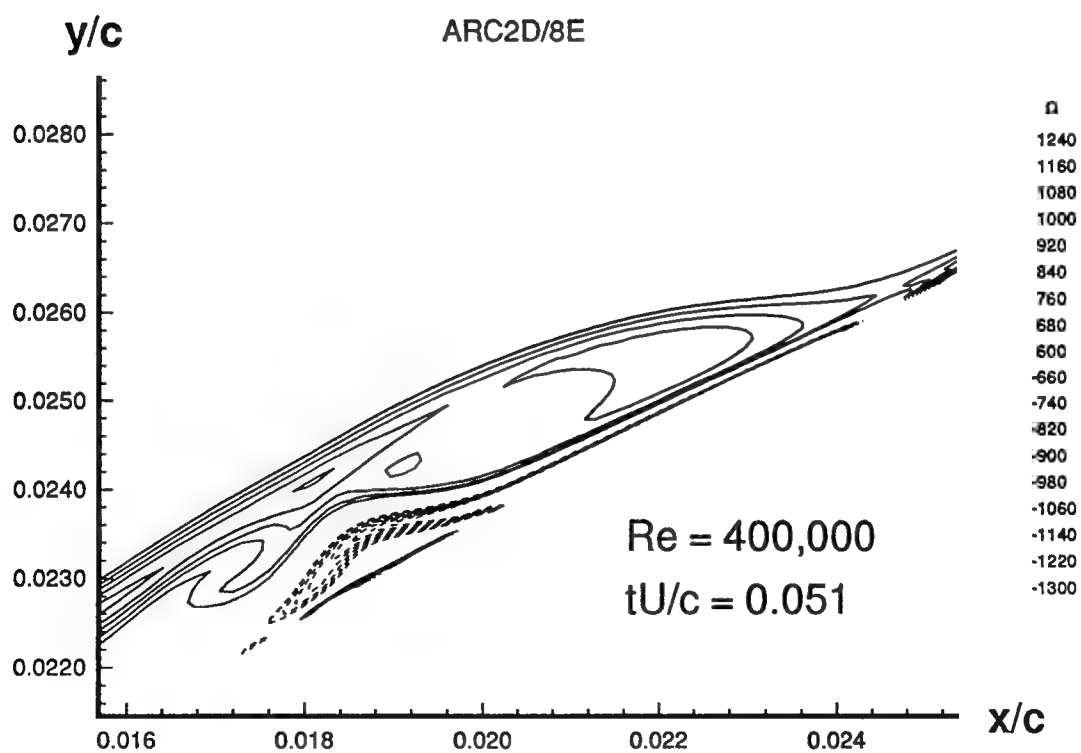
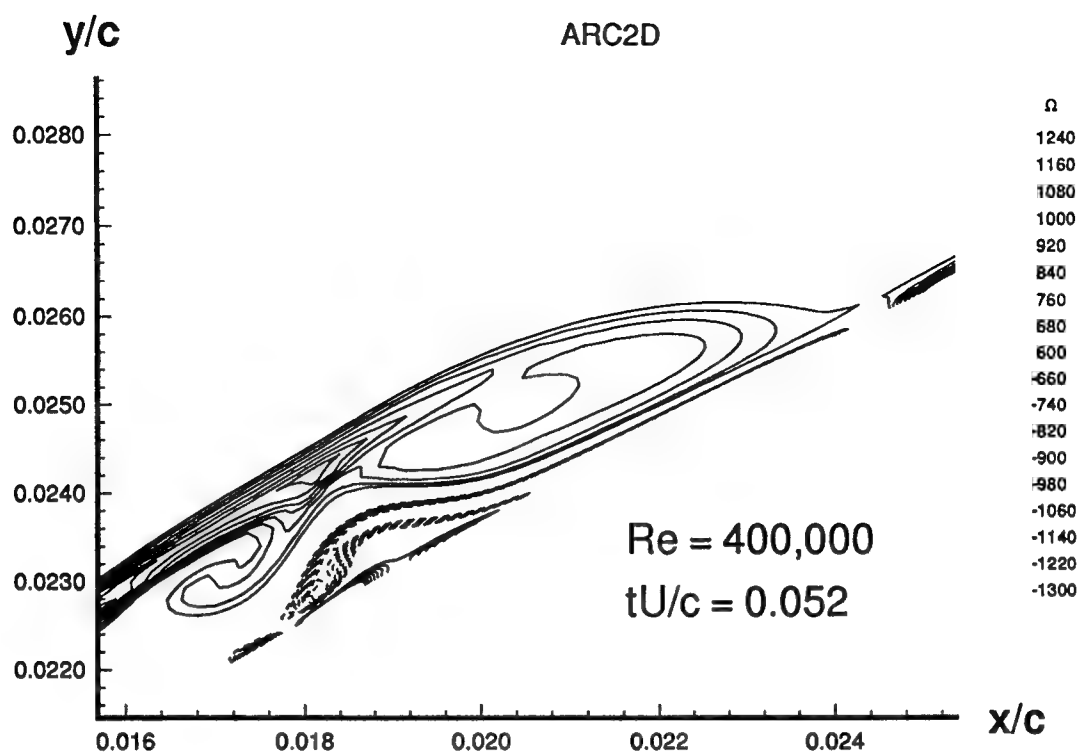


**Fig. C.2(b) Detailed Comparison of Instantaneous Vorticity Contours Computed Using ARC2D (Top) and ARC2D/8E (Bottom),  $tU/c = 0.051$ ,  $Re = 400,000$ . Continued from previous page.**

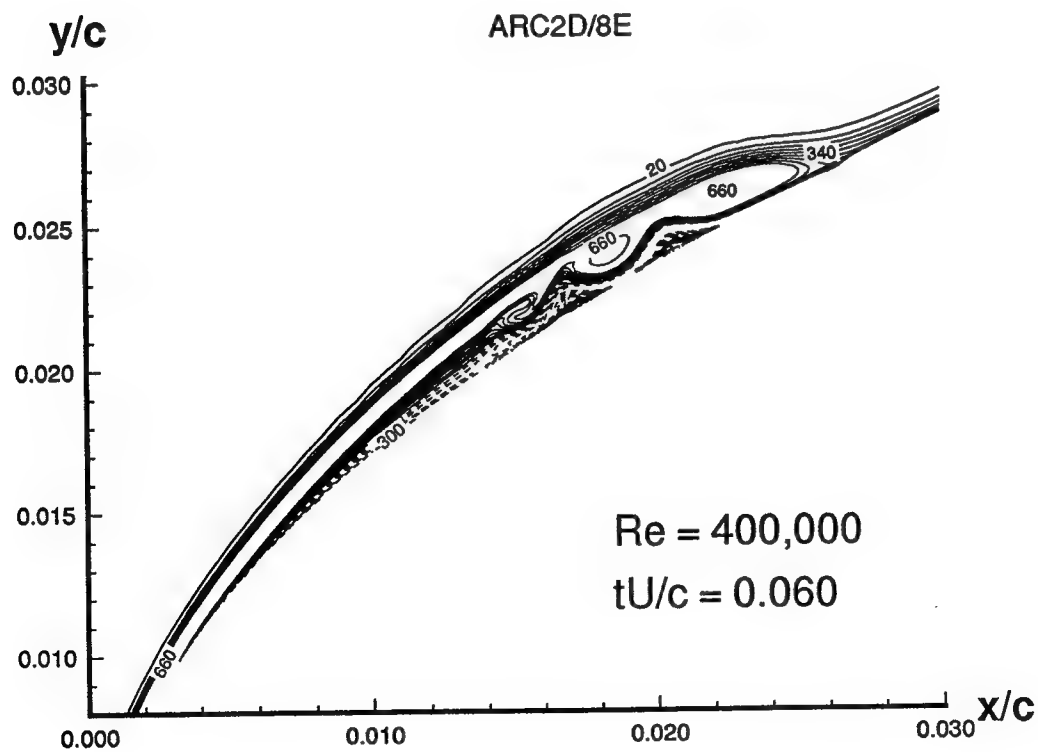
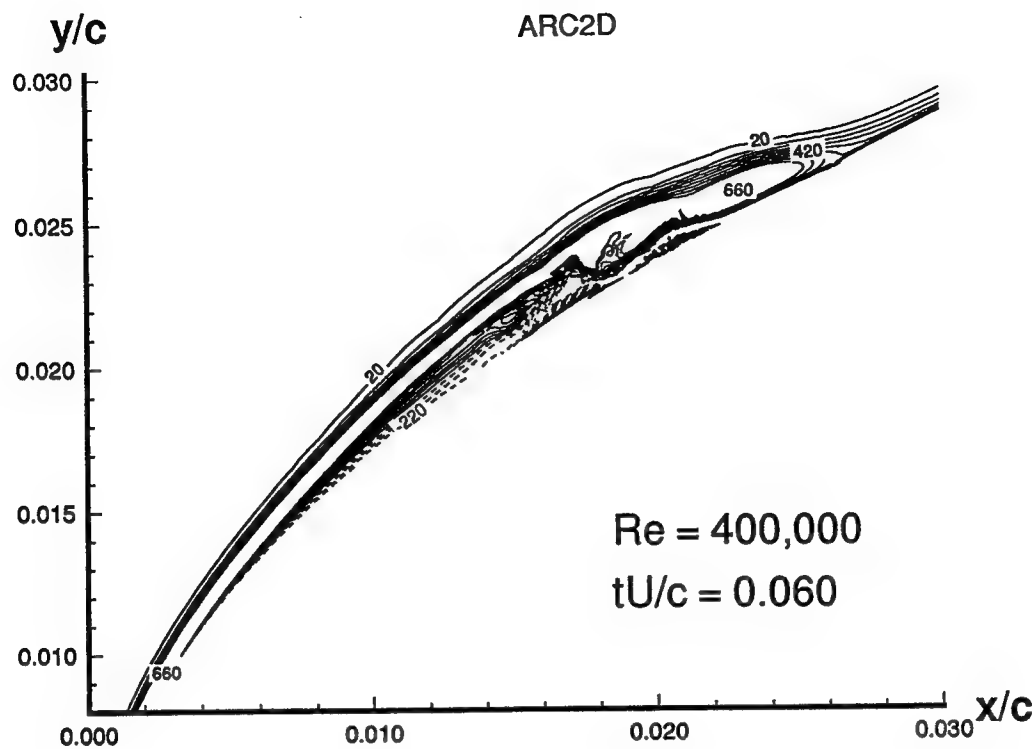


**Fig. C.3** Comparison of Instantaneous Vorticity Contours Computed Using ARC2D (Top) and ARC2D/8E (Bottom),  $tU/c = 0.060$ ,  $Re = 400,000$ . (Spacing between contours is  $\Delta\Omega = 80$ ; dashed lines indicate negative levels).

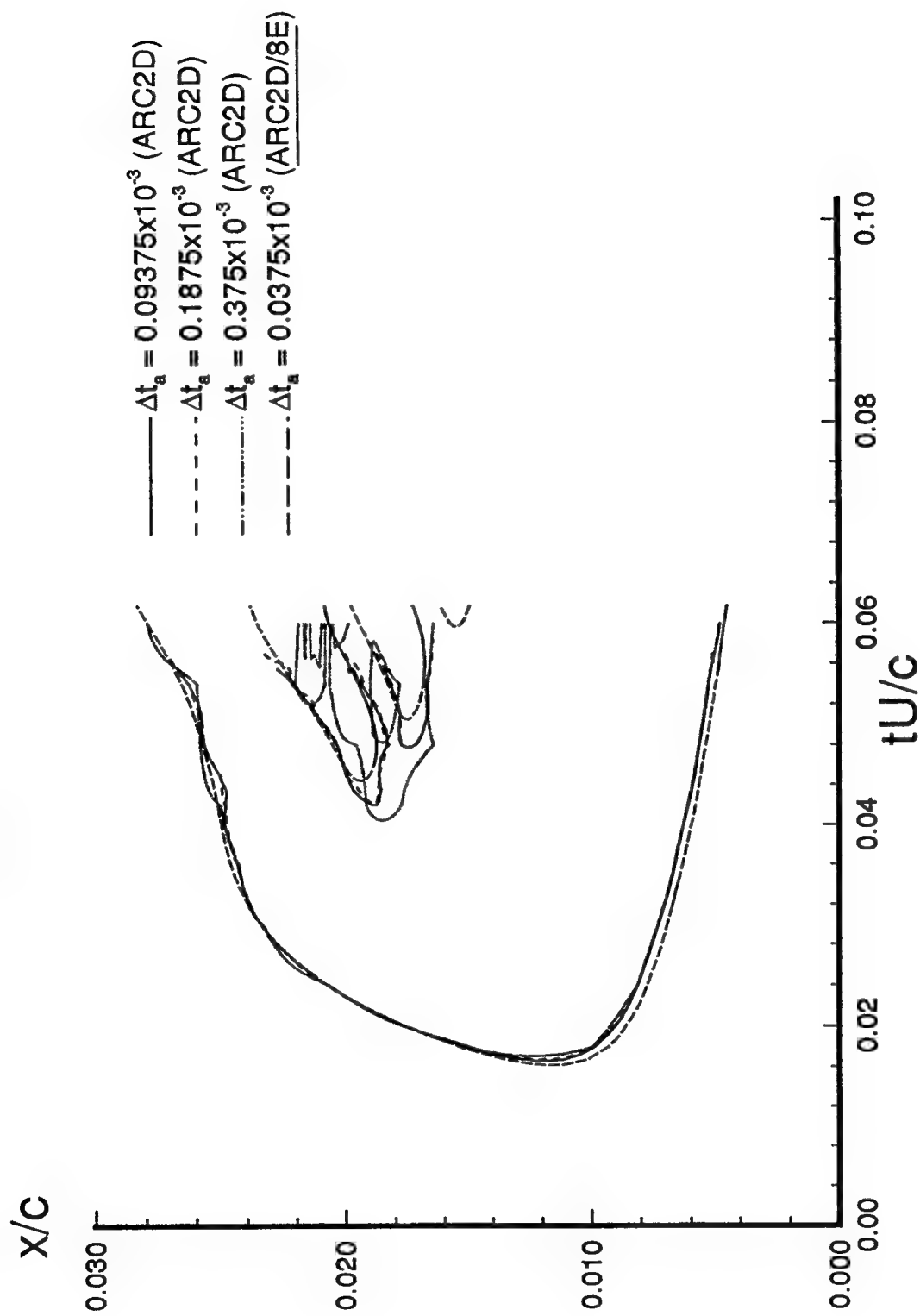


Fig. C.4 Time-Step Sensitivity of Surface Flow Topology Evolution Calculated with ARC2D, and Comparison with ARC2D/8E Results. (Lines are zero skin friction contours;  $\Delta t_a$  is time-step based on freestream speed of sound).

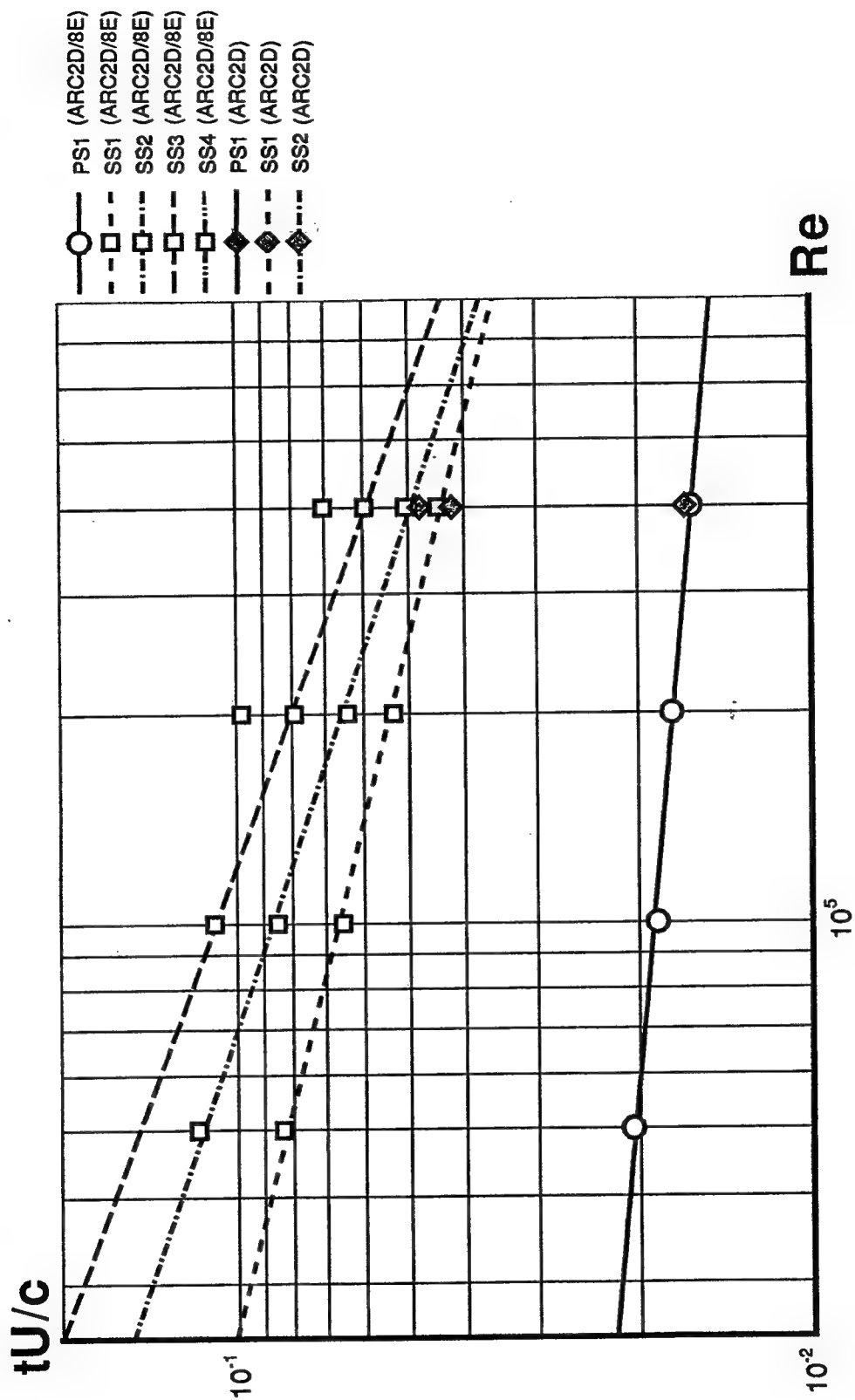


Fig. C.5 Reynolds Number Scaling of the Time of Appearance of Incipient Primary (PS1) and Secondary (SS1, SS2, SS3, SS4) Separation Bubbles.



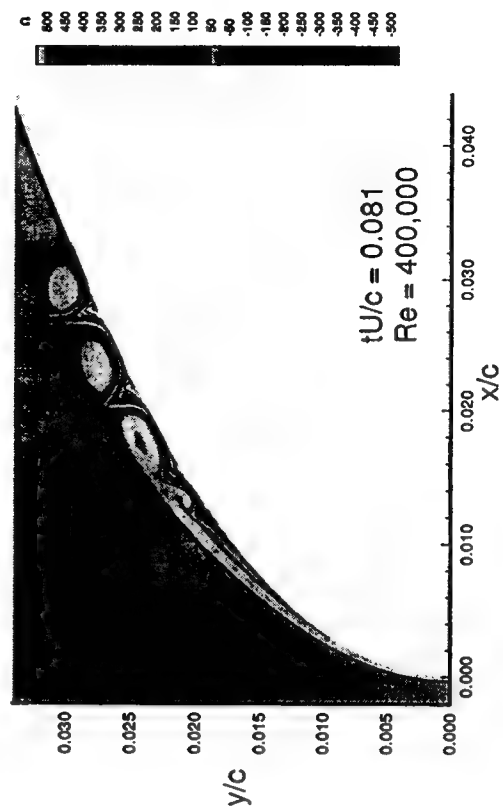
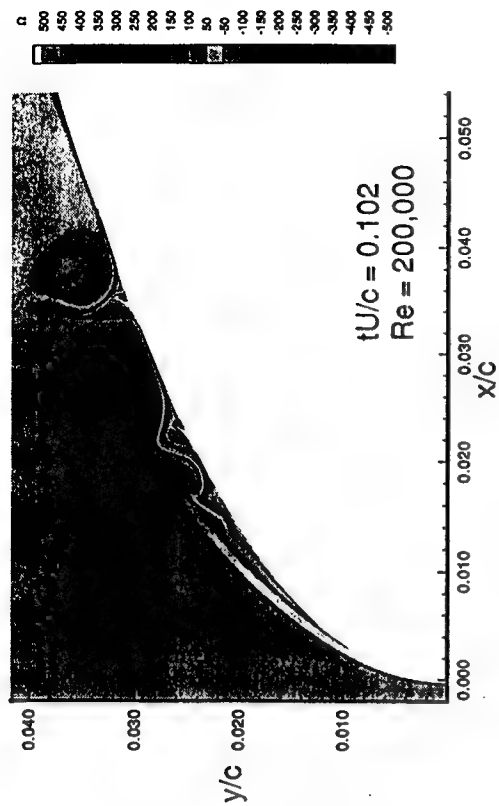
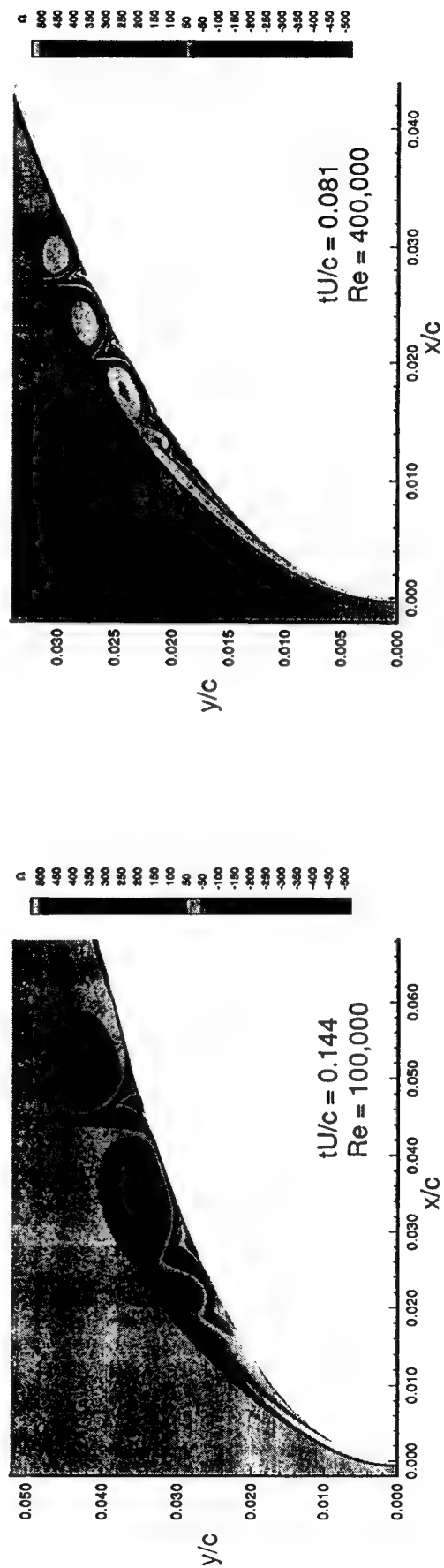
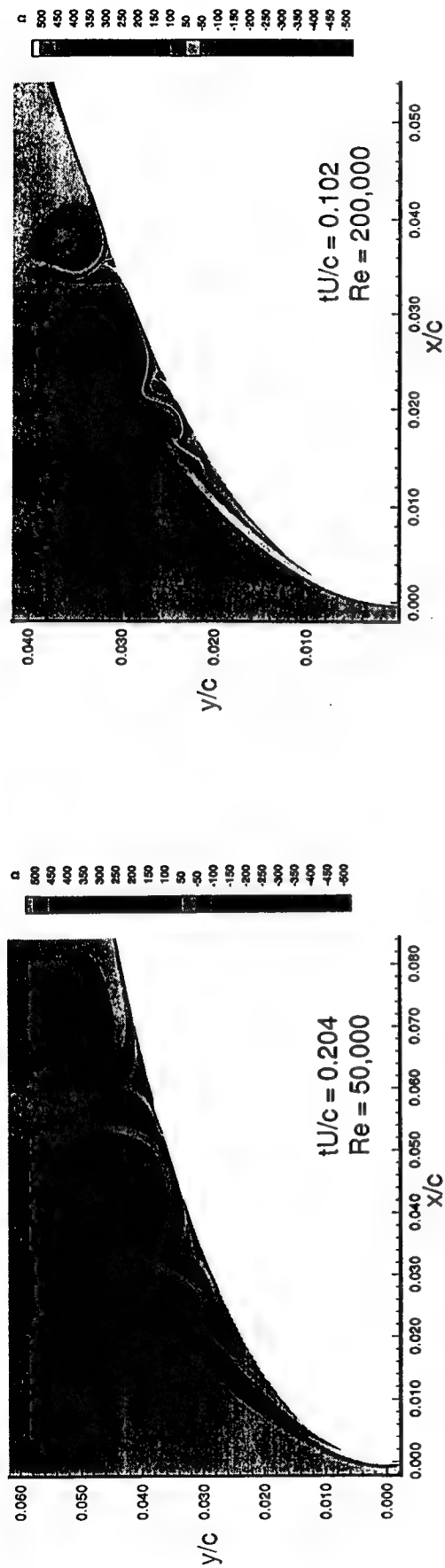


Fig. C.6 Comparison of Vorticity Fields Near the Time Beyond the End of Stage II for  $Re = 50,000$ ,  $Re = 100,000$ , and  $Re = 200,000$ . The (Vortex-Induced) Formation of Eruptive Plumes of Vorticity is Visible at the three highest Reynolds Numbers.

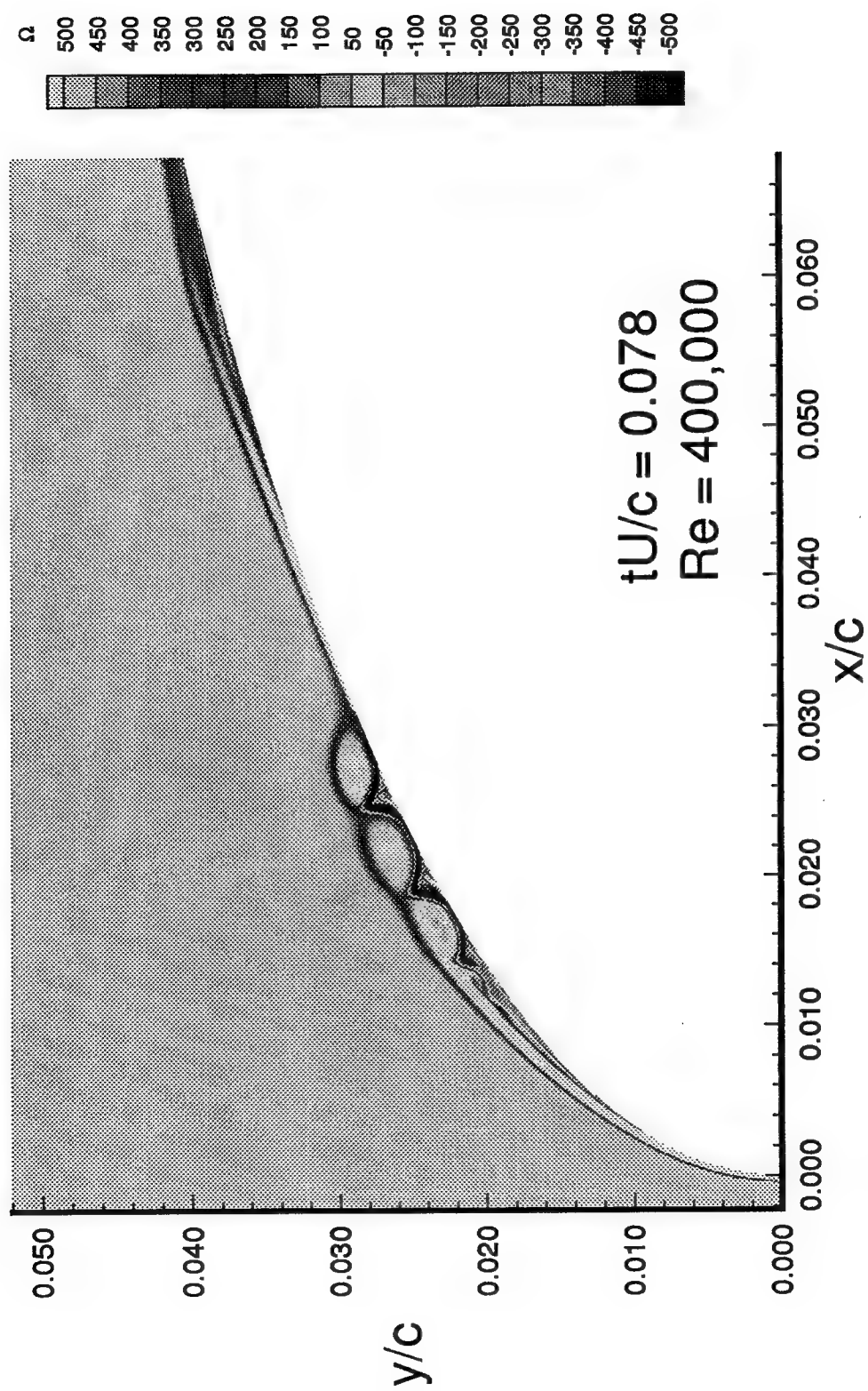


Fig. C.7 Instantaneous Vorticity Field Beyond Stage II at  $tU/c = 0.078$ ,  $Re = 400,000$ .

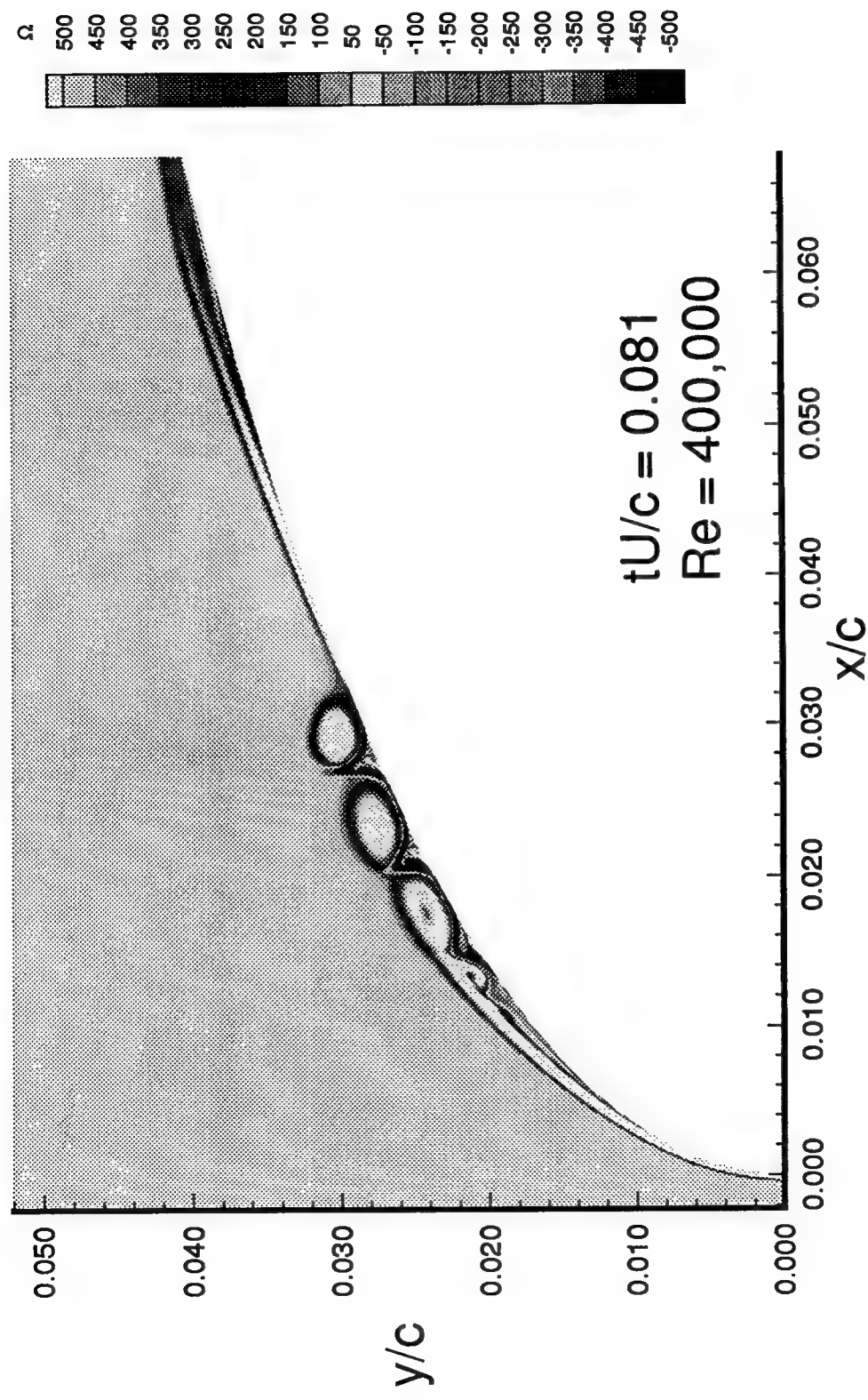


Fig. C.8 Instantaneous Vorticity Field Beyond Stage II at  $tU/c = 0.081$ ,  $Re = 400,000$ .

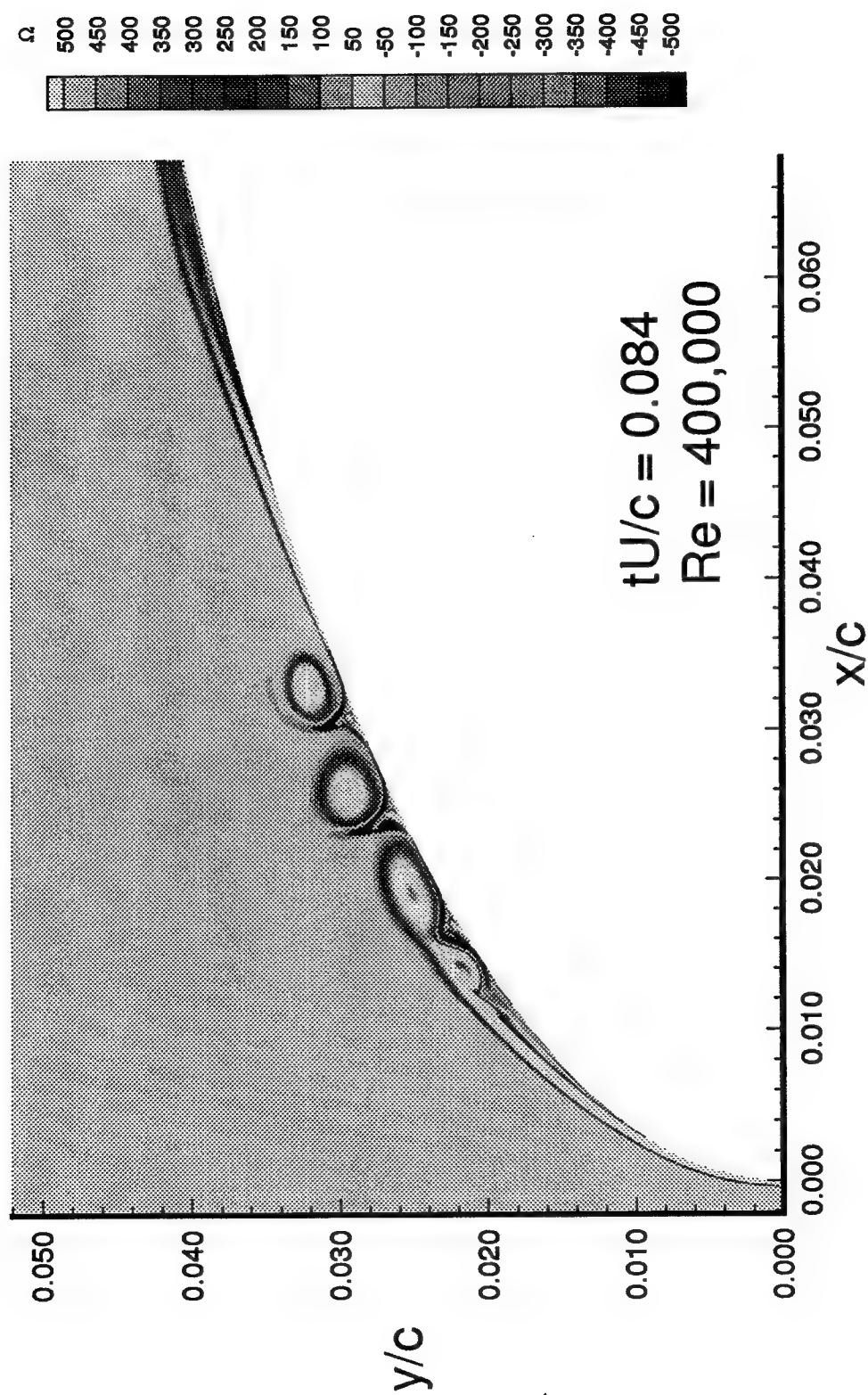


Fig. C.9 Instantaneous Vorticity Field Beyond Stage II at  $tU/c = 0.084$ ,  $Re = 400,000$ .

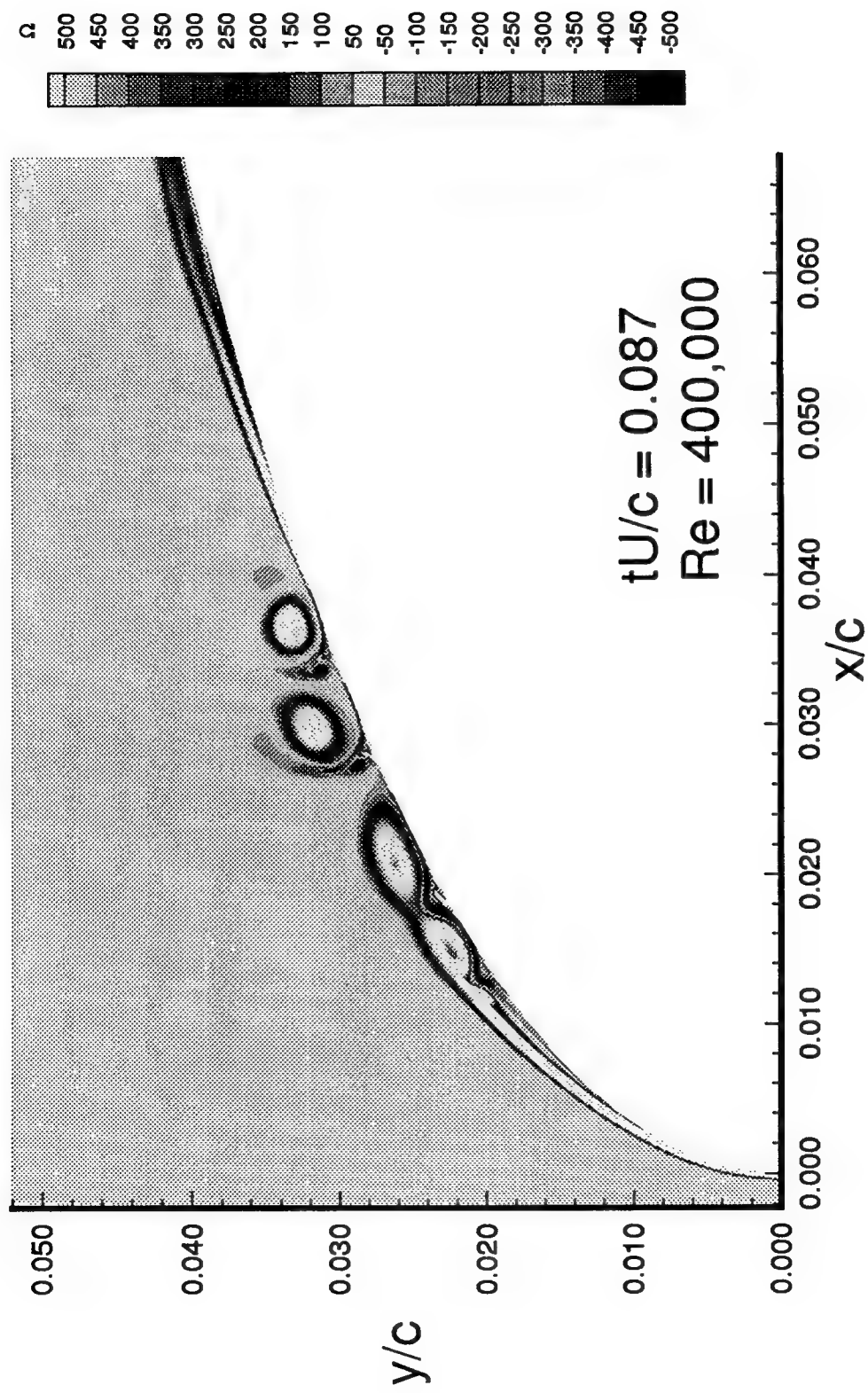


Fig. C.10 Instantaneous Vorticity Field Beyond Stage II at  $tU/c = 0.087$ ,  $Re = 400,000$ .

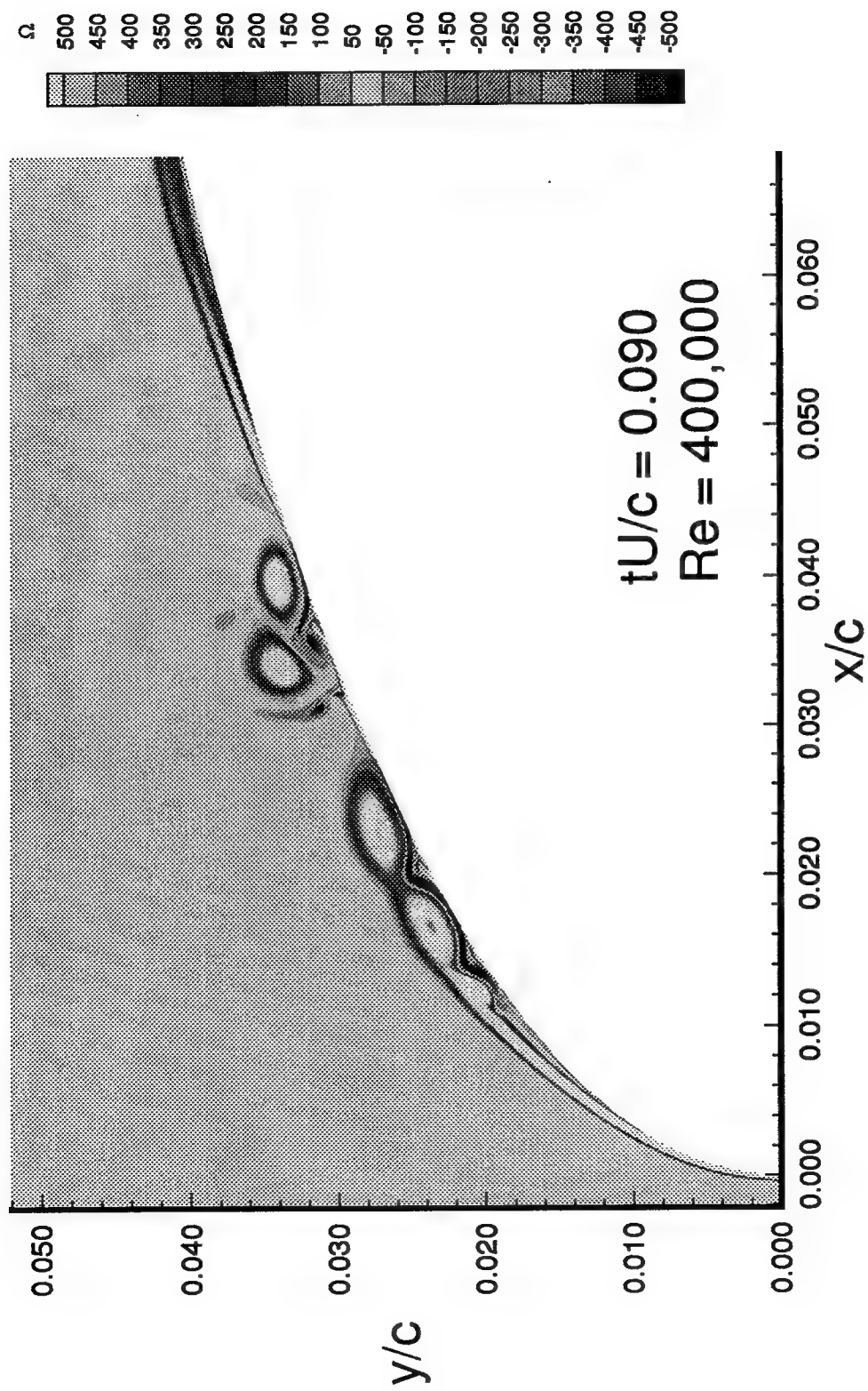


Fig. C.11 Instantaneous Vorticity Field Beyond Stage II at  $tU/c = 0.090$ ,  $Re = 400,000$ .

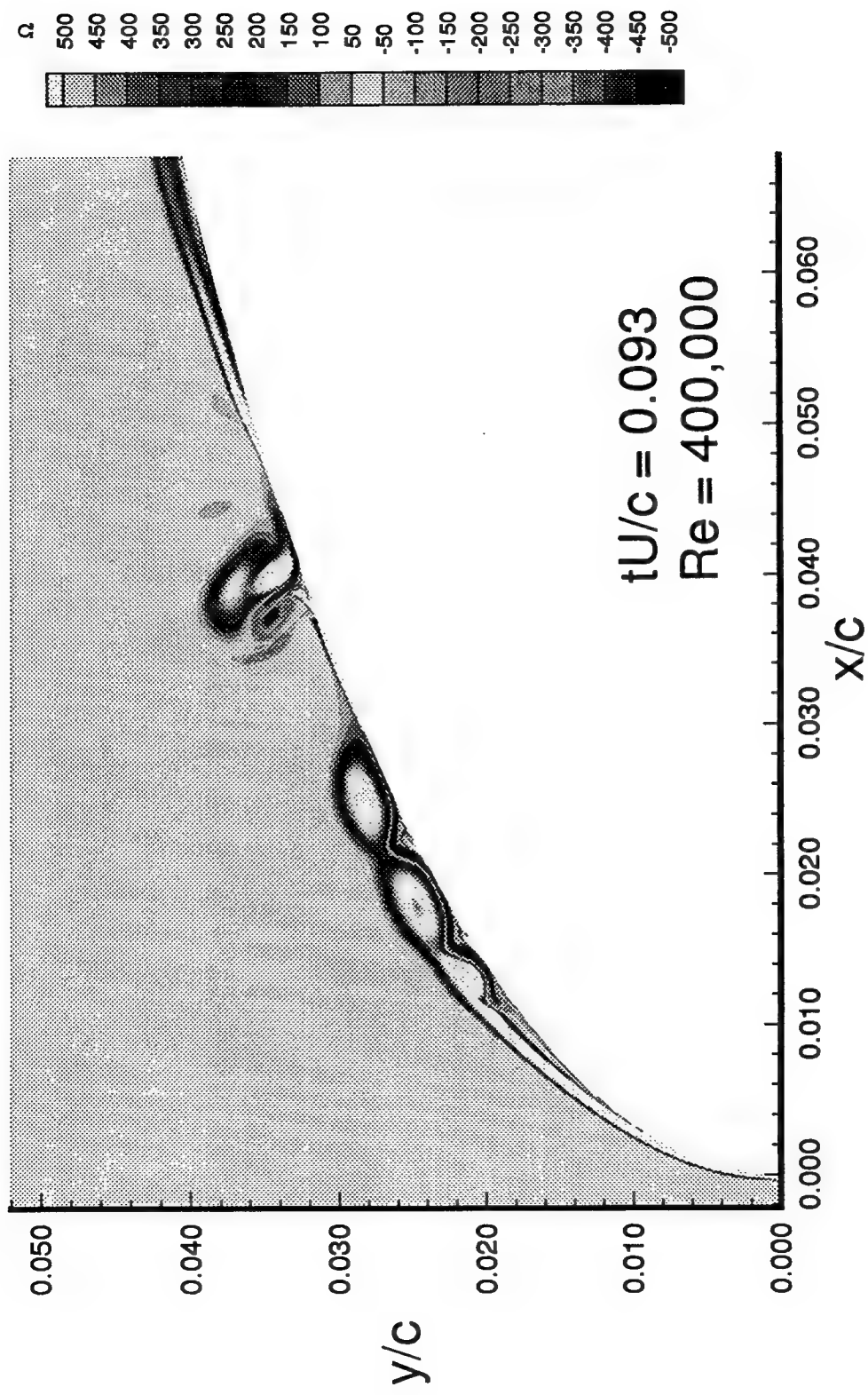


Fig. C.12 Instantaneous Vorticity Field Beyond Stage II at  $tU/c = 0.093$ ,  $Re = 400,000$ .



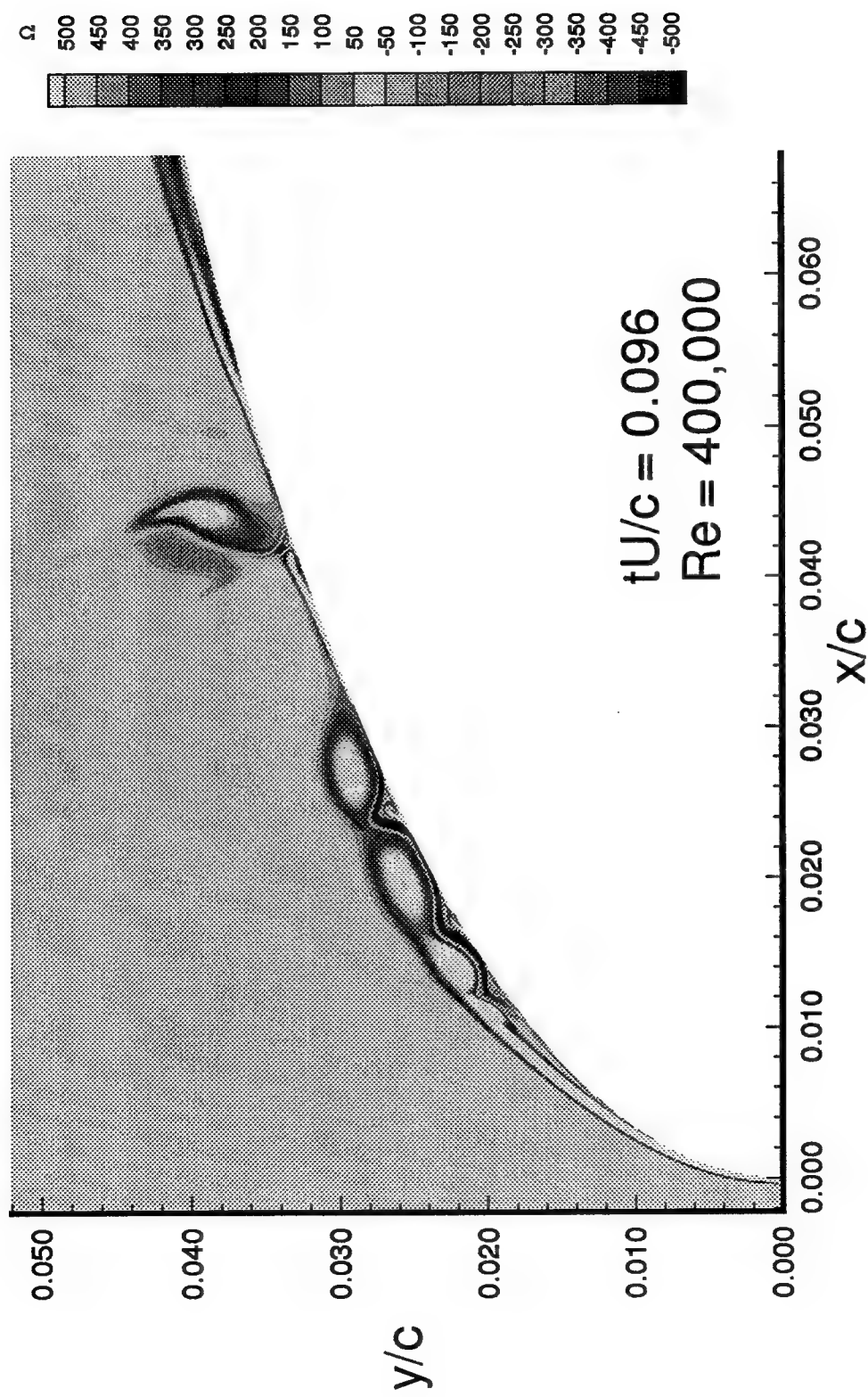


Fig. C.13 Instantaneous Vorticity Field Beyond Stage II at  $tU/c = 0.096$ ,  $Re = 400,000$ .

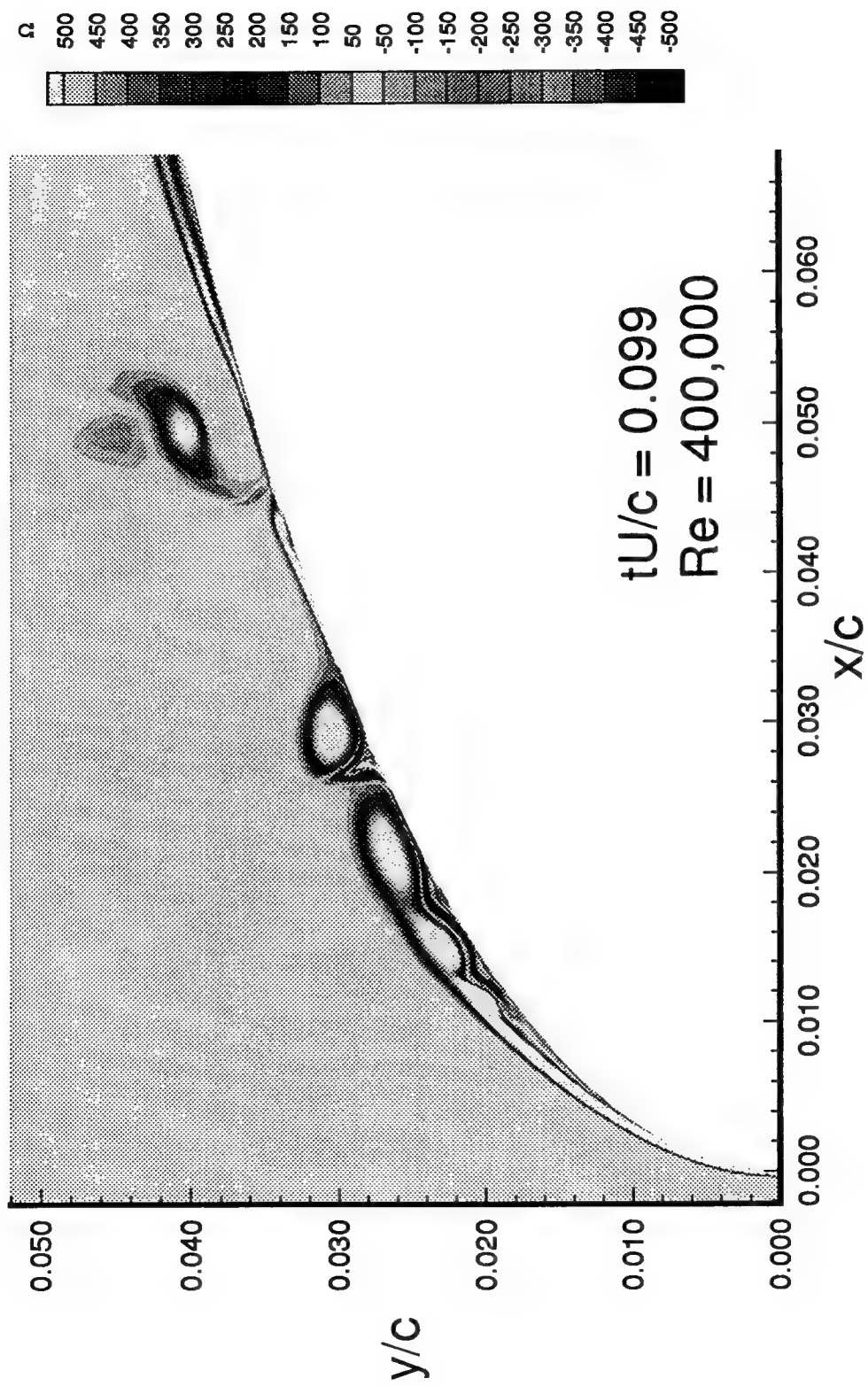


Fig. C.14 Instantaneous Vorticity Field Beyond Stage II at  $tU/c = 0.099$ ,  $Re = 400,000$ .

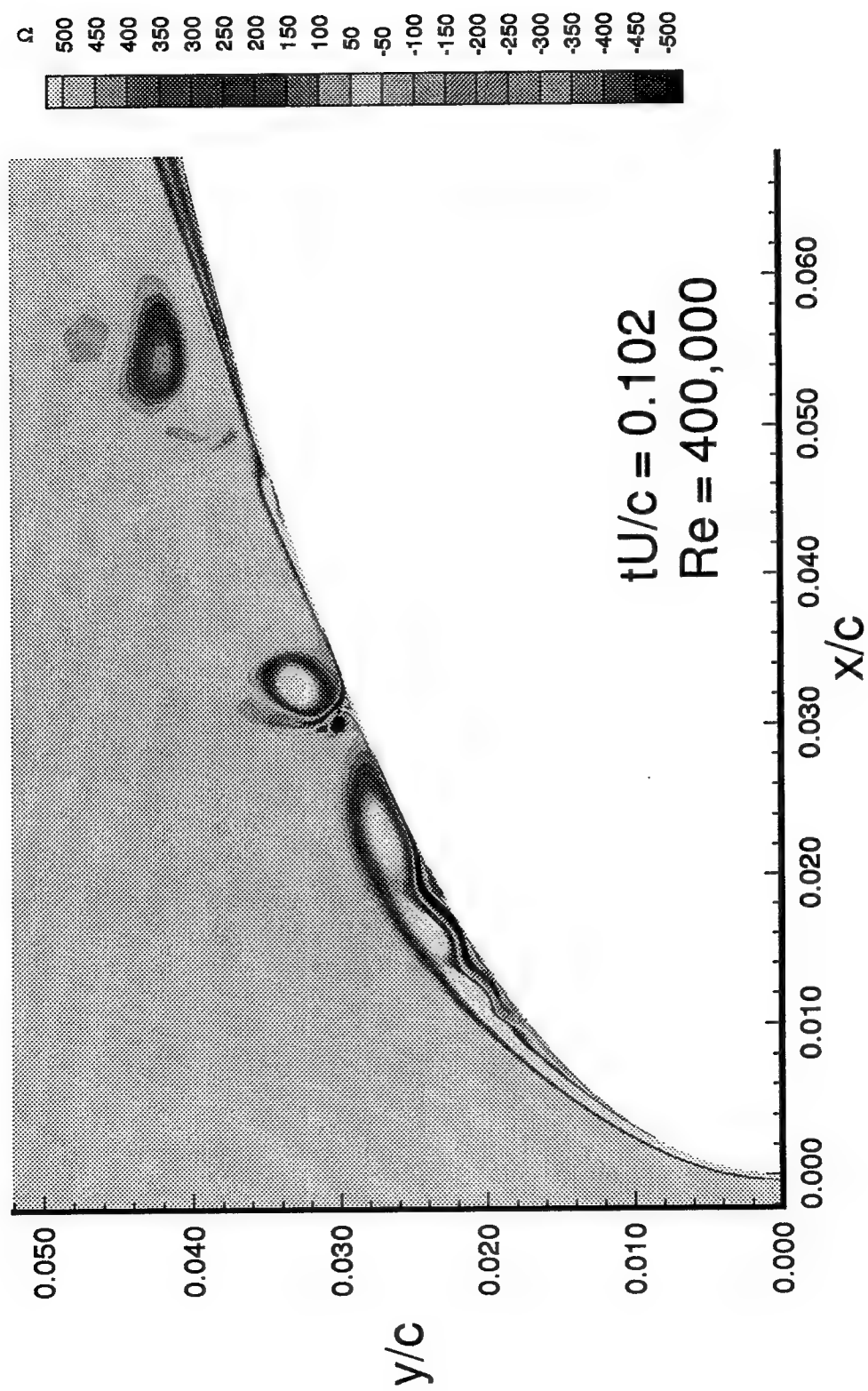


Fig. C.15 Instantaneous Vorticity Field Beyond Stage II at  $tU/c = 0.102$ ,  $Re = 400,000$ .

**THIS PAGE INTENTIONALLY LEFT BLANK**

**APPENDIX D**  
**FURTHER RESULTS ON THE REYNOLDS NUMBER SCALING**  
**OF INCIPIENT LEADING EDGE STALL**

## APPENDIX D – TABLE OF CONTENTS

	page
Title Page .....	D-1
Table of Contents .....	D-2
Grid Convergence Studies .....	D-3
Artificial Dissipation .....	D-4
Flowfield Description at $Re = 800,000$ .....	D-5
Dependence of Skin Friction on Reynolds Number .....	D-6
Dependence of Pressure Coefficient on Reynolds Number .....	D-7
Incipient Vortex Formation .....	D-9
Reynolds Number Scaling .....	D-10
Auxiliary Results .....	D-11
References .....	D-13
Figures	

## FURTHER RESULTS ON THE REYNOLDS NUMBER SCALING OF INCIPIENT LEADING EDGE STALL

In Appendix B (AIAA Paper No. 94-2339), four Reynolds numbers were investigated. These are (based on chord):  $Re = 50,000$ ,  $Re = 100,000$ ,  $Re = 200,000$ , and  $Re = 400,000$ . All simulations were for a fixed angle of attack  $\alpha = 15^\circ$ , and a freestream Mach number  $M_\infty = 0.2$ . The present appendix examines further results, obtained for  $Re = 800,000$ , and how these affect the conclusions drawn in Appendix B. These results will be presented in AIAA Paper No. 95-0780.

**Grid Convergence Studies.** The results shown here are computed for a NACA0012 airfoil with a rounded trailing edge (radius of curvature  $r/c = 0.0092$ ). This ensures that the CFL requirements with the present O-grid are not dictated by the trailing edge region, which is irrelevant to this study. The scaling relationships discovered in Ref. D1 provided guidance in the design of the computational grids at  $Re = 800,000$ , resulting in highly clustered meshes in the leading edge region of the airfoil. The region of highest circumferential clustering was located between  $x/c = 0.002$  and  $x/c = 0.025$ . In that region, the circumferential spacing was uniform, with either 470, 235, or 118 points, depending on the mesh.

Three computational meshes were constructed for the grid convergence studies conducted at  $Re = 800,000$ . Each mesh is assembled as the union of two zones. The grid in each zone is designed using NASA Ames's GRIDGEN hyperbolic grid generation program. This particular release of GRIDGEN (Version 2.0) allows for non-uniform initial spacing in the marching direction (i.e., normal to the surface). The ability to prescribe a variable initial grid spacing plays an essential role in the alleviation of CFL requirements at the trailing edge. For example, in all of the grids used here, the initial trailing edge spacing normal to the surface,  $\Delta y_{TE}$ , is 40 times greater than the initial normal grid spacing at the leading edge ( $\Delta y_{LE}/c = 1.25 \times 10^{-5}$ ). An example of a computational grid used in this study is given in Fig. D.1. For this grid, 666 points are used in the circumferential direction, 470 of which are placed within 2.3% of chord (525 in the first 3%), on the suction surface. A detail of the first (or "inner") grid zone is illustrated in the bottom graph of Fig. D.1. The inner grid zone ( $666 \times 32$  points) surrounds the airfoil, and is characterized by a relatively mild stretching factor,  $\Delta y_{j+1}/\Delta y_j = 1.065$ . The outer grid zone extends radially approximately seven chord lengths from the airfoil, with a stretching factor of 1.17. For all meshes the number of points in the direction normal to the airfoil was 91, with an initial spacing at the leading edge  $\Delta y_{LE} = 1.25 \times 10^{-5}$ . The value of  $\Delta y_{LE}$  was conservatively chosen to be one half of the value used at  $Re = 400,000$  and  $Re = 200,000$  (see Ref. D1).

It is worthwhile noting that, for the present problem, normal grid spacing is not an issue and can be based on standard boundary layer scaling arguments. What is at issue is the streamwise resolution needed, because of the possibility of self-focusing, eruptive plumes of vorticity.<sup>D2</sup> The effect of circumferential grid spacing was investigated on three computational meshes ( $666 \times 91$ ,  $394 \times 91$ , and  $258 \times 91$ ), and is shown in Figs. D.2, D.3, and D.4. The goal of this exercise is to find out when local grid independence is attained. By "local" we mean "in the first three percent of chord," where all of the important physics of incipient separation take place (at this Reynolds number and angle of attack).

Skin friction was used as a sensitive indicator of the relative accuracy of the numerical solutions. Figure D.2 illustrates the convergence of skin friction distribution between 0.5% chord and 3.0% chord, as the circumferential grid spacing is reduced from

$\Delta x_{\min} = 2.5 \times 10^{-4}$  to  $\Delta x_{\min} = 6.25 \times 10^{-5}$ . The results are shown at four instants in time ranging from  $tU/c = 0.0375$  to  $tU/c = 0.051$ . The two finest grids yield virtually identical results up to  $0.048 < tU/c < 0.051$ , just prior to the onset of the third occurrence of a secondary separation bubble (SS3). As previously observed at  $Re = 200,000$ , the accuracy of the numerical solutions is subject to a form of sensitivity to initial conditions; given enough time, two solutions will always diverge from one another, regardless of the resolution used. This is more clearly illustrated in Fig. D.3, where the evolution of the skin friction "error" is shown as a function of time. The skin friction "error" is defined as the L-1 norm of the difference between a given skin friction distribution and the "converged" skin friction distribution at some fixed instant in time. The "converged"  $C_f$  distribution is taken to correspond to the highest grid resolution case, which is characterized by  $\Delta x_{\min}/c = 6.25 \times 10^{-5}$ . This is, of course, an imperfect assumption but nothing substantially better can be done. It is important to realize that the type of grid convergence study considered here is *local*, not only spatially but temporally. The spatial and temporal "regions" where the solution is determined to be accurate are the factors used in the choice of an appropriate computational mesh. Because the  $666 \times 91$  mesh gave grid-independent results up to and beyond to point of vortex formation, it was considered adequate for the present purpose, i.e.: to obtain grid-independent results for incipient leading edge separation at  $Re = 800,000$ .

For completeness, the scaling of the skin friction error as a function of circumferential grid spacing is indicated for various times in Fig. D.4. The purpose of such plots is to determine the effective order of accuracy and degree of convergence of the method. The characteristic slopes associated with formal first, second, third, and fourth-order accuracy are also indicated (dashed lines) for reference. At small times, the scaling of error indicates an effective order of accuracy which lies between third-order and fourth-order. Similar results were obtained for the normal grid spacing study of Ref. D1 (Fig. 4, Appendix B) at  $Re = 200,000$ . This result is expected because initially the process is essentially a boundary layer process (i.e., viscous-dominated), and the viscous fluxes in the code are computed with fourth-order accuracy. In general, however, lower than fourth-order accuracy is expected because the formal accuracy of the differencing scheme degrades as one approaches the boundary. The effective order of accuracy on the skin friction remains about third-order up to  $tU/c = 0.0435$ , which will be shown to be beyond the time of primary vortex formation. By  $tU/c = 0.051$ , the accuracy degrades to first order. This is, again, an indication that the results should be interpreted with caution for  $tU/c > 0.048$ .

Artificial Dissipation. At the high laminar Reynolds numbers considered here, a possible concern is the extent to which artificial dissipation alters the effective viscosity of the flow. Therefore, the ratio between the added flux due to artificial dissipation,  $\Psi_{AD}$ , and the total viscous flux,  $\Psi_{\mu}$  (corresponding to the "natural" viscosity), was computed at every point within the region of interest. The result for  $Re = 800,000$  is shown in contour form in Fig. D.5, at a time  $tU/c = 0.06$ . Typically, the ratio  $\Psi_{AD}/\Psi_{\mu}$  is closely tied (a) to the high-wavenumber content of the solution, and (b) to the grid spacing. It will be shown that, at  $tU/c = 0.06$ , multiple fully-formed vortices are present in the solution and that the surface flow topology is complex, involving at least four distinct regions of secondary flow separation and two regions of tertiary separation. Also, the reattachment occurs around  $x/c = 0.025$ . Therefore the "active" vortical region of the flow extends roughly between 1.0% chord and 2.5% chord, and extends less than 0.5% in the direction normal to the surface. In this region, the dissipation flux ratio,  $\Psi_{AD}/\Psi_{\mu}$ , is seen to be less than 0.01%. The results discussed above are representative of the overall study. Similar tests were conducted at all



of the Reynolds numbers considered here ( $50,000 \leq Re \leq 800,000$ ). In none of these tests did  $\Psi_{AD}/\Psi_{\mu}$  ever exceed 0.1% over the region of interest. Thus, there is a good degree of confidence that the effective Reynolds number is indeed 800,000 for the results presented in this section.

**Flowfield Description at  $Re = 800,000$ .** A time sequence of the developing vorticity field is shown in Fig. D.6. At the very early stages ( $tU/c < 0.007$ ), a Stokes layer forms after imposing the no-slip boundary condition. The strong adverse pressure gradient eventually causes the low momentum fluid near the wall to change directions. The formation of a primary recirculation region (designated "PS1") is initiated around  $tU/c = 0.016$ , at a location indicated in Fig. D.6(b). This is followed by a period of spatial development of a thin recirculation bubble near the surface, the beginning and end of which are designated by the symbol "PS1" in Figs. D.6(c), D.6(d), and D.6(e). The bubble is initially roughly symmetric in shape about the location of maximum normal displacement, but eventually becomes lopsided as vorticity accumulates in the reattachment region. This is visible, for instance, at  $tU/c = 0.0375$  (end of Stage I).

The evolution of the flowfield is fairly rapid after this point. Similarly to the Reynolds number cases previously analyzed, a primary vortex forms in the downstream region of the primary recirculation zone. This vortex, in turn, induces at the wall a region of secondary flow separation. The extent of this secondary separation is indicated by the symbols "SS1" in Figs. D.6(f) through D.6(i). As time progresses, multiple vortices are formed as a result of induction and of shear layer instability and roll-up. Two vortices are present at  $tU/c = 0.045$ , three vortices at  $tU/c = 0.0525$ , four vortices at  $tU/c = 0.06$ , and five vortices at  $tU/c = 0.0675$ . As in the case of the primary vortex, the successive shear layer vortices induce new secondary separation regions. These multiple secondary recirculation zones eventually strengthen to the point that they too become vortices. These secondary vortices may induce tertiary separation. Using the same notation as in Appendix B, the successive regions of secondary flow are denoted SS1, SS2, SS3, etc., based on their order of appearance. A similar convention is used for regions of tertiary flow separation, TS1, TS2, and so on. Note that, for clarity, contours of negative vorticity are omitted from Fig. D.6.

Overall, the flowfield evolution at  $Re = 800,000$ , as depicted in Figs. D.6(a) through D.6(h), bears strong qualitative similarity with previously observed results at lower Reynolds numbers. For  $tU/c \leq 0.06$ , the main differences, aside from the usual spatial and temporal scales involved, are the complexity of the flowfield and in particular the number of successive shear layer vortices present in the solution at one time. For  $tU/c > 0.06$ , several qualitative differences were observed, as compared to the results of lower Reynolds numbers. At  $Re = 400,000$ , some differences were already observed, notably: the existence of *multiple* vortex-induced eruptions (Appendix C). However, these differences with respect to the behavior at lower Reynolds numbers occurred after the rupture of the primary feeding sheet. At  $Re = 800,000$  further differences are observed; these are described below.

The detailed events taking place between  $tU/c = 0.0675$  (Fig. D.6(i)) and  $tU/c = 0.075$  (Fig. D.6(j)) are depicted in Fig. D.7, using a smaller time increment between frames. Based on the experience gained at the lower Reynolds numbers, the appearance of the vorticity contours in Fig. D.6(i) suggests the most tenuous link in the vorticity feeding sheet to be between the second and third vortices, rather than upstream of the primary vortex. Instead, a rapid redistribution of the vorticity takes place between the two vortices, with much of the vorticity of the second vortex flowing into the primary vortex. Simultaneously, the

secondary and tertiary flow induced by the primary vortex begin to lift away from the surface, "pinching off" what had begun to look like the merging of the first and second primary vortices. This is clearly visible at  $tU/c = 0.069$  and  $tU/c = 0.0698$  in Fig. D.7. This "pinching off" halts the merging process, eventually reversing it (i.e., splitting the primary structure) at  $tU/c = 0.0705$ . This is, of course, a form of the vortex-induced eruptions previously observed at  $Re = 100,000$ ,  $Re = 200,000$ , and  $Re = 400,000$ . There is, however, a key difference: at  $Re = 800,000$  this eruption occurs underneath a vortex, primarily, rather than between two vortices.

For  $tU/c \geq 0.071$ , the primary vortex structure is no longer connected to its feeding sheet and begins to convect downstream. Meanwhile, the split upstream portion of the merged structure (referred to as "Vortex 2," for convenience) is engulfed into the third vortex. Thus, although a vortex-induced eruption is also observed at  $Re = 800,000$ , many of the details of the interactions surrounding this event differ from the lower Reynolds number cases. In particular, the key event is the vorticity eruption itself, rather than the rupture of the feeding sheet. For  $50,000 \leq Re \leq 400,000$  these events invariably coincided. In contrast, at  $Re = 800,000$ , a rupture of the vortex sheet between vortices does not occur. Instead, vorticity eruption takes place, and is sufficiently powerful to split the primary structure in two. For consistency with the terminology previously used in this work, the event taking place at  $tU/c = 0.0705$  (Fig. D.7(c)) will be referred to as the point of "rupture," in spite of the fact that its significance is somewhat different than at lower Reynolds numbers. The results of Fig. D.7 support previous conjectures that the vortex sheet rupture observed in other calculations is indeed *triggered* by the eruptive plume of vorticity.

*Dependence of Skin Friction on Reynolds Number.* Figures D.8 through D.12 depict the space-time evolution of the skin friction at  $Re = 50,000$ ,  $Re = 100,000$ ,  $Re = 200,000$ ,  $Re = 400,000$ , and  $Re = 800,000$ . Figures D.8 through D.12 characterize the instantaneous surface flow topology, which typically correlates well with the key features of the overall topological structure of the flow. Results on the pressure are presented in a subsequent section of this Appendix.

The qualitative similarity between the surface flow topologies at the different Reynolds numbers can be seen. As in Fig. D.6, the flow is always characterized initially by the formation and development of a primary separation bubble. A vortex subsequently forms in the downstream region of the bubble, inducing strong negative velocities (large negative skin friction) and the formation of a secondary separation bubble. This scenario is very much a recursive one: in time, a secondary vortex forms in the "downstream" region (upstream with respect to the main flow) of the secondary bubble, inducing strong positive velocities (large positive skin friction) and, possibly, the formation of a tertiary separation bubble. The presence of successive multiple vortices in the shear layer is clearly identified at the surface by their induced secondary separation regions, i.e., the number of regions of positive skin friction at any given  $x/c$ . As previously discussed, the number of formed shear layer vortices is seen to increase with Reynolds number.

Comparing Figs. D.8 through D.12, the solution that was carried out the farthest in time, relative to flowfield development, is at  $Re = 400,000$ . There, as well as at  $Re = 200,000$ , a break-away point exists (the rupturing event) after which the primary vortex and subsequent shear layer vortices start convecting downstream at a more rapid pace. This is indicated by the change in slope of the contours on the  $x$ - $t$  diagrams. In Fig. D.11, a pairing can be identified by the cross-over of negative skin friction regions (around  $tU/c = 0.05$  and

$x/c = 0.095$ ). This corresponds to the event depicted in Fig. C.13 of Appendix C. At  $Re = 800,000$  (Fig. D.12), the large negative skin friction region associated with the primary vortex appears to suddenly end at  $tU/c = 0.073$  and  $x/c = 0.025$ , instead of convecting downstream, as in the lower Reynolds number cases. This behavior is the surface signature of the event depicted in Fig. D.7(f), namely the ejection of vorticity and the lifting-away of the primary vortex structure. Although such lift-away is also noticed at  $Re = 400,000$  (Fig. D.11), it does not occur before the shedding of the primary vortex. Thus, the behavior of the flowfield at  $Re = 800,000$  does fundamentally and qualitatively differ from the behavior observed for  $Re \leq 400,000$ . However, these qualitative differences all pertain to the later stages of the incipient stall process namely, after the formation of the primary stall vortex. We may speculate that, as the Reynolds number is increased further, the complex vortex system will stay increasingly confined to the leading edge region before the eruption occurs. This is in contrast to the behavior observed for  $Re \leq 400,000$ , in which the vortex system was found to convect first, before breaking away from the surface.

The space-time skin friction diagrams of Figs. D.8-D.12 can be simplified to some extent by considering only the zero contours, corresponding to a sign reversal of the skin friction. In this manner, the lines delimit adjacent regions of forward and reverse flow at the surface. This permits the identification of primary, secondary and, if applicable, tertiary separation regions. The resulting surface flow topology diagrams are compared in Fig. D.13 for all five Reynolds numbers investigated in this study. The symbols "PS," "SS," and "TS" refer to primary separation, secondary separation, and tertiary separation, respectively. The numeral that follows each of these symbols indicates the temporal order of appearance, so that for example, "SS2" designates the second occurrence in time of a secondary separation region, etc. The surface flow topologies at the various Reynolds numbers are seen to differ in scale, both spatially and temporally. There is also a difference between  $Re = 800,000$  and the  $Re \leq 400,000$  cases: at lower Reynolds number cases are characterized by a bulk motion of the leading edge vortex system, corresponding to convection; in contrast, the surface flow patterns at  $Re = 800,000$  exhibit less bulk downstream motion, and more of a "break," as seen in Fig. D.12. Apart from these differences, the important point of Fig. D.13 is the remarkable degree of similarity, including many of the details, between surface flow topologies across the Reynolds number range. In light of the newest results at  $Re = 800,000$ , the qualitative similarity noted in Ref. D1 is found to hold, except after the point of vorticity eruption. This is, again, because the vortex-induced eruption at high Reynolds number does no longer coincide with the rupture of the vorticity feeding sheet as in Appendix B.

*Dependence of Pressure Coefficient on Reynolds Number.* The space-time evolution of the pressure field at the surface is documented in Figs. D.14 through D.18. Close examination of the pressure coefficient contours reveals many of the same conclusions drawn from the skin friction. Low pressure areas associated with the presence of vortices and high-pressure ridges associated with flow impingement immediately downstream of these vortices are noticeable features of the flow at all Reynolds numbers. The relief of the low pressure region downstream of the leading edge, as the boundary layer and separation bubble form, is also apparent.

By taking successive "horizontal cuts" of Figs. D.14-D.18, one obtains a more quantitative description of the pressure distribution and its temporal evolution. The resulting  $C_p$  distributions are shown in Figs. D.19-D.23. To further illustrate the qualitative similarity of the flowfields, the total time period shown in each figure corresponds to 6.4% beyond the time of rupture. For each Reynolds number this period is divided equally into

17 time increments. In the first frame of each figure, the decrease of the peak suction and the relief of the pressure gradient downstream of the leading edge are apparent. The development of the primary separation bubble is associated with a lowering of the pressure in the downstream part, followed by a relative increase in the pressure due to the stagnation point. The associated adverse pressure gradient is subsequently characterized by a sharp steepening during and after the period of formation of the primary stall vortex. This stage typically corresponds to the second frame in each figure. Finally (third frame), multiple primary and secondary vortices form, greatly complicating the interpretation of the surface pressure signature. Eventually, eruption occurs (corresponding to the time-trace before last), and the vortex system starts convecting (last trace in each figure). Again, the qualitative similarity between Reynolds numbers is observed.

We conclude this section with the calculation of the streamwise pressure gradient. For dynamic stall, the pressure gradient is by far<sup>D3</sup> the largest contributor to the production of vorticity at the wall. In the absence of blowing/suction or surface acceleration, the pressure gradient is directly proportional to the diffusive normal vorticity flux at the surface.<sup>D4</sup> It is useful, therefore, to attempt to obtain insights into the vorticity production process from inferences based on the pressure gradient. This approach was used, e.g., by Acharya and Metwally (Ref. D5) to show the existence of a "spike" in vorticity flux near the leading edge of a pitching airfoil at  $88,000 \leq Re \leq 120,000$ . For convenience, the streamwise derivative of the  $C_p$  distribution,  $\partial C_p / \partial x$ , was directly computed, rather than the true tangential derivative,  $\partial C_p / \partial s$ . For the present purpose, this makes no difference, since the same airfoil at the same angle of attack is used at all Reynolds numbers. The result is shown in Figs. D.24-D.28. The complicated spatio-temporal patterns which follow the evolution of the vortices are the most noticeable feature, but are of little interest in terms of discerning the origin of vortex formation, at least in the sense argued in Ref. D2.

The results obtained in the present study do not support the interpretation that the sudden appearance of an initial eruptive plume of vorticity (which would presumably be associated with a spike in vorticity flux) is responsible for the formation of the dynamic stall vortex. Instead, the present problem is characterized by the continuous presence of a strong vorticity flux near the leading edge. This vorticity flux is indeed the source of the vorticity feeding sheet. With time, this vorticity sheet lifts from the surface, creating a thin separation bubble, and eventually leads to the formation of the primary stall vortex. In this process, no qualitative differences were found across the investigated Reynolds number range. A consistent behavior for all Reynolds numbers is the initial decrease in the magnitude of the vorticity flux (Figs. D.24-D.28). This initial decrease is associated with the formation of the viscous boundary layer, which changes the effective shape of the airfoil and, thus, relieves the pressure gradient. This is fundamentally different from the occurrence in time of a spike in the vorticity flux, and may be an artifact of the present model problem. We note, however, that for Reynolds numbers exceeding 100,000 (Figs. D.25-D.28), the leading edge vorticity flux eventually increases again. Whether this has any connection with the formation of a spike (in the sense of Ref. D2) is, at best, speculative at this time. In any event, such strengthening takes place (for the present problem) after the formation of the dynamic stall vortex, which is more closely connected to the initial flux after the imposition of the no-slip boundary condition.

Incipient Vortex Formation. The manner in which the point of vortex formation is determined was alluded to in Appendix B. The present section attempts to clarify the methods used to determine both incipient vortex formation and the relation between the

topological "center" and a vortex, based on the results at  $Re = 800,000$ . "Vortex formation" can be defined as the transition between an elongated recirculation bubble (characterized primarily by counter-flowing streams separated by a thin shear layer) and a "fully-formed" vortex structure (characterized by significant momentum transfer normal to the wall and the existence of a low-pressure core).

In an attempt to quantitatively define the point of vortex formation, consider the temporal evolution of the pressure, Fig. D.29. At short times, the pressure field closely resembles the potential flow pressure field, with the exception of a small region of zero normal pressure gradient near the wall (the boundary layer). This can be seen, for example, in Fig. D.29(a). At  $tU/c \geq 0.03$  the pressure gradually lowers for  $x/c < 0.02$  while simultaneously increasing downstream of that point (see also Fig. D.23). Around a time  $tU/c = 0.037$ , the topology of the pressure field undergoes a transformation, namely the existence of pressure extrema away from the airfoil surface. The closed contours of minimum pressure coincide with the core of the nascent vortex. At that point, the evolution of the flowfield is very nonlinear: the low pressure core contributes to the further accumulation of vorticity in the vortex. The increased vorticity in turn increases the radial pressure gradient, and so on, until the vortex is fully formed. By  $tU/c = 0.045$  (Fig. D.29(g)), a second shear layer vortex has also formed, as indicated by the presence of low pressure cores. In the following, the transition of the pressure field from a boundary-layer-like behavior (i.e.,  $\partial p / \partial y = 0$ ) to one characterized by the existence of closed low-pressure contours away from the surface is defined as the point of vortex formation (in this case:  $t_{VF}U/c = 0.037$ ).

An important element is to establish the origin of the vortex, before it forms. To this end, and following the methodology used in Refs. D6 and D1, we use Perry and Chong's<sup>D7</sup> critical point theory. Knight and Choudhuri (Ref. D6) have shown how critical point theory can be used as a sensitive means to analyze the topology of the velocity field. In particular, these authors were able to pinpoint the origin of the dynamic stall vortex for a pitching airfoil at  $Re = 10,000$ . Using similar concepts, it can be shown that the critical points are "centers," characterized by essentially zero dilation,  $D \equiv \partial u / \partial x + \partial v / \partial y$ , and positive Jacobian,  $J \equiv (\partial u / \partial x)(\partial v / \partial y) - (\partial u / \partial y)(\partial v / \partial x)$ . Fig. D.30 exemplifies the method used to determine the location of the topological center. In this example ( $Re = 400,000$ ,  $tU/c = 0.03$ ), there is no vortex. The inset in Fig. D.30 shows the actual aspect ratio of the developed recirculation bubble. The grey contours in Fig. D.30 (both inset and main figure) are low Mach number contours ( $M \leq 0.01$ ) which help demarcate both the surface flow and the shear layer. The main figure is obtained by rotating and stretching the coordinates, as indicated by the (x-y) reference arrows. Also present in the figure are instantaneous streamlines which delineate the location of the center.

Close examination of such pictures at successive instants in time reveals that the presence of a topological center emerges very shortly after the onset of surface flow reversal. Immediately after applying the no-slip condition, the Jacobian is zero at the surface, indicating a "pure shear" situation. After the onset of flow reversal, the value of the jacobian  $J$  nears zero ("degenerate center"), then rapidly becomes positive ("center"). For a fairly long period of time corresponding to the development of the recirculation bubble, the center moves downstream, within the primary bubble, but does not correspond to a vortex. The later stages of this evolution are exhibited, for example, in Fig. D.31, which shows both instantaneous pressure contours and streamtraces for the  $Re = 100,000$  case. As previously noted, the presence of a vortex is characterized by significant momentum transfer normal to

the wall and the existence of a low pressure core. In Fig. D.31, this occurs between  $tU/c = 0.054$  and  $tU/c = 0.06$ . In all of the cases examined, the topological center is clearly the precursor of the stall vortex. Its trajectory is indicated by the dark symbols in the surface topology plot of Fig. D.32. The behavior at  $Re = 800,000$  is, again, qualitatively similar to the behavior observed at lower Reynolds numbers, for instance: Fig. 8 of Appendix B, for  $Re = 100,000$ . In particular, until the point of vortex formation (marked "VF" in Fig. D.32), the topological center moves towards the two-thirds downstream location within the primary bubble. After that point, its trajectory correlates well with the downstream edge of the primary and induced secondary bubbles.

The connection between flowfield topology and vortex formation is further explored in Fig. D.33. In this figure, the initial temporal increase of the Jacobian value at the critical point is characteristic of the emergence of a center, as discussed in Appendix B. After the point of vortex formation the Jacobian increases further; however, this growth shows no sign of correlation with the onset of secondary flow features, as was suggested at  $Re = 100,000$  (Fig. 10, Appendix B). The dark symbols in Fig. D.33 show how vortex formation is characterized by a drop in core pressure. This feature was observed at all of the investigated Reynolds numbers.

The following is a summary of the topological evolution of the flow at  $Re = 800,000$ . For a fairly long portion of time during Stage I, ( $tU/c \leq 0.038$  in Fig. D.32), the vorticity field topology corresponds to a lifted vorticity layer beneath which a thin region of reverse flow exists. During this portion, the location of the topological center "rides" the vorticity line, gradually moving from front to back and settling at about two thirds of the bubble extent. In contrast to the rather benign behavior of the vorticity during that portion, the end of Stage I is marked by a sudden change from boundary layer-like behavior (negligible normal pressure gradient) to vortex-like behavior, characterized by the presence of closed pressure contours associated with a low pressure core (Fig. D.29). At later stages of the evolution of the flow, local pressure and vorticity fields act to reinforce each other. The vorticity accumulates further in the low pressure region, and the increased vorticity results in a further lowering of the pressure. This interaction results in a formed vortex and marks the beginning of what was referred to earlier as Stage II. At that point, vorticity and pressure fields are well-correlated.

*Reynolds Number Scaling.* To complete the Reynolds number scaling investigation initiated in Ref. D1, the data obtained at  $Re = 800,000$  was processed in a fashion similar to that described in Appendix B. Figure D.34 shows the scaling with respect to Reynolds number of the time instants corresponding to the onset of flow reversal (PS1), vortex formation, and shear layer "rupture." The previously obtained power-law curve fits for  $50,000 \leq Re \leq 400,000$  are indicated by the lines in Fig. D.34. The data at  $Re = 800,000$  establish a noticeable departure from previous power-law scalings. In particular, both vortex formation and rupture occur "late," relative to the expected scaling based on the lower Reynolds number data. Of course, "rupture" of the feeding vorticity sheet *per se* did not take place at  $Re = 800,000$ . Instead, the vortex-induced eruption ended-up splitting the merged primary vortex. This event is depicted in Fig. D.7 (frames (b) and (c)). It is not clear at this point whether the delay of the rupturing event at  $Re = 800,000$  can be accounted for by the altered definition of "rupture" alone. This is, in fact, unlikely, because of the coincidence of the feeding sheet rupture with vorticity eruption for  $Re \leq 400,000$ . One of the key differences at the higher Reynolds number is the presence of pairing/merging events



before shedding occurs. Additionally, even the point of vortex formation appears to be somewhat delayed at  $Re = 800,000$ . This issue is explored further below.

In an attempt to understand further the scaling properties of incipient dynamic stall with respect to Reynolds number, the boundary layer thickness was calculated. Its scaling is shown in Fig. D.35. The boundary layer thickness,  $\delta_{\Omega,LE}$ , was defined as follows. The temporal growth of the boundary layer (initially a Stokes layer) was monitored at the leading edge, and was recorded once it reached steady-state (typically for  $tU/c \leq 0.006$ ). For convenience,  $\delta_{\Omega,LE}$  was defined as the normal distance from the wall at which the vorticity is 10% of its value at the wall. Thus,  $\delta_{\Omega,LE}$  is not the vorticity thickness but, rather, a measure of boundary layer thickness based on the normal damping of the vorticity profile. For reference,  $\delta_{\Omega,LE}$  corresponds in the case of a Blasius boundary layer to  $\eta = y(U_{\infty}/\nu x)^{1/2} = 4.52$ , or 6.8 momentum thicknesses (" $U/U_{\infty}$ " = 0.98). The slope of the power-law curve fit (solid line in Fig. D.35) is approximately  $-1/2$ , as expected for a laminar boundary layer.

The Reynolds number scaling shown in Fig. D.34 can, thus, be re-examined using different length scales than the airfoil chord. Indeed, the chord  $c$  (including in the definition of the Reynolds number) is rather irrelevant to the processes involved in incipient leading edge stall. Three alternative length scales are considered:  $b$  (the leading edge radius of curvature),  $\delta_{\Omega,LE}$  (upstream boundary layer thickness), and the viscous penetration length,  $(\nu t)^{1/2}$ . The latter is a natural candidate for the initial stages of the flow development, which are essentially similar to those occurring in Stokes' first problem. The re-scaled times  $tU/b$ ,  $tU/\delta_{\Omega,LE}$ , and  $tU/(\nu t)^{1/2}$  are shown in Fig. D.36. The Reynolds number scaling of the various times of onset is, of course, not expected to change by using  $b$  as the length scale, since the airfoil is the same and since  $b$  does not change with Reynolds number. The bottom two frames of Fig. D.36 suggest the following observations: (1) temporal normalization using boundary layer ( $\delta_{\Omega,LE}/U$ ) or viscous ( $(\nu t)^{1/2}/U$ ) time scales does not collapse the data, and (2) the relative tardiness of the vortex formation time appears to be eliminated by using either ( $\delta_{\Omega,LE}/U$ ) or ( $(\nu t)^{1/2}/U$ ). Of note is the almost perfect fit of the primary separation time of onset, when non-dimensionalized using the viscous length scale (bottom frame). The results of Fig. D.36 indicate that none of the characteristic length scales considered here make any of the recorded events Reynolds number independent. Furthermore, no single scale can be expected to collapse all of the data. This points to the existence of a hierarchy of scales, a view somewhat consistent with Ref. D8.

Finally, using the additional candidate length scales ( $\delta_{\Omega,LE}$  and  $(\nu t)^{1/2}$ ), we re-examine the scaling of the times of onset of the primary and secondary recirculation bubbles, adding the  $Re = 800,000$  case to the data presented in Appendix B. This is given in Fig. D.37. Again, the data appear to scale according to simple power-laws of the Reynolds number. No single time scale collapses any of the measured variables. With the exception of the rupturing event at  $Re = 800,000$ , it may be concluded from the qualitative self-similarity exhibited in Figs. D.36 and D.37 that the present study does not support the hypothesis of a Reynolds number bifurcation under laminar flow conditions.

**Auxiliary Results.** For completeness, the temporal evolution of the overall force coefficients for lift, drag, and moment are included in this report (Figs. D.38-D.40). Note that the results in Figs. D.38-D.40 are presented for  $tU/c > 0$ . No attempt is made to interpret these results in connection with the leading edge dynamic stall phenomena described in Appendices B, C, and D. This is because  $C_L$ ,  $C_D$ , and  $C_m$  are, to a large extent, determined by conditions at

the trailing edge. Since the present geometry considers a rounded trailing edge, the unsteady Kutta condition allows for the rear stagnation point to move, both in time and with Reynolds number. The details of this region of the flow, although critical for lift and drag, are largely irrelevant in the context of the present study. A natural question is to ask whether the choice of an airfoil geometry was the correct one, considering the specific goals of the research. With the presently clustered computational grids (notably at  $Re = 400,000$  and  $800,000$ ), the cost of the computational grid points associated with the airfoil (O-grid) geometry accounts only for a fraction of the total computational cost. This fraction decreases with increasing Reynolds number. In addition, the use of an airfoil ensures that the proper pressure gradient is imposed, without having to experiment with approximate boundary conditions.

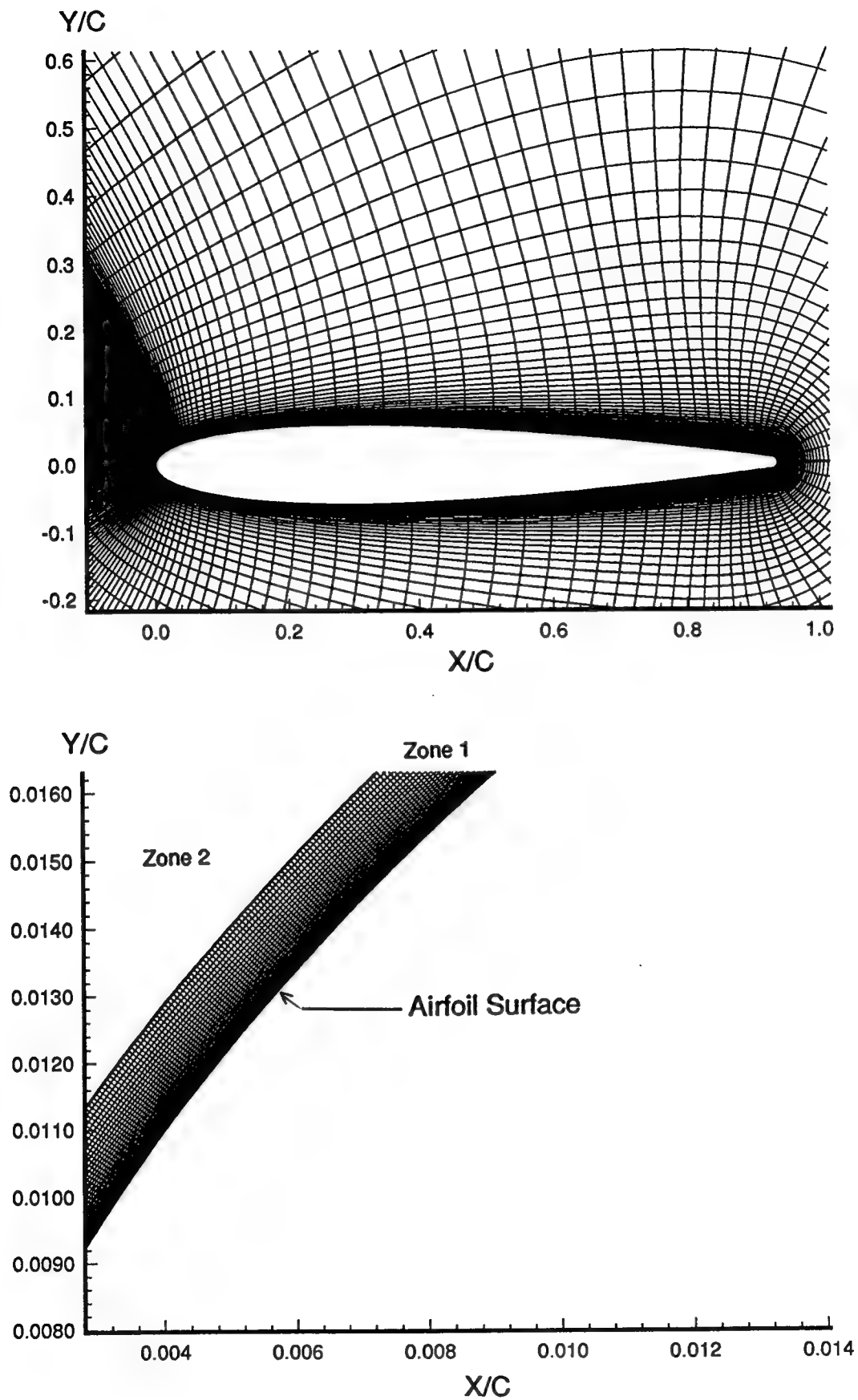
Finally, we conclude this appendix with the documentation of the temporal evolution of the vorticity fluxes at the leading edge. Although for different conditions ( $Re = 12,000$  pitching airfoil), Appendix A addressed the issue of predictability of the leading edge vorticity fluxes before and during the dynamic stall process, by means of a modified version of indicial theory. One of the important results was the conclusion that, although difficulties remained for predicting the fluxes directly, it appeared that a prediction of the vorticity accumulation based on indicial theoretical concepts is possible. For nonlinear motions ( $\Delta\alpha \sim 5^\circ$ ), this prediction is a relative one, permitting accurate prediction of one airfoil maneuver from the knowledge of another. The potential applications of these findings were never fully exploited in the course of the present study, in part because of changes in A.R.O. research priorities part-way through the research. In an attempt to begin bridging this gap, the last three figures document the evolution of the integrated tangential and normal fluxes of vorticity in the present semi-impulsive problem at  $Re = 800,000$ .

Figure D.41 depicts the temporal evolution of the normally-integrated tangential vorticity flux,  $\Phi_t$ , at  $0.0032 \leq x/c \leq 0.0282$ . At all locations, the flux is strongly dominated by the initial conditions of the present problem; notably, all fluxes initially decrease until the point of vortex formation. Figure D.42 documents the temporal evolution of the normal flux of vorticity,  $\Phi_n$ , tangentially integrated between  $x/c = 0.0$  and  $x/c = 0.03$ . The normal flux is shown at two locations: at the wall (solid line) and at 0.03% chord away from the wall. As in the case of  $\Phi_t$ , the behavior of the normal flux at the wall is initially dominated by its relaxation from the initial conditions. The temporal growth of the boundary layer can also be correlated to the initial increase ( $0 \leq tU/c \leq 0.006$ ) in  $\Phi_n$  away from the wall. This flux peaks and subsequently decreases just prior to the point of vortex formation ("VF"). Figure D.43 shows the evolution of the vorticity accumulation in the first 3% of chord. Also indicated for reference are the times of onset corresponding to primary separation (PS1), vortex formation (VF), secondary separation (SS1, SS2, SS3, SS4), and rupture (R). After its initial decrease, it is noteworthy that the vorticity accumulation begins to increase around  $tU/c = 0.03$ , which happens to coincide with the simultaneous strengthening of the topological center and the reduction in core pressure, as shown in Fig. D.33. More complete analyses of pitching/oscillating airfoil data need to be performed before one can establish a correlation between vorticity accumulation and incipient vortex formation. Should such a correlation exist, then the results of Appendix A imply that a semi-analytical prediction of dynamic stall is possible.



## References

- D1. Reisenthel, P.H. and Childs, R.E.: "A Study of Reynolds Number Effects on Incipient Leading Edge Stall," AIAA Paper No. 94-2339, 1994.
- D2. Doligalski, T.L., Smith, C.R., and Walker, J.D.A.: "Vortex Interactions With Walls," *Ann. Rev. Fluid Mech.*, Vol. 26, 1994, pp. 573-616.
- D3. Helin, H.E.: "The Relevance of Unsteady Aerodynamics for Highly Maneuverable and Agile Aircraft," in Symposium on Numerical and Physical Aspects of Aerodynamic Flows, Long Beach, CA Jan 16-19, 1989.
- D4. Reynolds, W.C. and Carr, L.W.: Review of Unsteady, Driven, Separated Flows, AIAA Paper 85-0527.
- D5. Acharya, M. and Metwally, M.H., 1992: "Unsteady Pressure Field and Vorticity Production Over a Pitching Airfoil," *AIAA J.*, Vol. 30, No. 2, 1992, pp. 403-411.
- D6. Knight, D.R. and Choudhuri, P.G.: "2-D Unsteady Leading Edge Separation On a Pitching Airfoil," AIAA Paper 93-2977, 1993.
- D7. Perry, A.E. and Chong, M.S.: "A Description of Eddying Motions and Flow Patterns Using Critical-Point Concepts," *Ann. Rev. Fluid Mech.*, Vol. 19, 1987, pp. 125-155.
- D8. Rothmayer, A. and Bhaskaran, R.: "Theoretical Aspects of Stability and Transition in High Reynolds Number Dynamic Stall," AIAA Paper No. 94-2336, 1994.



**Fig. D.1** Example of Two-Zone 666×91 Computational O-Mesh used at  $Re = 800,000$ . Top: Complete Mesh Illustrating Grid Clustering in the Leading Edge Region of the Airfoil. Bottom: Detail of the Inner Grid (Zone 1) in the Leading Edge Region.

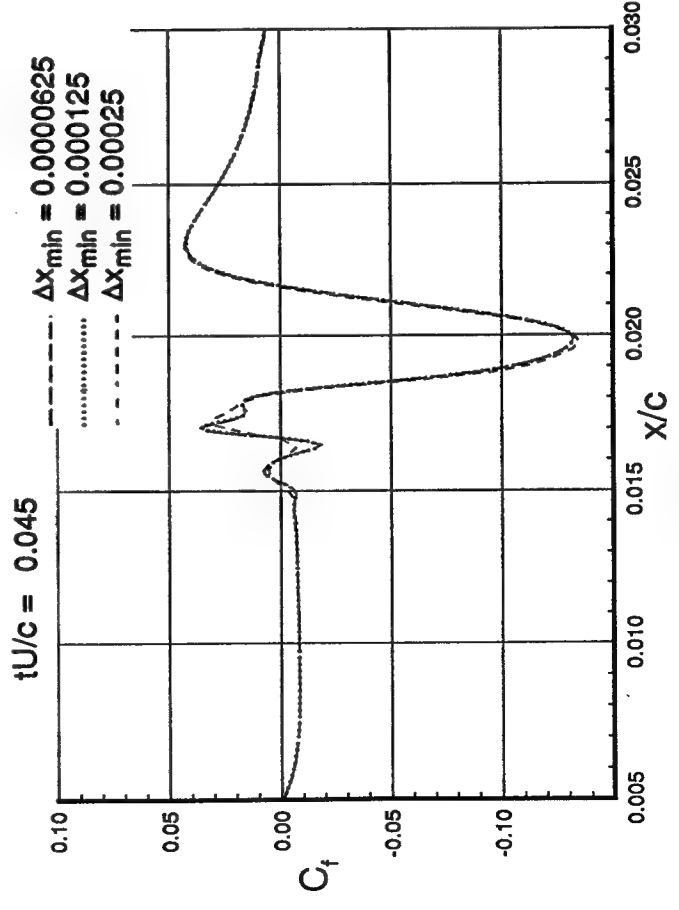
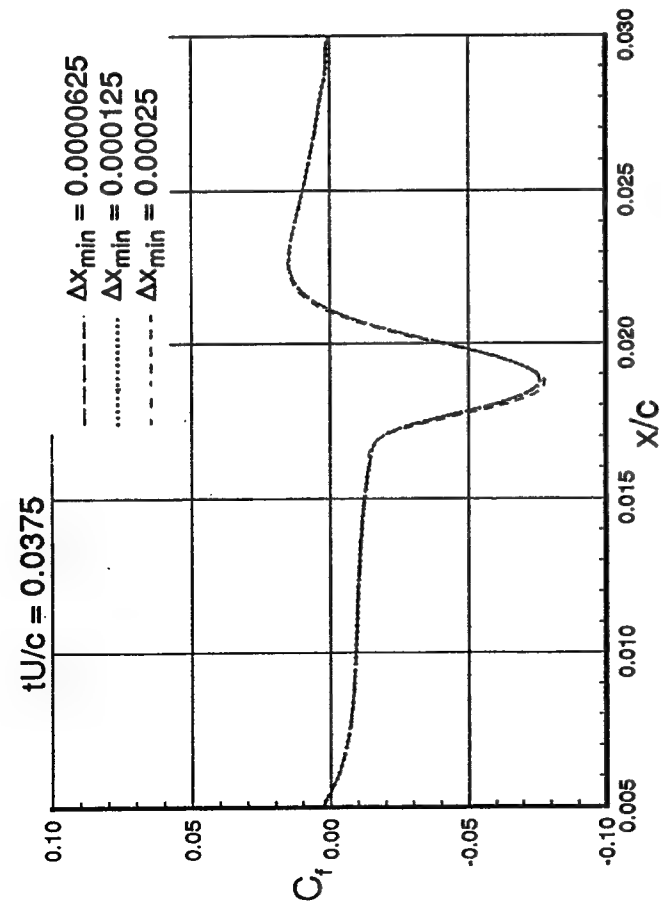
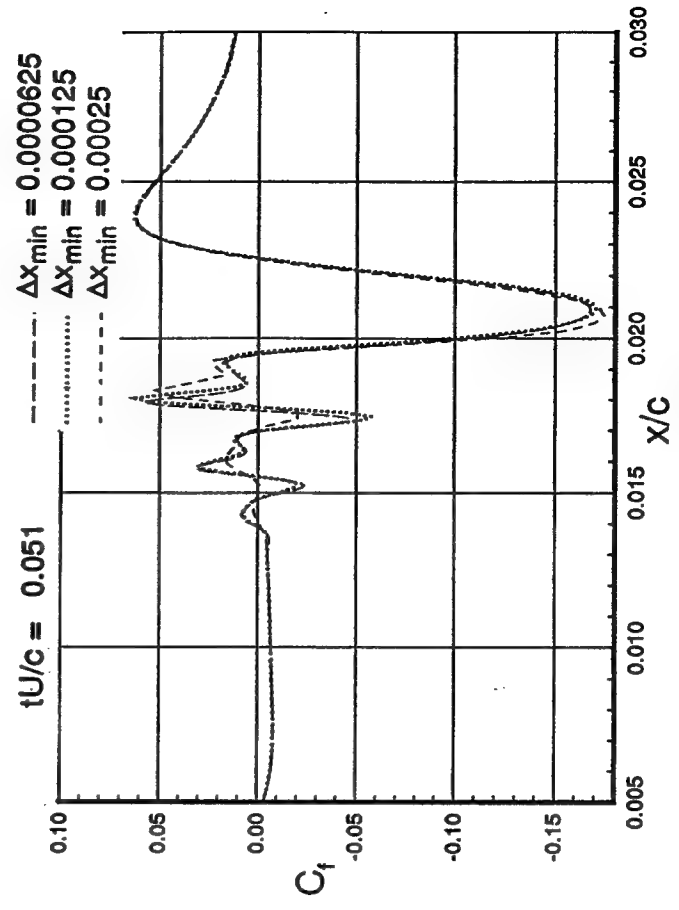
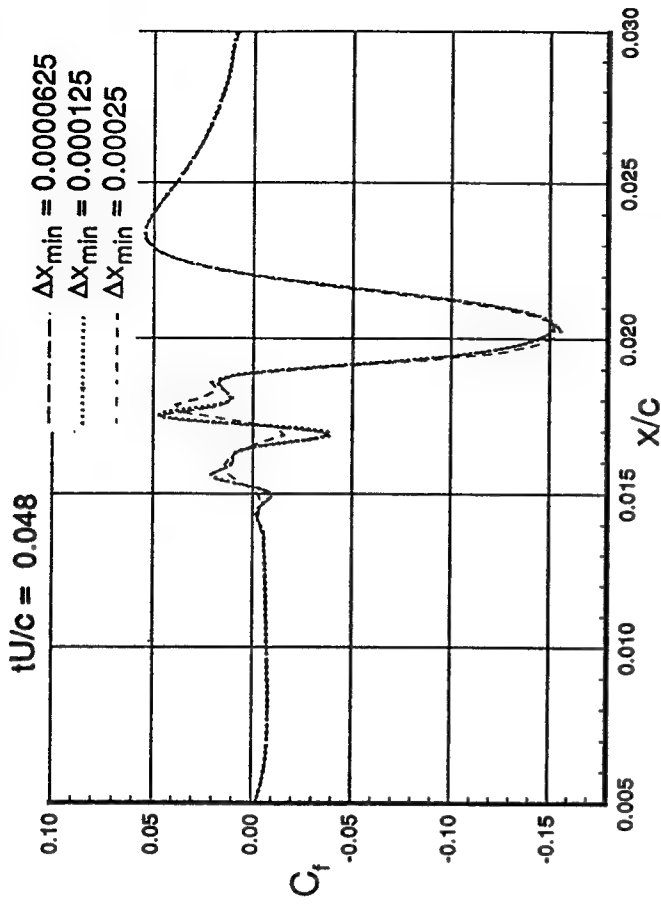


Fig. D.2 Circumferential Grid Spacing Sensitivity of the Instantaneous Skin Friction Distribution at Four Instants in Time ( $Re = 800,000$ ).

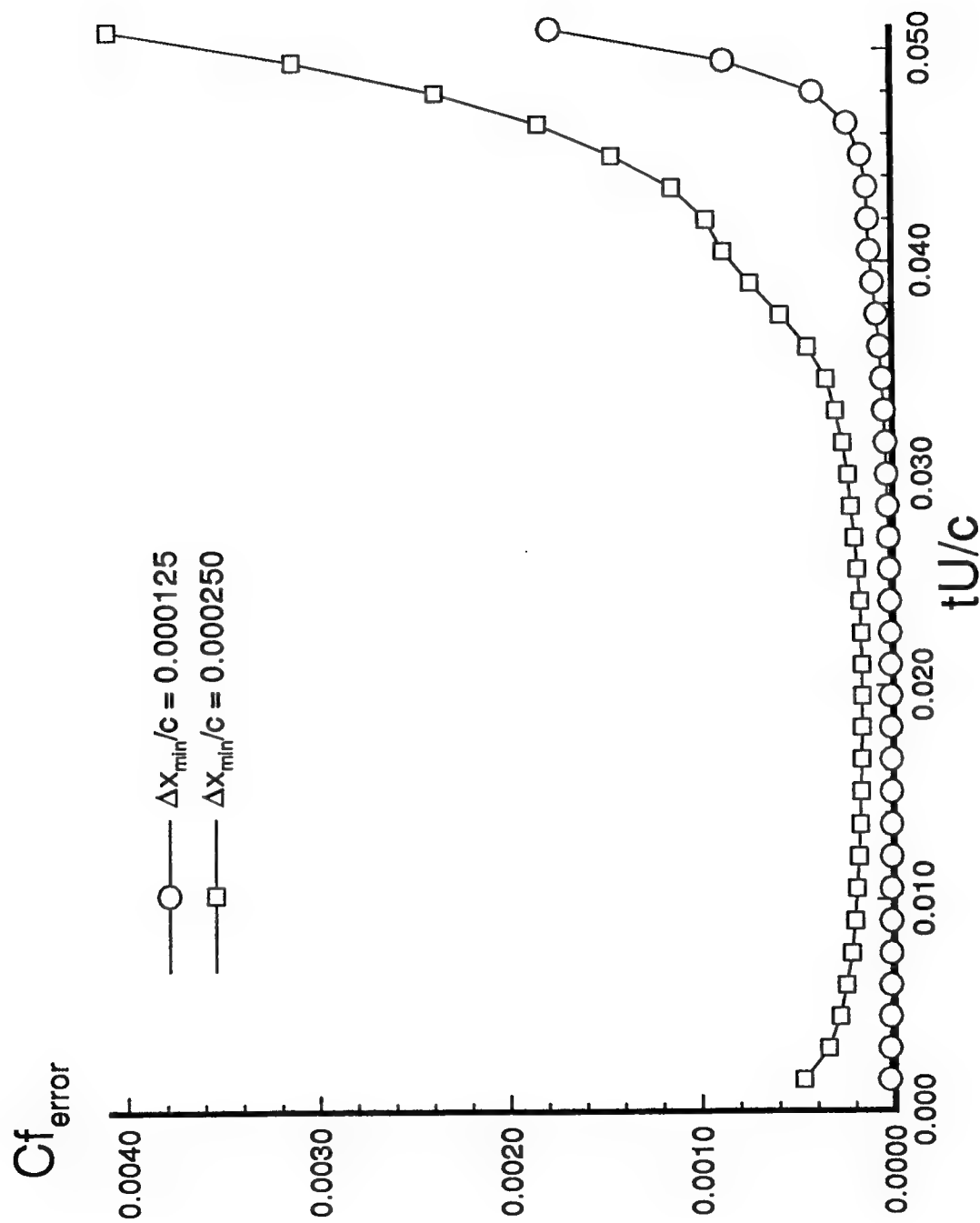


Fig. D.3 Temporal Evolution of Skin Friction Error With Respect to Finest Grid Solution (Re = 800,000).

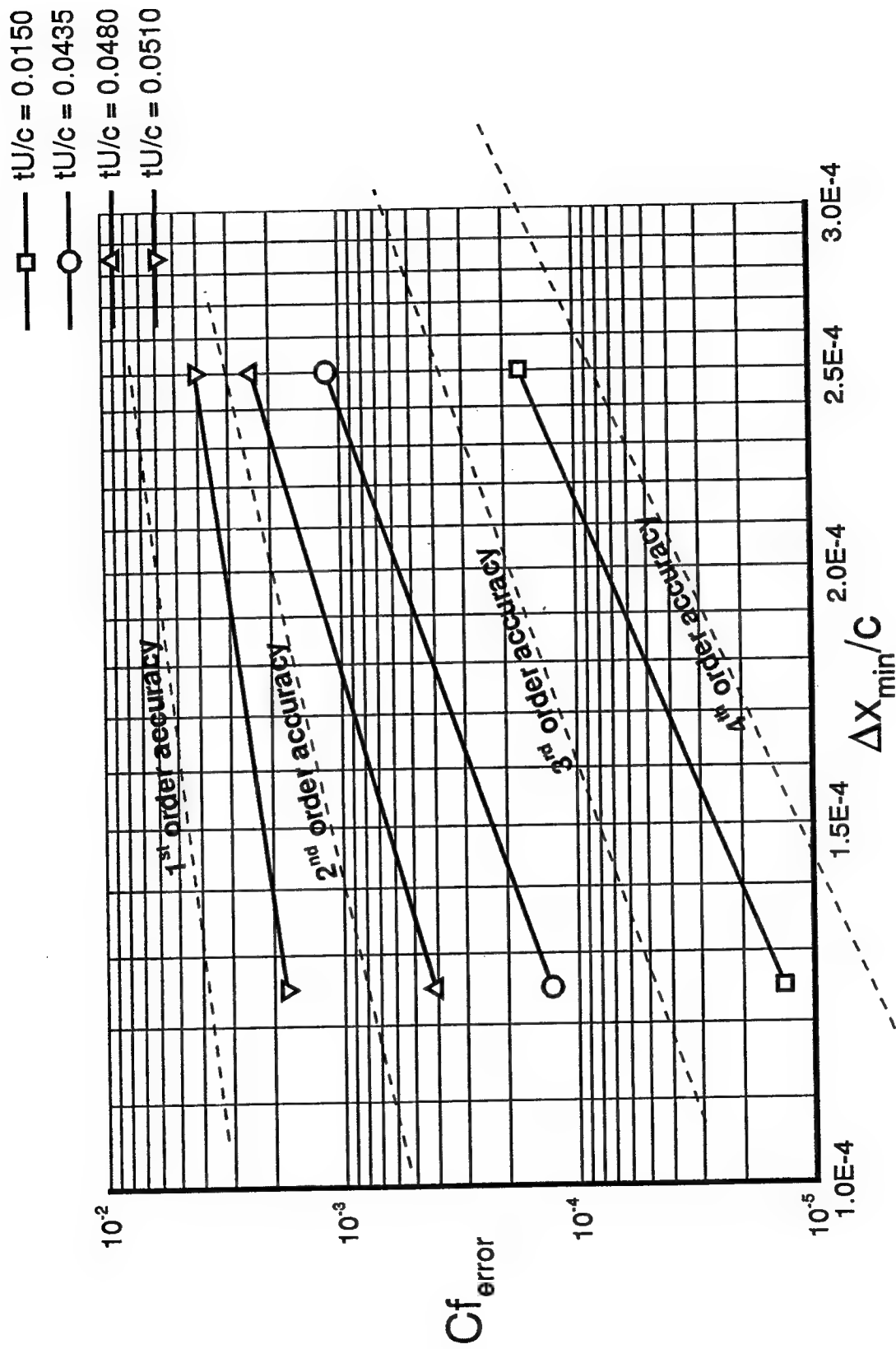


Fig. D.4 Scaling of Skin Friction Error as a Function of Circumferential Grid Spacing at Four Instants in Time ( $Re = 800,000$ ). (Dashed lines indicate slopes associated with formal first, second, third, and fourth order accuracy).

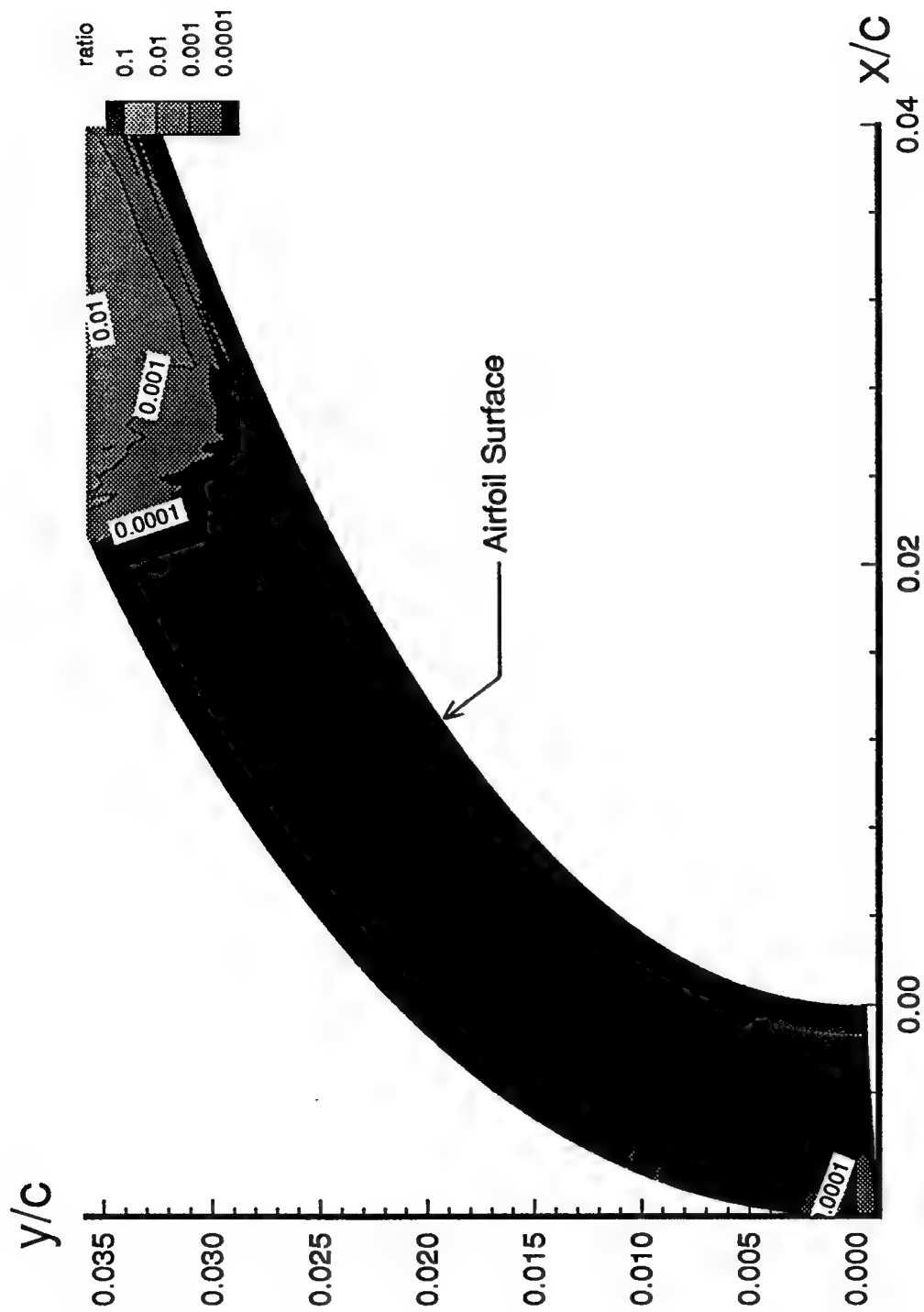


Fig. D.5 Contour Plot Indicating the Relative Magnitude of Artificial Dissipation Terms and Viscous Flux Terms in the Discretized Equations of Motion at  $tU/c = 0.06$ ,  $Re = 800,000$ .

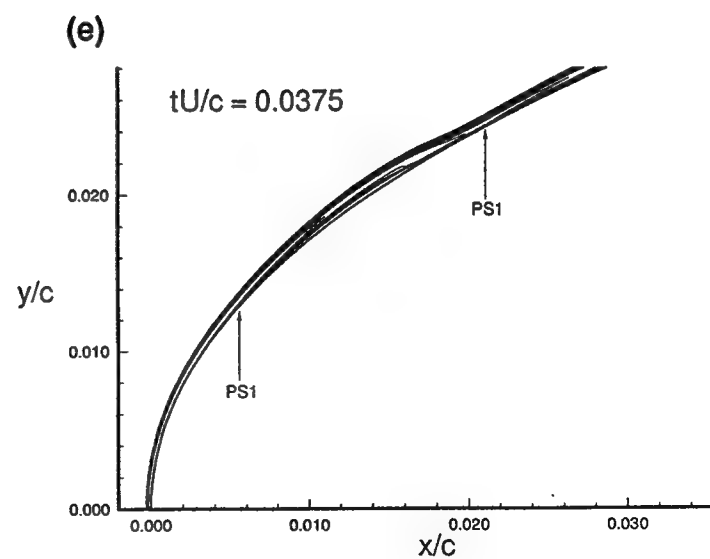
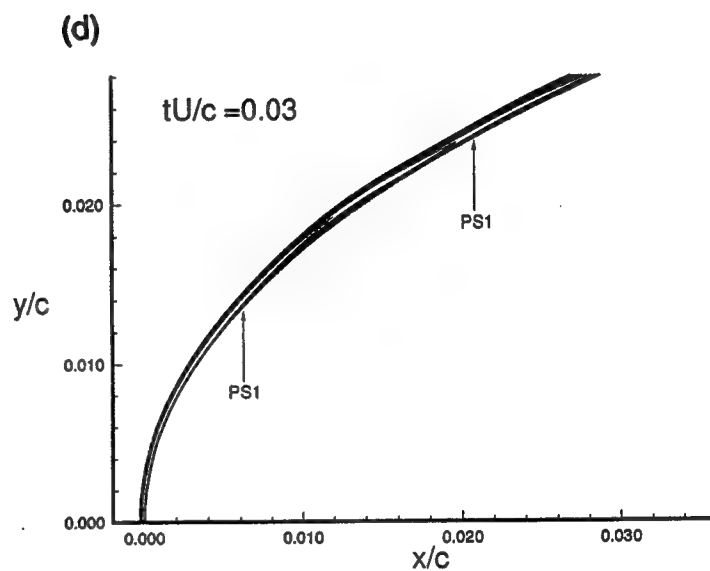
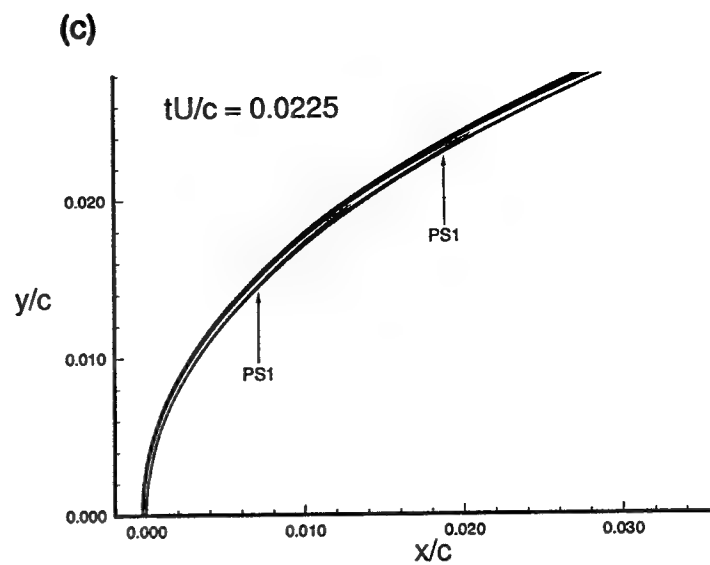
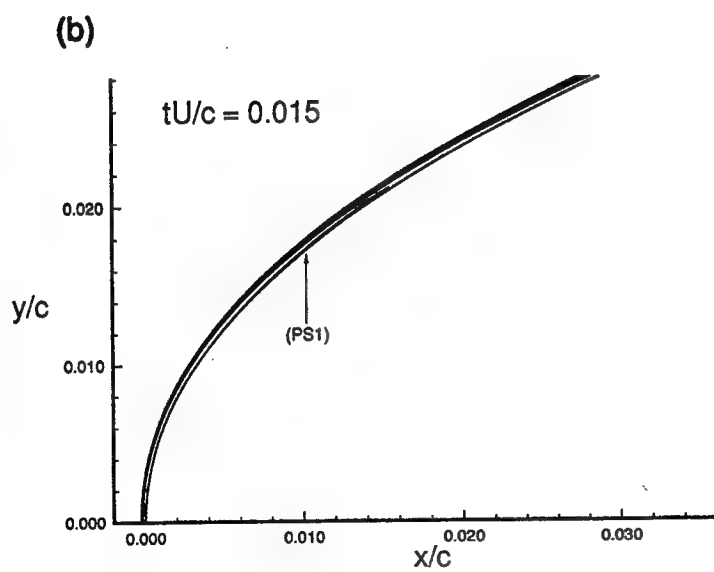
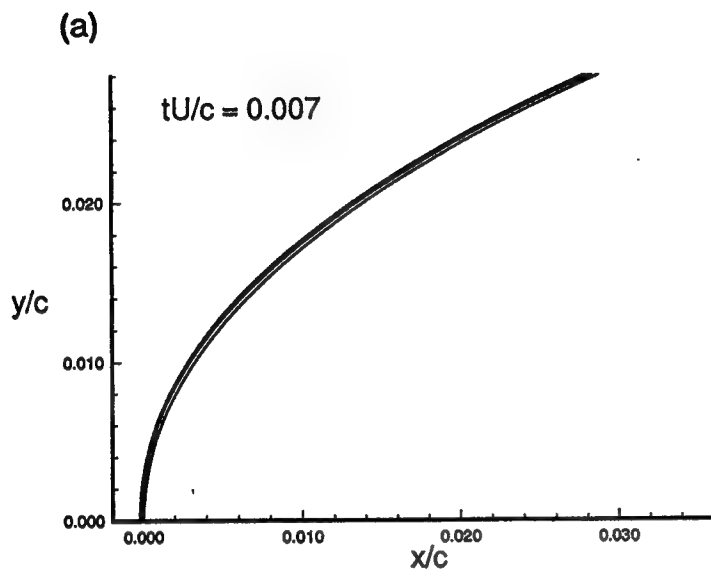


Fig. D.6 Temporal Evolution of the Vorticity Field at  $Re = 800,000$ . (Arrows indicate locations of skin friction sign reversal). (Continued on next page).

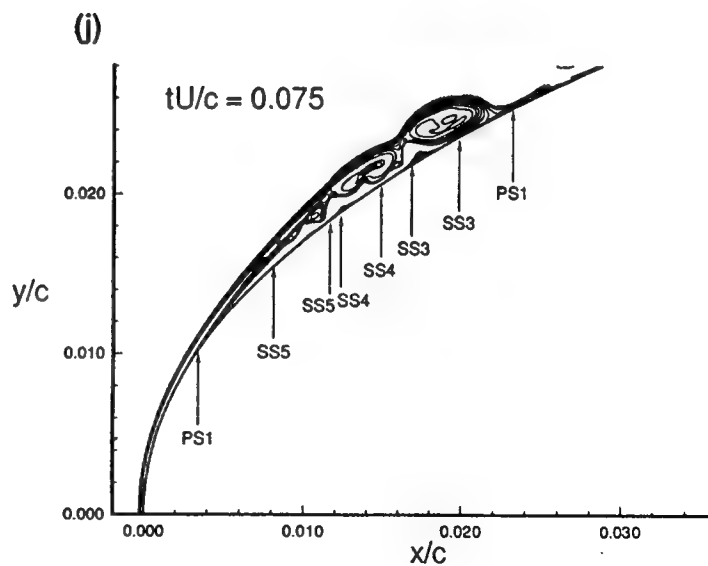
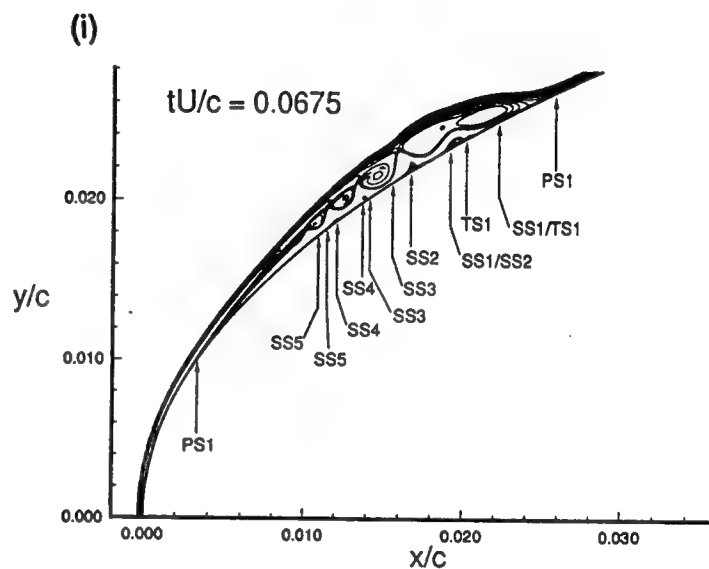
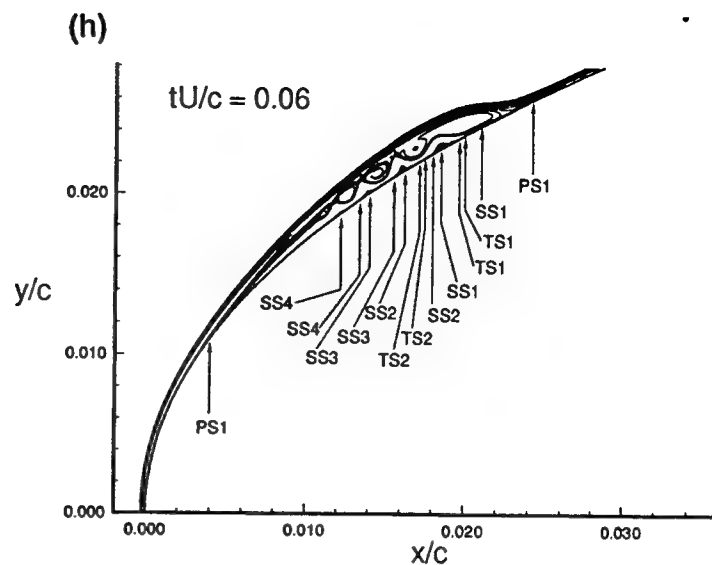
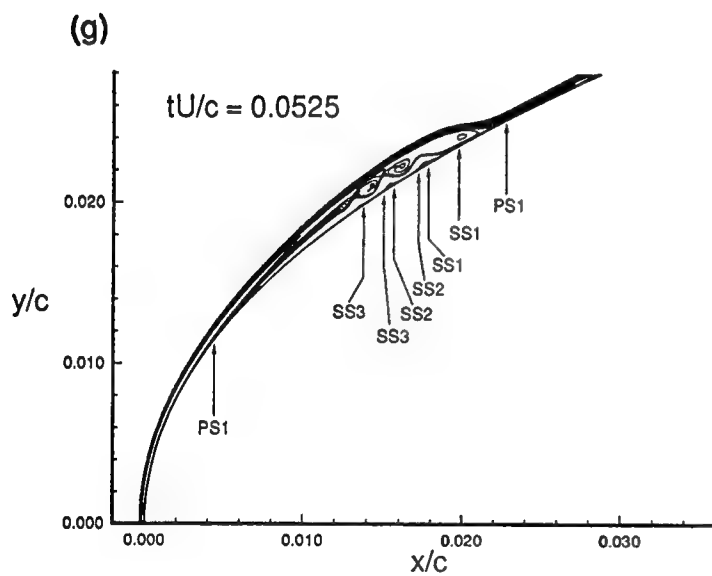
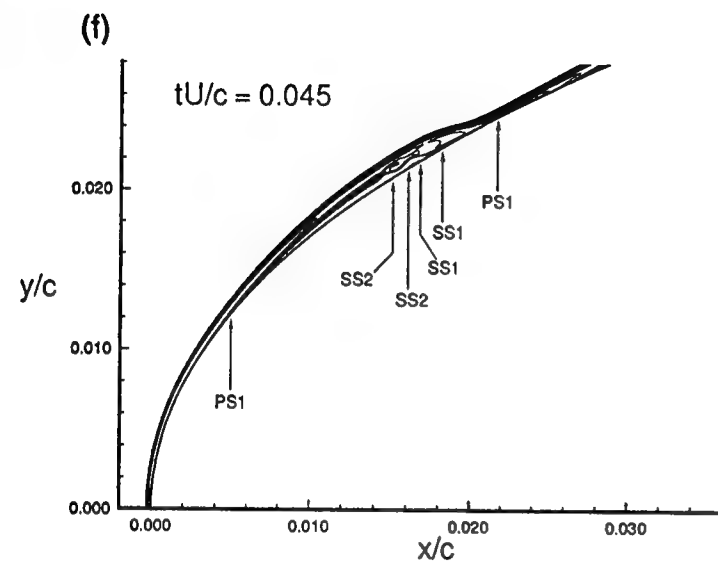
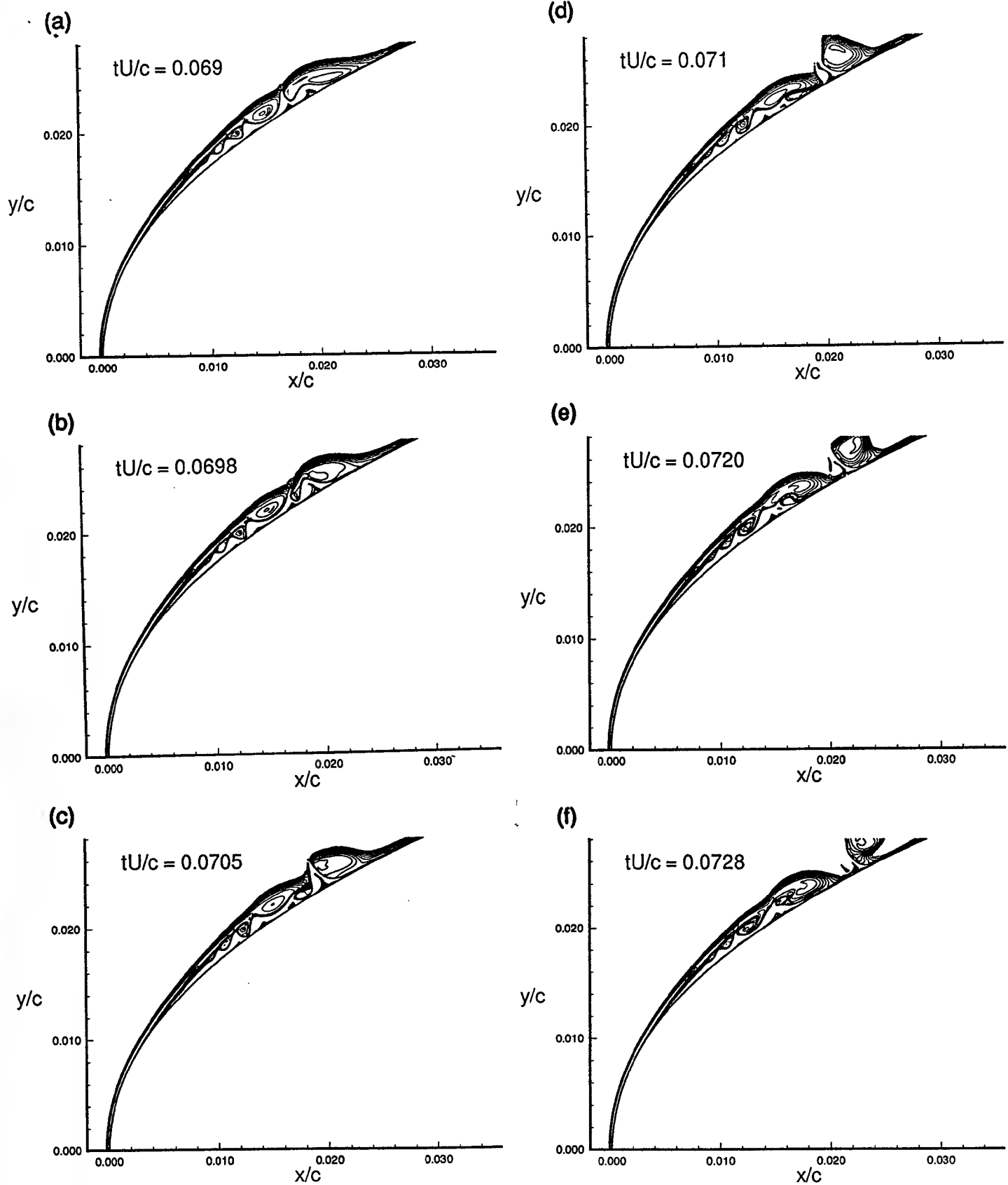


Fig. D.6 Temporal Evolution of the Vorticity Field at  $Re = 800,000$ . (Arrows indicate locations of skin friction sign reversal). (Continued from previous page).





**Fig. D.7 Detailed Vorticity Contours Illustrating the Temporal Evolution of the Flowfield Around the Time of Vortex-Induced Eruption ( $Re = 800,000$ ).**

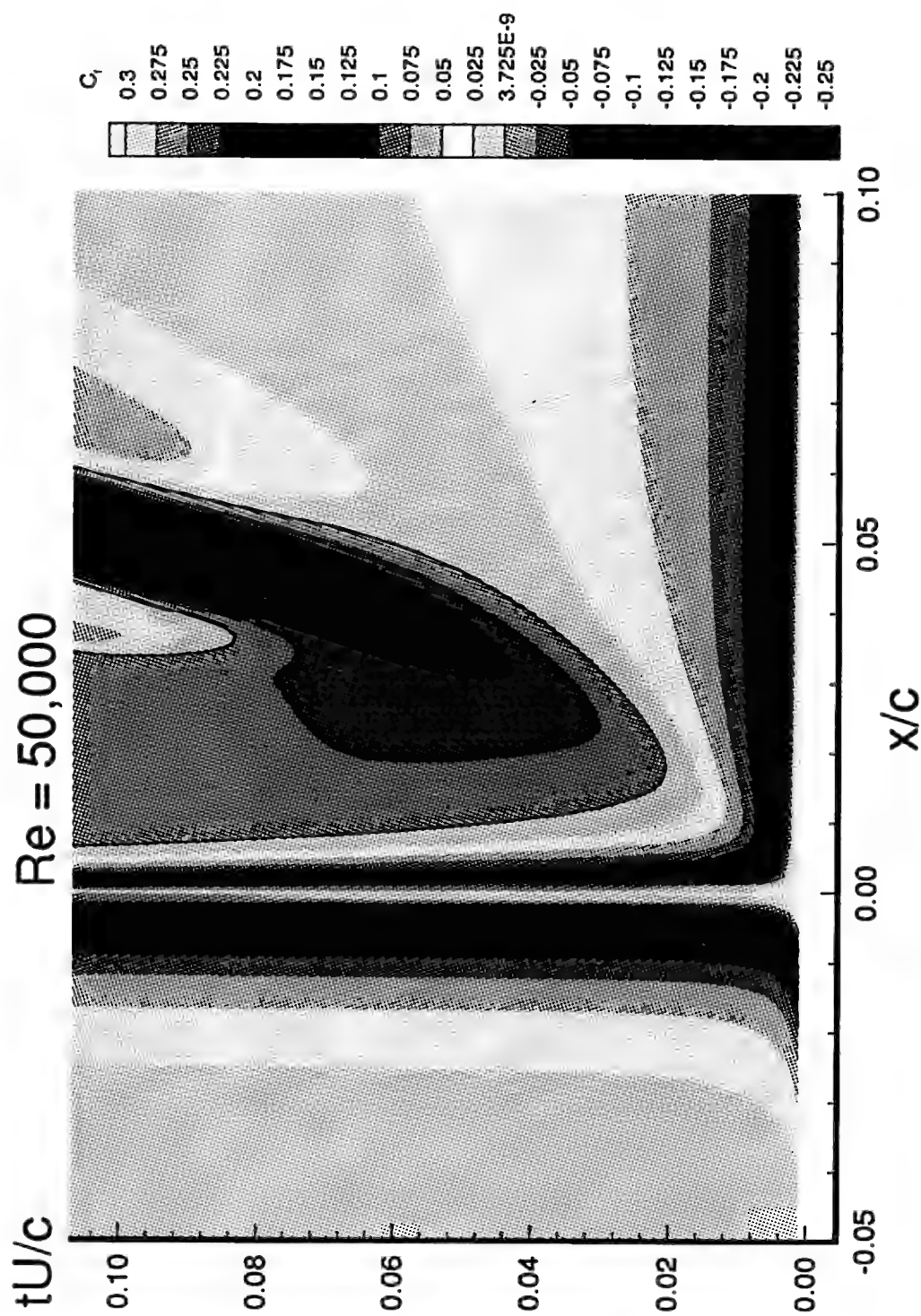


Fig. D.8 Contour Plot Illustrating the Space-Time Evolution of Skin at  $Re = 50,000$ . (Black lines indicate zero skin friction).

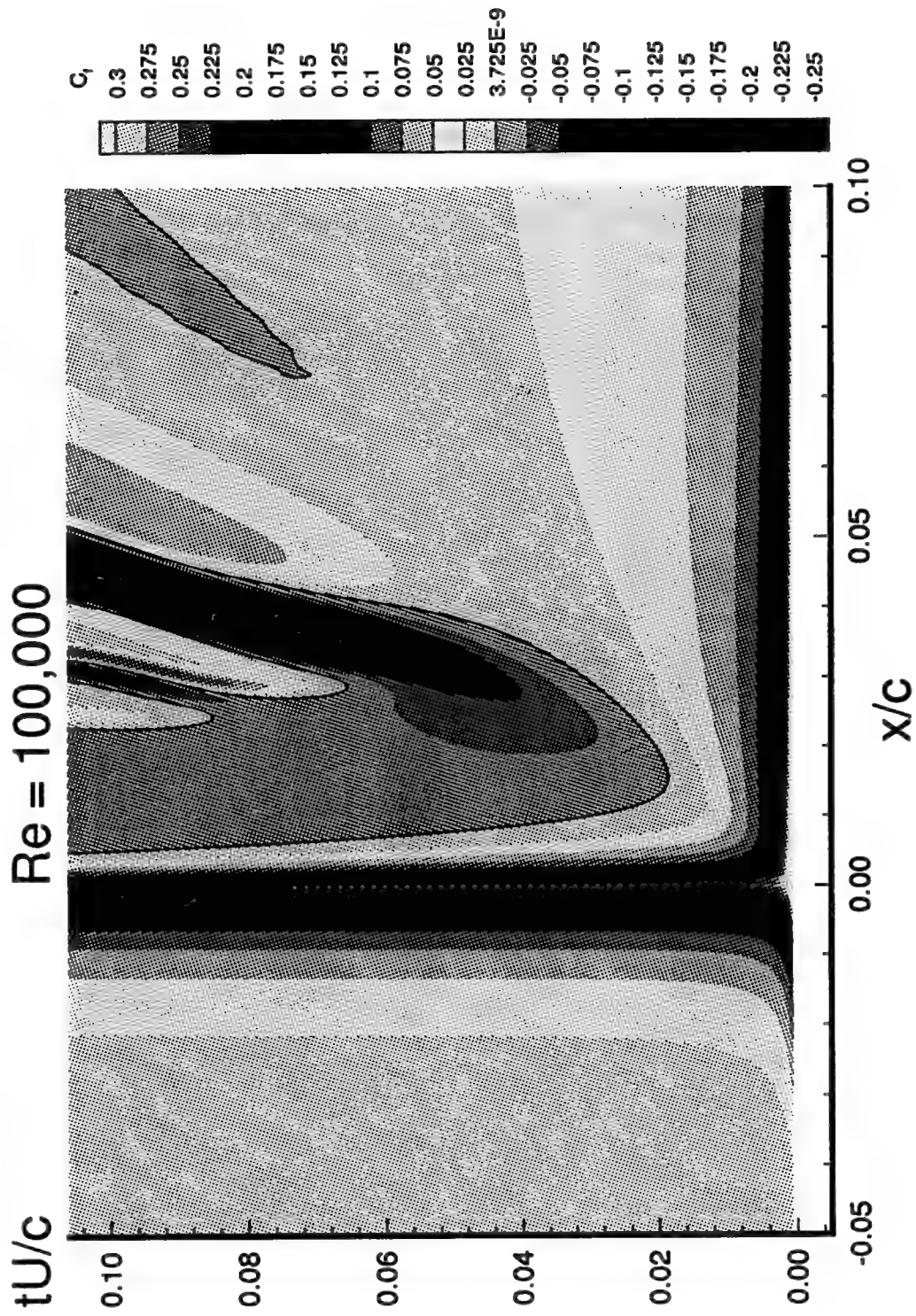


Fig. D.9 Contour Plot Illustrating the Space-Time Evolution of Skin at  $Re = 100,000$ .  
(Black lines indicate zero skin friction).

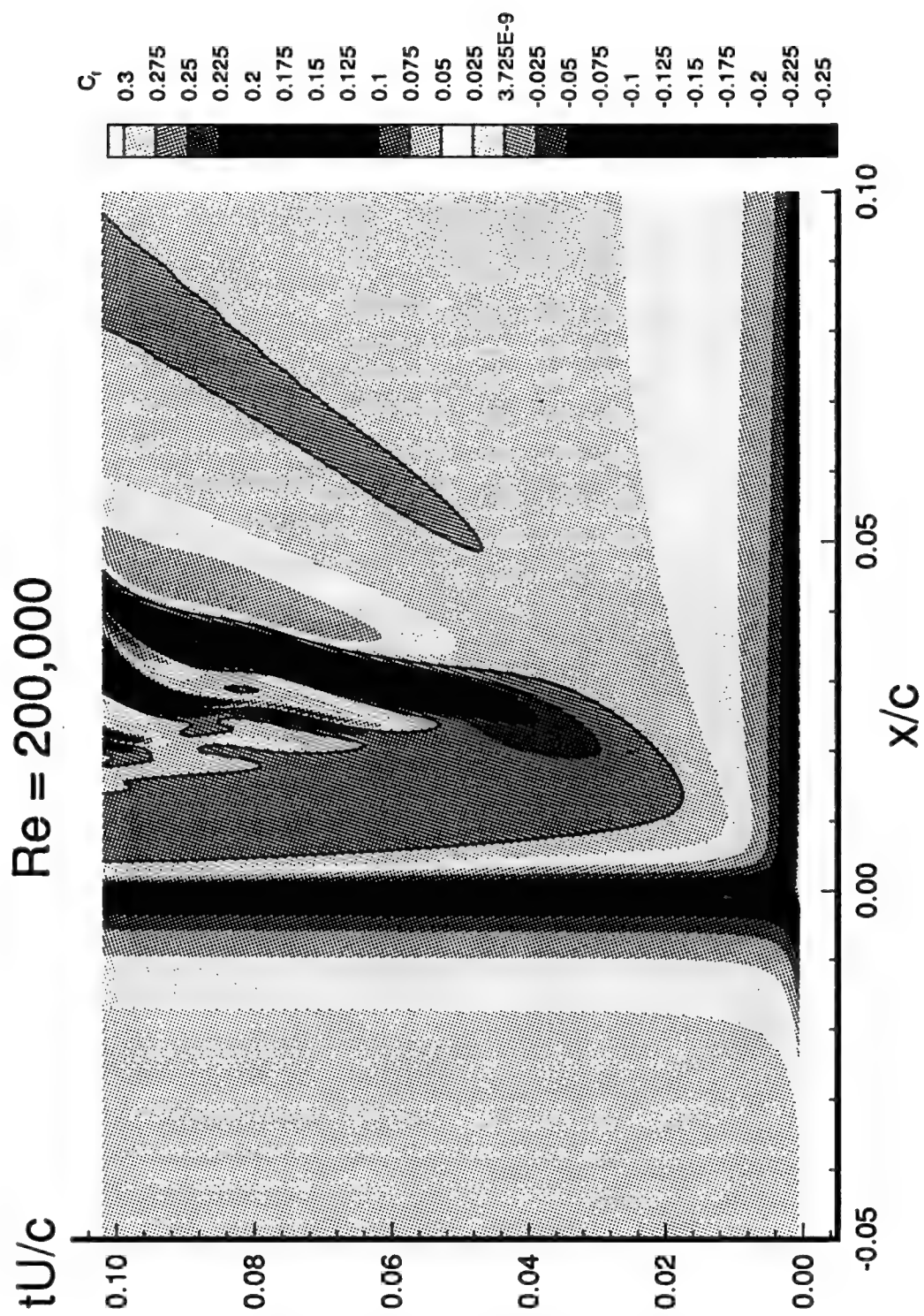


Fig. D.10 Contour Plot Illustrating the Space-Time Evolution of Skin at  $Re = 200,000$ .  
(Black lines indicate zero skin friction).

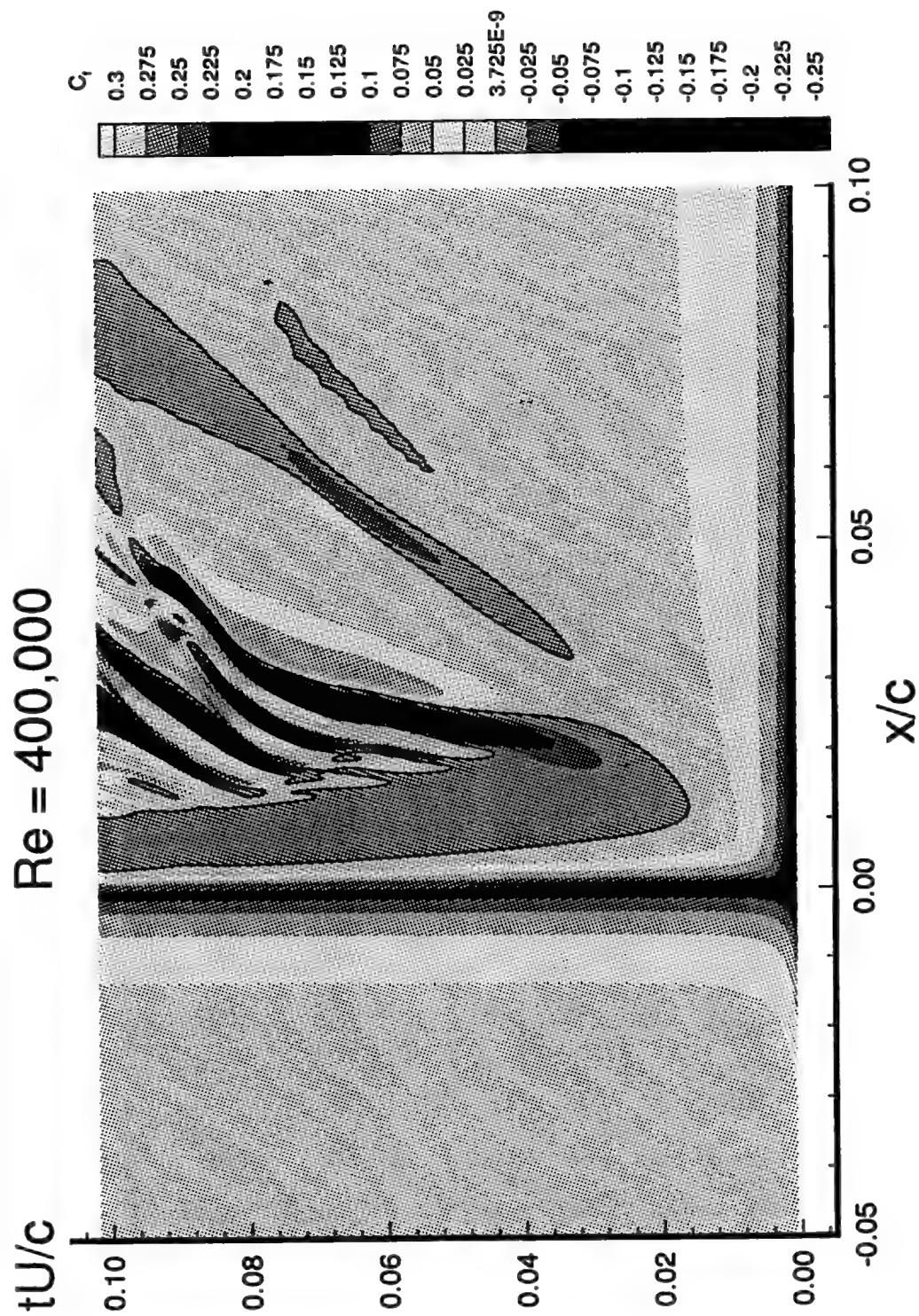


Fig. D.11 Contour Plot Illustrating the Space-Time Evolution of Skin at  $Re = 400,000$ .  
(Black lines indicate zero skin friction).

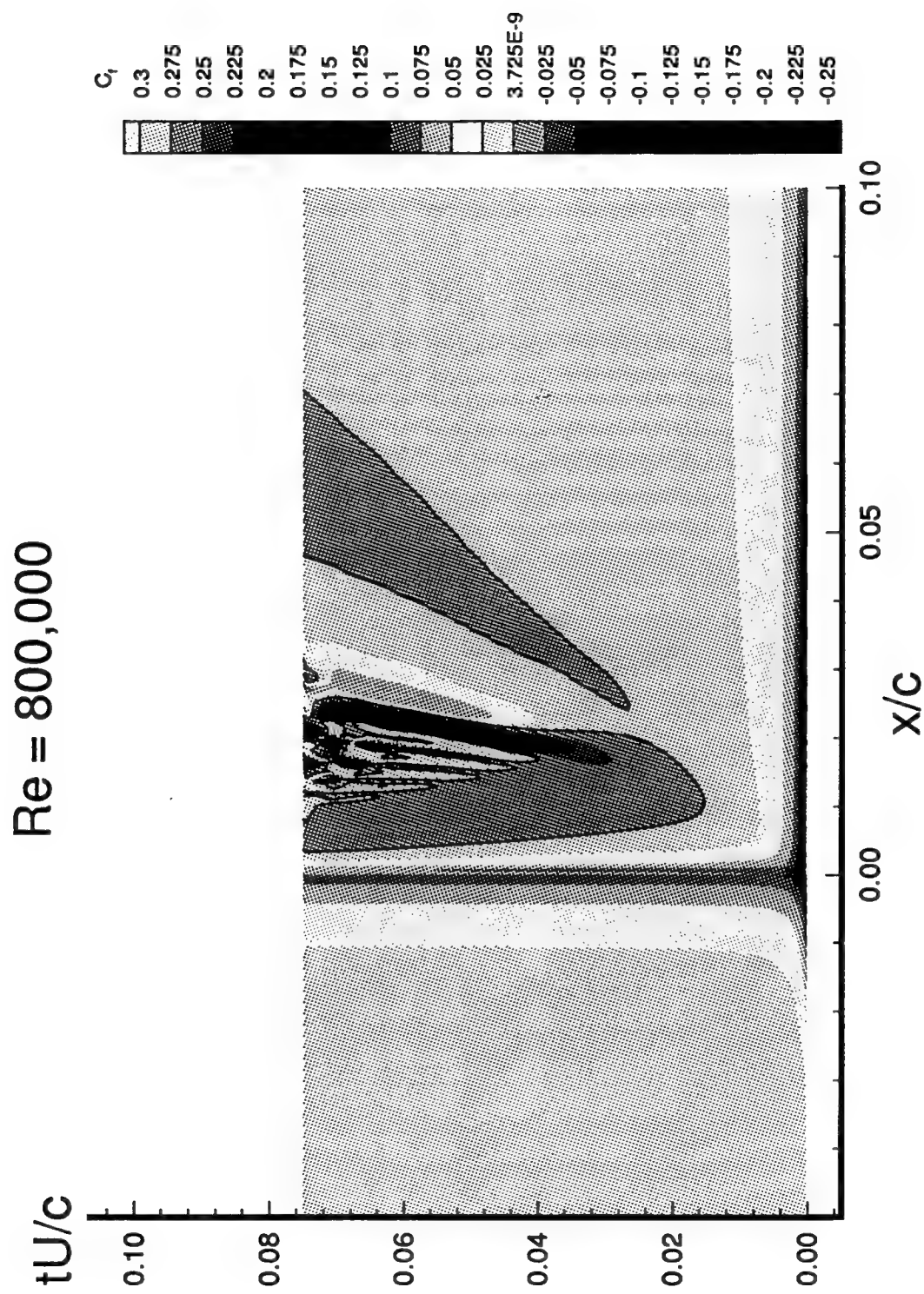


Fig D.12 Contour Plot Illustrating the Space-Time Evolution of Skin at  $Re = 800,000$ .  
(Black lines indicate zero skin friction).



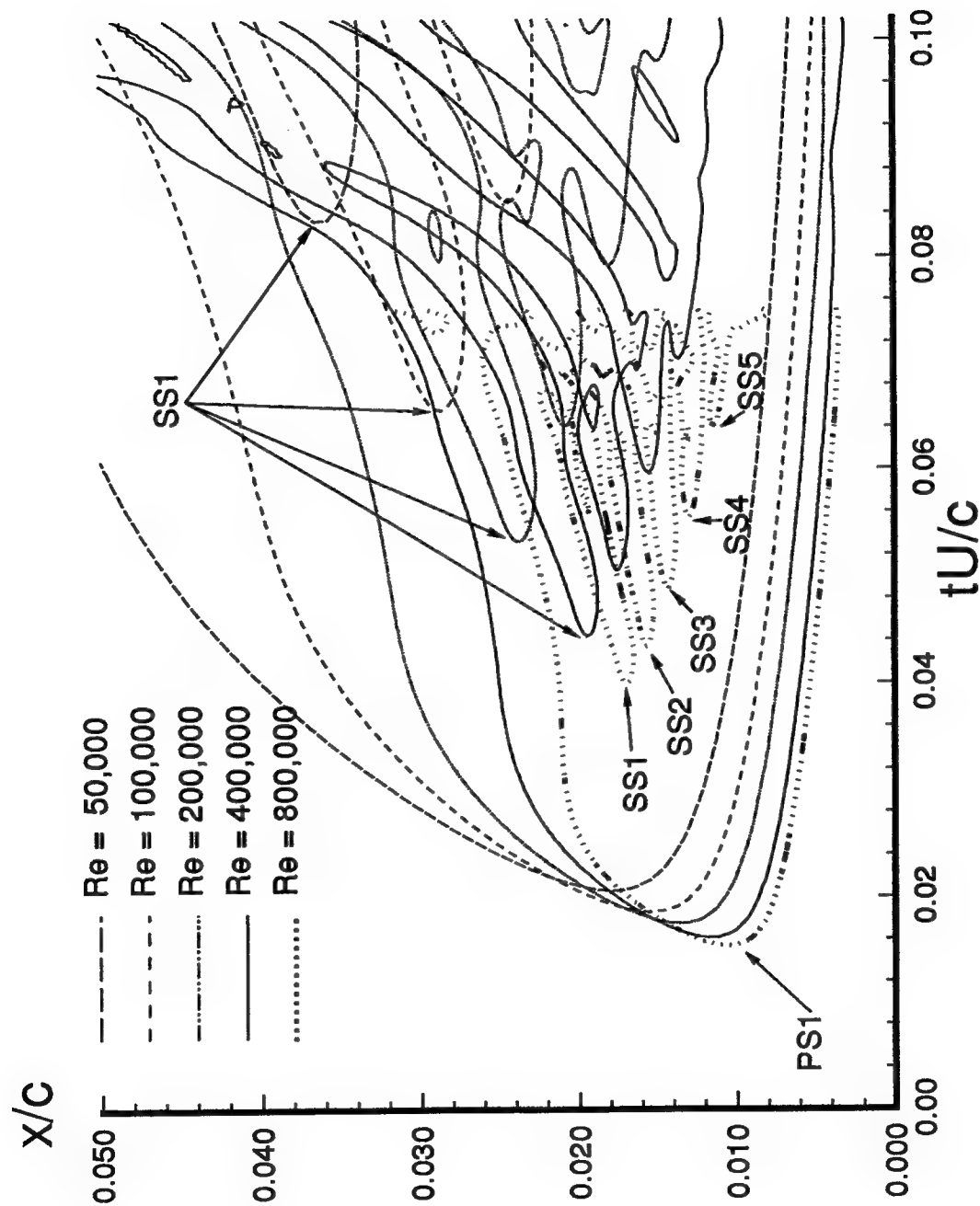


Fig. D.13 Zero Skin Friction Contours Illustrating the Similarity of Surface Flow Topologies Across the Reynolds Number Range.

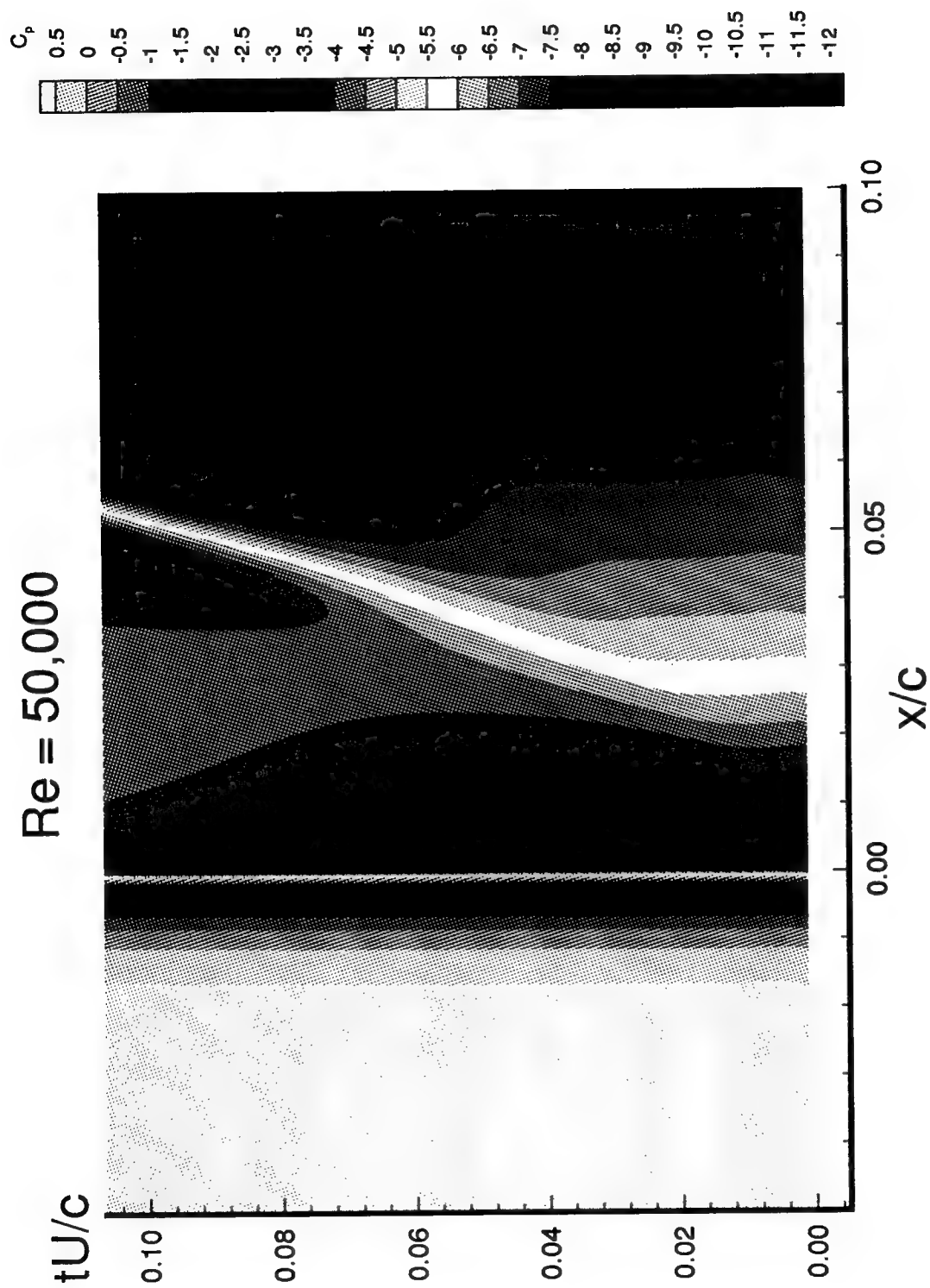


Fig. D.14 Contour Plot Illustrating the Space-Time Evolution of the Pressure Coefficient at the Surface,  $Re = 50,000$ .



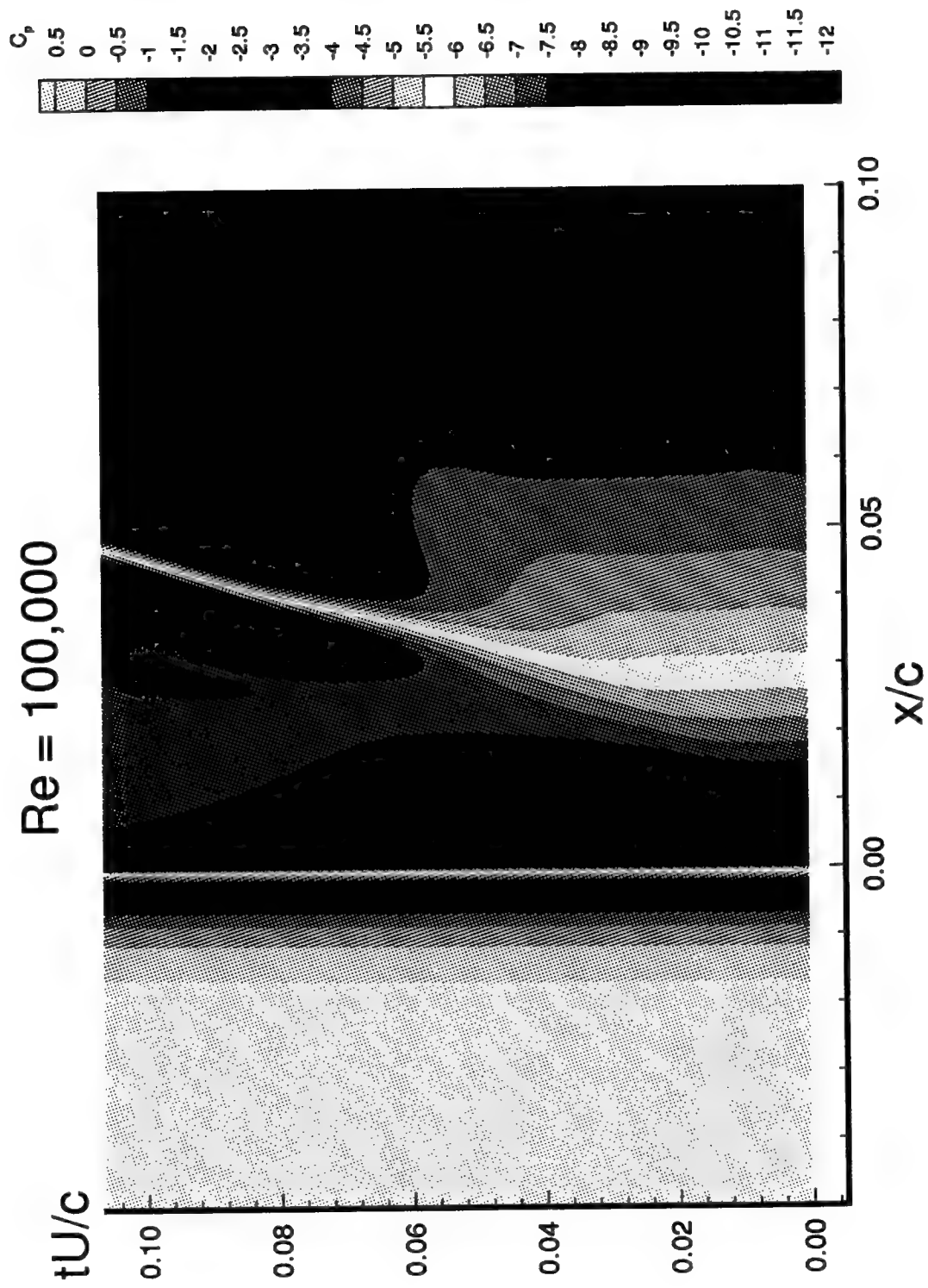


Fig. D.15 Contour Plot Illustrating the Space-Time Evolution of the Pressure Coefficient at the Surface,  $Re = 100,000$ .

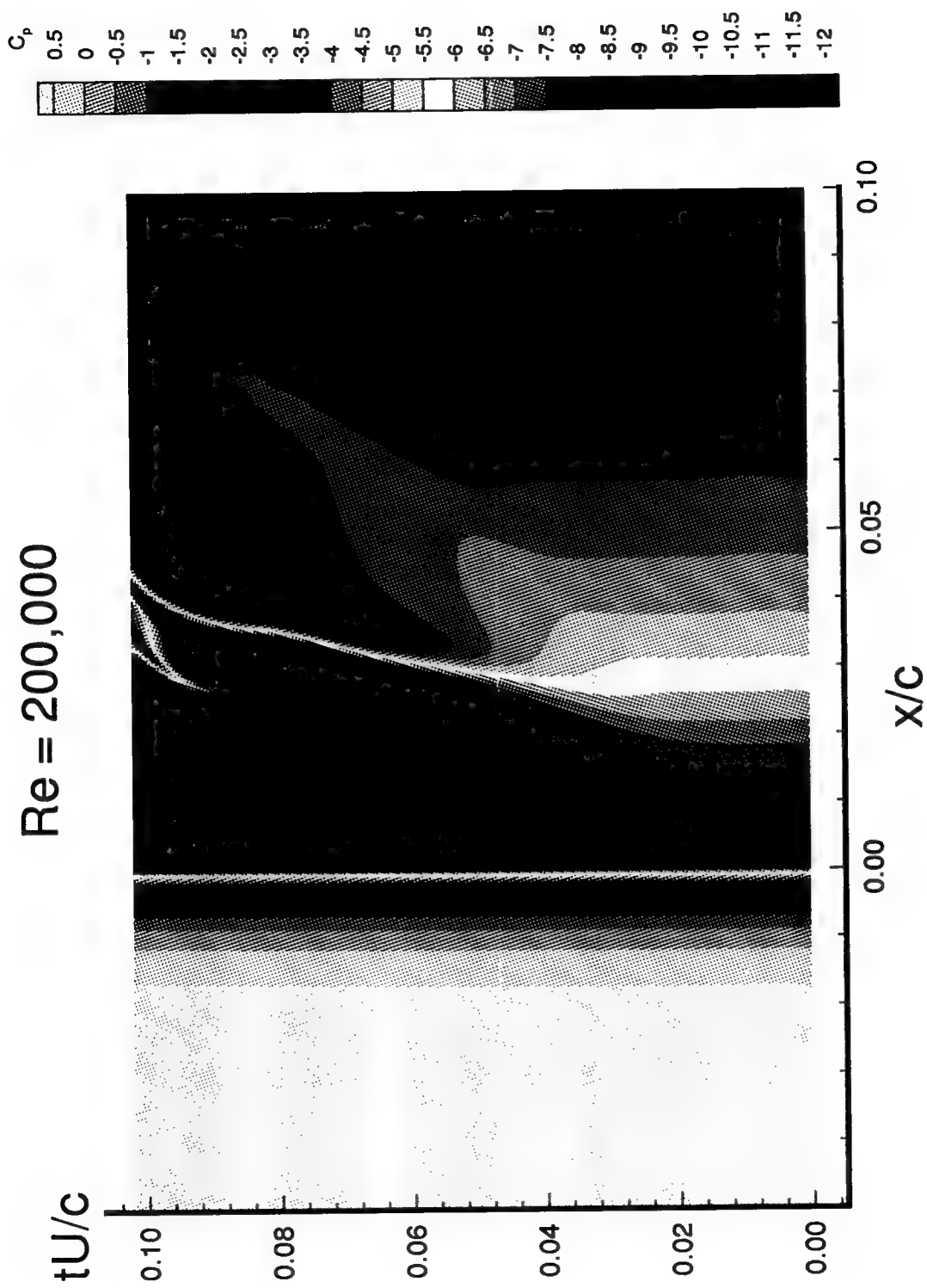


Fig. D.16 Contour Plot Illustrating the Space-Time Evolution of the Pressure Coefficient at the Surface,  $Re = 200,000$ .

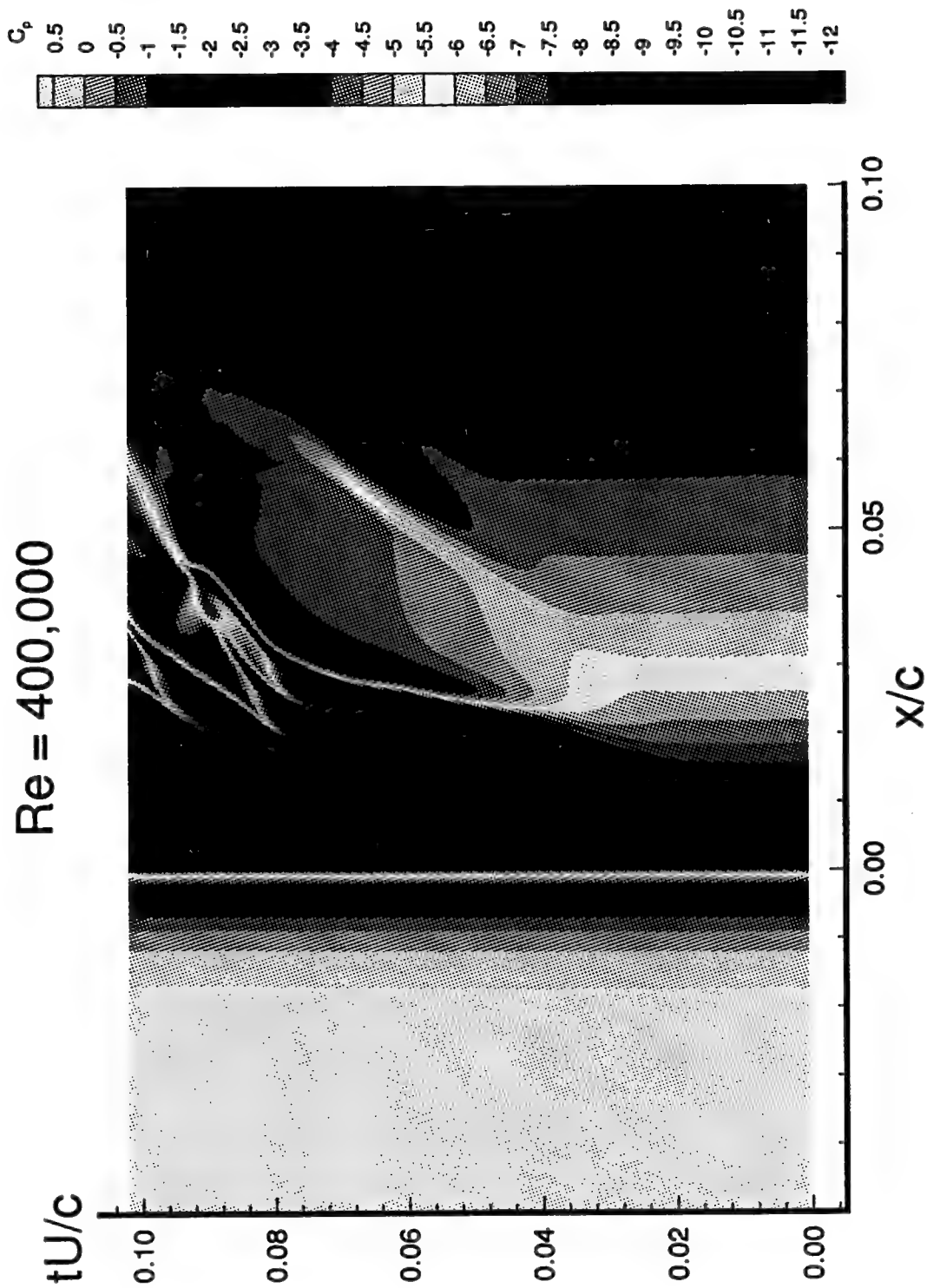


Fig. D.17 Contour Plot Illustrating the Space-Time Evolution of the Pressure Coefficient at the Surface,  $Re = 400,000$ .

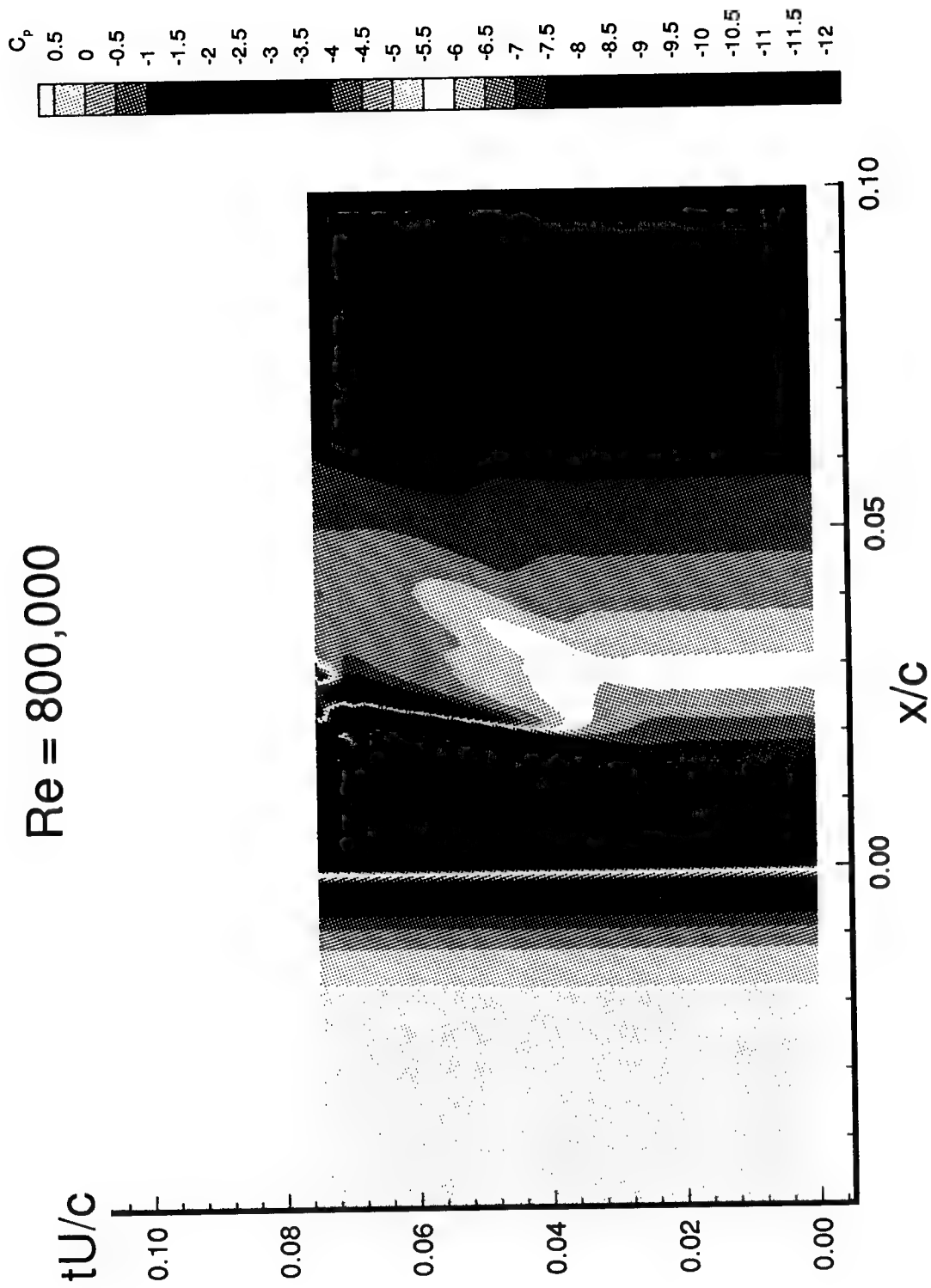


Fig. D.18 Contour Plot Illustrating the Space-Time Evolution of the Pressure Coefficient at the Surface,  $Re = 800,000$ .

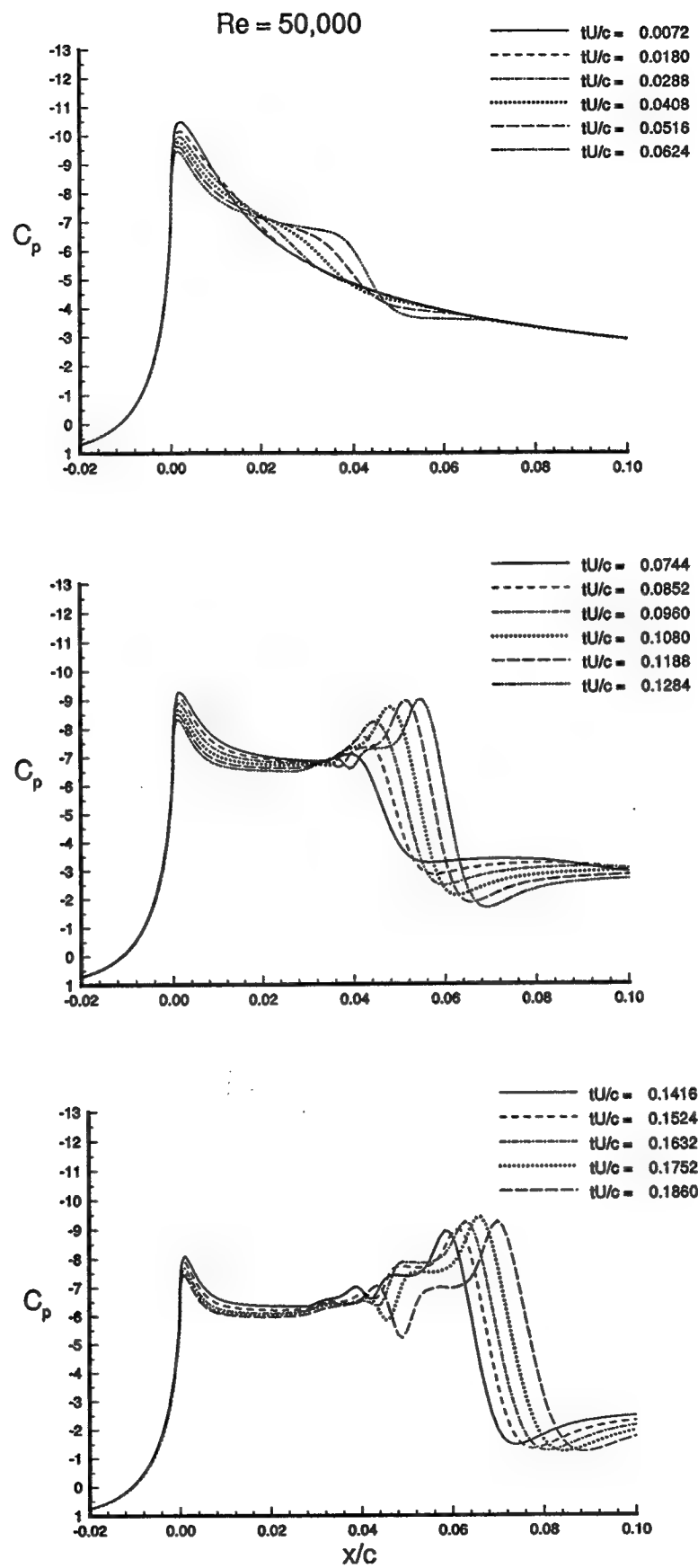


Fig. D.19 Pressure Coefficient Distribution as a Function of Time,  $Re = 50,000$ .

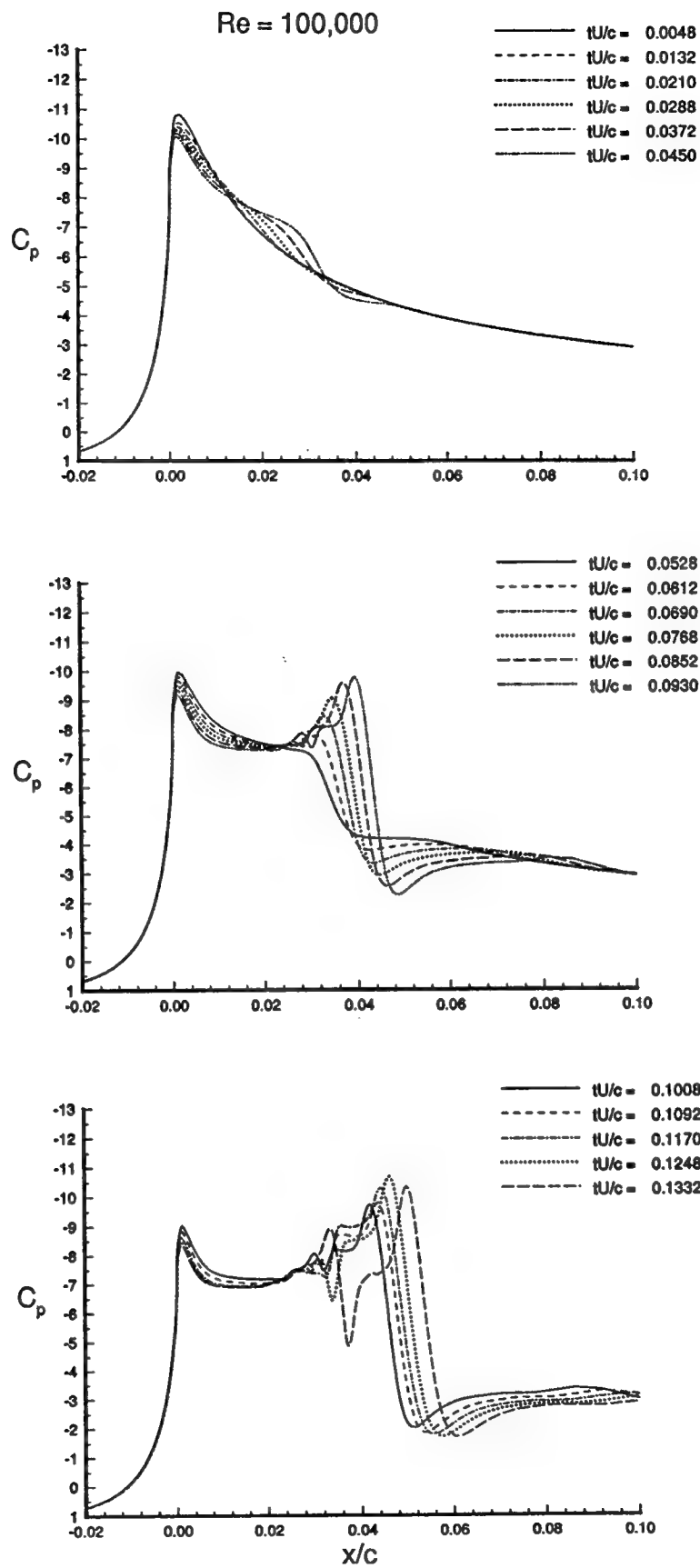


Fig. D.20 Pressure Coefficient Distribution as a Function of Time,  $Re = 100,000$ .

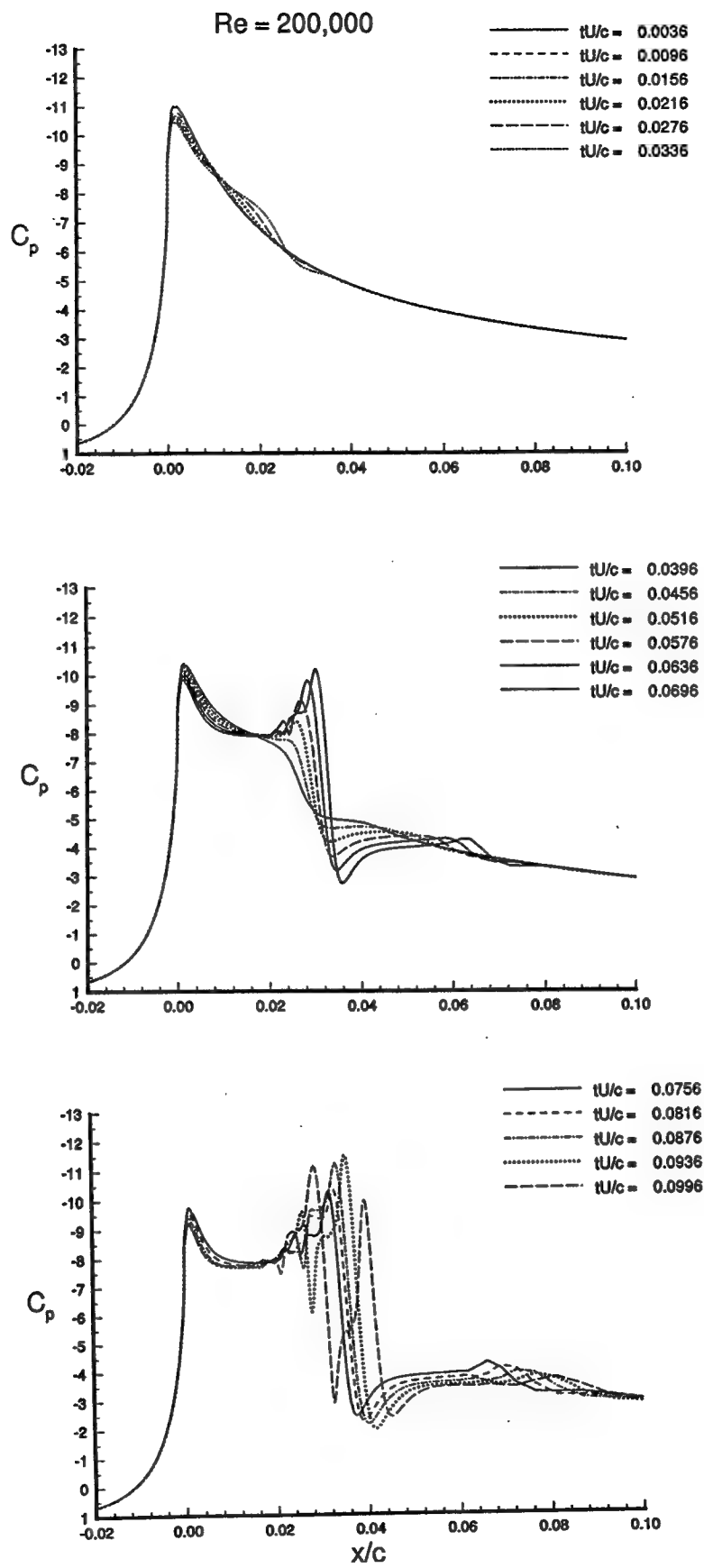


Fig. D.21 Pressure Coefficient Distribution as a Function of Time,  $Re = 200,000$ .

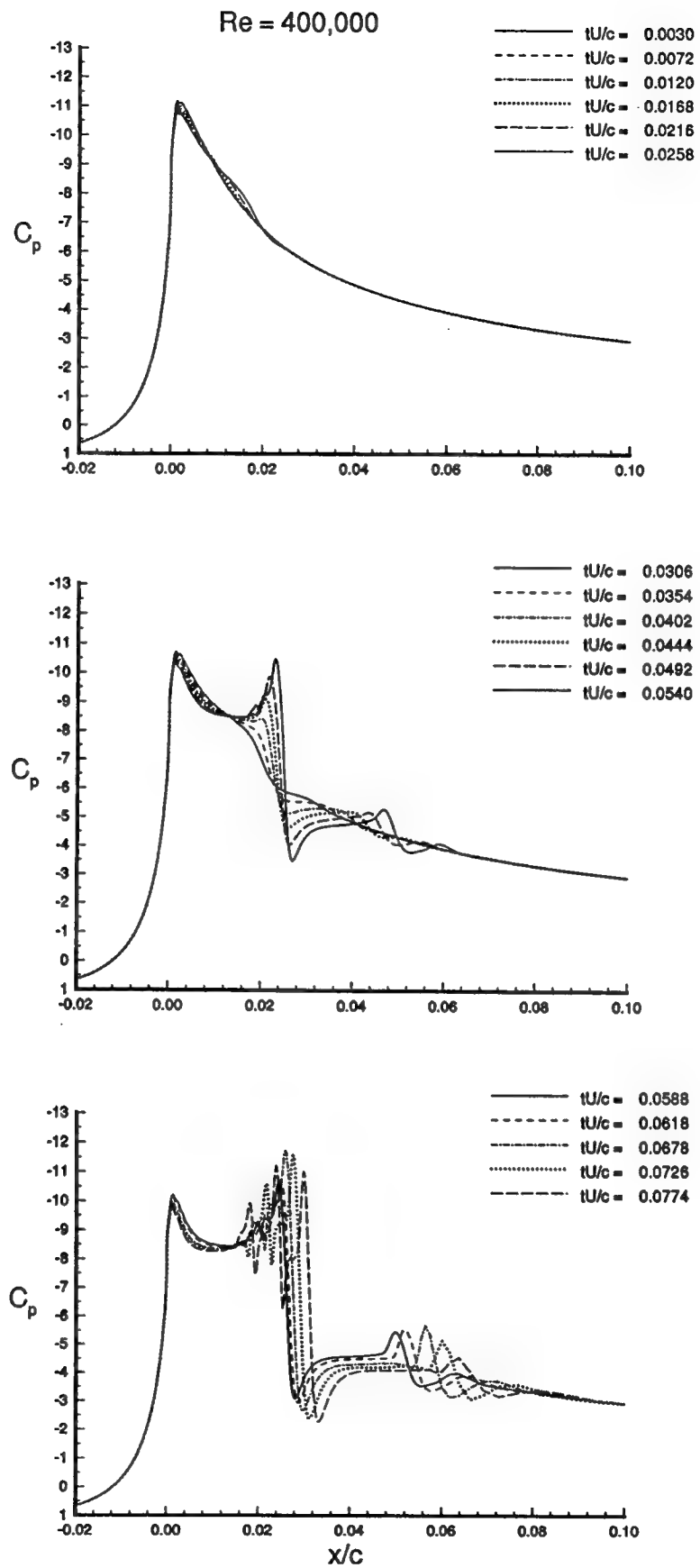


Fig. D.22 Pressure Coefficient Distribution as a Function of Time,  $Re = 400,000$ .



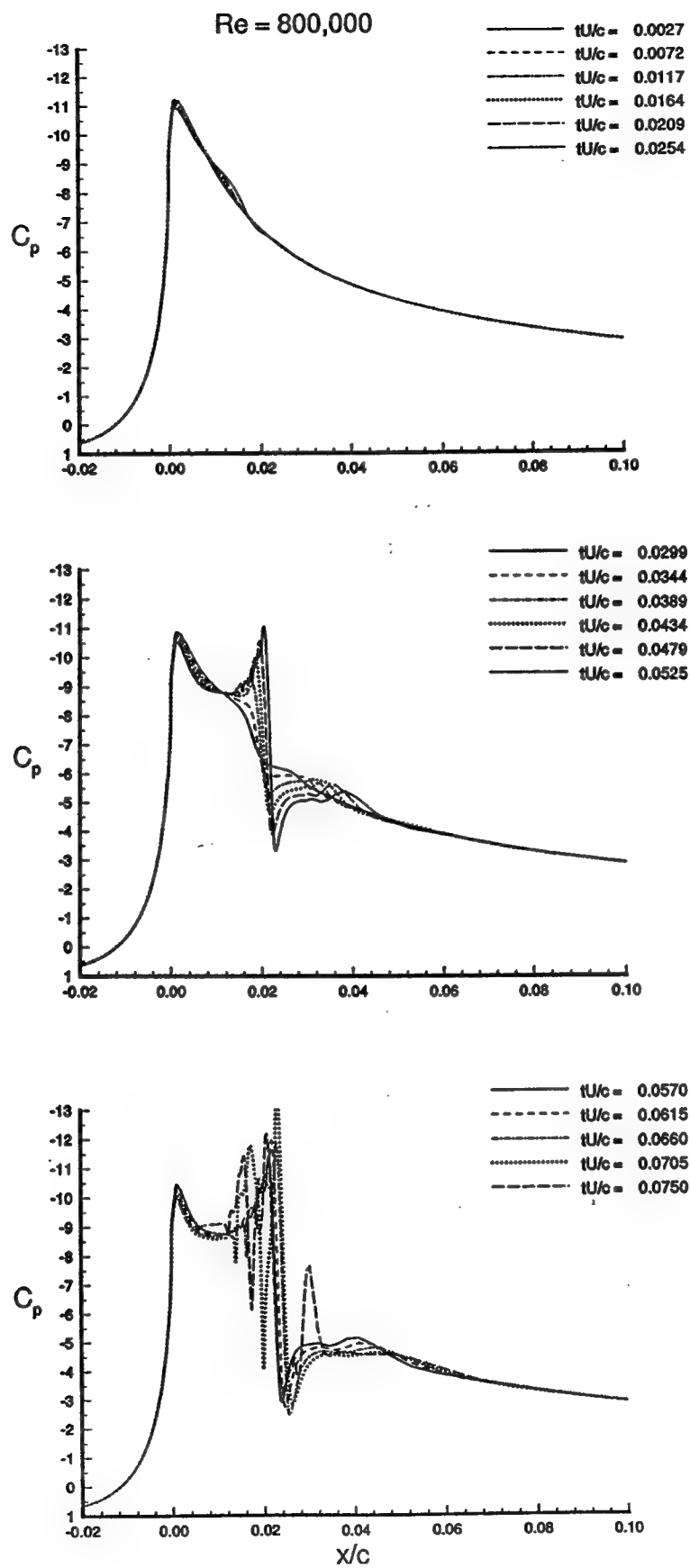


Fig. D.23 Pressure Coefficient Distribution as a Function of Time,  $Re = 800,000$ .

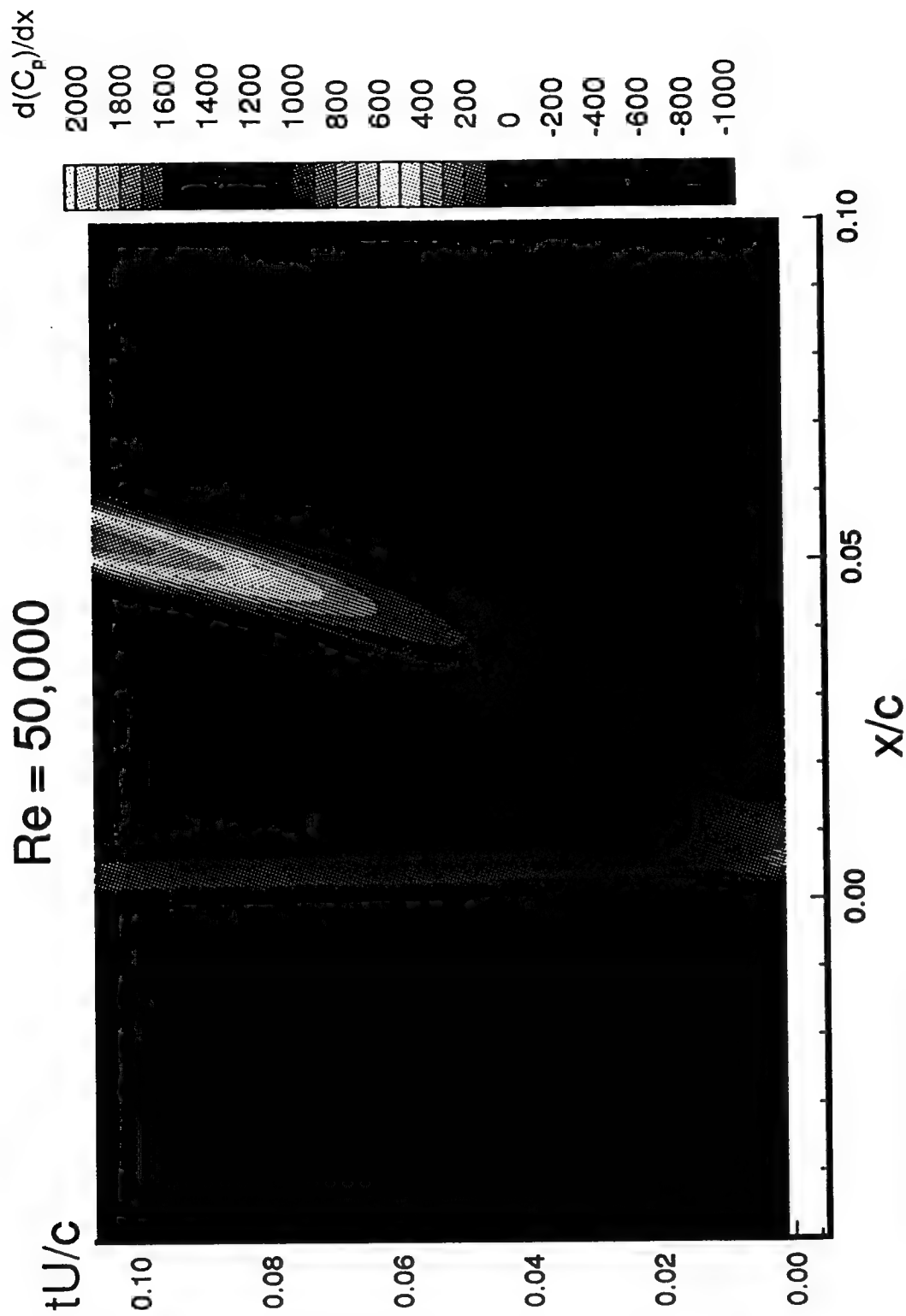


Fig. D.24 Contour Plot Illustrating the Space-Time Evolution of the Streamwise Pressure Gradient at the Surface,  $Re = 50,000$ .

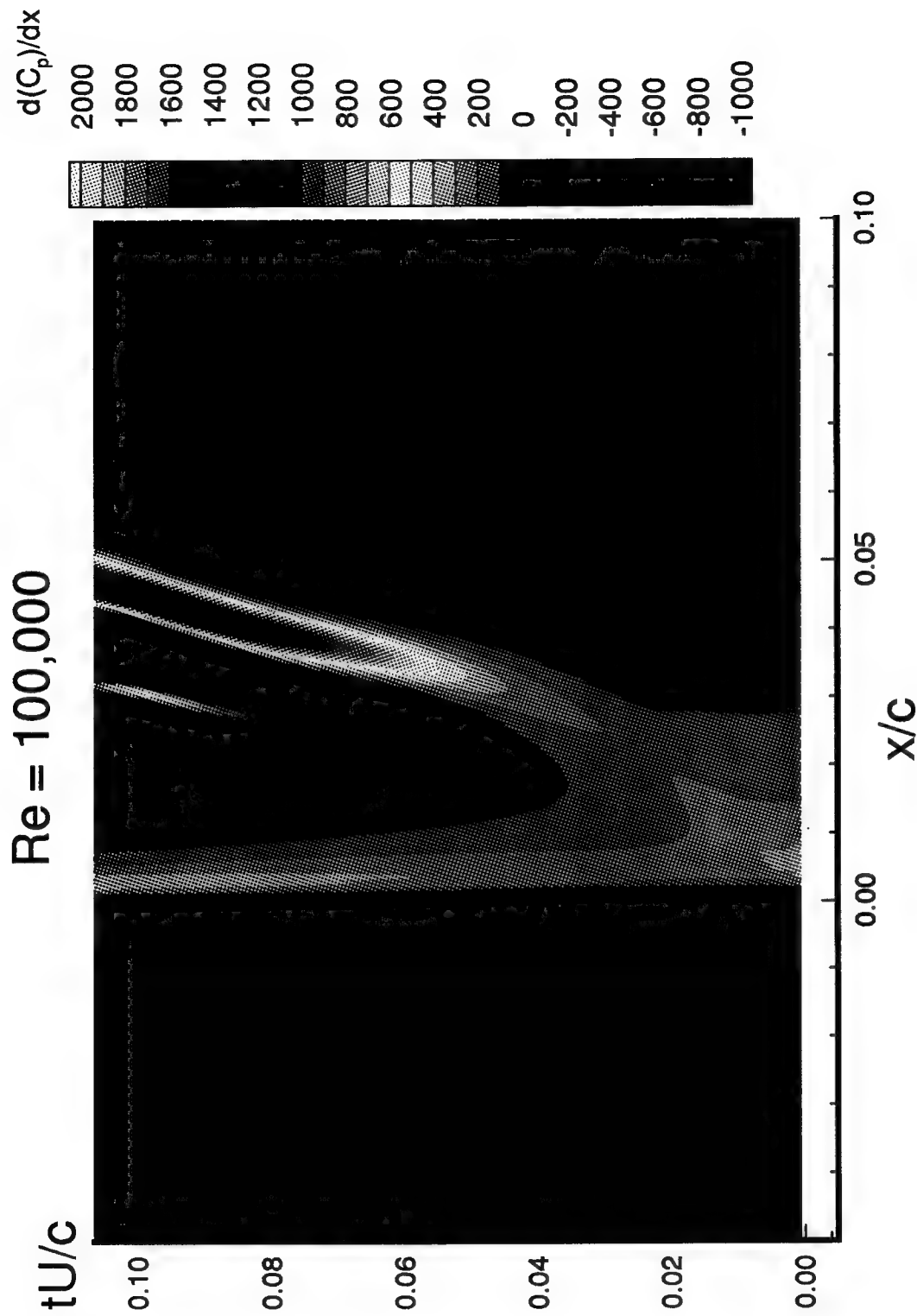


Fig. D.25 Contour Plot Illustrating the Space-Time Evolution of the Streamwise Pressure Gradient at the Surface,  $Re = 100,000$ .

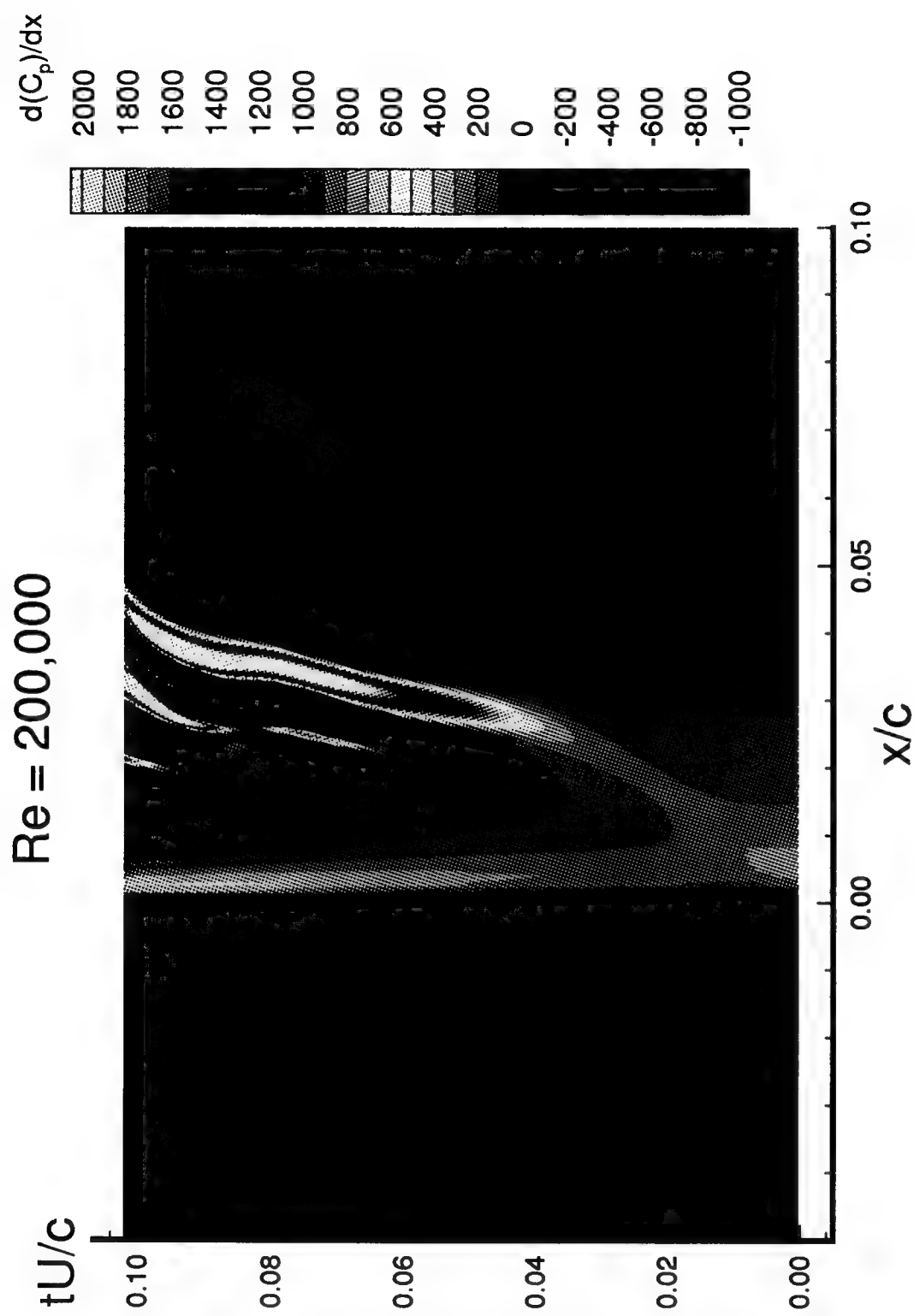


Fig. D.26 Contour Plot Illustrating the Space-Time Evolution of the Streamwise Pressure Gradient at the Surface,  $Re = 200,000$ .

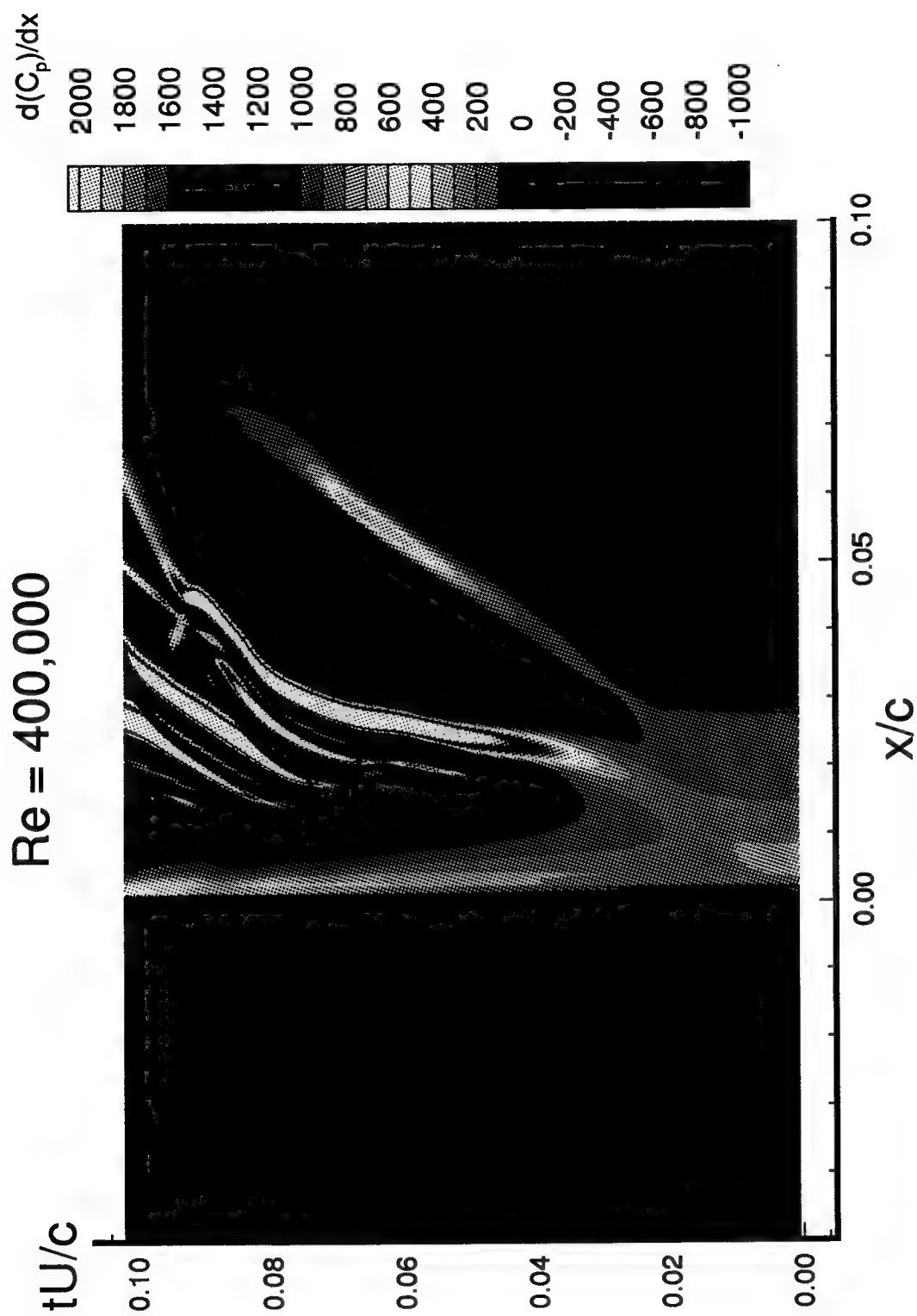


Fig. D.27 Contour Plot Illustrating the Space-Time Evolution of the Streamwise Pressure Gradient at the Surface,  $Re = 400,000$ .

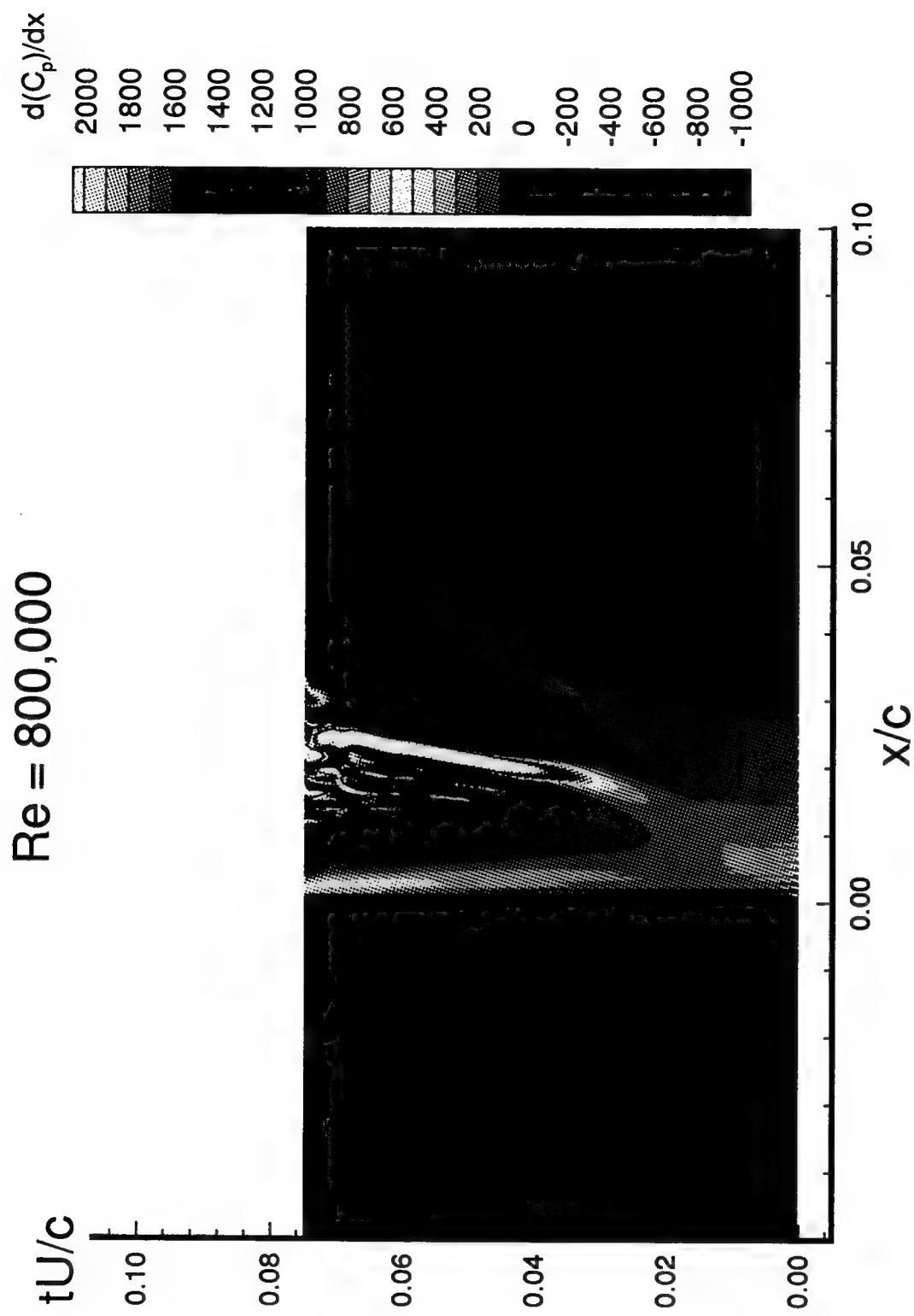


Fig. D.28 Contour Plot Illustrating the Space-Time Evolution of the Streamwise Pressure Gradient at the Surface,  $Re = 800,000$ .

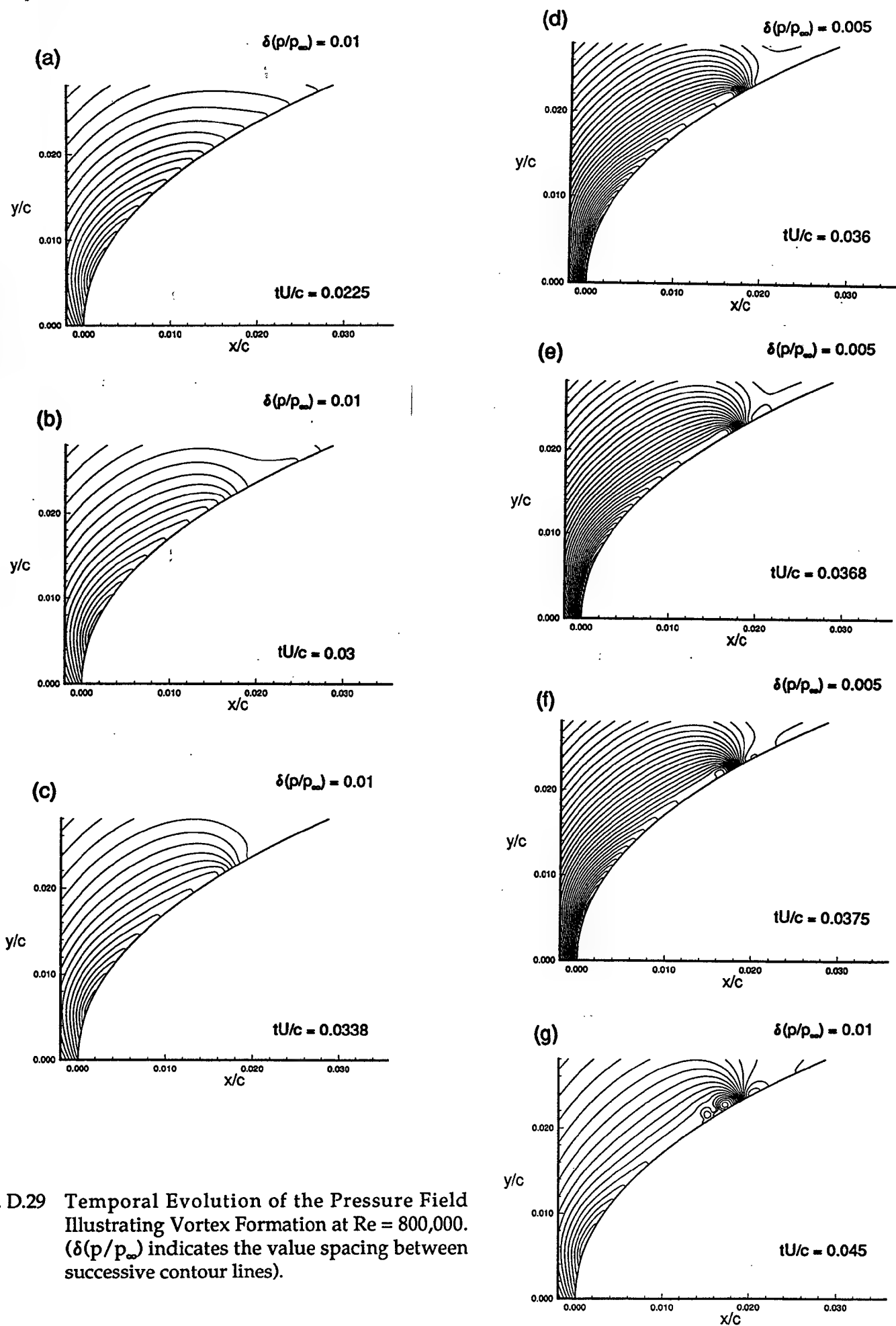


Fig. D.29 Temporal Evolution of the Pressure Field Illustrating Vortex Formation at  $Re = 800,000$ . ( $\delta(p/p_\infty)$  indicates the value spacing between successive contour lines).

$Re = 400,000$   
 $tU/c = 0.030$

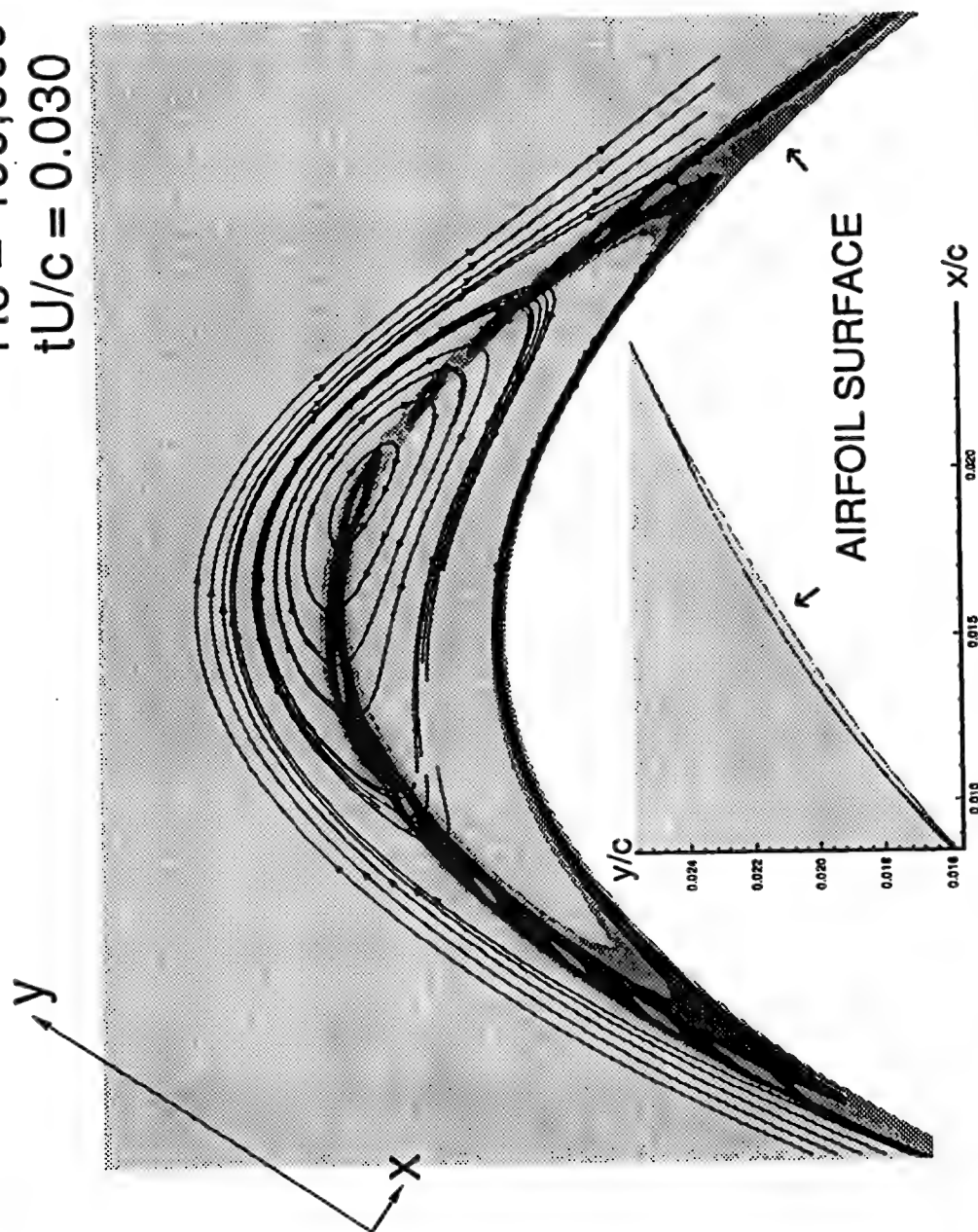


Fig. D.30 Schematic Illustration of the Methodology Used to Determine the Location of the Topological Center at  $tU/c = 0.03$ ,  $Re = 400,000$ . (The inset depicts the extent of the un-rotated, un-scaled recirculation region using iso-contours the Mach number, for  $M \leq 0.01$ . Lines in the main graph are instantaneous streamtraces).



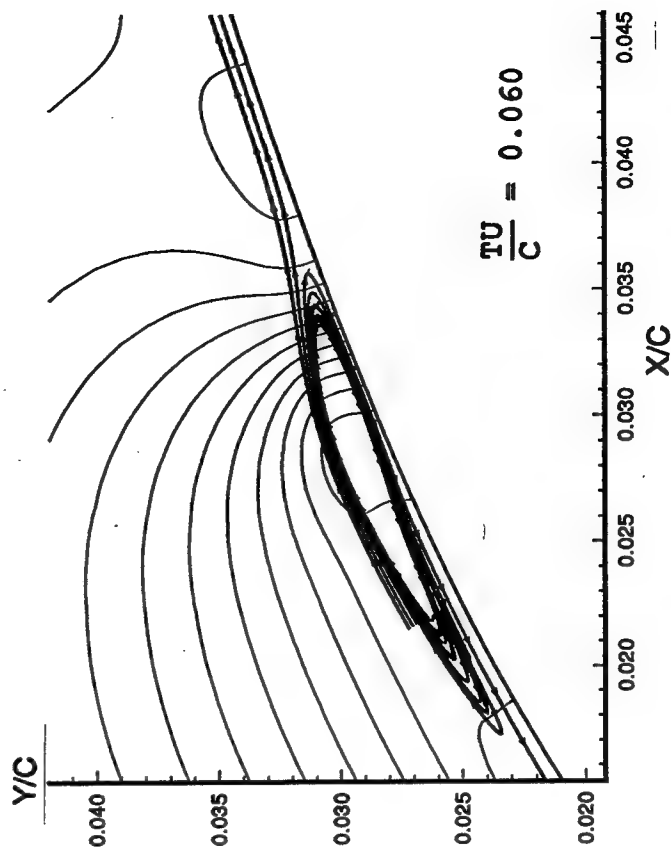
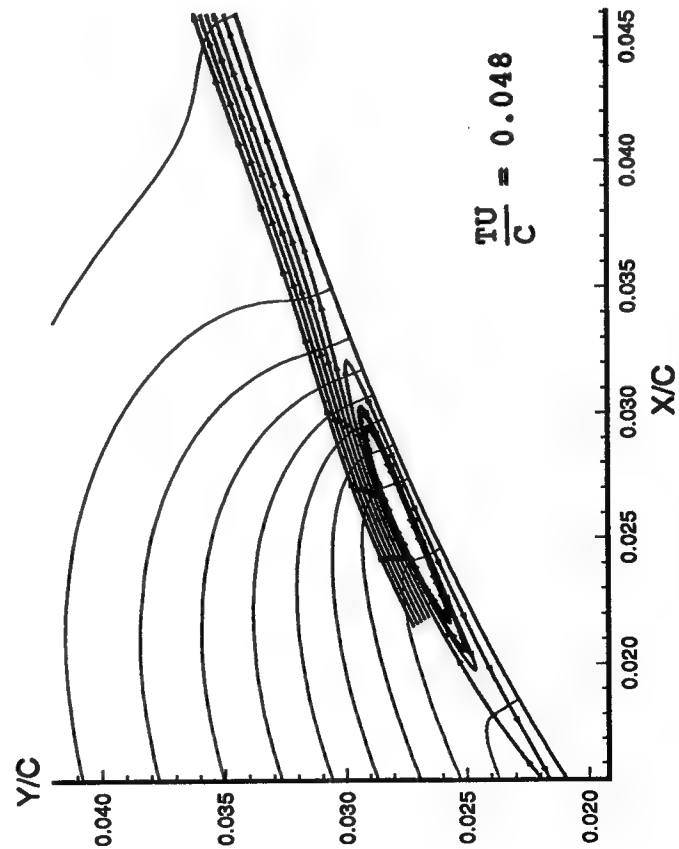
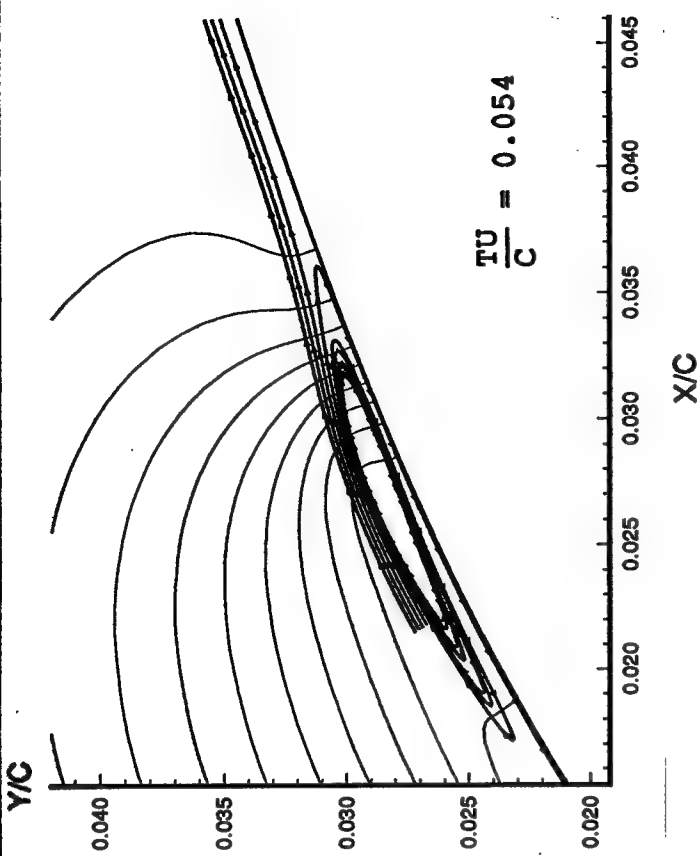
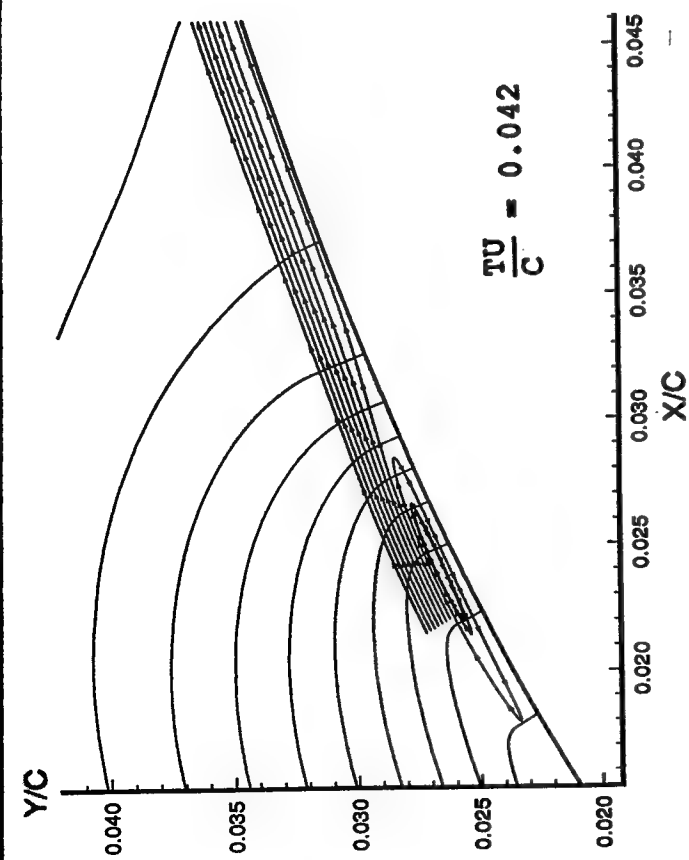


Fig. D.31 Temporal Evolution of the Pressure Field and of Streamtraces Illustrating the Connection between the Topological Center and the Formation of the Primary Vortex,  $Re = 100,000$ .

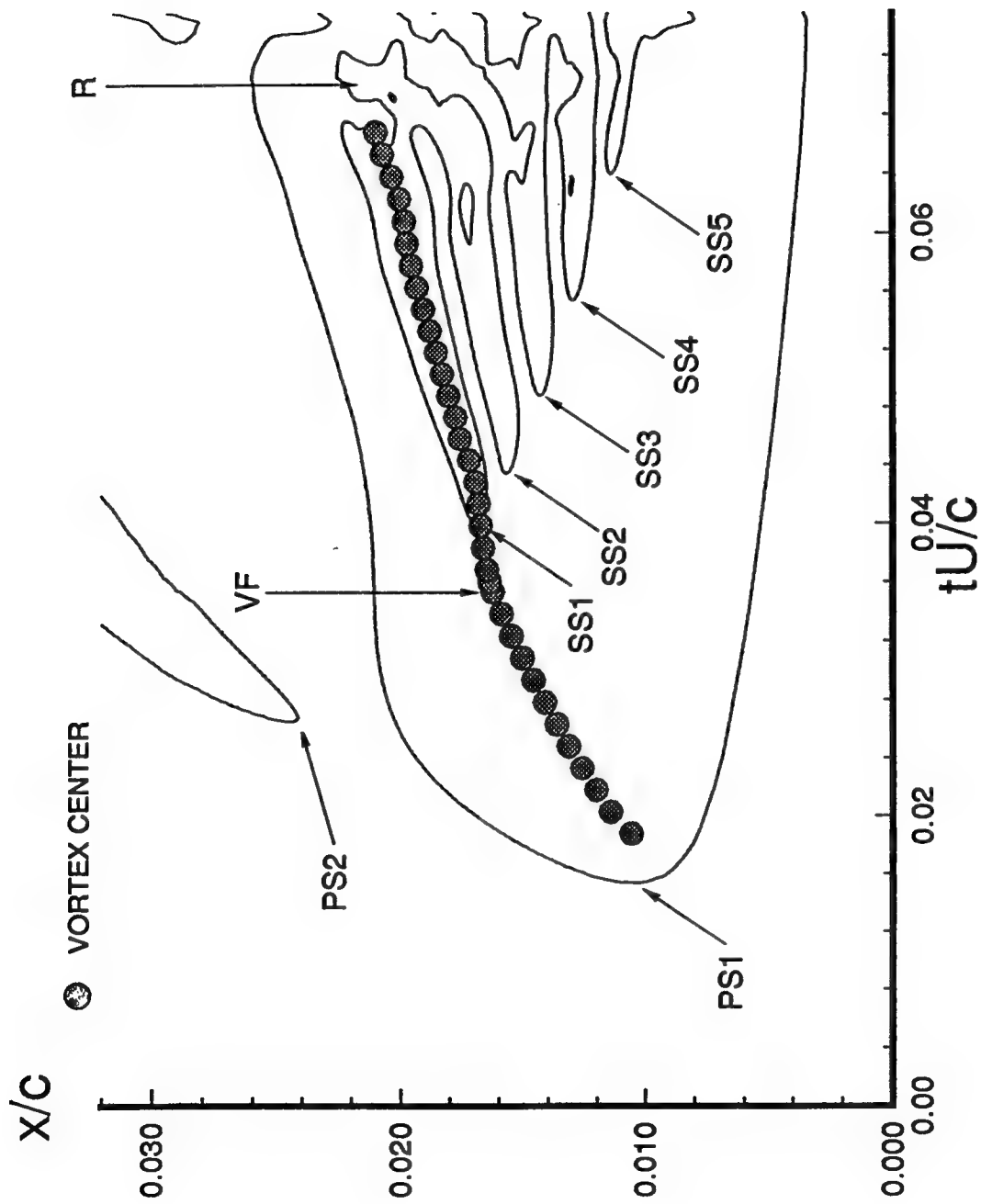


Fig. D.32 Temporal Evolution of Surface Flow Topology and Primary "Vortex/Center" Trajectory at  $Re = 800,000$ . (Lines are zero skin friction contours; "VF" denotes vortex formation; "R" denotes rupture).

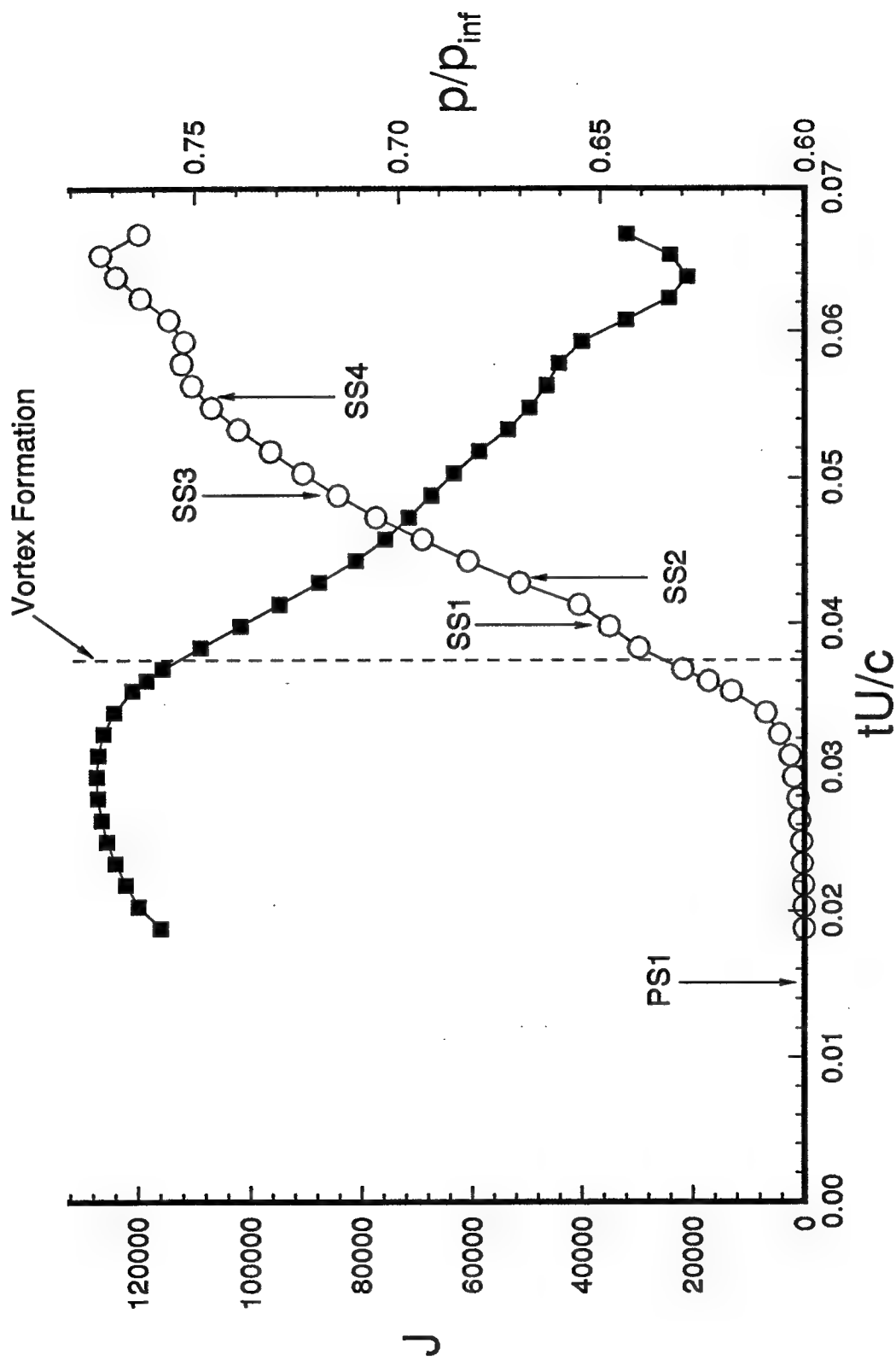


Fig. D.33 Temporal Evolution of Key Features Used to Describe the Primary Vortex History at  $Re = 800,000$ . (○ jacobian, ■ pressure at the core).

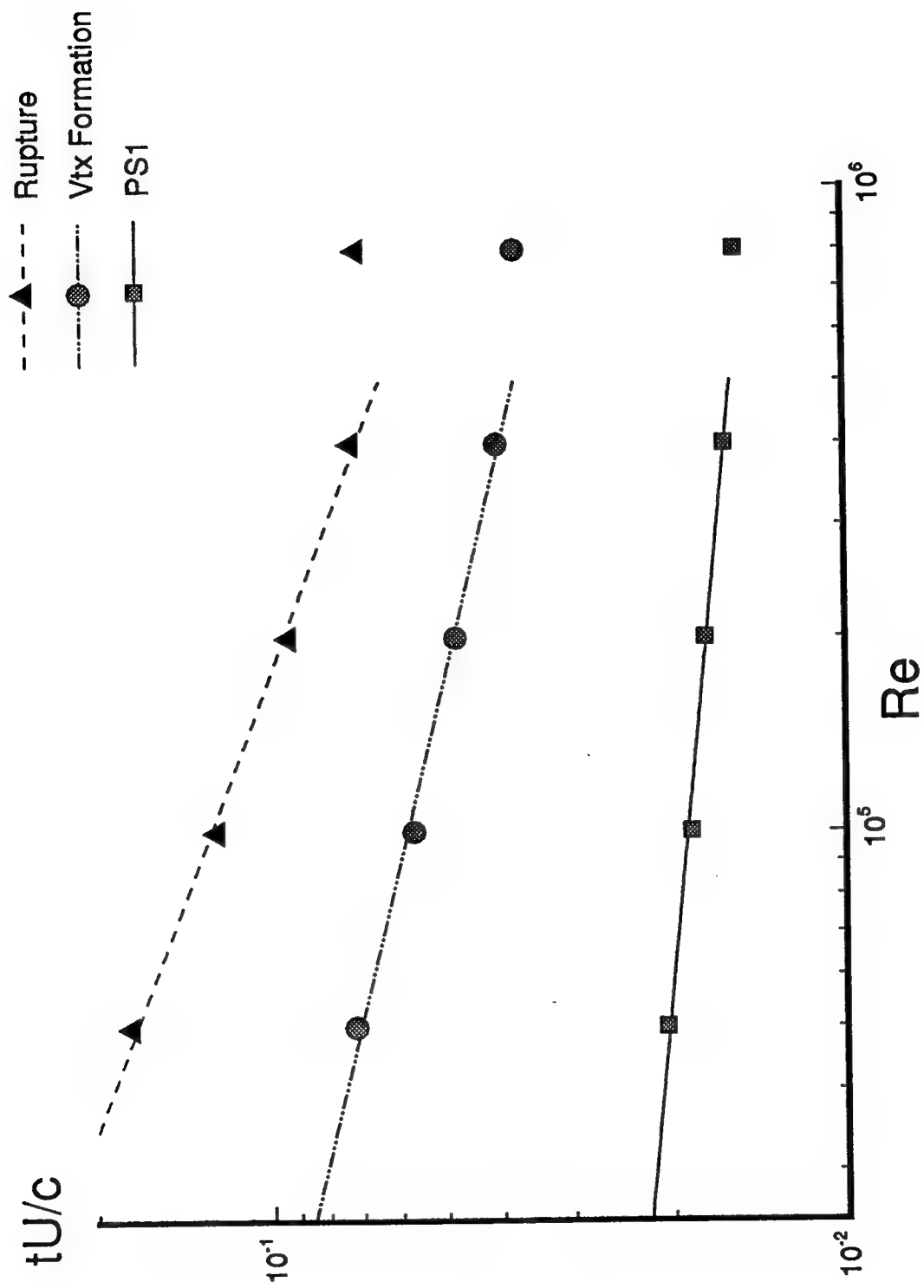


Fig. D.34 Reynolds Number Scaling of Onset Times for Primary Separation, Vortex Formation, and Rupture.

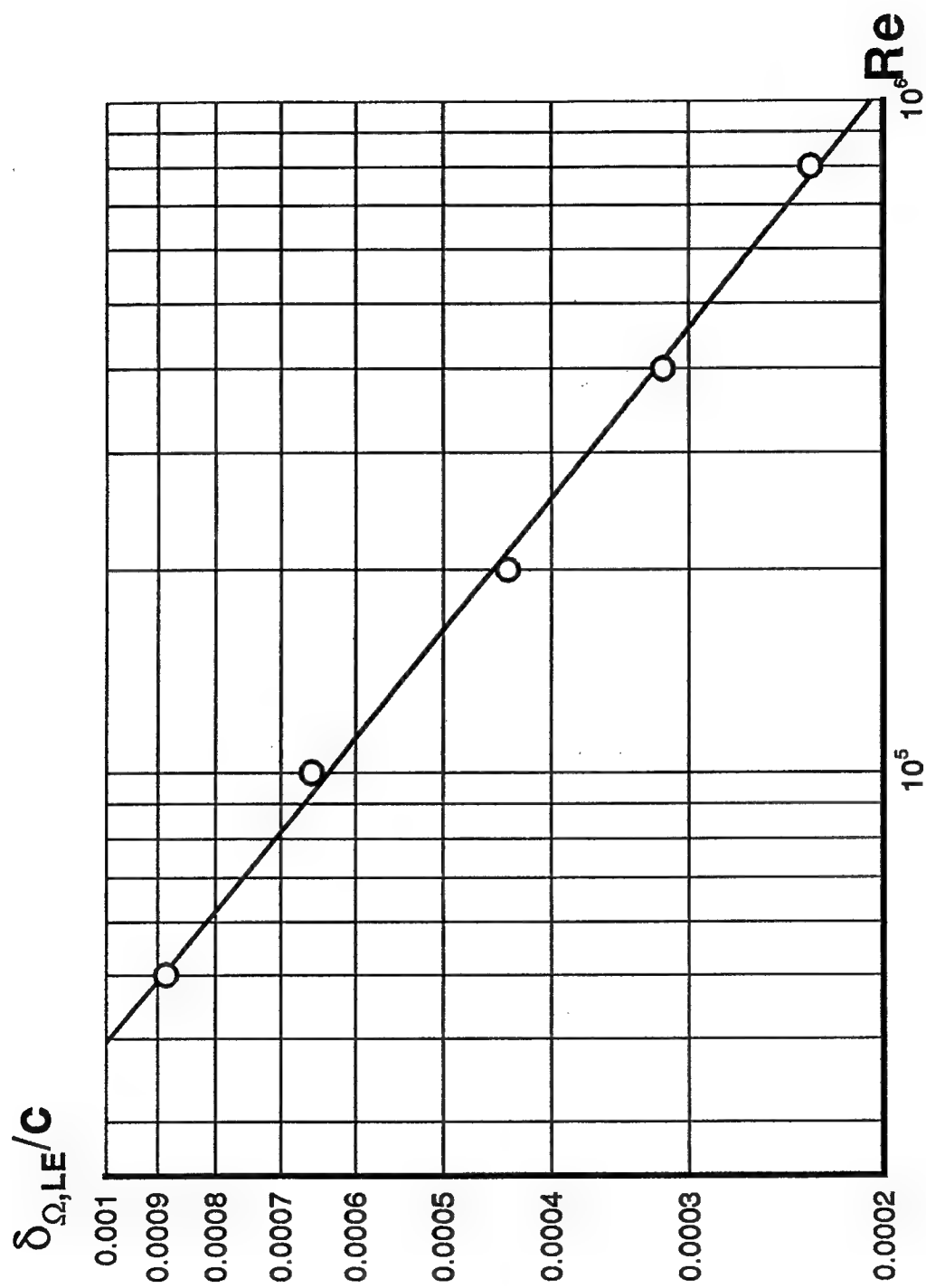


Fig. D.35 Scaling of the Upstream Boundary Layer Thickness with Reynolds Number.

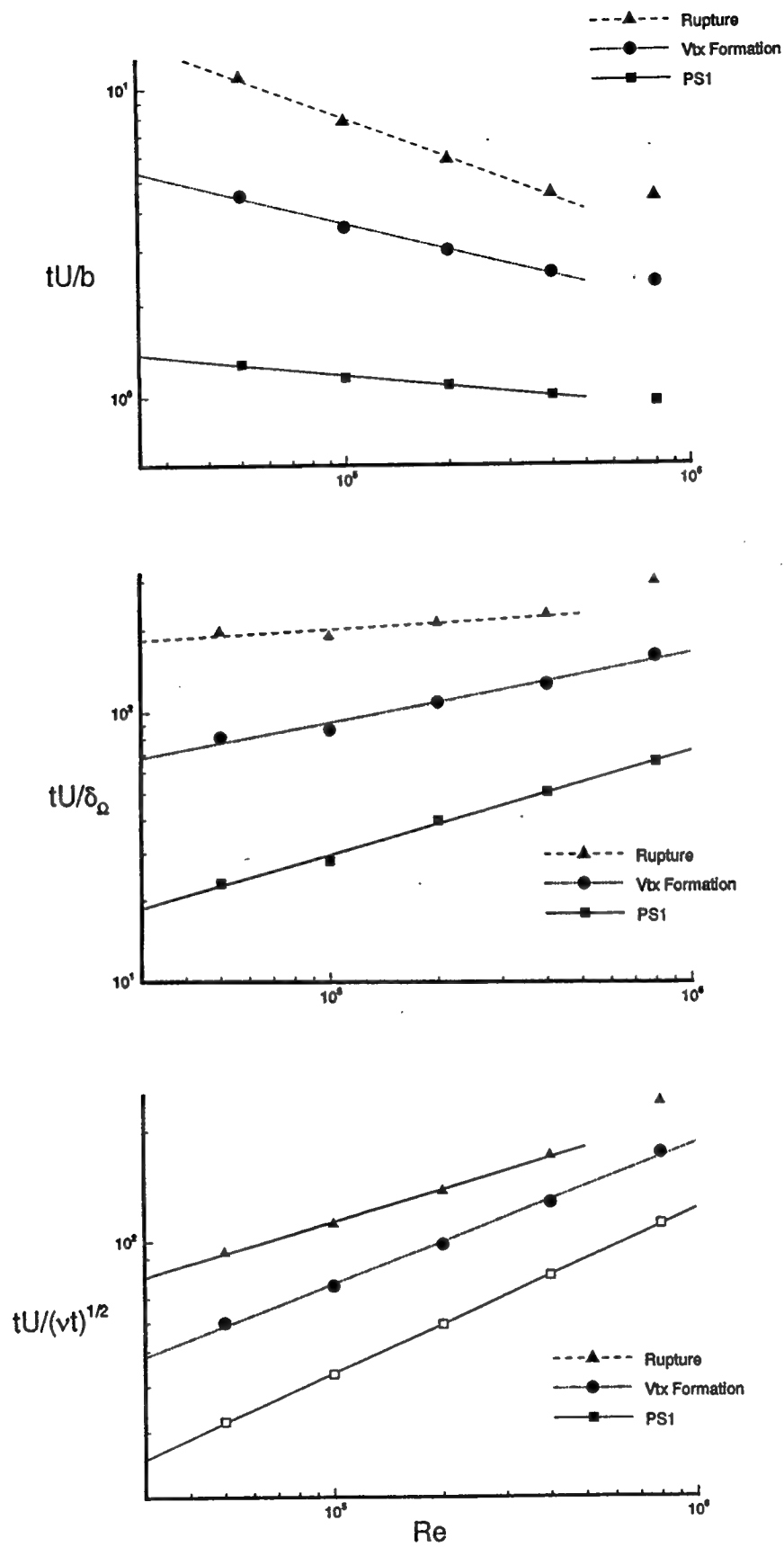


Fig. D.36 Alternate Reynolds Number Scaling of Onset Times for Primary Separation, Vortex Formation, and Rupture, Using Various Characteristic Length Scales (Top: Radius of Curvature, Center: Boundary Layer Thickness, Bottom: Viscous Length Scale).

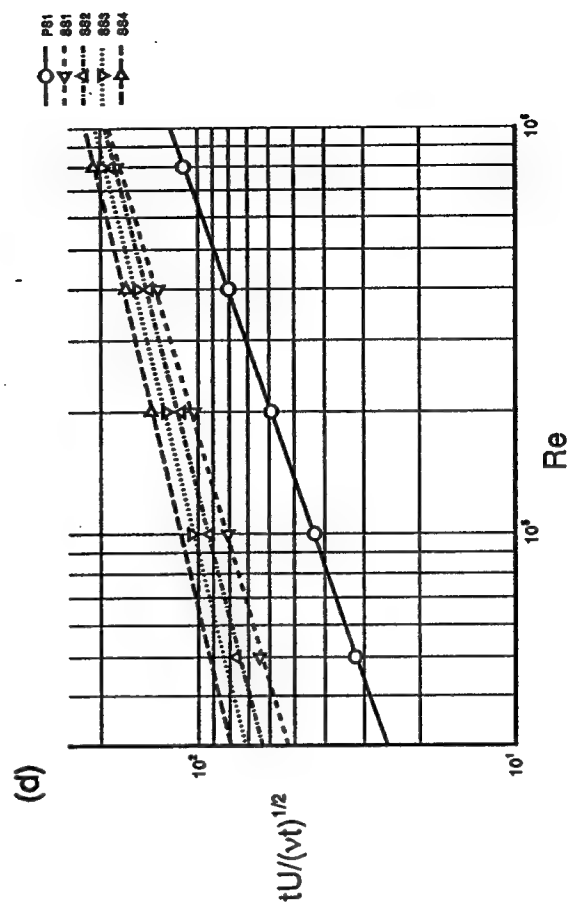
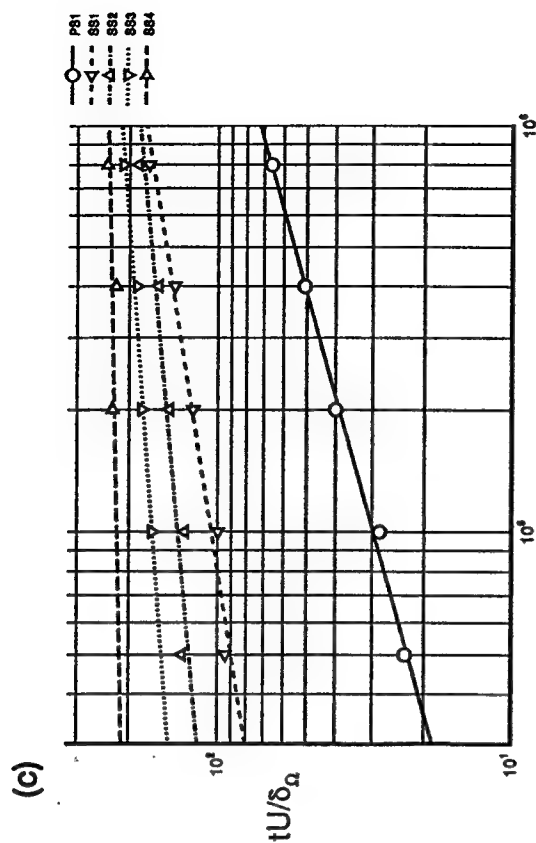
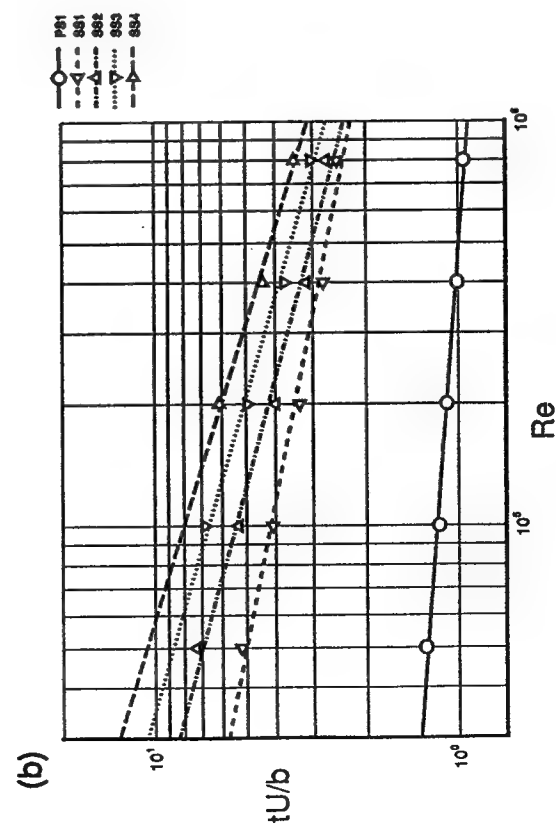
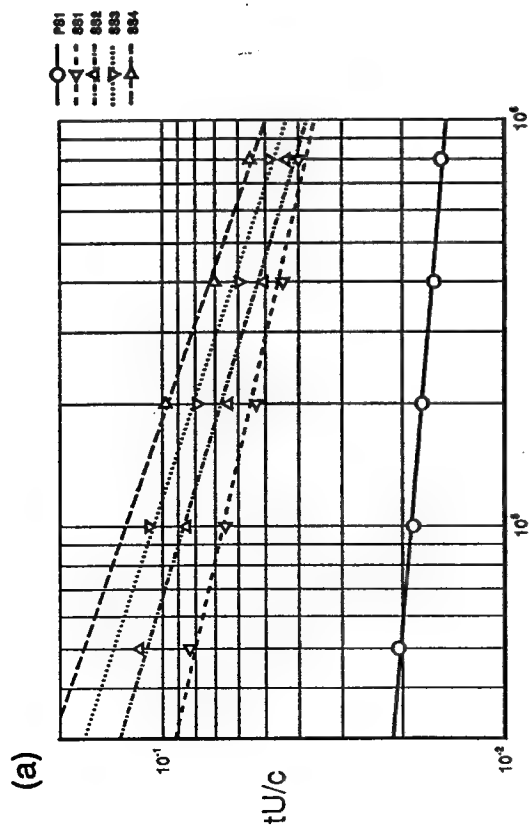


Fig. D.37 Alternate Reynolds Number Scaling of Onset Times for Incipient Primary (PS1) and Secondary (SS1, SS2, SS3, SS4) Separation Bubbles, Using Various Characteristic Length Scales ((a) Airfoil Chord, (b) Radius of Curvature, (c) Boundary Layer Thickness, (d) Viscous Length Scale).

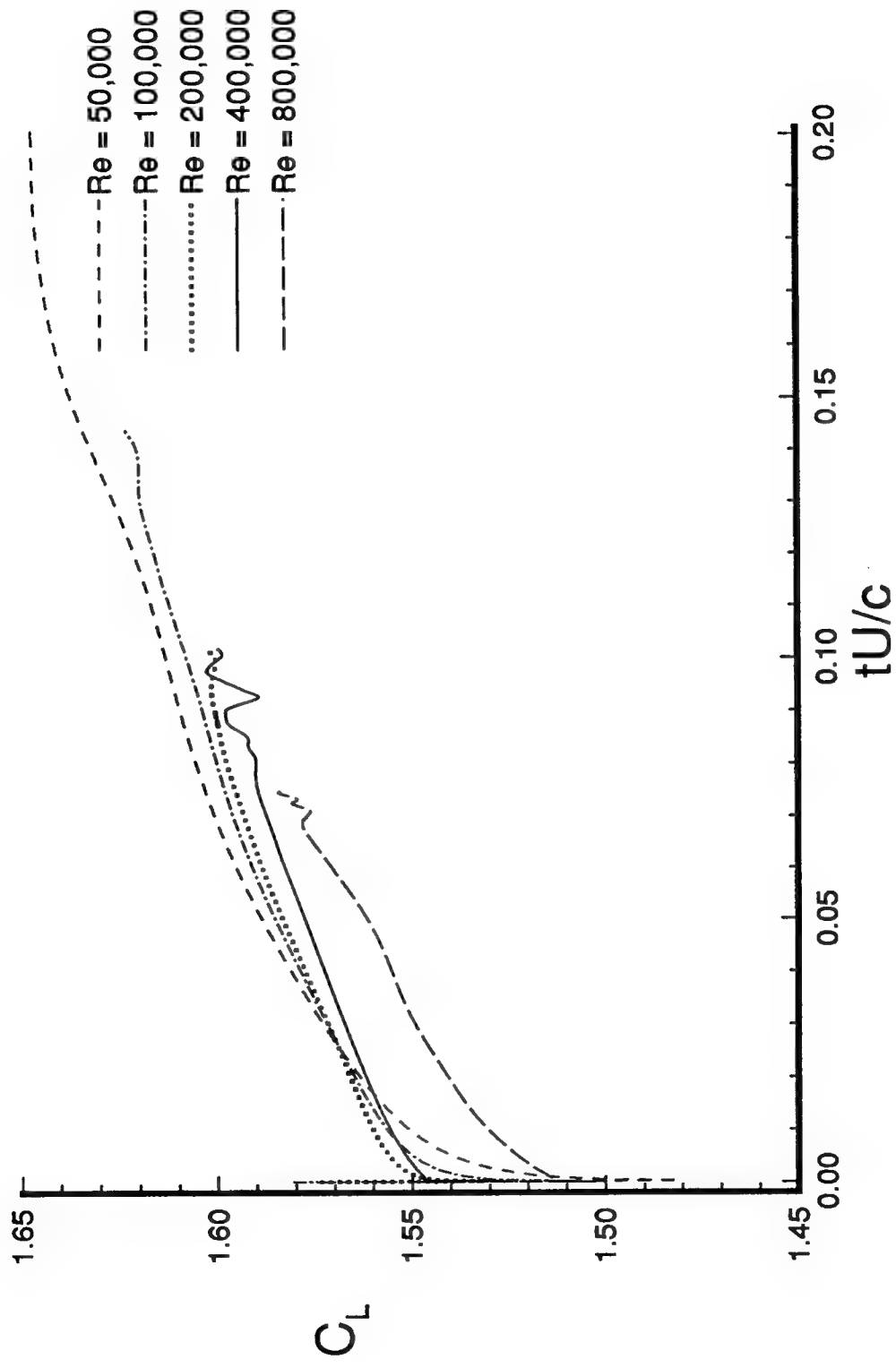


Fig. D.38 Lift Coefficient Time Histories.



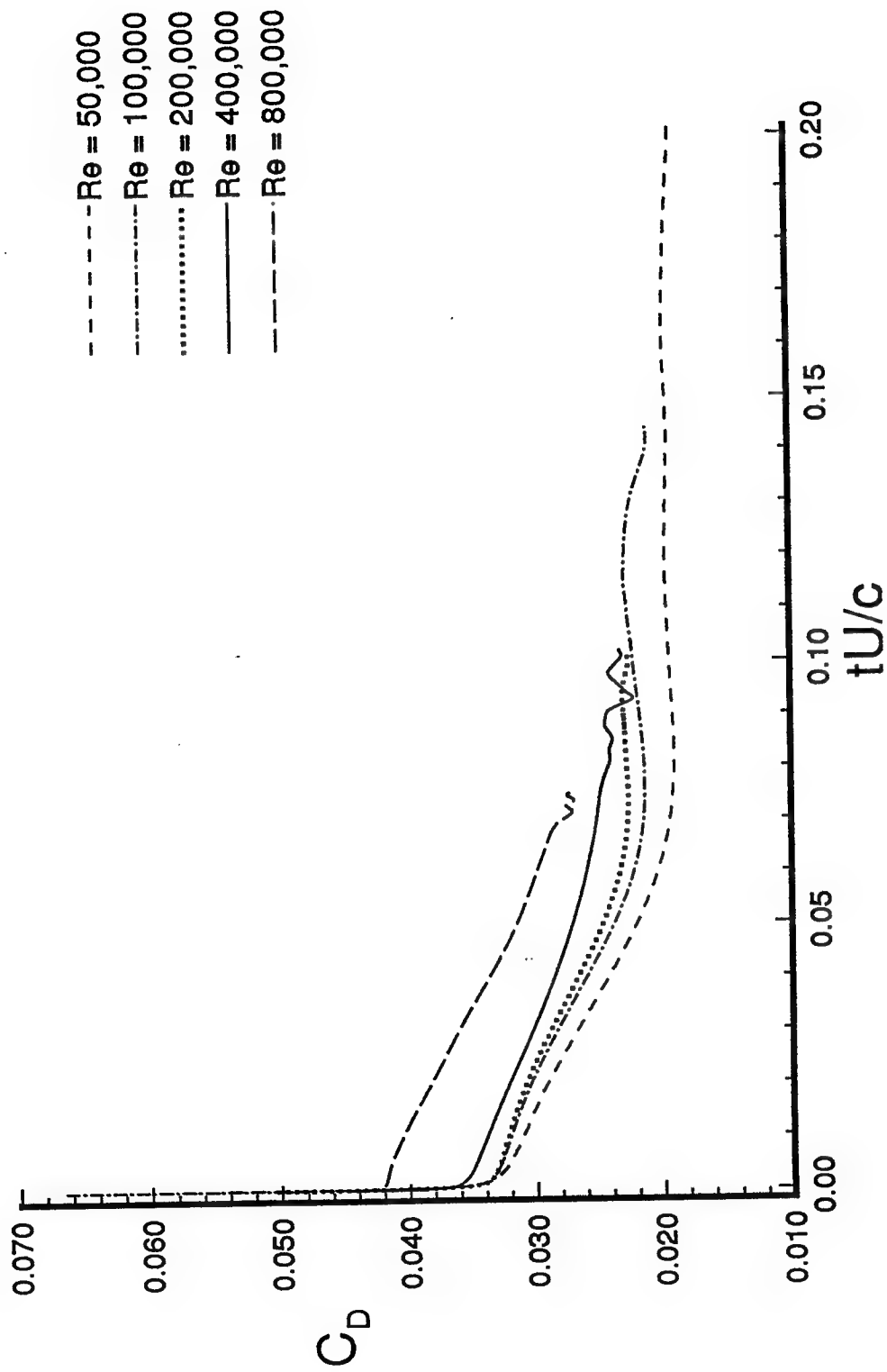


Fig. D.39 Drag Coefficient Time Histories.

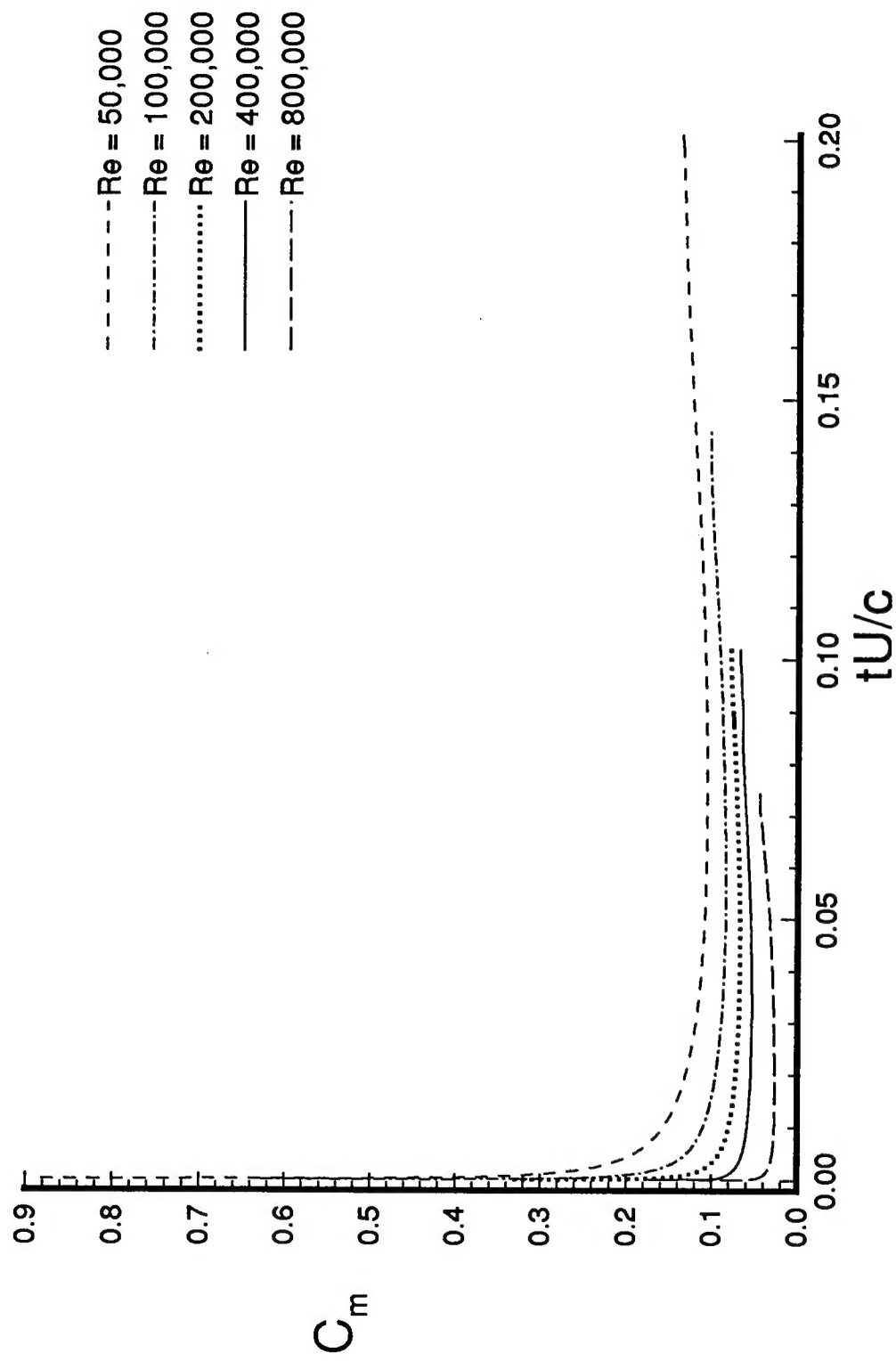


Fig. D.40 Pitching Moment Coefficient Time Histories.

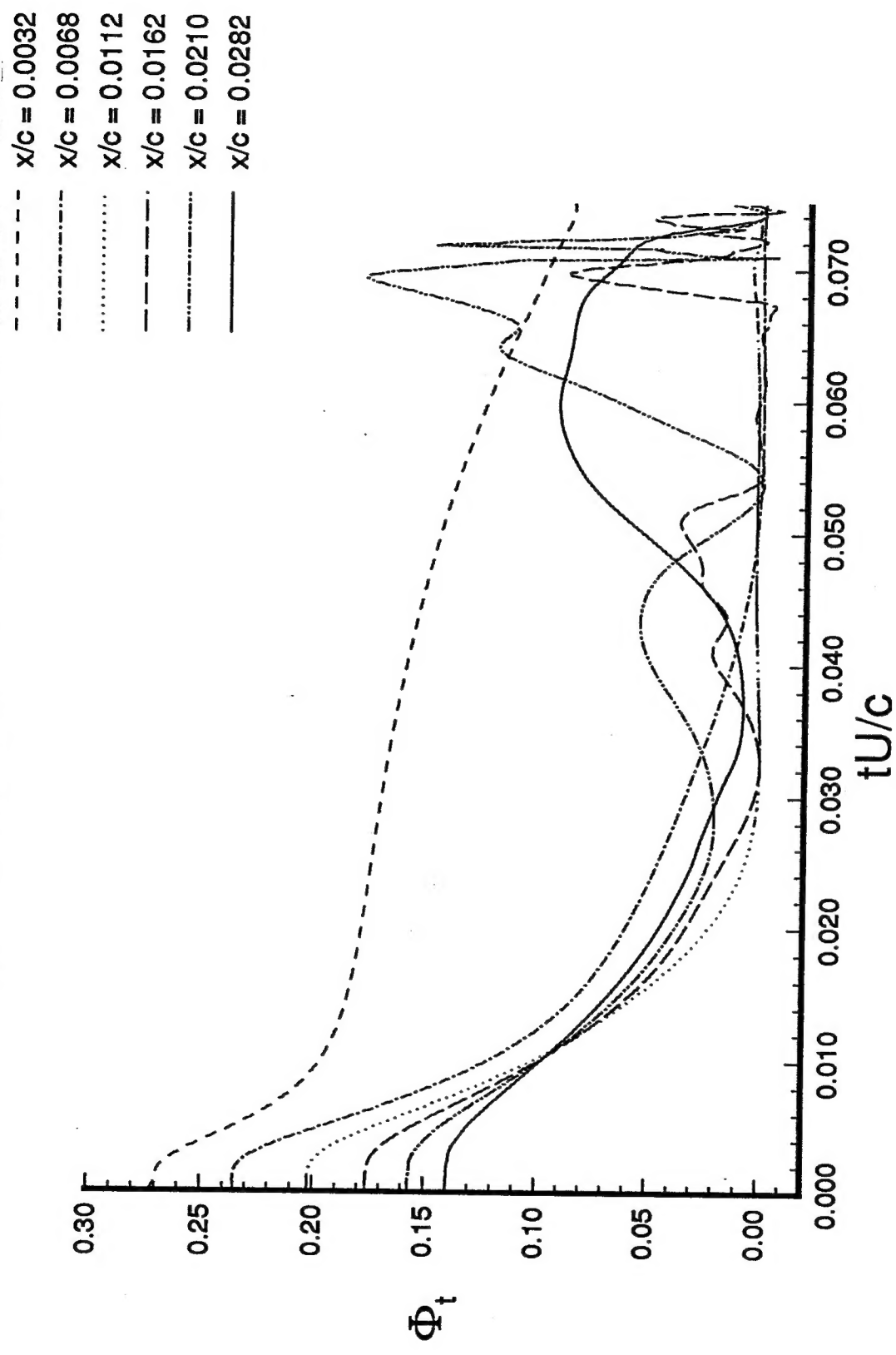


Fig. D.41 Time History of the Integrated Tangential Vorticity Flux at the Leading Edge,  
 $Re = 800,000$ .

—  $y/c = 0.0000$   
 - - -  $y/c = 0.0003$

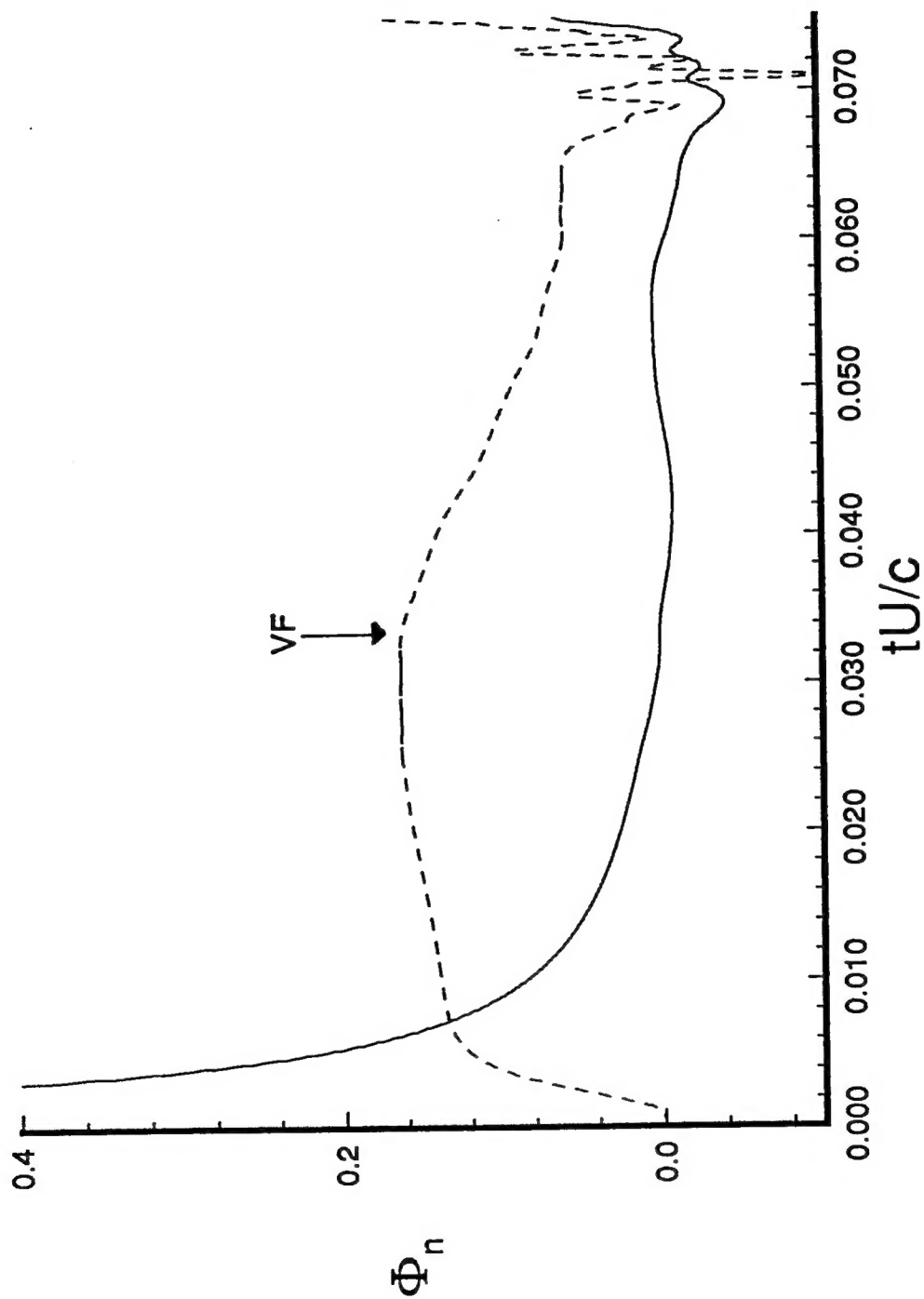


Fig. D.42 Time History of the Integrated Normal Vorticity Flux at the Leading Edge,  
 $Re = 800,000$ .

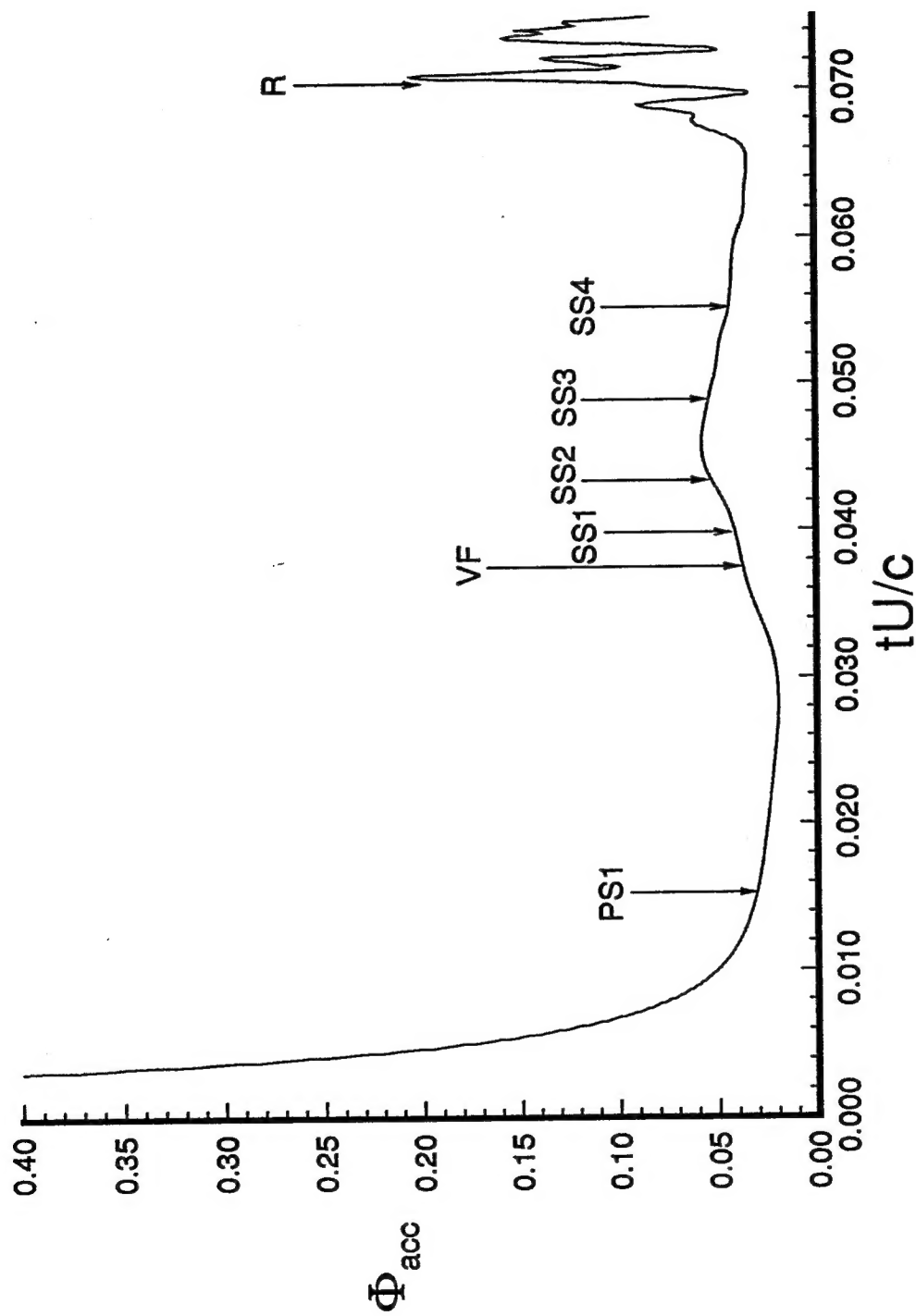


Fig. D.43 Time History of the Vorticity Accumulation at the Leading Edge,  $Re = 800,000$ .